ABSTRACT

Title of dissertation: PERFORMANCE AND LOADS OF VARIABLE TIP SPEED ROTORCRAFT AT HIGH ADVANCE RATIOS

Graham M. Bowen-Davies
Doctor of Philosophy, 2015

Dissertation directed by: Professor Inderjit Chopra
Department of Aerospace Engineering

The objective of this work is to develop a refined comprehensive analysis to predict performance and loads of high advance ratio rotors. High speeds, greater than 230 knots, are an important capability of the next generation rotorcraft. To avoid compressibility effects, the rotor tip speed has to be reduced and this means high advance ratios. At increasing advance ratios, the reverse flow region grows wherein the rotor faces flow reversal, high angles of attack and pitch rates, and large variations in dynamic pressures. A large region of flow reversal has implications for trim, performance and loads, which need to be understood in order to design high speed rotorcraft. The focus of this work is to describe the capabilities and limitations of a lifting line-based comprehensive analysis to predict high advance ratio performance with a particular focus on the thrust reversal phenomena.

Tip speed can be varied by either radius variation or rotor speed variation. Before focusing on high advance ratios, both approaches are investigated in the context of a standard helicopter configuration in free flight at a representative range

of flight conditions.

Reducing the rotor radius acts to decrease profile power at the expense of increased induced power. At moderate to high speeds, the decrease in profile power on a reduced radius rotor is greater than the increase in induced power and overall performance can be improved. Reducing rotor speed reduces profile power without impacting induced power and thus larger power reductions can be achieved across the entire flight envelope than with radius reduction. Neither approach allowed trimming the helicopter at advance ratios above 0.4 because of severe retreating side stall, which limited thrust and increased power. Augmented lift and thrust are needed for either concept to achieve significantly higher advance ratios. Vibratory loads were reduced at low speeds, but increased above the baseline at high airspeeds for both variable radius and rotor speed concepts. Variable rotor speed provides larger performance gains and appears more technologically feasible and is the better solution to high advance ratio rotorcraft.

The high advance ratio study focused on two wind tunnel tests. The UH-60A slowed rotor wind tunnel test up to an advance ratio of 1.0 measured rotor performance, airloads and vibratory loads. The analysis is modified and refined by evaluating the correlation to the UH-60A performance and airload test data. The modifications included new aerodynamic models for the fuselage and blade root, yawed flow corrections and refinements to the wake modeling. The refinements are shown to be important for correctly predicting the thrust, drag and power of the UH-60A rotor up to an advance ratio of 1.0. Flap bending loads are sensitive to strong wake interactions on the advancing tip and on the rear of the disk and can

only be predicted if the correct root aerodynamic description and location of root trailers are known. The prediction of lift near the blade root is not satisfactory and this is attributed to the highly unsteady airloads in the reverse flow that are not yet adequately understood and require more detailed testing.

Mach-scaled high advance ratio tests at the University of Maryland are the second set of test data investigated. The Maryland test included data beyond thrust reversal. The refined analysis is able to predict thrust, including thrust reversal, satisfactorily up to 1.2 advance ratio. Thrust reversal ends when the reverse flow stalls, which is seen in both the test and analysis. The test shows greater post-stall reverse flow lift and this is attributed to lift from dynamic stall. Shaft power and rotor drag are well predicted. The validated analysis is used to study the impact on thrust reversal due to blade twist, shaft angle, root cut-out, reverse flow stall angles, and yawed flow corrections. Negative blade twist shifts the region of thrust reversal to lower collectives while aft shaft angle moves thrust reversal to higher collectives. Increasing the root cut-out delays thrust reversal to higher advance ratios. Yawed flow corrections and increasing the stall limits of the reverse flow airfoil both extend the linear region of thrust reversal. The flap bending moments of the Maryland rotor are dominated by the 4/rev component and this is because the second flap mode is near 4/rev. The 4/rev harmonic content grows with advance ratio and results in large 4/rev vibratory loads at high advance ratio. The blade torsional moment includes higher harmonic oscillations that determine the peak-to-peak torsional loads and these can be simulated in the analysis by simulating dynamic stall in the reverse flow.

PERFORMANCE AND LOADS OF VARIABLE TIP SPEED ROTORCRAFT AT HIGH ADVANCE RATIOS

by

Graham M. Bowen-Davies

Dissertation submitted to the Faculty of the Graduate School of the
University of Maryland, College Park in partial fulfillment
of the requirements for the degree of
Doctor of Philosophy
2015

Advisory Committee:
Professor Inderjit Chopra, Chair/Advisor
Associate Professor James Baeder
Professor Roberto Celi
Professor Sung Lee
Professor Ramani Duraiswami
Dr. Anubhav Datta

This thesis is dedicated to all those who have endeavored to keep a smile on my face. My parents, my siblings, my wife, my friends and Monty Python.

Acknowledgments

I would be remiss not to take a moment to thank all of those who have played a part in my doctorate degree.

None of this would have happened without a professor taking an interest in a Zimbabwean kid from a South African University with a naive desire to study *Aerospace*. There is no way to adequately thank Dr. Inderjit Chopra for the faith that he has put in me from day one. Always patient, always one step ahead of me, always challenging me to push harder and persistently ignoring me when I told him that there was no way that I could make a deadline. He helped me to solve problems with a firm hand, but without holding mine and continues to provide me, and all his students, the support and time we need.

The first time that I met Dr. Chopra he mentioned that he once had a South African student by the name of Andy Bernhard. I am convinced that Andy's example is what got me here, and for that I thank him.

As well as mentoring my research, Dr. Chopra invited me to take part in the Gamera Human Powered Helicopter (HPH) project. A once-in-a-life-time experience, the project broadened by practical understanding of rotorcraft, challenged my conceptions about what was possible, provided me an outlet to get my hands dirty, found me lifelong friends, taught me more than any class could and delayed my graduation date by about two years. Dr. Chopra and Dean Pines convinced the University to support us and I will be forever grateful.

My committee members, Drs. Baeder, Celi, Datta, Lee and Duraiswami, for

engaging with my research and offering support and for the lessons that I learned under their instruction – thank you.

Dr. Nagaraj, VT, has been ever-ready to talk me down from whichever catastrophic turn my research took that month. He provided his insights and experience in helicopter design to the abstract problems I faced and he was always ready to provide me much appreciated critical feedback.

Anubhav Datta, who knew his UMARC analysis code better than anyone and helped me find enough of a foothold to now call it my own. Kumar Ravichandran battled with me against our codes, providing insight and a second perspective. Dr. Robert Ormiston of the Army AFDD always took an interest in my work and provided me valuable feedback and kind words. Dr. Tom Norman of NASA Ames and Hyeonsoo Yeo of ARMDEC were invaluable in providing insight into the analysis of the UH-60A test data. Ben Berry has been my close workmate, my HPH partner in crime, conference buddy and friend. We spent many a late night working together. Joe Schmaus has helped me untangle countless problems, was always at hand to bounce questions off and continues to find the bugs that I hid for him in UMARC.

My time at Maryland would not have been as rich without the friends I have made. Brandon Bush showed me around on my first day, took me skiing and tried to teach me drums for *Aerospace Has Got Talent*. Chen Friedman and Ananth Sridharan pulled me through 14 classes with equal parts laughter and heated debate. Chen – generous and ever ready to help me in a pinch, but never ready to cede the point in many a fruitful argument. Ananth – a frightening ability to out "Math" anyone I know and always happy to help me solve for X once we agree that it even

matters. Will Staruk, Robbie Vocke, Jared Grauer, Jürgen Rauleder, Elizabeth Weiner and many others each brought new perspectives and talents that helped my endeavors, and office chitchat that helped less, but enriched my time here.

Lizzie Nolan, my wife, has provided me just the right mix of support when I needed to work a little bit harder and longer, and a scolding when I tried working too hard and too long. She was an HPH-widow before we ever married. She has endured all the highs and lows, my long hours and late nights, my frustrations and joys and all of my promises of "one last year". I could not have hoped for more understanding, support and love. Lizzie knows how to pick me up when I'm down, lift me higher when I'm feeling up and has made this all more doable.

Of course, I could not have achieved anything without the love that my parents have given me all my life. I wanted for nothing that I needed and for little that I wanted. Their example of how to live my life, how to approach my problems and how to treat people is something that I will always be striving to replicate.

Table of Contents

List of Tables x

List of Figures xi

List of Abbreviations xvi

1 Introduction 1
1.1 Variable Rotor Radius State-of-Art . . . 2
1.2 Variable Rotor Speed for Performance . . . 7
1.2.1 Variable Rotor Speed State-of-Art . . . 8
1.2.2 Challenges for Variable Rotor Speed Implementation . . . 10
1.2.2.1 Blade Resonance . . . 11
1.2.2.2 Variable Speed Turbines Efficiency . . . 12
1.2.2.3 Variable Speed Transmission . . . 15
1.3 High Advance ratios . . . 16
1.3.1 High Speed Rotorcraft . . . 16
1.3.2 Measured Test Data for Validation Studies . . . 19
1.3.2.1 High Advance Ratio Tests Before 2010 . . . 21
1.3.2.2 UH-60A Slowed Rotor Testing . . . 23
1.3.2.3 University of Maryland Testing . . . 26
1.3.3 Prediction Tools . . . 28
1.3.3.1 Comprehensive Analysis . . . 30
1.3.3.2 Coupled CFD-CSD . . . 31
1.3.3.3 Limitations of Prediction Tools at High Advance Ratios . . . 33
1.3.4 Prediction and Validations . . . 35
1.3.4.1 Simplified Models . . . 36
1.3.4.2 Comprehensive Analysis . . . 38
1.3.4.3 CFD-CSD . . . 43
1.4 Present Research . . . 48
1.4.1 Objective . . . 48
1.4.2 Scope . . . 49

1.5 Contributions of this Dissertation . . . 52
1.6 Overview of Dissertation . . . 54

2 Variable Rotor Radius 56
2.1 Modifications to UMARC . . . 57
2.1.1 Description of Baseline Analysis . . . 58
2.1.2 Definitions of Power . . . 59
2.1.3 Variable Radius Algorithm . . . 62
2.2 Variable Radius Model . . . 67
2.2.1 Baseline UH-60A Rotor Model . . . 67
2.2.2 Description of Radius Variation Concept . . . 69
2.3 Variable Radius Performance . . . 71
2.4 Aerodynamic Analysis . . . 77
2.5 Trim with Radius Variation . . . 82
2.6 Vibratory Hubloads . . . 84
2.7 Alternative Radius Variation Concepts . . . 88
2.8 Chapter Summary . . . 90

3 Variable RPM for performance 93
3.1 Rotor Model . . . 94
3.2 Measure of Performance . . . 95
3.3 Slowed Rotor Performance . . . 95
3.4 Analysis of Slowed Rotor Aerodynamics . . . 102
3.5 Slowed Rotor Trim . . . 110
3.6 Vibratory Hubloads . . . 110
3.7 Blade Loads . . . 117
3.8 Turbine Efficiency . . . 121
3.9 Chapter Summary . . . 125

4 Investigation of the UH-60A Rotor at High Advance Ratios 130
4.1 UMARC Modifications . . . 133
4.1.1 Trim procedure at High Advance Ratios . . . 134
4.1.2 Table Look-Up in Reverse Flow . . . 136
4.1.3 Fuselage Model . . . 142
4.1.3.1 Rankine Ovaloid . . . 144
4.1.4 Trailed Wake Models . . . 147
4.1.4.1 Weissinger-L like Nearwake Models . . . 149
4.1.4.2 Fixed Geometry Nearwake . . . 151
4.1.4.3 Free Geometry Nearwake . . . 153
4.1.4.4 Farwake Trailers . . . 156
4.1.5 Yawed Flow Corrections . . . 157
4.1.6 Root Cut-Out Aerodynamics . . . 161
4.2 Description of UH-60A Test . . . 164
4.3 Performance Results . . . 167
4.3.1 Baseline Results . . . 167

4.3.2 Root Cut-Out Model . . . 172
4.3.3 Fuselage Model . . . 172
4.3.4 Yawed Flow Corrections . . . 178
4.3.5 Nearwake in Reverse Flow . . . 178
4.3.6 Wake Trailers . . . 181
4.3.6.1 Dual Wake Trailers . . . 181
4.3.6.2 Dual Wake Trailers and Root Trailer . . . 184
4.3.7 Summary of Performance Prediction . . . 189
4.4 Airloads Prediction . . . 191
4.4.1 Baseline Sectional Airloads . . . 191
4.4.2 Modified UMARC results . . . 198
4.4.2.1 Dual Wake Trailers . . . 198
4.4.2.2 Root Modeling . . . 200
4.4.2.3 Nearwake . . . 202
4.4.3 Airloads Summary . . . 203
4.5 Blade Loads Predictions . . . 204
4.5.1 Flap Bending Moment . . . 207
4.5.2 Torsion Moment and Pitch Link Loads . . . 207
4.6 Chapter Summary . . . 211

5 University of Maryland High Advance Ratio Tests 216
5.1 UMARC Modeling . . . 218
5.2 Test Description . . . 219
5.3 High Advance Ratio Performance Validation . . . 222
5.3.1 Thrust Prediction . . . 223
5.3.2 Physics of Thrust Reversal Prediction . . . 227
5.3.3 Shaft Power and Rotor Drag . . . 230
5.3.4 Trim Cyclics . . . 234
5.4 High Advance Ratio Studies . . . 236
5.4.1 Shaft Angle . . . 237
5.4.2 Blade Twist . . . 239
5.4.3 Reverse Flow Stall . . . 242
5.4.4 Root Cut-out . . . 242
5.4.5 Yawed Flow Corrections . . . 244
5.5 High Advance Ratio Structural Loads . . . 246
5.5.1 Flap Bending Loads . . . 246
5.5.2 Torsion Bending Loads . . . 251
5.5.3 Vibratory loads . . . 255
5.6 Airloads Correlation . . . 258
5.6.1 Description of CFD . . . 258
5.6.2 Low Advance Ratio Validation with CFD . . . 259
5.6.3 Normal Force Collective Sweeps . . . 261
5.6.4 Comparison to UH-60A Airloads . . . 266
5.7 Chapter Summary . . . 267

6 Summary and Conclusions 271
6.1 Key Conclusions 273
6.2 Future Work 279

Bibliography 283

List of Tables

2.1 Rotor properties. 68
2.2 Variation of key aerodynamic properties 70
2.3 Summary of variable radius cases evaluated 71
2.4 Aircraft blade loading coefficient with increasing gross weight 74

3.1 Summary of variable rotor speed cases evaluated 94

4.1 UH-60A blade properties. 165
4.2 Test conditions for the UH-60A tests. 166
4.3 Airload and bending moment comparison points. 166
4.4 Summary of UMARC modifications for the UH-60A test. 187
4.5 Blade frequency variation at 100% and 40% RPM. 204

5.1 Maryland rotor properties (at 100% rotor speed). 219
5.2 Blade sectional properties. 219
5.3 Test conditions for the Maryland rotor tests. 222
5.4 Trim controls spanning thrust reversal at $\mu = 1.03$. 225

List of Figures

1.1 Variable radius rotor concepts identified by Linden. 4
1.2 Variable diameter rotor (VDR) using two telescoping sections, built by Young at Bell. 5
1.3 Schematic of the Sikorsky TRAC rotor concept. 6
1.4 Typical envelope of tip speed selection for edgewise rotors. 7
1.5 The Boeing A-160 Hummingbird used rotor speed variation (up to 60%) to achieve high endurance. 9
1.6 Fanplot of the UH-60A Black Hawk rotor. 100% = 258 RPM. 11
1.7 Typical variation of SFC with turboshaft speed. 13
1.8 High speed rotorcraft flight demonstrators and production tiltrotors. . 17
1.9 Two recent high advance ratio rotor tests. 24
1.10 RCAS predicted collective for constant thrust rotor at high advance ratio. 37
1.11 CAMRAD II correlation with high advance ratio teetering rotor. . . . 39
1.12 CAMRAD II correlation of induced + profile power for two high advance ratio tests. 40
1.13 CAMRAD II correlation by Yeo of induced plus profile power, showing effect of shank drag. 41
1.14 CAMRAD II correlation by Yeo of sectional normal force and pitching moment at r/R = 0.92. 42
1.15 Wake visualizations with increasing advance ratio from Helios. 44
1.16 Comparison of prediction from Helios, RCAS and CAMRAD II of the sectional normal force. 46
1.17 Comparison of prediction from Helios, RCAS and CAMRAD II of the sectional pitching moment. 47

2.1 Components of rotor power vs. airspeed for a 14,000 lb thrust rotor. . 61
2.2 Variable radius concept: Morphing area, with nominal mass redistribution. 64
2.3 Variable radius concept: Variable root cut-out, with nominal mass redistribution. 64
2.4 Variation of blade twist with radius – 100% and 80%. 66

2.5 Validation of UMARC power prediction with UH-60A Black Hawk airloads data ($C_T/\sigma = 0.0783$). 67
2.6 Schematic of variable radius concept with morphing blade area. . . . 69
2.7 Variation of rotor power at 14,000 lb with varying rotor radius. 72
2.8 Reduction of rotor power at 16,000 lb, 18,000 lb and 20,000 lb with varying rotor radius. 75
2.9 Maximum % power reduction and associated radius schedule (14,000 lb - 20,000 lb). 76
2.10 Induced and profile power variation with reducing rotor radius (W = 18,000 lb) 77
2.11 Angle of attack and stall locus at 120 knots (W = 18,000 lb) (Disc area is scaled to represent the radius and the dashed circle indicates the baseline rotor) 79
2.12 Total and profile power locus at 120 knots (W = 18,000 lbs) 81
2.13 Vehicle trim control and shaft orientation angles vs. airspeed at 18,000 lb with varying rotor radius 83
2.14 Variation of rotor frequencies with radius. 84
2.15 4/rev hubloads vs. airspeed at 18,000 lb with varying rotor radius . . 85
2.16 4/rev hubloads vs. advance ratio at 18,000 lb with varying rotor radius 87
2.17 Alternative variable radius concepts 88
2.18 Comparison of power for alternative radius variation concepts at 14,000 lb. 89

3.1 Variation of rotor power at 14,000 lb with varying RPM. 96
3.2 Reduction of rotor power at 16,000 lb, 18,000 lb and 20,000 lb with varying RPM. 99
3.3 Maximum % power reduction and associated RPM schedule (14,000 lb - 20,000 lb). 100
3.4 Change in torque for the minimum power RPM schedule (14,000 lb - 20,000 lb). 100
3.5 Induced power vs. airspeed at 18,000 lb with reduced RPM 102
3.6 Profile power vs. airspeed for reduced RPM 103
3.7 Angle of attack and stall locus for 18,000 lb thrust case at 80 knots with RPM variation. 104
3.8 Non-dimensional total power vs. advance ratio. 105
3.9 Low and high advance ratio aerodynamic environment, effect of RPM. 106
3.10 Sectional lift to drag ratio at 75% span and 80 knots. 108
3.11 Comparison of the baseline and power-optimized non-dimensional thrust for each rotor thrust. 108
3.12 Trim angles vs. airspeed at 18,000 lb with reduced RPM 111
3.13 Fanplot for the UH-60A Blackhawk. 112
3.14 4/rev hubloads vs. airspeed at 18,000 lb 113
3.15 Contours of percent change in 4/rev hubloads as a function of rotor speed and airspeed. 115

3.16 4/rev vertical and in-plane shear forces and moments vs. advance ratio at 18,000 lb. . . . 116
3.17 Half peak-to-peak flap bending vs. spanwise location at 18,000 lb. . . 118
3.18 3, 4 and 5/rev harmonics of flap bending vs. spanwise location at 18,000 lb. . . . 118
3.19 Half peak-to-peak torsion moment vs. spanwise location at 18,000 lb. 120
3.20 Typical variation of SFC with turboshaft speed. . . . 122
3.21 Variation of SFC with shaft power. . . . 123
3.22 Maximum % fuel flow rate reduction and associated RPM schedule. . 123
3.23 SFC for minimum fuel flow rate. . . . 124

4.1 Error in normal force from small angle approximations. . . . 139
4.2 Error in lift from small angle approximations in table look-up. . . . 140
4.3 NASA's Large Rotor Test Apparatus (LRTA) fuselage. . . . 142
4.4 Inflow at the rotor plane due to HART fuselage. . . . 143
4.5 Rankine Oval in 2D. . . . 144
4.6 Sketch of LRTA fuselage with the induced upwash at advance ratios of 0.3 and 1.0. . . . 146
4.7 Trailed near and far wake geometry. . . . 147
4.8 CFD wake visualization of underside of retreating blade at increasing advance ratios showing the formation of multiple trailers 148
4.9 Effective angle of attack and circulation strength at $\mu = 1.0$, fixed geometry nearwake. . . . 152
4.10 Nearwake geometry deformed with the free stream at $\mu = 1.0$. . . . 153
4.11 Effective angle of attack and circulation strength at 270° azimuth, $\mu = 1.0$, free geometry nearwake 154
4.12 Effective angle of attack and circulation strength at 180° azimuth, $\mu = 1.0$, free geometry nearwake 155
4.13 Geometry of yawed flow across a blade. . . . 158
4.14 Radial flow angles (degrees) around the azimuth at high advance ratio. 159
4.15 UH-60A root geometry. . . . 162
4.16 Baseline rotor performance and predictions for increasing advance ratio. 168
4.17 Thrust coefficient corrected for offset. . . . 169
4.18 Effect of root cut-out model on performance predictions. . . . 171
4.19 Effect of fuselage on performance predictions. . . . 173
4.20 Contours of the effect of the fuselage on angle of attack and power. . 174
4.21 Effect of yawed flow corrections on performance predictions 176
4.22 Contours of the effect of the yawed flow corrections on stall. . . . 177
4.23 Effect of reverse flow nearwake inflow on performance predictions. . . 179
4.24 Contours of the effect of nearwake in the reverse flow on stall. . . . 180
4.25 Effect of dual wake trailers on performance predictions. . . . 182
4.26 Dual wake system and contours of the change in normal force and power from dual wake trailer system, $\mu = 0.7$. . . . 183
4.27 Effect of dual wake trailers and root trailer on performance predictions. 185
4.28 Root wake system and contours of the change in normal force, $\mu = 0.3$. 186

4.29 Contours of the change in normal force and power from dual wake trailer system, $\mu = 0.9$, 4° collective, 0° shaft angle) 187
4.30 Rotor performance and predictions with UMARC modifications, for increasing advance ratio. 188
4.31 UH-60A lift-to-drag ratio with baseline and modified predictions. . . 190
4.32 Sectional normal force, r/R = 92%. 192
4.33 Sectional normal force, r/R = 22.5%. 193
4.34 Sectional pitching moment, r/R = 92%. 196
4.35 Sectional pitching moment, r/R = 22%. 197
4.36 Sectional normal force with dual wake trailers, r/R = 92%. 199
4.37 Sectional normal force with dual wake trailers, $\mu = 0.4$. 201
4.38 Effect of reverse flow nearwake on normal force and pitching moment,r/R = 22.5%, $\mu = 0.5$. 202
4.39 Oscillatory flap bending moment, r/R = 50%. 205
4.40 Vibratory (3-5/rev) flap bending moment, r/R = 50%. 206
4.41 Oscillatory torsional moment, r/R = 50%. 208
4.42 First 16 harmonics of torsional moment, r/R = 50%. 209
4.43 First 16 harmonics of torsional moment at pitch link, r/R = 5%. . . . 210
4.44 Pitch link loads 211

5.1 University of Maryland rotor in Glenn L. Martin wind tunnel. 220
5.2 Layout of the strain gauges and pressure sensors on the blade. 221
5.3 Rotor thrust versus collective. 224
5.4 Change of thrust slope with advance ratio, $\alpha_s = 0°$. 225
5.5 Airloads showing thrust reversal trend with increasing collective, $\mu = 1.03$ 226
5.6 Rotor trim cyclic at thrust reversal, $\mu = 1.03$. 229
5.7 Pressure distribution at 30% radius showing dynamic stall vortex. . . 229
5.8 Shaft power versus collective. 231
5.9 Shaft drag versus collective. 232
5.10 Rotor lift-to-drag ratio versus thrust. 233
5.11 Trim cyclics versus collective 235
5.12 Thrust reversal with 4° aft shaft angle. 238
5.13 Aft shaft angle delays stall in reverse flow to higher collectives. 239
5.14 Effect of negative blade twist on performance and thrust reversal, $\mu = 1.03$. 240
5.15 Stall locus for a rotor with blade twist. 241
5.16 Thrust reversal with modified tables. 241
5.17 Effect of root cut-out on performance, $\mu = 1.03$. 243
5.18 Effect of root cut-out on thrust slope with advance ratio. 244
5.19 Effect of yawed flow corrections on performance, $\mu = 1.03$. 245
5.20 Fanplot for 2014 Maryland rotor. 247
5.21 Oscillatory flap bending moment (M_β) at r/R = 50%. 248
5.22 Harmonics of flap bending moment at r/R = 50%. 248
5.23 Sensitivity of flap bending to 2^{nd} flap frequency at r/R = 50%. 249

5.24 Effect of root wake trailer on flap bending loads at r/R = 50%. 249
5.25 Oscillatory torsional moment ($M_{Torsion}$) at r/R = 30%. 252
5.26 Harmonics of torsional moment at r/R = 30%. 252
5.27 Dynamic stall simulated with normal force impulse at $^3/_4$ chord in reverse flow, $\mu = 1.03$. 253
5.28 Torsion moment with dynamic stall-like lift increment for $\mu = 1.03$ at r/R = 30%. 253
5.29 4/rev Vertical shear force versus collective. 256
5.30 4/rev hubloads versus collective. 257
5.31 Sectional normal force comparison with CFD, r/R = 30%. 259
5.32 Sectional normal force, r/R = 30%, $\mu = 0.62$. 262
5.33 Sectional normal force, r/R = 30%. $\mu = 1.03$. 264
5.34 Sectional normal force comparison of Maryland and UH-60A, $\mu \approx 0.6$. 265

List of Abbreviations

a	Distance of source/sink pair from center of Rankine ovaloid
AoA	Angle of attack
A	Rotor disc area
c	Chord
c_d	Airfoil drag coefficient
$c_{d_{2D}}$	Airfoil drag coefficient in two dimensional flow
$c_{d_{shank}}$	Drag coefficient of the blade shank
c_l	Airfoil lift coefficient
$c_{l_{2D}}$	Airfoil lift coefficient in two dimensional flow
c_m	Airfoil pitching moment coefficient
$c_{m_{2D}}$	Airfoil pitching moment coefficient in two dimensional flow
c_r	Radial drag coefficient
$c_{0,1}$	Linear coefficients of lift
$d_{0,1}$	Linear coefficients of lift
f	Flat plate drag
$f_{0,1}$	Linear coefficients of lift
C_C	Blade chordwise force coefficient
$C_{Ci,Co}$	Blade chordwise force from airfoil lift (i), drag (o) coefficient
C_C	Rotor drag force coefficient
C_H	Axial force coefficient
$C_{Hi,Ho}$	Axial force from airfoil lift (i), drag (o) coefficient
C_M	Blade pitching moment coefficient
C_N	Blade normal force coefficient
C_P	Shaft power coefficient
C_Pi	Induced power coefficient
C_Po	Profile power coefficient
C_Pp	Parasitic power coefficient
C_Q	Shaft torque coefficient
$C_{Qi,Qo}$	Shaft torque from airfoil lift (i), drag (o) coefficient
C_T	Thrust coefficient
$C_{Ti,To}$	Thrust from airfoil lift (i), drag (o) coefficient
C_X	Propulsive force coefficient, wind axis
F_{xy}	4/rev in-plane force
F_z	4/rev vertical shear force
$I_{j,i}$	Influence coefficients
L_v	Aerodynamic force in chordwise direction (positive forward)
L_w	Aerodynamic force in normal direction (positive up)
L/D_e	Rotor lift to drag ratio
M	Mach number
M_{ADV}	Advancing tip Mach number
M_{xy}	4/rev in-plane moment
M_ϕ	Aerodynamic pitching moment about quarter chord (positive nose up)
N_b	Number of rotor blades
R_o	Radius of Rankine ovaloid

RPM	Revolutions per minute
u_p	Velocity normal to chord
u_{p_i}	Induced velocity normal to chord
u_r	Velocity along span
u_t	Velocity normal to airfoil leading edge
V	Wind speed
V_{b_i}	Velocity induced by the bound vortex
V_{NWK_i}	Velocity induced by the trailed wake
V_{tip}	Tip speed
x_s	Stagnation point
α	alpha
α_e	Effective angle of attack (with nearwake inflow)
α_s	Longitudinal shaft angle (positive aft)
β_{1C}	Longitudinal flapping angle
β_{1S}	Lateral flapping angle
γ	Lock number
Γ	Source/sink or circulation strength
λ	Total inflow coefficient
λ_i	Induced inflow coefficient
Λ	Yawed flow angle
μ	Advance ratio
ϕ_s	Lateral shaft angle (Positive for advancing side up)
ρ	Density
σ	Rotor solidity
θ_0	Collective
θ_{1C}	Longitudinal cyclic
θ_{1S}	Lateral cyclic

Chapter 1: Introduction

The motivation of this dissertation is to investigate the aeromechanics of a helicopter rotor at high advance ratios. High speeds in excess of 220 knots is the specific goal for the next generation of military rotorcraft, while high speeds help provide critical capability to search and rescue operations and can improve cost effectiveness for civilian applications. Helicopters' high speed performance is now limited by compressibility effects on the advancing side tip and reversed flow including stall on the retreating side, which in turn result in high power requirements and excessive vibrations. Relieving advancing side compressibility can be achieved by reducing the rotor tip speed through either radius or rotor speed reduction. Because hover performance always remains important for any rotorcraft, high tip speeds continue to be necessary at low airspeeds and therefore variable tip speed rotors appear an attractive option. The first objective of this research is to investigate both variable radius and variable rotor speed for their suitability to a high speed rotorcraft concept. Following this, the aeromechanics of a rotor with slowed tip speed at high airspeeds is investigated. Reducing the tip speed relative to the airspeed implies high advance ratios. At high advance ratios, a large region of reverse flow exists on the retreating side, which reduces rotor thrust and makes steady-level and trimmed

flight more challenging. The highly asymmetric flow and large cyclic inputs contribute to large lift differentials, complex wake formation, unsteady airloads and a potential for dynamic stall. These complex airloads and their interaction with the rotor are investigated using a comprehensive rotorcraft analysis, with modeling refinements, to gain a fundamental understanding of rotor performance and loads at high advance ratios.

This chapter introduces the subjects of variable rotor radius and variable rotor speed, focusing on improving rotor performance within the normal flight envelope. Next, the history of high advance ratio aircraft to date is discussed, followed by descriptions of rotor experiments that achieved high advance ratios and the state-of-art in high advance ratio predictive capability. Finally, the goals, scope and important conclusions of the current research are summarized followed by an overview of the dissertation.

1.1 Variable Rotor Radius State-of-Art

Variable radius rotors have been investigated for both edgewise rotors and tiltrotors to reduce the compromise between hover and cruise performance. In hover, larger disc area reduces the rotor induced power for a given thrust, while reducing radius minimizes profile power by avoiding compressibility effects at higher airspeeds as well as through the reduction of exposed surface area. Variable radius concepts require mechanisms in the rotating rotor frame that are able to extend and retract each rotor blade. Designing a concept to be light weight, robust and damage tolerant

in the high centrifugal loading environment is quite challenging, and as a result, variable radius actuation has not been used in a production helicopter. There have been some research activities on this topic and the following is an overview of important tests and analyses that have investigated variable radius concepts.

Linden [1] carried out a survey of known radius variation concepts including patents dating to 1913. The aim of the study was to identify the concepts that could be applied to a large compound rotorcraft and evaluate the most promising concepts. Linden described three broad types of radius variation concepts. Telescoping blades are composed of at least two blade sections with some mechanical mechanism to withdraw or extend one section over another to achieve a desired radius (fig. 1.1a). The second concept of folding rotors incorporates hinges along the span that allow the blades to fold in flight (fig. 1.1b). The folding rotor concept was intended for parachute-like deployment where the rotor extends and locks at start up with no provision for retraction, and hence, is not suitable for active radius variation. The third concept of a flexible rotor requires a portion of the rotor to be extremely flexible so that it can be retracted by rolling onto a drum (fig. 1.1c). Linden judged that the final flexible rotor concept was the most promising although significant challenges relating to control were identified. Sicard and Sirohi [2] modeled and tested this concept on a small scale rotor (diameter of 18 inches) on the benchtop and showed that the concept remained free from flutter when fully deployed.

The telescoping blade concept has shown the most potential for the practical implementation of radius variation. Fenny [3] describes the history of the Variable Diameter Rotor (VDR) rotor as well as his recent contributions. The VDR rotor,

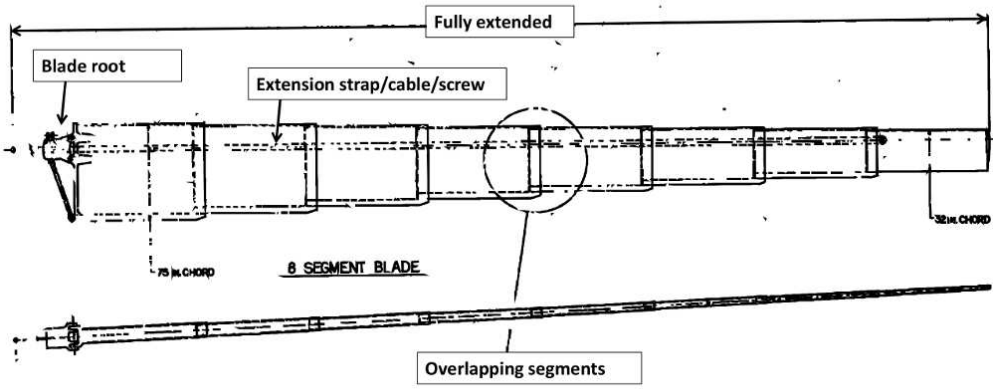

(a) Telescoping blade concept.

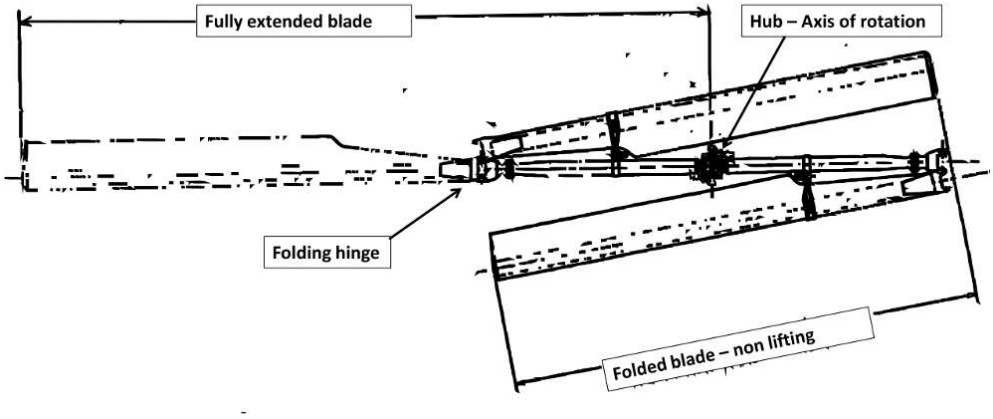

(b) Folding blade concept.

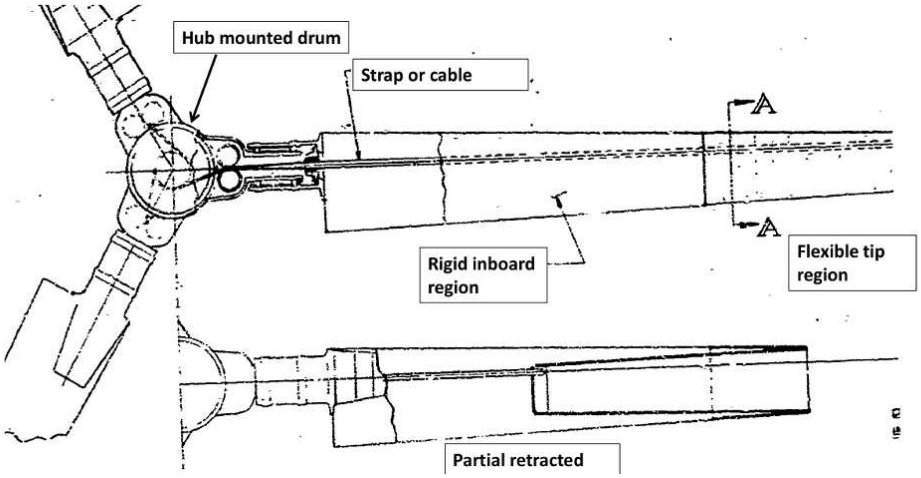

(c) Flexible blade concept.

Figure 1.1: Variable radius rotor concepts identified by Linden [1] (edited for clarity).

(a) Fully extended. (b) Retracted.

Figure 1.2: Variable diameter rotor (VDR) using two telescoping sections, built by Young at Bell [3].

built by Young and based on his own patent, is reported to be the first full scale rotor to achieve powered radius variation (37.5%) at full operating RPM in 1964 (fig. 1.2). The design used centrifugal extension and cable retraction of the outboard rotor section. The VDR rotor was further developed at Bell until the end of the program in 1971. Fenny identified many of the technology hurdles that stalled a practical implementation of the VDR rotor and in his 2005 paper showed a design for a new extension/retraction mechanism which, together with digital flight control and health monitoring, may overcome many of those hurdles.

Sikorsky's telescoping TRAC rotor (name derived from telescoping rotor aircraft) used a jack screw concept to actively control rotor radius by moving the blade along the spar [4, 5]. The one eighth dynamically scaled rotor was tested in 1969, 1970 and 1972, and performance, blade stresses, vibrations and aeroelastic stability were measured at maximum radius up to 150 knots and at minimum radius up to 400 knots. The TRAC concept showed the potential for improved performance and reduced vibration for a compound or stopped rotor configuration. The concept was

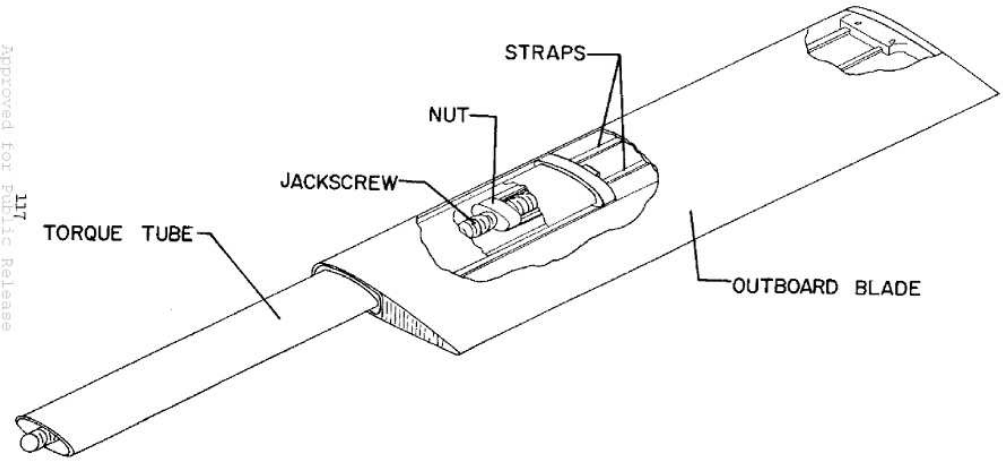

Figure 1.3: Schematic of the Sikorsky TRAC rotor concept [4].

redeveloped as the VDTR (Variable Diameter Telescoping rotor) in the 1990s for tiltrotor applications, and wind tunnel tests were carried out [6]. The tests successfully demonstrated the feasibility of the VDTR concept for tilt rotor applications and included data points in hover, conversion and cruise. No instabilities were encountered and blade loads were considered acceptable. The model did not allow for full tip speed testing (half tip-speed was used) and control stops limited the test envelope during conversion. Prabhakar and Gandhi [7] developed a centrifugally actuated variable radius concept for a model-scale rotor, which was tuned via a spring connecting the outboard sliding portion to a fixed inboard portion. Variation in rotor speed directly varied rotor radius. They found that the performance of the concept degraded significantly as compared to a baseline rotor because of the high rotational speeds required to achieve extension (although, they suggested that the inclusion of a blade locking mechanism could deliver improved performance).

Recently, an analysis was carried out by Mistry and Gandhi [8] to evaluate

the performance potential of both radius and rotor speed variation. They showed that radius variation was more effective to improve performance for high thrust, high altitude rotors at low speeds and that larger improvement could be achieved by reducing RPM in combination with radius variation. These studies are very insightful, but incorporated simplified structural and aerodynamic modeling of the blades.

In summary, the variable radius concept offers a potential for performance improvement but it is quite mechanically involved to implement radius variation devices in a full-scale system.

1.2 Variable Rotor Speed for Performance

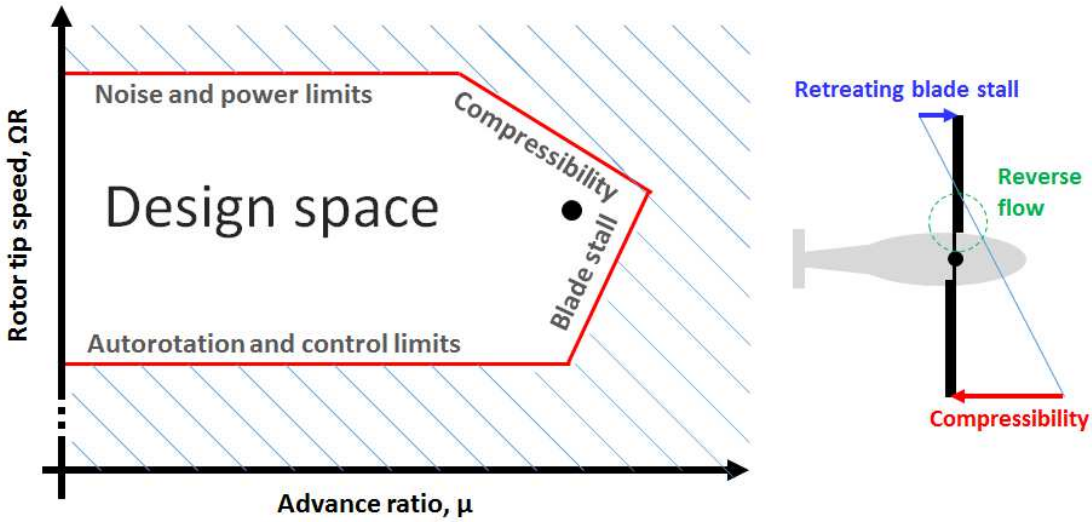

Figure 1.4: Typical envelope of tip speed selection. Adapted from Leishman [9]

Except for a few notable examples, all rotorcraft operate at a fixed rotor speed normally resulting in a tip speed of 650 - 750 ft/s for the reasons shown in fig. 1.4. At hover and low airspeeds, faster tip speeds result in unacceptable noise levels,

while reducing tip speed limits rotor thrust and reduces autorotative ability. In cruise and at high airspeeds, high tip speeds are limited by compressibility, while reducing the tip speed is limited by stall. However, most helicopters operate across a range of airspeeds and gross weights and a variable rotor speed can take advantage of improving performance by optimizing rotor speed at each flight condition. At high speeds, off-loading the retreating side rotor with compound wings, or by using coaxial rotors can remove or reduce the limitations from stall.

Despite the apparent benefits that could be realized by utilizing variable rotor speed on conventional helicopters, this has been historically avoided due to the risk of blade resonance and the poor efficiency of varying engine or transmission speed. The following sections describe the current state of variable rotor speed research followed by a brief outline of the challenges faced in implementation.

1.2.1 Variable Rotor Speed State-of-Art

A 1946 report by Gustafson and Gessow [10] evaluated the effect of tip speed on hover performance and maximum airspeed. The study recommended that tip speeds be lowered below what was typical (500 ft/s) to improve hover performance and increased in forward flight to improve maximum airspeed by delaying stall. (Maximum airspeed at the time did not approach the transonic regime and so increasing tip speed was beneficial for achieving high speed without retreating blade stall). The authors recommended that a two speed gear box was required to achieve both objectives.

Figure 1.5: The Boeing A-160 Hummingbird used rotor speed variation (up to 60%) to achieve high endurance [11].

The unmanned Boeing A-160 Hummingbird (fig. 1.5) used the Optimum Speed Rotor concept [11, 12] to achieve unprecedented endurance, setting a record flight of 18.7 hr in 2008. Developed by Frontier (then bought by Boeing), the A-160 used a two speed transmission to minimize power required as a function of airspeed, weight and altitude. The rotor blades were designed with extremely high stiffness to weight ratio so as to avoid resonance at the rotor speeds of interest. The low power, low disk loading rotor was powered by a piston engine for which a variable speed transmission was less challenging than with turbine engines. Recently, the A-160 program was canceled due to scheduling delays after excessive vibrations caused a crash.

In 2008, Steiner and Gandhi [13, 14] evaluated the influence of gross weight, altitude and airspeed on the power of a UH-60A Black Hawk helicopter with vari-

able rotor speed. A 15% rotor speed variation was chosen to limit efficiency losses in the transmission, although the specifics were not discussed. The study showed that an 18% power reduction was possible for low altitude and low gross weights. The first order analysis modeled rigid blade flap and used blade element theory (BET) together with table look up and a linear inflow model. Guo and Horn [15] built a controller that controlled optimum rotor speed for the UH-60A helicopter during climbing, diving and turning flight. The flight dynamics model was based on a modified version of GENHEL [16] for the UH-60A helicopter made available by NASA. The study predicted the potential for performance improvement via rotor speed variation and showed that a controller could successfully follow the commanded rotor speed schedule. In 2009, Mistry and Gandhi [8, 17] extended the results of Steiner and Gandhi to include a prescribed wake model. The simulation, again based on the UH-60A rotor, studied both variable rotor speed and variable radius for reduced power. The study showed that for low thrust and low altitude conditions, up to 14% power reduction could be achieved by saturating the possible reduction in rotor speed (-11%). The performance improvements reduced with increasing gross weight, altitude and at low speeds. Only limited insight could be gained from these simplified models.

1.2.2 Challenges for Variable Rotor Speed Implementation

Most helicopters maintain a constant rotor speed to avoid resonance and because of the complexity, additional weight and decreased efficiency of varying the

rotor speed through a variable speed transmission or by throttling the engines. The following sections discuss these issues briefly.

1.2.2.1 Blade Resonance

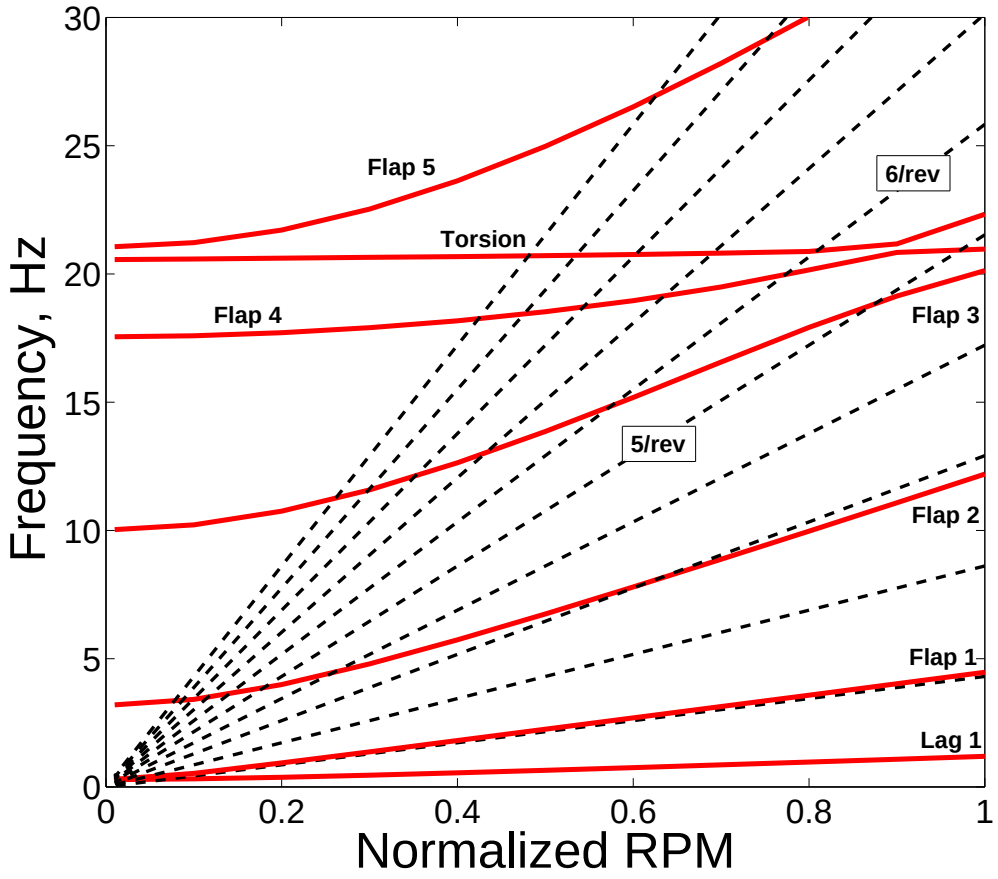

Figure 1.6: Fanplot of the UH-60A Black Hawk rotor. 100% = 258 RPM.

An example of a UH-60A fanplot is shown in fig. 1.6, which indicates the challenges faced when varying the rotor speed. The modal frequencies of rotating blades are a function of the rate of rotation because of centrifugal stiffening. At 100% rotor speed, the blade is carefully designed to ensure that none of the first few blade frequencies are near those of the aerodynamic forcing frequencies (which are

at multiples of the rotor frequency). Changing the rotor speed risks approaching the resonance condition that can cause enormous excitation of one or more of the blade modes. Unless well damped, resonance results in large deflections, vibrations, large dynamic loads and can be potentially hazardous.

Approaches to overcome resonance when varying rotor speed can be implemented through advanced blade design or tailored rotor speed controllers. Modern manufacturing with composite materials allows for new, very light and stiff blades that are more resistant to resonance such as were used by the A-160 (claimed in patent by Karem [12]). Alternatively, advanced controllers or two stage (or more) transmissions, chosen to avoid rotor speeds near resonance have been used successfully on some high speed rotorcraft such as Sikorsky's X-2 Technology Demonstrator (20% RPM reduction [18]), Airbus's X^3 (20% RPM reduction [19]) and the V-22 Osprey (18% RPM reduction [20]).

1.2.2.2 Variable Speed Turbines Efficiency

Modern turbine engines are designed to operate with peak efficiency at a single output shaft speed. Turbine efficiency decreases quickly if it is required to operate at off-design speeds. The decrease in turbine efficiency with both decreasing speed and torque is shown in fig. 1.7 in terms of increased specific fuel consumption (SFC, lower is better). For illustration, consider a rotor optimized for 100% engine output power at 100% turbine speed resulting the baseline SFC. Slowing the turbine speed to 50% and assuming that the engines remain power limited results in over 30% increase in SFC. Alternatively, maintaining the turbine at full speed but requiring

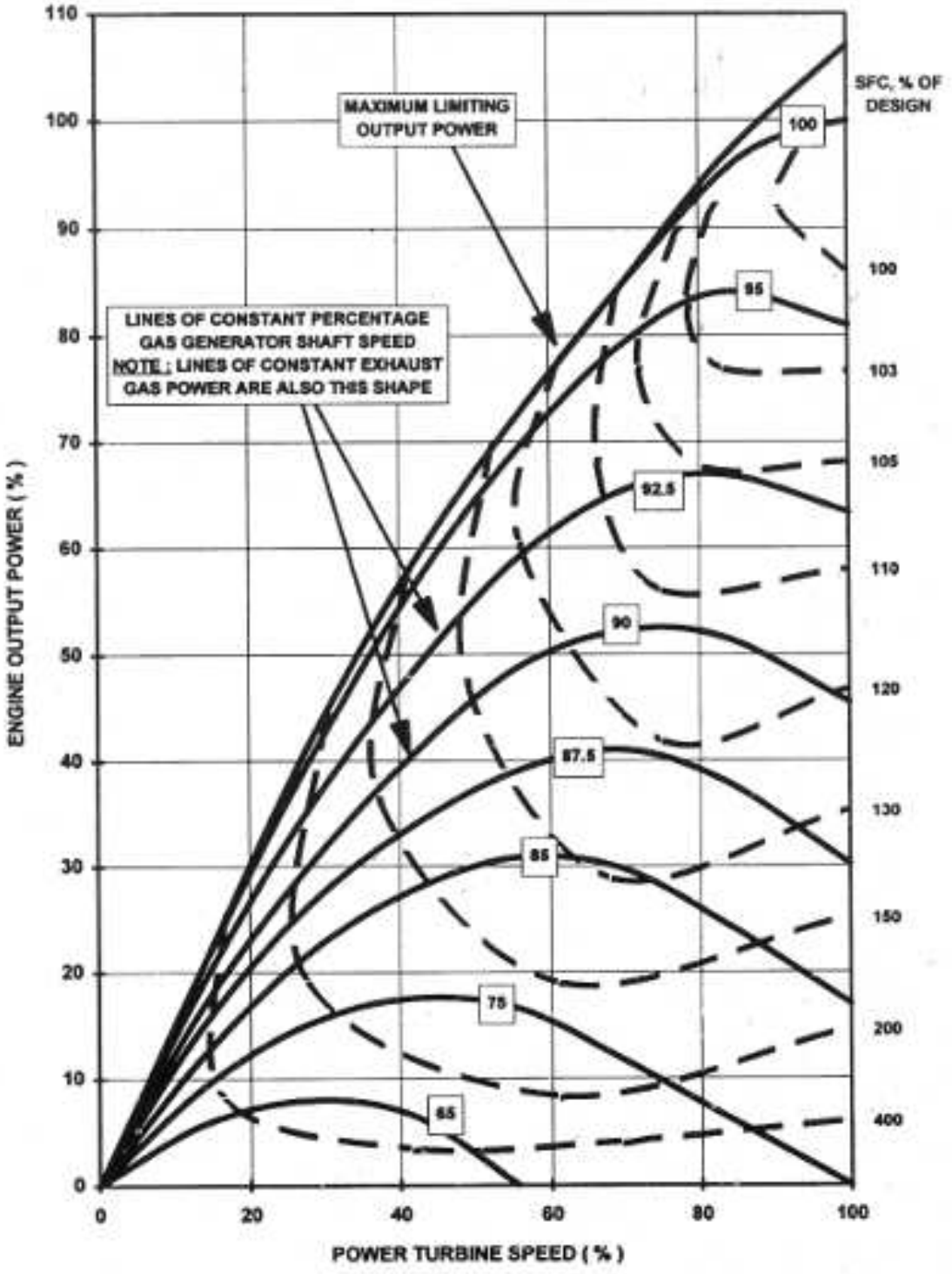

Figure 1.7: Typical variation of SFC with turboshaft speed [21].

70% of its power (comparable to power at 50% turbine speed) costs only 3%–5% increase in SFC. The increase in SFC for the reduced speed turbine can more than overcome any power gain available due to the rotor.

A report by D'Angelo [22] gave the conclusions of NASA's investigation of tilt-rotor concepts, which identified that a means of propulsion with efficient, widely-variable output speeds was a key technology for improved tiltrotor efficiencies at high airspeed. Turbine efficiency drop-off limits the rotor speed reduction to 18% even though 50% speed reduction was optimal at high speeds. This trade-off cost 15%-22% in overall efficiency. D'Angelo modeled a theoretical turbine, optimized for variable turbine speed and showed a 14% overall efficiency increase was possible. Welch [23, 24] used 2D and 3D CFD to confirm the performance trends shown by D'Angelo.

Garavello and Benini [25] and Misté and Benini [26] each looked at variable turbine speed engine performance specifically for helicopter applications. Garavello and Benini used a simple rotor analysis to determine the power requirements of a nominal UH-60A helicopter in steady flight with variable rotor speed. These were used as inputs to a first order turbine engine model to determine the fuel flow rate. For the 16,000 lb case considered, the net decrease in fuel mass flow rate for the optimum speed rotor was judged not worthy of the effort of variable rotor speed because of reduced turbine efficiency. Misté and Benini implemented a steady state model of a turbine engine to use with a simple rotor analysis, coupled to an optimization routine. The optimization targeted minimizing system power and realized a 16% reduction in fuel flow in cruise for a 16,000 lb UH-60A helicopter.

Increasing the resolution of the rotor analysis and the steady flow turbine model were suggested for future improvements.

1.2.2.3 Variable Speed Transmission

A multi/variable speed transmission can change rotor speed relatively efficiently, but with a weight penalty. A 2008 report by Stevens et al. [27] evaluated several transmission concepts for their feasibility for the large civil tilt rotor (LCTR) investigation conducted by NASA. Two-speed and variable-speed transmissions were evaluated. The challenge of a two speed transmission is to ensure continuous power delivery. A two input differential planetary gear was identified as a viable solution to a continuous change in rotor speed between two speeds. Lewicki et al. [28] and then DeSmidt et al. [29] developed a dynamic model of the transmission, which compared well with experiment. The weight penalty of the system was not detailed. Saribay et al. [30, 31] investigated a pericyclic variable speed transmission for helicopter applications showing it to be a feasible replacement for conventional helicopter transmissions with weight and volume reductions compared to standard transmissions (evaluated against the KMAX transmission). A patent by Palcic et al. [32] describes a two-speed transmission with smooth RPM changes for use on dual engine rotorcraft by placing a clutched intermediate gearbox between each engine and the main gearbox.

1.3 High Advance ratios

Following from the initial studies investigating variable radius and variable rotor speed concepts to achieve improved performance, the study of high advance ratios will focus on variable rotor speed alone. Variable rotor speed has fewer technological hurdles and has a greater scope for performance improvement than variable rotor radius. This section provides an overview of aeromechanics activities of rotorcraft that used variable rotor speed to attain high speeds. This is followed by descriptions of controlled wind tunnel experiments that achieved high advance ratios. Finally the current state-of-art in the analysis of high advance ratio performance and loads is reviewed.

1.3.1 High Speed Rotorcraft

Slowing the rotor to achieve high speeds has been applied to numerous rotorcraft including autogiro, tilt-rotor and compound aircraft.

Autogiro Rotorcraft: The 1951 McDonnell XV-1 convertiplane (fig. 1.8a) was a tip jet driven compound autogyro [41]. Full rotor speed (410 RPM) was used during takeoff and landing, but the rotor was slowed and offloaded in forward flight. Unacceptable noise and new engine technology lead to cancellation of the project. The British Fairey Rotordyne (fig. 1.8b) also used a tip driven rotor and included two turboprop engines for forward flight. However, it was canceled due to budget cuts and concerns about noise. Carter Aviation developed their technology demonstrator (fig. 1.8c) that is the first rotorcraft to exceed $\mu = 1.0$ in 2005 [42]. The heavy rotor

(a) McDonnell XV-1 [33].

(b) Fairey Rotodyne [34].

(c) Carter Copter [35].

(d) Bell XV-3 [36].

(e) Bell-Agusta Westland BA609 [37].

(f) Lockheed XH-51A [38].

(g) Sikorsky XH-59 [39].

(h) Sikorsky X-2^{TM} [40].

Figure 1.8: High speed rotorcraft flight demonstrators and production tiltrotors.

was spun up before take off before disengaging a clutch and increasing collective during takeoff. Wings and a propeller provide lift and propulsion in forward flight. Because the autogiro rotor is not powered in flight, it is considered distinct from the high advance ratio concepts considered here. An autogiro does not offer the same capabilities as a powered rotor.

Tilt-Rotor Rotorcraft: The Bell XV-3 was the first stable conversion tilt-rotor. Rotor speed was decreased from 532 RPM in hover to 324 RPM in airplane mode to limit helical tip Mach number [43]. The XV-1 suffered numerous crashes and delays owing to stability problems, notably from prop whirl flutter, and was canceled after a final incident in the NASA Ames 40x80 wind tunnel. The XV-3 did not achieve its high speed goals (maximum speed achieved was 184 mph) but the technology improvement and the development of stability analyses for high speed flight paved the way for the success of the XV-15 (first flight 1977) and eventually the V-22 Osprey (first flight 1989). Combining a tilting rotor axis with reduced rotor speed in forward flight (20% tip speed reduction), the Osprey has a maximum airspeed of 275 knots (sea level, 305 knots at 15,000 ft) with a useful payload, a feat which cannot be achieved by any other rotorcraft [20]. A civil variant of the tilt rotor is being developed, started by Bell and Boeing, then Bell and AgustaWestland and now developed solely by AgustaWestland as the AW609 (earlier BA609 shown in fig. 1.8e). Tip speed variation is achieved on all these aircraft by engine speed alone

Compound Rotorcraft: In 1967, the compound variant of the Lockheed XH-51A (fig. 1.8f) used a 5% reduction in rotor speed to avoid critical Mach number on

the advancing tip. A larger rotor speed reduction was not feasible due to structural resonance of the test rotor. Vibration levels increased at speeds above 220 knots and limited the maximum airspeed [44, 45]. More recently, Eurocopter developed the X^3 experimental high speed helicopter, which set an unofficial speed record of 255 knots. The X^3 uses short span wings and two tractor propellers to off-load the rotor at high speeds and slows the main rotor by up to 15% to alleviate compressibility [46].

Coaxial Rotorcraft: The Sikorsky XH-59 coaxial (fig. 1.8g), compound rotorcraft reduced tip speed from 650 ft/s in hover to 450 ft/s at high speed (236 knots) [47]. High 3/rev vibrations (3 bladed rotor) were attributed to challenges with rotor speed variation and a heavy, old technology rotor system. Sikorsky's X-2 Technology Demonstrator coaxial helicopter (fig. 1.8h) used a 20% reduction in rotor speed to achieve high efficiency and high speeds upto 250 knots ([48]) with low vibrations in part due to fly-by-wire controls, active vibration control and advance rotor blade design [49].

1.3.2 Measured Test Data for Validation Studies

In order to be able to develop the next generation high speed rotorcraft, the aeromechanics of edgewise rotors at high advance ratios needs to be understood and reliable prediction tools need to be developed, which are validated for the extreme flight conditions. Developing an accurate predictive capability requires access to test data of representative rotors in these regimes. This section discusses the high advance ratio wind tunnel tests that are available, as well as the limitations and

challenges faced with testing.

Wind tunnel test data is ideally of full-scale rotors that closely represent the desired high speed concept rotor. However, full-scale testing is expensive and complex, while high advance ratio testing specifically increases the risk relative to lower advance ratio tests. The cost of full-scale testing comes from the use of a large facility (such as the National Full-Scale Aerodynamic Complex – NFAC), acquiring and instrumenting a rotor system, and the large team required to conduct the test. Also, designing a specific rotor system for high advance ratio research is prohibitively expensive. For this reason, wind tunnel tests typically reuse existing rotors, not optimized for high advance ratios. Slowing the rotor to achieve high advance ratios incurs additional risk. Centrifugal stiffness on a slowed rotor is reduced, resulting in the potential for larger flapping angles and blade loads. At high advance ratios, the rotor approaches its stability limits, which may not be well predicted. Changing the rotor speed can result in resonance and possible failure, although a test matrix can be designed to avoid critical resonant conditions. Also, reverse flow phenomena can result in unexpected dynamics and high loads. Finally, at high advance ratios, trimming the rotor becomes more difficult, which decreases the margins for error. For these reasons, there have only been a few full-scale, high advance ratio wind tunnel tests and, with the exception of the most recent one, these have had only limited data collection.

Scaled wind tunnel tests offer a less expensive alternative to full-scale testing. In order to represent the important phenomena at high advance ratios, the rotor speed must be at least match the full speed tip Mach number of the full-scale rotor.

Mach-scaled rotors are smaller and cheaper to produce than full-scale rotors and require less expensive facilities to test. This can allow testing and comparison of various rotor configurations that cannot be attempted at full-scale. The risk factors persist but are less costly at small-scale. However, at reduced scales, the smaller blade dimensions can make instrumentation more difficult and greater care must be taken to ensure similarity of each rotor blade. The continuing miniaturization of digital sensors has made it possible to instrument Mach-scale rotors to about the same extent as full-scale rotors, although in practice it remains difficult to achieve all the details at the model scale.

The following sections are an overview of three full-scale and one small-scale, high advance ratio wind tunnel tests conducted prior to 2010. These are followed by descriptions of the full-scale UH-60A rotor tests at high advance ratios and the University of Maryland High Advance Ratio tests that are investigated in this dissertation.

1.3.2.1 High Advance Ratio Tests Before 2010

Pitcairn PCA-2 autogiro: In 1935, the 45 ft diameter Pitcairn PCA-2 Autogiro was tested in the NACA (predecessor of NASA) full scale wind tunnel in auto-rotation, reaching an advance ratio of 0.7 [50]. The rotor was unpowered and rotor speed was controlled by setting tunnel wind speed and pitch angle. The test was particularly interesting in that it measured the rotor drag to determine the Lift-to-Drag ratio (L/D) of the rotor free of the fuselage. In addition to fixed frame loads, a survey of the inflow in a plane 1.5 ft about the rotor disc was conducted.

Teetering rotor model: Jenkins [51] described a two bladed, untwisted, teetering rotor with a 15.5 ft diameter, constant chord and NACA0012 airfoil section. The rotor was tested at advance ratios of 0.65 – 1.45 in the Langley full-scale wind tunnel to investigate high speed compound rotor systems. Rotor forces, torque and flapping angles were measured and blade tufts were used to visualize the flow over the airfoil section. The study concluded that high rotor efficiency (lift-to-drag ratio greater than 13) was possible. Jenkins also showed the first experimental evidence of a thrust reversal phenomena at high advance ratios (μ greater than 1.0). Jenkins described a reduction in the slope of rotor thrust versus collective for increasing advance ratio. For advance ratios above 1.0, the slope became negative. The author used a simple analysis based on [52], concluding that thrust reversal was due to increasing sensitivity of flapping response to collective pitch compared to flapping response to angle of attack.

H-35 and UH-1 rotors: A 1968 paper by McCloud and Biggers [53] summarized a test conducted by NASA on five rotors in the 40 x 80 wind tunnel. Two articulated rotors based around the H-34 transmission and three rotors based around the UH-1 transmission. The combined test envelope varied twist, articulation and tip airfoil section. The untwisted articulated rotor was tested to an advance ratio of 1.05, one of the teetering rotors (with tapered blade tips) was tested to 1.00 and the remaining rotors were tested to $\mu = 0.5$. Hub forces and moments and control settings were measured. Charles and Tanner [54] evaluated two of the teetering rotors with then-current (1969) predictive capability. They showed that the quasi-static, two-dimensional analysis techniques gave satisfactory prediction up to about

$\mu = 0.5$, but prediction of propulsive force broke down for higher advance ratios. High Mach number effects were also investigated independently of advance ratio and where predicted well up to an advancing tip Mach number of 0.94 and an advance ratio of 0.45. It was further noted that the rotor became increasingly difficult to trim at high advance ratios with long transient responses to control inputs at $\mu = 1.1$.

Scaled rotor: Quackenbush et al. [55] carried out a crude high advance ratio test up to $\mu = 2.0$ using an off-the-shelf remote control helicopter in the Glenn L. Martin Wind Tunnel. The rotor was tested in autorotation only and was not trimmed during testing and so provides limited value. Hubloads and flow visualization (blade tufts) were measured.

1.3.2.2 UH-60A Slowed Rotor Testing

In response to a renewed interest in high advance ratio rotorcraft, a comprehensive study in 2008 by Harris [56] evaluated the state-of-art of comprehensive analyses to predict high advance ratio loads and performance. The study highlighted discrepancies in predictive capability for both comprehensive and computational fluid dynamics at high advance ratios. The available high advance ratio data did not offer sufficient detail to identify the source of the discrepancies in the prediction. In response, the UH-60A rotor was tested at high advance ratios to provide important new detailed data.

In 2010, a full-scale UH-60A rotor was tested at the U.S. National Full-Scale Aerodynamics Complex (NFAC) (fig. 1.9a). The rotor blades were the same as those

(a) UH-60A rotor in NFAC wind tunnel.

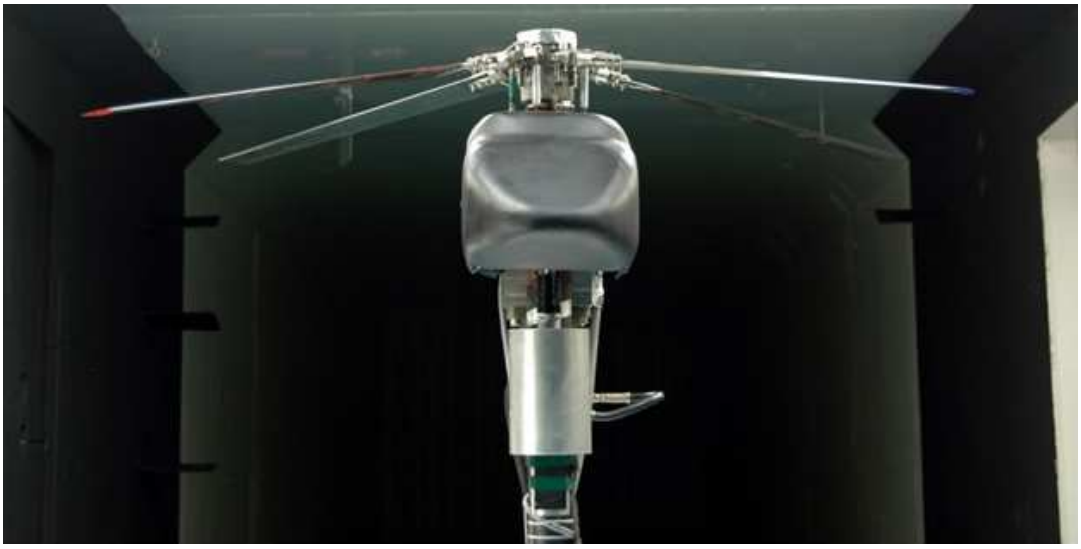

(b) University of Maryland rotor in Glenn L. Martin wind tunnel

Figure 1.9: Two recent high advance ratio rotor tests.

used in 1993 flight tests as part of the airloads program [57]. The wind tunnel test was designed to complement the airloads flight tests by repeating measurements in a controlled environment and making measurements not previously possible. A portion of the test matrix was allocated for high advance ratio testing. The instrumentation for the slowed rotor testing included measurements of airloads (normal force, chord force and pitching moment), structural loads, control positions, shaft bending moments, oscillatory hub loads, blade deformations and rotor wake measurements. A detailed account of the experimental setup, including complete instrumentation and hardware descriptions can be found in Norman et al. [58].

The slowed rotor portion of this test was conducted to provide a comprehensive set of data from which to learn about high advance ratio aeromechanics and to validate existing modeling capability. Datta et al. [59] described the slowed rotor portion of the test in detail. Rotor speeds of 100% ($M_{tip} = 0.65$), 65% ($M_{tip} = 0.42$) and 40% ($M_{tip} = 0.26$) and wind tunnel speeds up to 182 knots were investigated, restricted primarily by safety of flight considerations. For each airspeed and rotor speed combination, the collective was set (nominally in 1° and 2° increments) and the rotor trimmed to 0° first harmonic flapping (measured at the blade root). Shaft angles of 0°, 2° and 4° aft where investigated. The test envelope included advance ratios between $\mu = 0.3$ and $\mu = 1.0$ in 0.1 increments. The slowed rotor testing was conducted late into the test matrix, due to high perceived risk, and by that time a number of the sensors had failed. Most notably, only three airloads stations, 22.5%, 86% and 92.5%, gave reliable data.

In the discussion of the results, Datta, Yeo and Norman noted some important

observations: the decreasing sensitivity of thrust to collective at increasing advance ratios was shown and appeared to result in no sensitivity at $\mu = 1.0$ for the 0° shaft angle case. The dynamic loads on the slowed rotor at high advance ratio were larger than for the nominal rotor despite the slowed rotor producing significantly less thrust. High elastic twist was being excited by a large nose up pitch impulse in the reverse flow region at high advance ratios. Reverse chord dynamic stall was identified in the reverse flow region by vortices sweeping forward along the chord. Vibratory loads decreased significantly for the slowed rotor, despite increased structural loads, which was attributed to a large frequency gap around 4/rev in the blade modes in the slowed condition.

The UH-60A slowed rotor data is investigated in chapter 4 of this thesis.

1.3.2.3 University of Maryland Testing

At the University of Maryland, Berry and Chopra [60–64] have carried out scaled rotor tests on twisted and untwisted 4-bladed articulated rotors in the Glenn L. Martin wind tunnel (fig. 1.9b). Beginning in 2011, Berry and Chopra have conducted five wind tunnel tests up to $\mu = 1.6$.

The first rotor tested had a 3 ft radius, constant chord of 2.67 inches, the cambered SC1095 airfoil and -12° twist. It was tested to $\mu = 0.65$ [60] and later to $\mu = 1.2$ [61]. A second rotor that was untwisted with a 2.77 ft radius, 3.15 inch chord and NACA0012 airfoil section was tested to an advance ratio of 1.0 in 2012 [62]. The authors found that thrust reversal occurred for both rotors between $\mu = 0.80$–0.9 and appeared to be unaffected by any of: twist, camber or airfoil differences. Mean

thrust and advancing tip Mach number were not an indicator of 4/rev blade loads while some possible blade resonance was identified in the 2^{nd} flap at 3/rev.

In 2013, Berry and Chopra built on the previous tests to extend the advance ratio envelope to $\mu = 1.4$. The test included a station of 24 pressure sensors at 49% radius to measure the airloads, particularly in reverse flow. A second blade included two stations of strain gauges for flap bending (26% and 49% radius), one lag strain gauge (37% radius) and three torsion strain gauges (26%, 41% and 76%). The strain gauge locations were chosen to coincide with the peak curvatures of the blade modes. Finally, two of the pitch links were instrumented. In the fixed frame, the rotor balance measured three forces (F_x, F_y, F_z) and two moments (M_x, M_y) and rotor torque was measured by a torque sensor the shaft. The loads calibration included a dynamic calibration of the balance to correct for dynamic interactions of the degrees of freedom. The test was nominally run at 700 RPM (30% of full tip speed) and limited points at 560 RPM (24%) for the highest advance ratio cases. They noted that the rotor response became highly sensitive to control input above $\mu = 0.8$ and that dissimilarity between instrumented rotor blades and non-instrumented blades (arranged in opposite pairs) made achieving consistent trim difficult. The 4/rev vibratory hubloads increased substantially at advance ratios above $\mu = 0.8$, but it was not possible to isolate whether trim issues or high advance ratio loads were the cause. It was suggested that high 3, 4 and 5/rev airloads on the advancing side were the source of the increasing vibrations. Failure of over half of the pressure sensors made integration for sectional airloads inaccurate. Lessons learned from this test were applied to the final wind tunnel test in 2014.

A final test by Berry and Chopra in 2014t [64], using the same rotor geometry as the 2013 test, moved the advance ratio boundary to 1.61. The test once again included a single station of pressure sensors (19) installed at 30% radius in order to maximize the measurements of the reverse flow region. There were just two pressure sensor failures during the test, and improved construction techniques meant that the pressure data was generally improved over the earlier test. Full bridge strain gauges measured flap bending and torsion bending at 30%, 40%, 50%, 60% and 70% stations. Lag bending was not measured. Two pitch links were instrumented and the fixed frame hubloads were measured. Care was taken to balance and trim the rotor so that the blade trim at high advance ratios was normally within $\pm 1^\circ$ of the 0° flapping target. This set of data is investigated in Chapter 5 of this thesis.

1.3.3 Prediction Tools

In order to predict the loads experienced by an edgewise rotor at high advance ratios, the complex interactions of the aerodynamic environment and the structural response must be modeled. The aerodynamic forcing for the system originates at the rotor blades and causes a dynamic structural response (both elastic and rigid body motions) in the rotor blade. The aerodynamic and resulting inertial forces on each blade are integrated at the blade root and transferred to the hub and into the airframe. The airframe itself has aerodynamic qualities (lift, drag, side force and pitching moments), as well as being a complex flexible structure, which interact with the rotor forces. Finally, trimming the helicopter ensures that the forces generated

at the rotor are sufficient to achieve the targeted flight conditions (thrust, airspeed, rates) or flapping response (wind tunnel trim). All of the above systems must be modeled accurately within a comprehensive rotorcraft analysis tool.

The first documented comprehensive code was C81. Bennett [65] stated the objective of C81 as:

> First, the analysis must describe a wide variety of helicopter configurations – single rotor, compound, tandem, or side-by-side; it must also cover a broad range of flight conditions – hover, transition, cruise, or high speed. The analysis must have a uniform texture; i.e., the level of complexity of the different phases (aerodynamic, dynamic, and rotor analysis) must be uniform. The program must be applicable to diverse types of analysis – performance, stability and control, or rotor loads. The program must be user oriented in terms of preparing the input data and interpreting the results. And finally, the output format must facilitate comparison with flight and tunnel test data.

Furthermore, it is important to maintain the computational cost of the computations low enough that the analyses are useful at the early design stage. This implied a number of simplifications such as blade element aerodynamics and 1D beam modes. Growing computational power has allowed expansion of these models to include unsteady aerodynamics, freewake, and finite element based blade models. More recently, computational fluid dynamics (CFD) models have been used to augment the lifting line analysis to give improved aerodynamic simulations. This type

of analysis is called a CFD-CSD analysis.

The following sections summarize the state-of-art in rotorcraft comprehensive analysis and CFD-CSD analysis.

1.3.3.1 Comprehensive Analysis

RCAS: RCAS was developed as a follow on from 2GCHAS [66] as outlined in [67]. RCAS is a comprehensive, multi-disciplinary system capable of modeling diverse rotorcraft configurations from hover to maneuvering flight. The RCAS structural model employs a hierarchical, finite element, multibody dynamics approach for coupled rotor-body systems with multi-load path structures [68]. The lifting line aerodynamic model has options for both a dynamic inflow model (normally used) and prescribed wake models. In addition to being used in isolation, its framework allows straight forward coupling with CFD.

CAMRAD II: CAMRAD II is a commercial aeromechanic analysis of helicopters and rotorcraft that incorporates a combination of advanced technology, including multibody dynamics, nonlinear finite elements, structural dynamics, and rotorcraft aerodynamics [69]. Lessons learned in the development of the predecessor CAMRAD/JA ([70]) showed the need for a modular architecture and flexible implementation to easily accommodate a variety of rotor configurations. The aerodynamic model is lifting line and the wake resolution can choose from uniform inflow, dynamic inflow, and various prescribed and free wake models. Various unsteady models can be used and there are models for reverse flow aerodynamics, spanwise flow corrections and accounting for radial drag. CAMRAD II is a proprietary code

but is the current benchmark of comprehensive code capabilities, having been extensively validated against a variety of test data.

UMARC: The comprehensive analysis UMARC has been developed at the University of Maryland by student researchers and its approach was described by Bir et al. [71]. The structural model solves the Hodges and Dowell [72] 2^{nd} order beam equations using finite elements with modal reduction. The solution in time is by finite elements in time (FET) for steady flight conditions. Quasi-steady aerodynamics are calculated with a lifting line model with the Leishman-Beddoes unsteady and dynamic stall corrections. The far wake can be modeling with varying complexity including both prescribed and freewake models [73, 74].

1.3.3.2 Coupled CFD-CSD

Computational fluid dynamics (CFD) have been developed to provide detailed predictions of rotor aerodynamics and offer a significant improvement over the capabilities of lifting line analyses. It was with this in mind that attempts were made at coupling the structural and trim solutions of comprehensive analyses (CSD) with the improved resolution of the aerodynamics provided by CFD. A more complete overview of the development of CFD-CSD coupling can be found in [75].

The following is a brief survey of key progress in CFD-CSD analyses.

UMARC–TURNS: Datta et al. [76], from the University of Maryland, coupled UMARC with TURNS (Transonic Unsteady Navier Stokes) modified by Sitaraman [77]. In this approach, the CFD analyzed the rotor near-field while far field inflow was captured with a Lagrangian free-wake model. Abhishek [78] developed

UMARC2 and coupled it with TURNS. UMARC2, expanded on UMARC to allow for large deflections by using a multibody type blade model.

OVERFLOW–CAMRAD: OVERFLOW-D is a Reynolds-averaged Navier-Stokes computational code based on OVERFLOW, a general purpose fluid dynamics code developed by NASA. OVERFLOW-2 was modified to allow time dependent rigid body motions necessary for rotor modeling. Unlike the approach of Datta and Chopra [79], Potsdam et al. [80] modeled both the near-field and far-field using CFD to evaluate UH-60A airloads flight test data. RCAS was similarly coupled with OVERFLOW-D by Nygaard et al. [81].

HELIOS Framework: The HELIcopter Overset Simulations software (Helios) is a software framework that has consolidated the earlier efforts within a single software package. Helios uses the structural modeling form RCAS to form another approach to CFD-CSD capability. Helios is being developed by the Department of Defense (DoD) with a goal to transform the analysis–test paradigm in the rotorcraft design community to one based on high performance computing [82]. It uses a Python framework to connect analysis modules (possibly written in different languages) in an efficient manner. It uses a dual mesh approach with an unstructured near-body mesh (for ease of meshing) and a structured far-field mesh (for efficient data handling). The near-body CFD solver is NSU3D, which is an unsteady Reynolds-Averaged Navier-Stokes (URANS) code for unstructured meshes and the far-field uses the ARC3D solver. The correlation of Helios with high advance ratio experiments is discussed in detail in a following section.

1.3.3.3 Limitations of Prediction Tools at High Advance Ratios

Comprehensive analyses and CFD-CSD have been extensively validated against flight test data for advance ratios below $\mu = 0.4$, with the most rigorous validations with the UH-60A airloads flight test data [57, 79, 80]. Comprehensive analyses provided reasonably good prediction of rotor performance (thrust, power and trim controls), satisfactory sectional airloads predictions (pitching moment prediction degrades approaching compressibility or near stall) and the peak-to-peak blade load trends are generally captured (better for flapwise bending, then torsion moments and worst for lagwise bending). For normal advance ratios (below 0.4), comprehensive analyses can be a useful design tool to predict rotor performance and loads quickly, especially when a new design is an iteration on a well validated model. However, new concepts and designs continue to require extensive wind tunnel testing to validate the analyses and tune the models.

CFD-CSD codes have grown quite robust and, because of a higher resolution aerodynamic model, offer more refined, detailed and accurate predictions of the key structural loads. Compared to comprehensive analyses, CFD-CSD has shown very good prediction of important blade bending loads (flap, lag and torsion) and pitch link loads for normal flight conditions (low advance ratio and low thrust). However, performance prediction (power) remains a relative weakness of CFD compared to comprehensive analysis due to the difficulty in resolving skin friction drag. CFD-CSD calculations are considerably more computationally intensive than comprehensive analyses and single cases can take days to compute rather than minutes.

CFD-CSD also relies on very detailed information about the exact rotor geometry, not always available in early design stages. For these reasons, CFD-CSD has not yet replaced the comprehensive analysis in design, although they increasingly provide a reliable means to validate simpler analyses, rather than relying on expensive experiments and wind tunnel tests.

Neither comprehensive analyses nor CFD-CSD codes have been extensively validated to advance ratios above $\mu = 0.4$, which results in low confidence in either approach for design of new high speed rotorcraft concepts. Experience with new configurations has shown that both approaches rely on validation against test data in order to tune the analysis or to investigate new aerodynamic regimes. High advance ratios are characterized by a large region of reverse flow where the airfoil sections operate at low Reynolds numbers and with a blunt trailing edge. The airfoil motion is highly unsteady and the trailed wake system is complex. Large regions of the rotor may operate in and beyond stall, and spanwise flow on the fore and aft rotor can impact the lift and drag characteristics of the airfoil sections there. These phenomena are not encountered or are small enough to be ignored at low advance ratios and their relative importance at high advance ratios is not well understood. For these reasons, both comprehensive analyses and CFD-CSD need to be systematically validated against good quality test data at high advance ratios, before either can be used for the design of high speed rotorcraft.

The following section discusses the state-of-art of high advance ratio prediction and validation with both comprehensive and CFD-CSD analyses.

1.3.4 Prediction and Validations

A 2008 survey of state-of-the-art predictive capability of high advance ratios by Harris [56] compared the high advance ratio rotor tests of the H-34 (untwisted), UH-1 (34 ft blades) and PCA-2 rotors with state-of-the-art comprehensive codes and CFD-CSD. The comprehensive codes evaluated included CAMRAD II [69], RCAS [67], the freewake code CHARM [83], and a CFD-CSD case where OVERFLOW-2 [84] was coupled with CAMRAD II. Some of the key Harris' key conclusions were:

1. None of the analyses were able to reliably predict thrust, rotor drag and power at advance ratios above $\mu = 0.62$.

2. Above $\mu = 0.62$, the lack of lift, drag and pitching moment measurements in the reverse flow made it difficult to identify the deficiencies in the analyses.

3. Some of the high advance ratio data was called into question, in part due to unsatisfactory rotor trim.

4. All the analyses under-predicted thrust at 0° collective (ideally there should be no thrust for untwisted rotors at 0° collective). This had been attributed to measurement error but Harris suggested that unknown blade torsional response in the reverse flow could result in a thrust offset.

5. The CFD results were satisfactory at low advance ratios when the reverse flow region was small, but degraded with increasing reverse flow area. The ability of CFD to predict airfoil properties in reverse flow was called into question.

6. Rotor axial (H) force was generally under-predicted and shaft power was over-predicted by each of the analyses, worsening with increasing advance ratio.

7. Harris also suggests that the drag of the blade shank (blade root end) was important for axial force predictions.

8. The thrust reversal behavior was predictable with all the analyses.

9. Finally, the inability to extrapolate predictions from $\mu = 0.5$ to $\mu = 1.0$ made relative comparison of high advance ratio helicopter concepts, important for evaluating high speed concepts, impossible.

The H-34 and UH-1 high advance ratio tests were used to validate predictive codes in the context of the Heavy Lift Rotorcraft Systems Investigation under NASA [85–95]. A few of these are highlighted below before focusing on the recent work on the UH-60A Tests.

1.3.4.1 Simplified Models

Ormiston [96] investigated the induced power of a helicopter rotor up to high advance ratios ($\mu = 1.4$) using a simplified analysis. The model used rigid, untwisted, cantilevered blades and linearized airfoils. The aerodynamic model included only lift and no unsteady effects. The inflow was modeled alternatively as uniform or using the Peter-He [97] dynamic inflow model. Ormiston identified a "critical advance ratio" when the predicted shaft torque was discontinuous (ignoring stall) or where multiple trim solutions existed fig. 1.10. This advance ratio corresponds to thrust

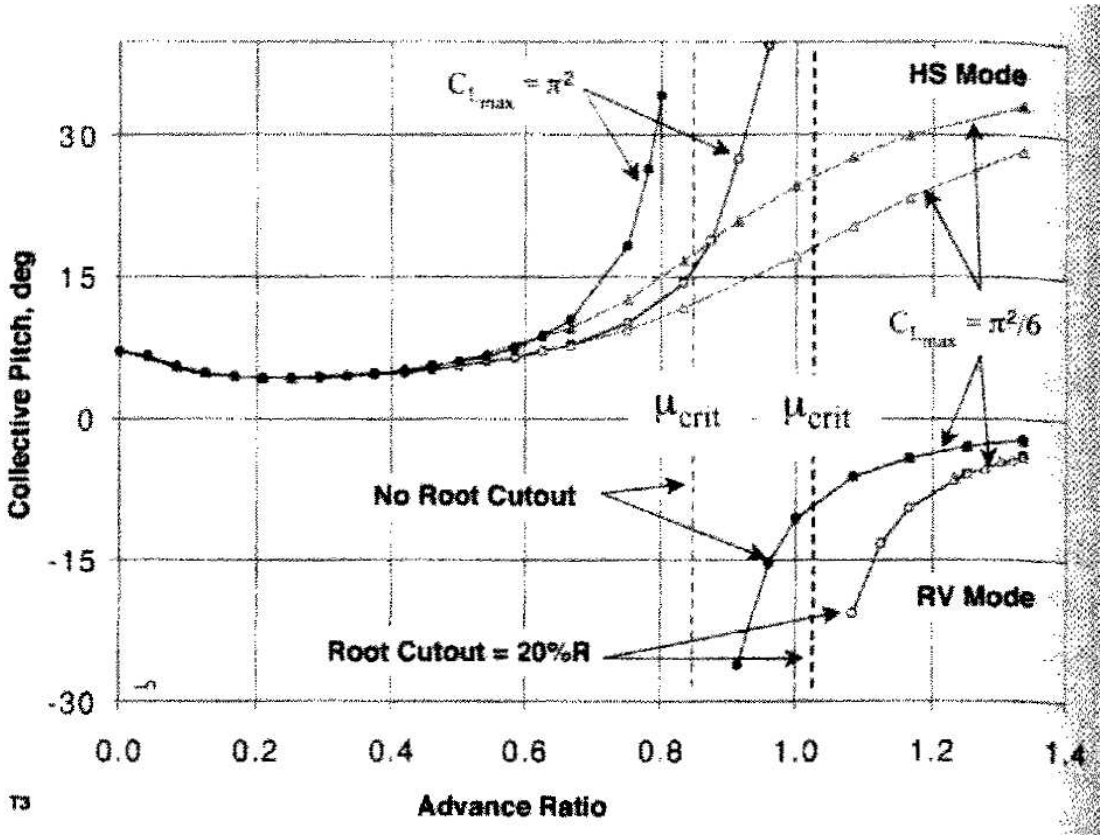

Figure 1.10: RCAS predicted collective for constant thrust rotor at high advance ratio [96].

reversal. An interesting result was that the inclusion of a root cut-out increased the "critical advance ratio".

1.3.4.2 Comprehensive Analysis

Floros and Johnson [95] performed an analysis of a notional slowed rotor compound configuration using the 15 ft teetering rotor high advance ratio tests (Jenkins [51]) to validate CAMRAD II up to $\mu = 1.45$. The CAMRAD II model used rigid blades and a rigid, prescribed wake model. The analysis predicted thrust sensitivity to collective satisfactorily for all advance ratios at 0° shaft angle, but with a persistent thrust offset (attributed to measurement error) fig. 1.11a. The thrust prediction degraded for 5° aft shaft tilt. At high advance ratios and high collectives, the analysis predicted a flattening of the thrust slope (vs. collective) that was not evident in the test data and this was attributed to unknown reverse flow aerodynamics. The predicted shaft torque is shown in fig. 1.11b after the measurements are corrected for suspected bias (δC_Q:-0.0001, $\delta\theta_0$:-2.5). The prediction shows the correct general trend with increasing advance ratio, but the absolute values, and the predictions at negative collectives, are not satisfactory.

In 2009, Yeo and Johnson [93] used CAMRAD II for correlation of the H-34 and the UH-1D rotor performance at high advance ratios. The rotor aerodynamic model included non-uniform inflow from a free wake geometry and unsteady aerodynamics. The authors suggest that reverse flow and yawed flow models [98] were important for correlation. Finally, shank and doubler drag was tuned based on achieving a good correlation of power. Only the results for the rotor induced and profile power

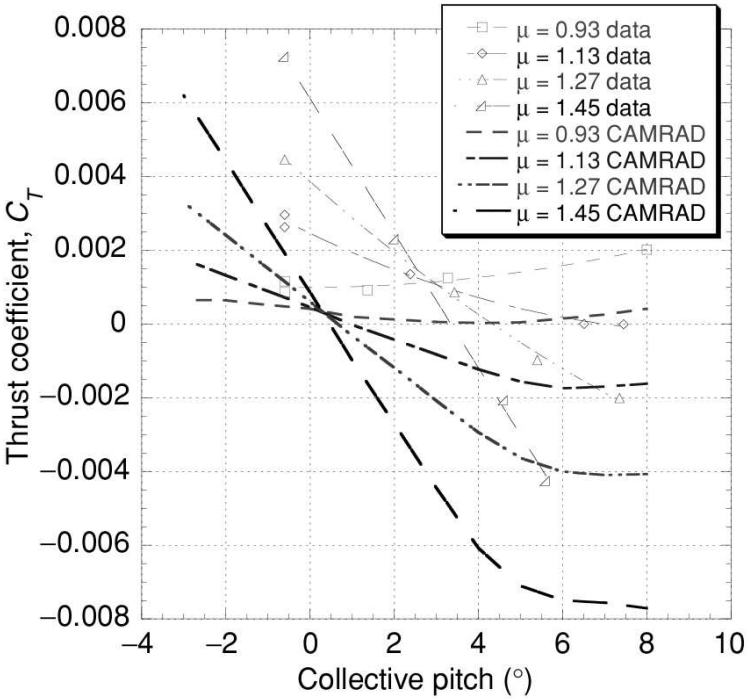

(a) Thrust, $\alpha_s = 0.5°$, showing thrust offset.

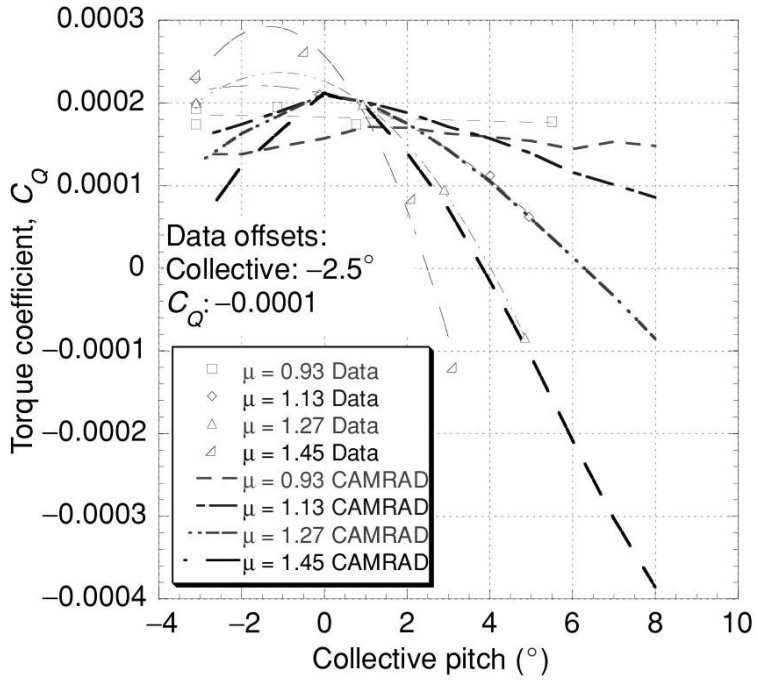

(b) Torque, $\alpha_s = 0.5°$, torque bias correction included.

Figure 1.11: CAMRAD II correlation with high advance ratio teetering rotor by Floros and Johnson [95].

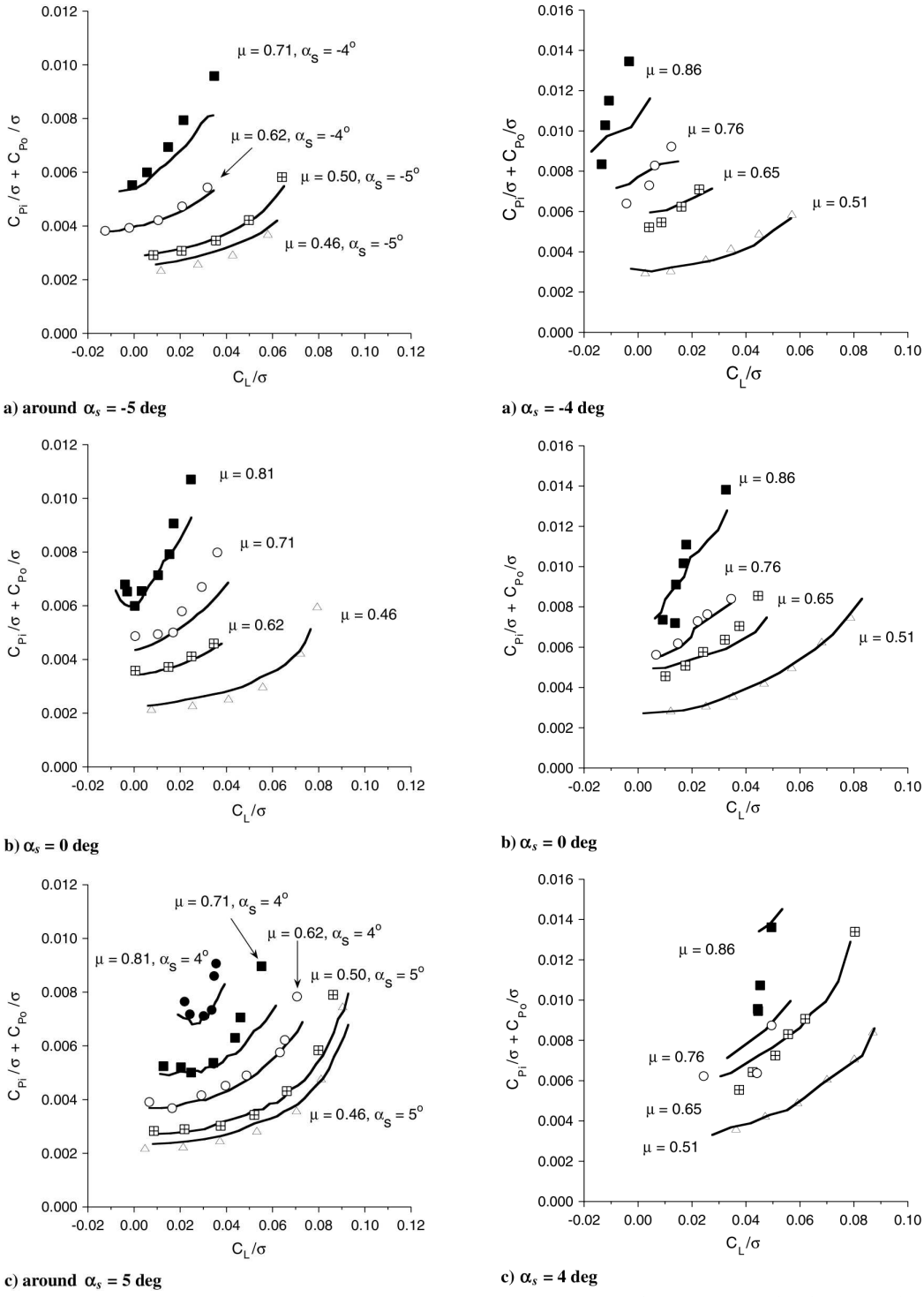

(a) H-34. (b) UH-1D.

Figure 1.12: CAMRAD II correlation of induced + profile power for two high advance ratio tests (symbols: wind-tunnel test, lines: analysis) by Yeo and Johnson [93].

were studied as shown in fig. 1.12. The analysis shows generally good correlation, even though total power and drag had errors, showing the main source of error was shank drag. At high thrusts, the analysis tended to under-predict the power and the authors suggested that this could be due to optimistic stall characteristics.

Kottapalli [99] showed preliminary correlations of a comprehensive analysis, CAMRAD II, to the slowed UH-60A wind tunnel tests at high advance ratios. The study used a simplified rotor model to predict performance, thrust, shaft torque and rotor drag force, and some limited structural loads (torsional, flapwise and edgewise half peak-to-peak bending) at 0° shaft angle. Correlation of trends below $\mu = 0.7$ was generally satisfactory, but the magnitudes were not as well predicted. Correlation was generally poor for all performance metrics at high advance ratios.

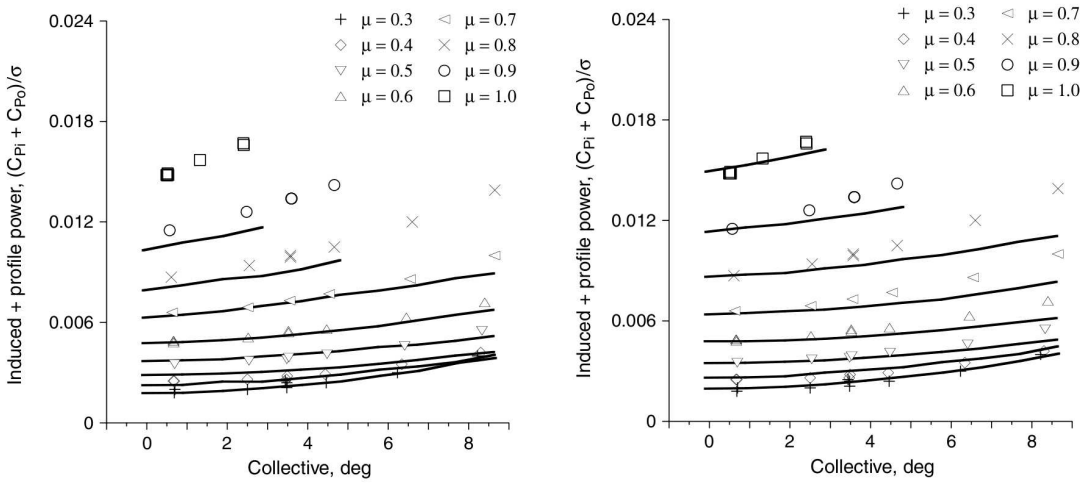

(a) Without shank drag.

(b) Including shank drag.

Figure 1.13: CAMRAD II correlation by Yeo of induced plus profile power, showing effect of shank drag ($C_D = 0.4$) [100].

Yeo [100] followed the work of Kottapalli with a more detailed CAMRAD II model of the slowed UH-60A rotor that included a dual peak wake model, yawed

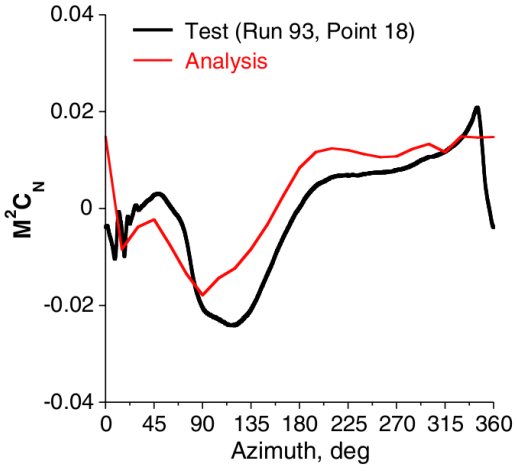

(a) Normal force, $\mu = 0.4$.

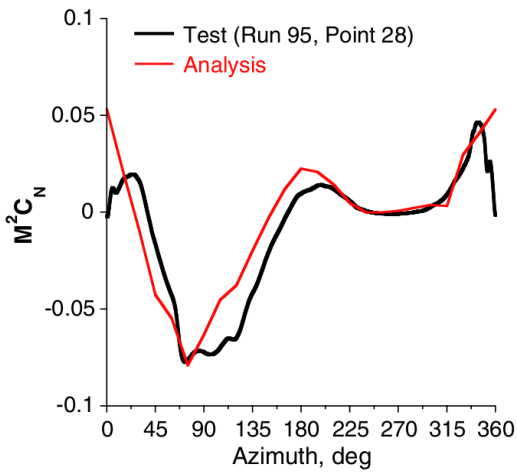

(b) Normal force, $\mu = 0.9$.

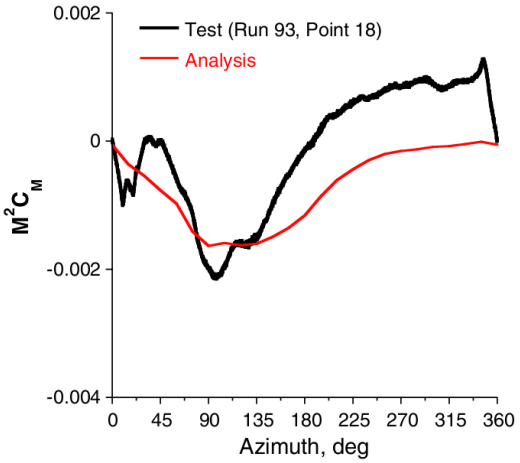

(c) Pitching moment, $\mu = 0.4$.

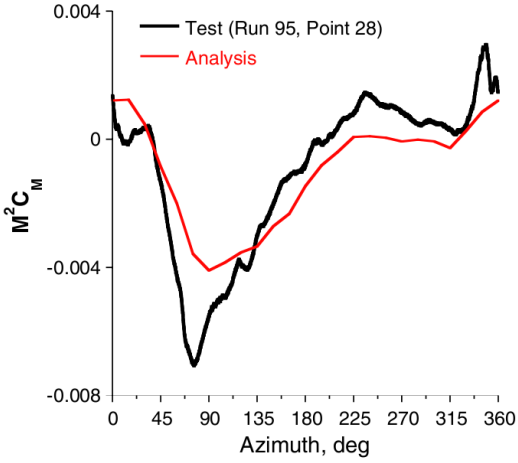

(d) Pitching moment, $\mu = 0.9$.

Figure 1.14: CAMRAD II correlation by Yeo of sectional normal force and pitching moment at r/R = 0.92 [100].

flow and shank drag. The work focused on correlation of performance predictions with some sectional airloads and blade loads. The analysis showed a good prediction of thrust at all advance ratios, while tuning the shank drag ($C_D = 0.4$) was required to predict the total power (fig. 1.13).. Sectional normal force predictions were satisfactory (figs. 1.14a and 1.14b), but sectional pitching moments were generally poor (figs. 1.14c and 1.14d).

Ormiston [101] used RCAS to investigate the UH-60A slowed rotor performance data as well as the H-34 and UH-1 rotor tests, pertinent to high advance ratio compound aircraft. The thrust was under predicted for all advance ratios while the trends were captured. In addition to the thrust reversal phenomena, the analysis predicted a non-linear thrust behavior at high collectives (similar to [95]), but significant experimental scatter made correlation questionable. Rotor shaft torque prediction was not satisfactory.

1.3.4.3 CFD-CSD

Potsdam et al. [102] were the first to use a coupled CFD-CSD analysis (Helios) to validate and investigate the slowed UH-60A rotor at high advance ratios. The goals of the work were to validate the analysis and investigate important phenomena at high advance ratios. This study was the first visualization of the full reverse flow in trimmed flight, highlighting the importance of root vortices-blade interactions. The results showed that the prediction of normal force was quite good with magnitude, phase, trends and finer detail predicted well. The pitching moments were somewhat poorly predicted considering the high level of correlation achieved with the full

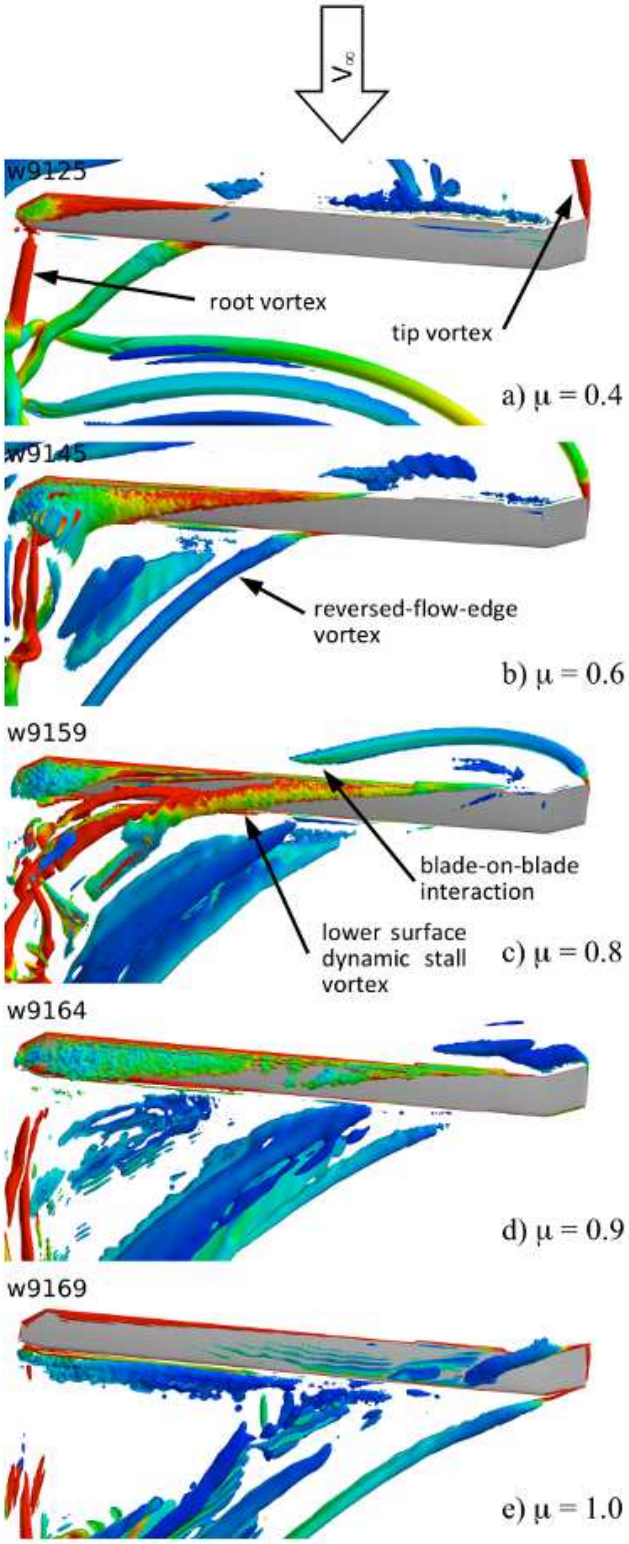

Figure 1.15: Wake visualizations with increasing advance ratio from Helios. View from underside of retreating blade [102].

speed (100% RPM) data. The prediction of performance (power, thrust, drag and control angles) were "not reliable" and thrust and hub drag continued to be under-predicted. Wake interactions were determined to be important in exciting 3/rev lift and moment impulses seen on the advancing side. The wake visualization showed complex interactions of vortices released from the tip, inboard stations, leading and trailing edge and from the blade root (fig. 1.15). The CFD predicted dynamic stall on the reverse flow airfoil (reverse chord dynamic stall). Finally, it was noted that the flow direction at 0° and 180° azimuth was significantly radial and CFD predicted a high radial force.

Potsdam et al. [68] completed further correlation of CFD-CSD (Helios) with the UH-60A high advance ratio tests that included a first order model of the blade shank and root fixtures. They estimated that the drag in this region was or the order C_D = 0.15-0.18, substantially less than was used to correlate CAMRAD (C_D = 0.4) or RCAS (C_D = 1.5).

The CFD analysis provided a unique visualization of some key phenomena including dynamic stall, the wake formation and blade deformations that were not measured in the test. The visualization helped direct some of the analysis in this work.

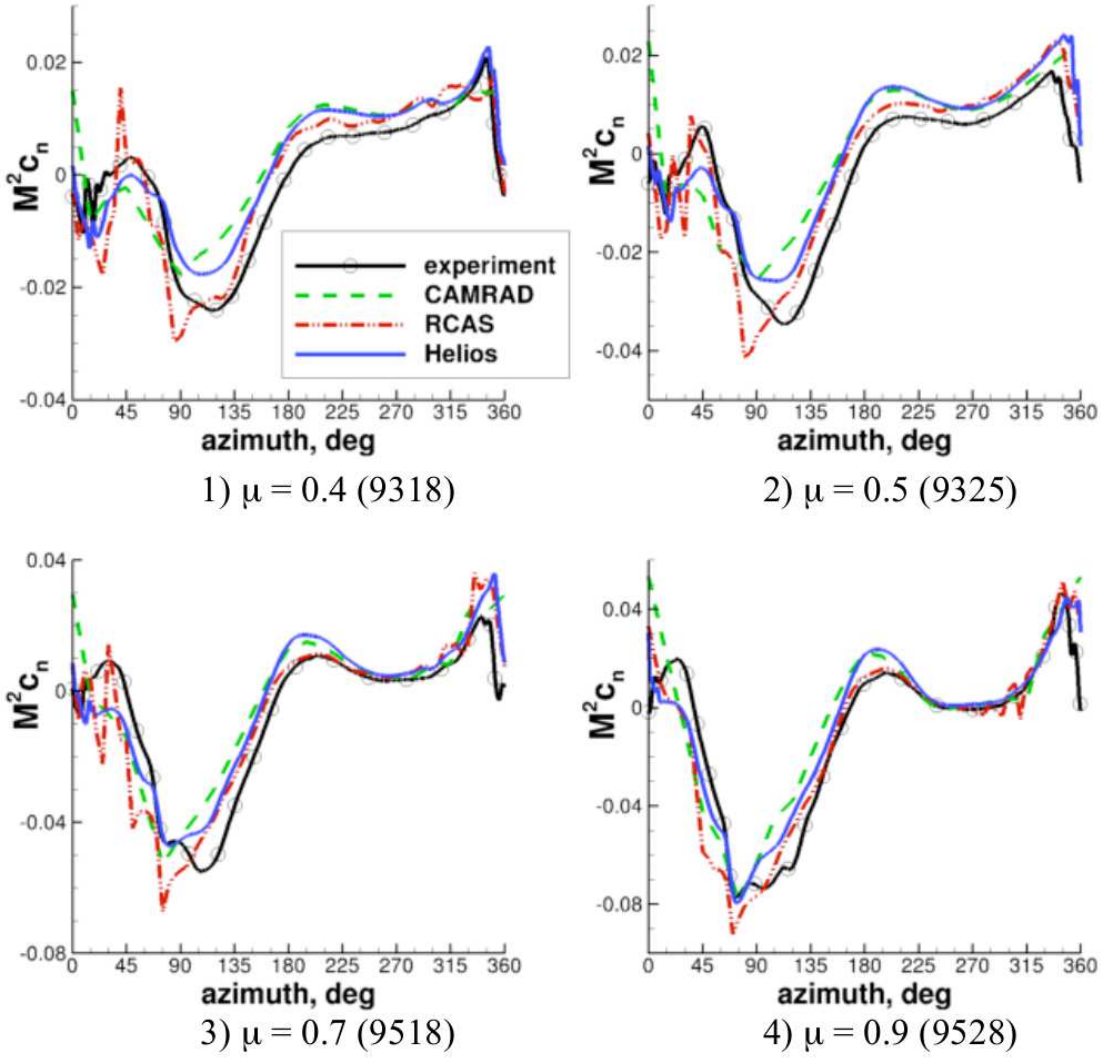

Figure 1.16: Comparison of prediction from Helios, RCAS and CAMRAD II of the sectional normal force at r/R = 0.92, $\alpha_s = 4°$ [68].

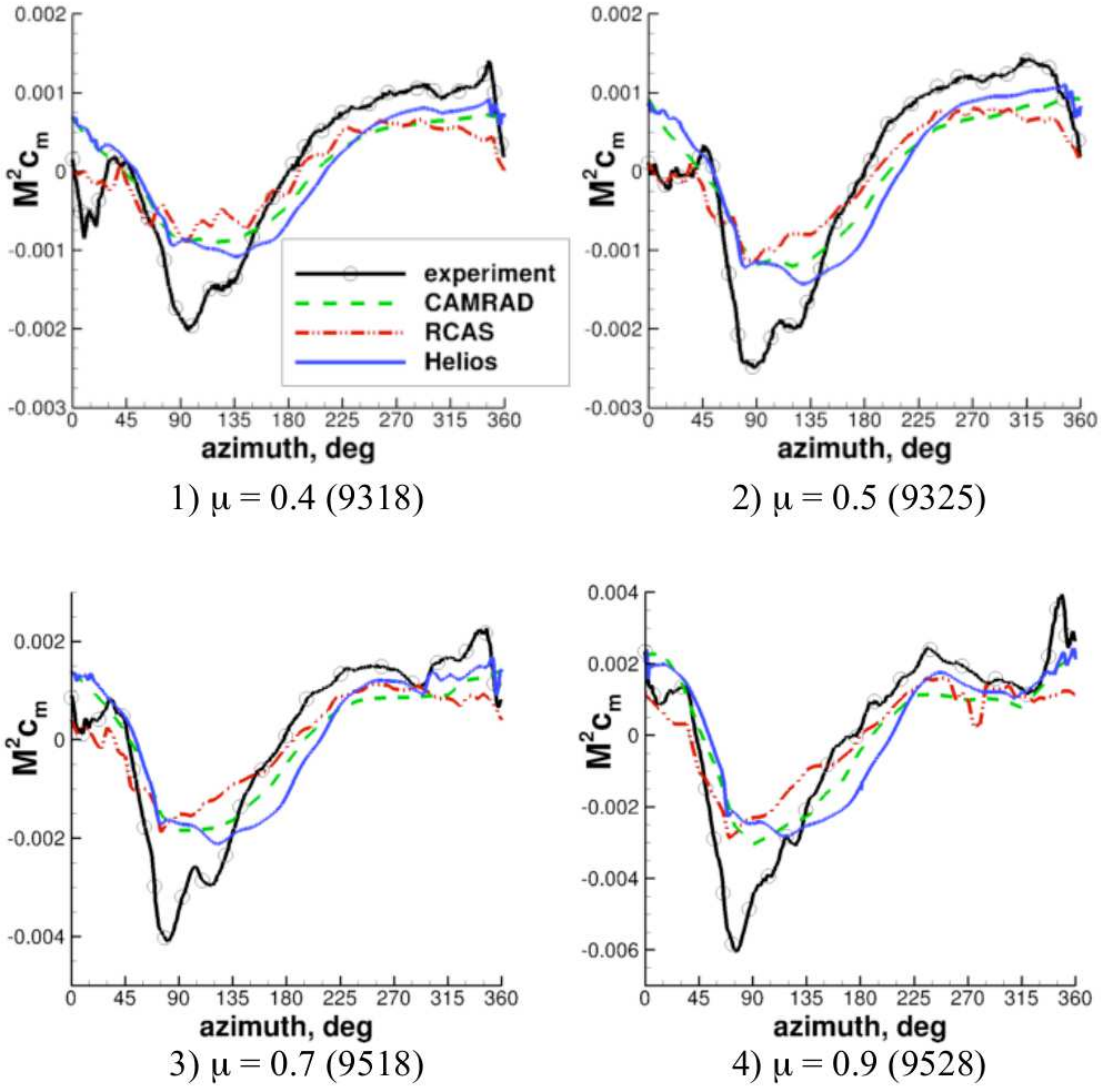

Figure 1.17: Comparison of prediction from Helios, RCAS and CAMRAD II of the sectional pitching moment at r/R = 0.92, $\alpha_s = 4°$ [68].

1.4 Present Research

1.4.1 Objective

The current research investigates the potential of variable radius and variable rotor speed to achieve high advance ratios. The focus of this dissertation is then to refine the comprehensive analysis tools to study the fundamental physics and aeromechanics of an isolated rotor at high advance ratios. Compounding and fuselage aerodynamic interaction are secondary and out of the scope of this work.

Thus far, analyses of variable radius and variable rotor speed concepts have made use of simplified models that excluded, for example, blade flexibility and non-uniform inflow. These analyses have generally used power as the comparison metric and ignored the effect of tip speed variation on vibratory loads. The objective of this research is to perform a comprehensive analysis of these concepts, including complete rotor dynamics with non-uniform inflow and unsteady aerodynamics, with a lifting line analysis to determine the potential for improved performance as well as the implications for structural loads and vibrations.

Following from this, high advance ratio aeromechanics that result from reduced rotor speed are investigated. The variable radius concepts are determined to be too complex to be practical, with large technological hurdles and less performance potential compared to reducing rotor speed. The comprehensive analysis is then correlated with high advance ratio wind tunnel tests and the capability of the analysis is compared to the current state-of-art CFD-CSD analyses.

The final objective of this study is to identify the sensitivity of the analysis to increasing modeling resolution including the impact of the wake model, unsteady airloads in the reverse flow, airfoil characteristics in reverse flow, spanwise flow and radial drag and the impact of the fuselage. The impact of each level of modeling refinement on the predicted performance and important loads are evaluated and the shortcomings relative to higher order analyses are identified.

1.4.2 Scope

The focus of this research is to refine the comprehensive analysis tools to study the aeromechanics of high advance ratios rotorcraft and to evaluate the potential of variable rotor speed and variable radius to achieve high advance ratios. The refinements are introduced in the baseline comprehensive prediction code UMARC (University of Maryland Advanced Rotorcraft Code), which is based on finite element discretization in space and time. The system equations are derived from Hamilton principles including coupled elastic flap, elastic lag, elastic twist and axial deformation consistent to second order terms [72]. The solution procedure uses finite elements in space, each element consisting of 15 degrees of freedom with modal reduction to reduce the size of the problem. Finite elements in time solve the periodic rotor response. Typically, 20 spatial elements and 12 time elements were used in this study, while 10 coupled blade modes are used in modal reduction. The aerodynamic problem is solved using a lifting line analysis including table look-up format for airfoil coefficients. The near trailed wake is modeled with Weissinger-L

nearwake model that extends 30° behind the blade, and the far wake is modeled with the Bhagwat–Leishman free wake model [74] for 2 or 4 turns of the wake at 10° or 15° azimuthal resolution. The unsteady effects of the shed wake are modeled with the Leishman–Beddoes attached unsteady [103] and dynamic stall [104] models. For the independent analysis of the performance of variable rotor radius and variable rotor speed, the trim solution solves the six degree of freedom vehicle trim equations (thrust, side and axial forces, rolling, pitching and yaw moments) iteratively to obtain the blade deflections and trim control settings for the helicopter in free steady level flight. For the high advance ratio study, comparison with wind tunnel experimental data called for trimming to 0° first harmonic flapping at the blade root for a fixed collective pitch.

The evaluation of variable rotor radius and rotor speed is achieved by imposing independent changes to the baseline rotor speed and radius through a high fidelity baseline simulation of a UH-60A helicopter. A selection of thrust and airspeed conditions are investigated. Performance is evaluated with reference to the baseline performance of the UH-60A helicopter. The objective is to evaluate the performance improvements possible at the rotor and for this reason the details of the mechanism of variable radius are ignored and no losses to system efficiency are included. The impact of variable turbine speed efficiency on variable rotor speed performance is discussed briefly. The implications of variable tip speed on rotor vibrations, specifically in terms of the 4/rev magnitudes are discussed.

High advance ratios, achieved with large reductions in rotor speed, are compared and correlated with wind tunnel data. Two rotors are modeled, the UH-60A

slowed rotor tested in the U. S. National Full-Scale Aerodynamics Complex (NFAC) and the slowed rotor tests conducted at the University of Maryland.

For the UH-60A rotor, the trim and performance metrics (cyclics, thrust, power and drag) are predicted for 0° shaft tilt up to an advance ratio of 1.0. The sensitivity of the results to the wake model, reverse flow unsteady characteristics, reverse flow airfoil properties, blade root aerodynamic characteristics, radial flow and spanwise drag and wind tunnel corrections are evaluated. A fuselage model is added to the analysis and its effects are evaluated. The sectional airloads (normal force and pitching moment) and blade loads (flap bending and torsion) are compared over a range of advance ratios ($0.3 - 0.9$) and the effect of the farwake and nearwake models on the airloads are investigated. The features of the airloads for correct prediction of the important structural loads are highlighted and shortcomings in the analysis investigated.

The University of Maryland high advance ratio tests are evaluated up to $\mu = 1.2$. The mechanics of the thrust reversal phenomena is explained and the sensitivity to reverse flow airfoil characteristics is investigated with parametric changes to the airfoil properties. The rotor vibratory loads before and after thrust reversal are predicted and described in terms of the rotor trim condition, aerodynamic loading and blade response.

1.5 Contributions of this Dissertation

The contributions of this work has been to understand the performance and loads of high advance ratio rotors. Important refinements to a comprehensive analysis that are necessary to predict high advance ratio aeromechanics have been identified through correlation with wind tunnel test data. The validated analysis has then been used to investigate some implications of rotor design at thrust reversal.

Key contributions are:

1. **Methodology Development:** The in-house comprehensive analysis has been refined and corrected for large angles to achieve high advance ratios. New capability includes a logic for consistent variable radius/rotor speed morphing, which can be easily extended; a simplified aerodynamic interference model of the fuselage on the rotor plane; aerodynamic properties of the root cut-out; freestream deformable nearwake; and yawed flow corrections. New wind tunnel trim options have been included in the analysis and a reliable approach to high advance ratio trim has been developed.

2. **Prediction, Analysis and Validation:** A full-scale UH-60A slowed rotor wind tunnel test reaching an advance ratio of 1.0, and a new Mach-scale articulated rotor test from the University of Maryland that reached 1.2 advance ratio were analyzed and the predicted performance and blade loads are validated. The UH-60A test evaluated the predictions against a representative, modern rotor including multiple airfoils, twist and sweep. The Maryland rotor

is new and with a simpler geometry to allow for a more generic prediction. The Maryland test also reached higher advance ratios that included the important thrust reversal phenomena, which was important for the validation.

3. **Fundamental Understanding:** The role of reverse flow lift and stall in the prediction of high advance ratio performance, especially near thrust reversal, was studied and understood. The aerodynamic lift, drag and wake from the blade root at high advance ratios is investigated in terms of the sectional airloads and bending moment predictions. The role of the nearwake and far-wake modeling in the airloads and their importance for the prediction of blade bending loads are shown and understood.

Specific conclusions are:

1. At advance ratios above thrust reversal (near 1.0), a rotor can produce large negative thrusts for positive collectives, which is influenced by root cut-out, blade twist, shaft angle, unsteady airloads and the stall characteristics of the airfoil in reverse flow.

2. The blade–wake interactions on the advancing side and on the rear of the rotor are significant for the peak outboard sectional airloads and blade bending loads on the advancing side. The retreating side, outboard airloads are benign. Unsteady loads within the reverse flow are most important for the airloads and bending moments near the blade root.

3. The presence of a fuselage under the rotor can increase the rotor thrust some-

what at high advance ratios by adding upwash on the front of the rotor.

4. Yawed flow appears to alter the reverse flow stall behavior and this is important for predicting thrust and loads at high advance ratios beyond thrust reversal.

1.6 Overview of Dissertation

Chapter 1 introduces the background and motivations of investigating variable tip speed aeromechanics for high advance ratios. This section includes a literature review on previous concepts, wind tunnel experiments and rotorcraft that have employed variable tip speeds for improved performance at high speeds followed by an overview of the state-of-art in prediction of performance and loads at high advance ratios. Finally the chapter summarizes the objective and scope of this dissertation.

Chapter 2 investigates the performance of a variable radius concept evaluated on a conventional helicopter (based on the UH-60A Black hawk). A conceptual model of the radius variation is presented and then evaluated for performance and vibrations.

Chapter 3 follows the same approach as chapter 2, to investigate variable rotor speed for improved performance as well as vibratory loads. The implications of the system efficiency of variable rotor speed (including engine efficiency) are briefly considered. Variable rotor speed is selected as the most viable for high advance ratio studies in chapter 4.

Chapter 4 presents the results of the correlation of the analysis with two sets of wind tunnel data from the UH-60A slowed rotor test and from a rotor tested

to high advance ratios at the University of Maryland. Refinements to the analysis that are important for the correlation are made and evaluated. Finally, some key aspects of the rotor geometry are evaluated in terms of improving performance and reducing structural loads.

Chapter 6 summarizes the key conclusions of this work and recommends future work.

Chapter 2: Variable Rotor Radius

Achieving high advance ratio rotorcraft requires reducing the tip speed to avoid compressibility on the advancing rotor, which acts to drive up power requirements and increases blade loads and vibrations. Variable tip speed can be achieved by radius variation or rotor speed variation. Before investigating the performance and loads at high advance ratios, the potential for performance improvement of each method for variable tip speed is investigated for a typical utility helicopter. This chapter and the next investigate the performance of variable radius and then variable rotor speed concepts respectively, before moving on to focus on high advance ratio aeromechanics.

This chapter presents the prediction of basic performance, airloads and vibrations for a variable radius rotor concept in steady level flight. The helicopter model is based on the well validated UH-60A helicopter. The focus of this chapter is to determine the potential of varying rotor radius, in a steady manner, to achieve improved performance. The details of the mechanism and the associated efficiencies of the means to achieving variable radius are of secondary important and are not considered in any detail. Steady changes in radius, implies that radius variation is a function of flight condition (thrust, altitude and airspeed), requiring slow changes,

and there is no variation with azimuth.

The approach is to investigate a parametric sweep of radius for different thrust conditions and airspeed. For each thrust, airspeed is increased until a trim solution can no longer be achieved. Radius is varied in 2% steps until further changes in radius achieve no additional improvements in performance. The change in radius is done in a simplified manner but ensures that the blade inertial properties, mass and mass distribution, are consistent and assumptions are made about the blade stiffness redistribution.

The chapter begins by describing the modification made to the analysis code, UMARC, to accommodate variable radius and variable rotor speed concepts. This is followed by a description of the baseline UH-60A model and the assumptions made for the variable radius study. Following this, the results are presented for the predicted power, trim and vibratory loads with a discussion of the implications of variable radius in each case. The impact of an alternate concept for radius variation is discussed briefly before concluding the chapter.

2.1 Modifications to UMARC

The following additions to the baseline analysis are those specific to the discussion of radius and rotor speed variations. Chapter 4 introduces more extensive modifications and additions to UMARC that are important at high advance ratios. After the introduction of the analysis, the modifications include how the rotor power and its components are calculated in the analysis, following by the algorithm used

to describe variable radius and variable rotor speed within the analysis is defined.

2.1.1 Description of Baseline Analysis

The University of Maryland Advanced Rotor Code (UMARC) [79, 105] was used as a baseline platform for this study to model a representative utility helicopter. The blades are modeled as second order, nonlinear, isotropic, Euler-Bernoulli beams, each element is capable of 15 degrees of freedom to allow for coupled flap, lag, torsion, and axial motion. The equations of motion are solved using a variational methodology with modal reduction in conjunction with finite elements in space and time with twenty spatial elements and twelve time elements (each of 5^{th} order) were used in this study, while ten coupled blade modes are used in modal analysis. The lifting-line aerodynamic model implements quasi-steady aerodynamics by means of a table look-up for section lift, drag, and pitching moment coefficients. Near wake is modeled via a Weissinger-L representation and assumed to trail 30° behind the rotor in-plane with the trailing edge. The trailed wake is discretized into three azimuthal segments. The far-wake is modeled by the Bagai–Leishman relaxation free-wake model [73]. A 15° azimuthal discretization of the wake, with 2 turns of wake tracking, gave satisfactory resolution of performance parameters. The far-wake is represented by a single wake trailer defined to release from the blade tip with a circulation strength equal to the peak blade circulation outboard of 50% radius. Unsteady airloads that model attached and separated flow are captured by the Leishman-Beddoes unsteady model [103]. The coupled blade response and the

six degree of freedom vehicle trim equations (thrust, side and axial forces, rolling, pitching and yaw moments) are solved iteratively to obtain the blade deflections and trim control settings.

2.1.2 Definitions of Power

It is useful to discuss the components of the total power, induced and profile power, when comparing variable radius or variable rotor speed performance. To do so with a comprehensive analysis requires some care to ensure consistency, i.e. so that the power components sum to the total power. The following definitions of power are used throughout this dissertation.

The total power, C_P, is equal to the mean shaft torque, C_Q, in non-dimensional form and is composed of contributions from lift (c_l, subscript 'i') and drag (c_d, subscript 'o'), and can be separated into:

$$C_P = C_Q = C_{Qi} + C_{Qo} \tag{2.1}$$

Adding and subtracting $\mu \cos\alpha_s C_H = \mu \cos\alpha_s (C_{Hi} + C_{Ho})$, where μ is the tip speed ratio ($\frac{V}{\Omega R}$), gives

$$C_P = C_{Qi} + \mu \cos\alpha_s C_{Hi} + C_{Qo} + \mu \cos\alpha_s C_{Ho} - \mu \cos\alpha_s C_H \tag{2.2}$$

Recognizing that $C_{Qi} + \mu \cos\alpha_s C_{Hi}$ is the power contribution from lift only,

and is equivalent to $\int \lambda \mathrm{d}C_T$ gives:

$$C_P = \int \lambda \mathrm{d}C_T + C_{Qo} + \mu \cos\alpha_s C_{Ho} - \mu \cos\alpha_s C_H \tag{2.3}$$

Then separating the inflow into induced and airspeed contributions, $\lambda = \lambda_i - \mu \sin\alpha_s$, and the thrust into contributions from lift and drag, $C_T = C_{Ti} + C_{To}$, gives:

$$C_P = \int \lambda_i \mathrm{d}C_{Ti} + \int \lambda_i \mathrm{d}C_{To} + C_{Qo} + \mu \cos\alpha_s C_{Ho} - \mu \sin\alpha_s C_T - \mu \cos\alpha_s C_H \tag{2.4}$$

Noting that $C_T \sin\alpha_s + C_H \cos\alpha_s = C_D = -C_X$ is the propulsive force required to overcome parasitic drag so that the parasitic power is given by $C_{Pp} = \mu C_X$, the induced power (C_{Pi}) and profile power (C_{Po}) are defined as:

$$C_{Pi} = \int \lambda_i \mathrm{d}C_{Ti} \tag{2.5}$$

$$C_{Po} = \int \lambda_i \mathrm{d}C_{To} + C_{Qo} + \mu \cos\alpha_s C_{Ho} \tag{2.6}$$

$$C_{Pp} = \mu C_X \tag{2.7}$$

So that finally:

$$C_P = C_{Pi} + C_{Po} + C_{Pp} \tag{2.8}$$

In practice in UMARC, the total power is found directly from the steady

component of the total shaft torque. Parasitic power is trivial to calculate from the hub forces and trimmed shaft angle or directly from the parasitic drag as $C_{Pp} = \frac{1}{2} f \mu^3$. The induced power and profile power both require that the aerodynamic forces be separated into contributions from lift and drag. This is done by duplicating the airload calculations with either lift or drag components ignored, and then subtracting the difference from the total to find the compliment so that the normal force becomes $C_T = C_{Ti} + C_{To}$ and the chord force becomes $C_c = C_{ci} + C_{co}$. Only one of the profile or induced power has to be calculated using eq. (2.9) or eq. (2.10) respectively, the other found from the solution of eq. (2.8).

$$C_{Po} = N_B \int x \mathrm{d}C_{co} + \mu \sin(\psi) \mathrm{d}C_{co} + \lambda_i \mathrm{d}C_{To} \tag{2.9}$$

$$C_{Pi} = N_B \int \lambda_i \mathrm{d}C_{Ti} \tag{2.10}$$

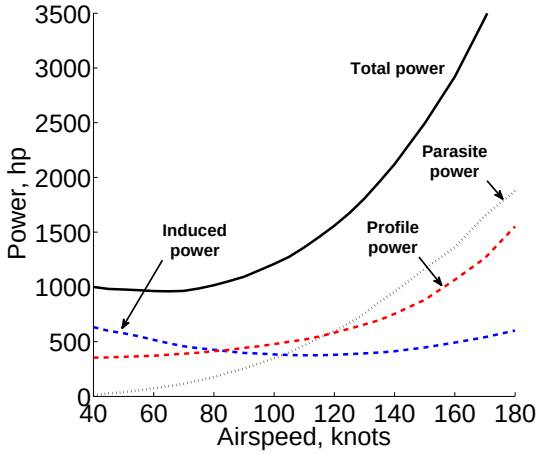

Figure 2.1: Components of rotor power vs. airspeed for a 14,000 lb thrust rotor.

The baseline rotor power is broken down into its constituent parts in fig. 2.1.

At low speeds, induced power is the dominant power component, but its magnitude reduces with airspeed up to near 120 knots. At high airspeeds, the induced power increases due to non-uniformities in the flow. The profile power is initially lower than the induced power at low airspeeds. As the airspeed increases, the profile power increases (initially slowly) to become larger than the induced power. Profile power increases more rapidly at higher airspeeds due to increasing dynamic pressure on the advancing rotor and ultimately due to compressibility. The parasitic power scales quadratically with airspeed and is the largest component of power at high speeds (greater than 130 knots in this case).

The flat plate drag is nominally constant although it is a weak function of fuselage pitch angle (α_s), which does not change significantly with rotor radius. Because the rotor is trimmed to the correct propulsive force in each case, the parasitic drag and the associated power are a function of airspeed only and nominally constant for varying radius. The parasitic power has been subtracted from the total power in the discussion for clarity except when dealing with percentage overall changes when it must be included. Finally, the discussion of performance is meaningful in physical dimensions (hp, lb) rather than non-dimensional (C_P, C_T), for a variable speed rotor.

2.1.3 Variable Radius Algorithm

UMARC is a non-dimensional analysis, which facilitates straight forward comparisons between the performance of rotor concepts. However, when comparing

variable radius or variable rotor speed concepts it is important to ensure that the rotor description and sectional properties remain consistent. For example, the total mass of a variable radius rotor must remain constant. Also, the inputs to UMARC are non-dimensionalized by the blade mass per unit length (m_0), rotor radius (R) and rotor speed (Ω) so that the inputs must be re-derived for each variation in radius or rotor speed.

In order to avoid user error, a preprocessor has been added to UMARC that finds the updated mass, twist and airfoil distributions and then calculates an updated mass per unit length (if necessary) with which to correct the non-dimensional rotor description and sectional properties. The mass redistribution after radius variation requires some engineering judgment to ensure that the rotor total mass is maintained. The algorithm allows for two approaches to radius variation, selected by user input. These are the morphing area concept and the variable root cut-out concept.

Morphing Area Concept: A schematic for the morphing area concept is shown in fig. 2.2, which shows the planform and blade mass distribution (m_b) at 100% and 90% radius. The example has 15 finite elements and a uniform mass distribution for the baseline rotor. The concept assumes that the change in radius is achieved by morphing the blade area such as could be achieved with a flexible airfoil surface. The morphing region is defined by elements 3 and 7 for the example, but can be any arbitrary sequence of blade elements. After radius variation, it is assumed that changes to the blade mass distribution (or any property) are isolated to the morphing region and the mass is uniformly redistributed over the morphing

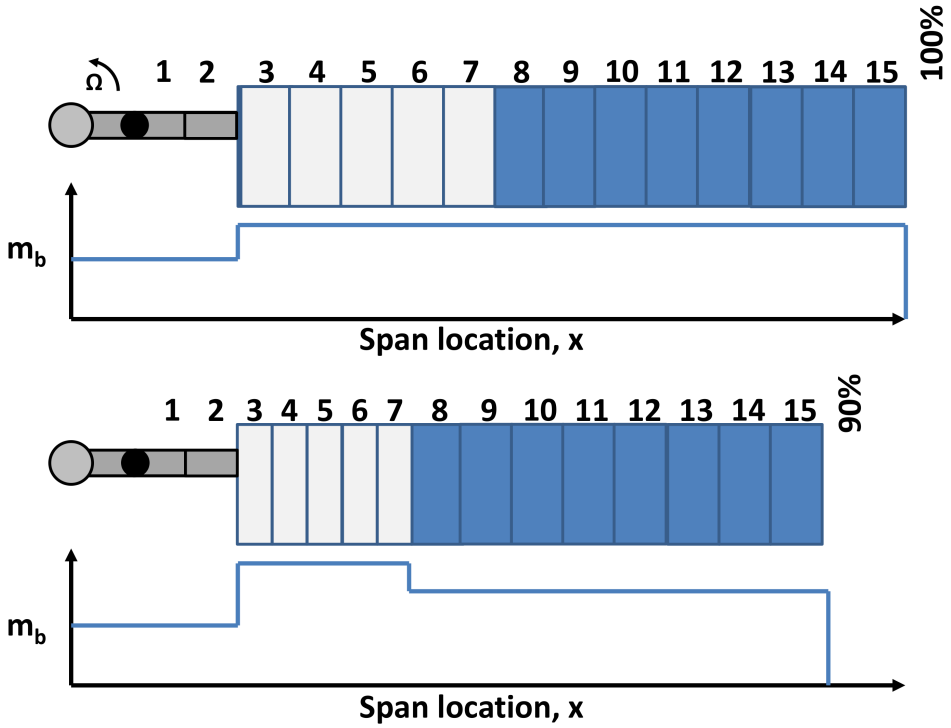

Figure 2.2: Variable radius concept: Morphing area, with nominal mass redistribution.

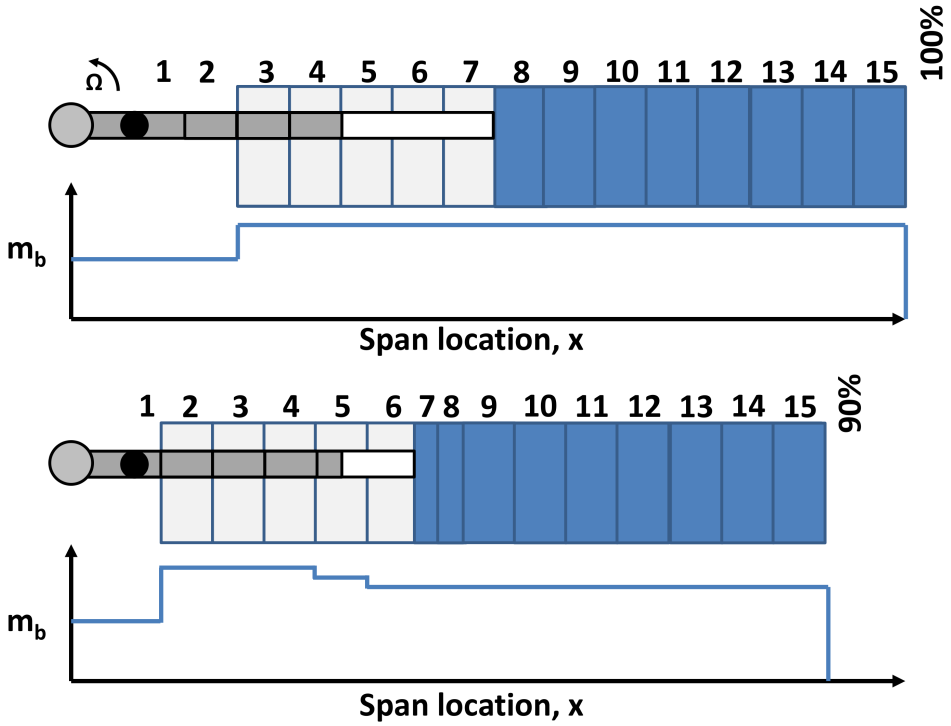

Figure 2.3: Variable radius concept: Variable root cut-out, with nominal mass redistribution.

region alone. The size of the elements in the morphing region scale to accommodate the change in radius.

Variable Root Cut-out Concept: The variable root cut-out concept is shown in fig. 2.3. This concept assumes that the lifting blade area is constant, so that radius variation is achieved by sliding the outer blade over the stationary spar at the root cut-out. In this case, blade elements 3 and 7 define the maximum region of overlap, and element 4 defines the length of stationary spar. Engineering judgment, or rather a detailed design, determines the length of spar overlap necessary at the maximum radius. With radius reduction, the mass in the spar elements (1 and 2 at 100% radius) is transferred to the overlapping blade elements of the blade (2–5 at 90% radius). Note that when the radius reduction results in reducing the number of blade elements, additional blade elements are added to the outboard blade by splitting existing elements (7 and 8 after radius reduction). Partial overlap of the spar and a blade element (element 5 after radius reduction) is handled by uniformly distributing the mass over the element.

Once the new mass distribution is found by either concept, the blade flapping inertia (I_β) is found by integration:

$$I_\beta = \int_e^R m_b x^2 \mathrm{d}x \tag{2.11}$$

Which is needed to calculate the updated lock number (γ), which defines the ratio of aerodynamic and inertial forces. The blade mass per unit length , m_0,

needed for the non-dimensionalization is:

$$m_0 = \frac{3I_\beta}{R^3} \tag{2.12}$$

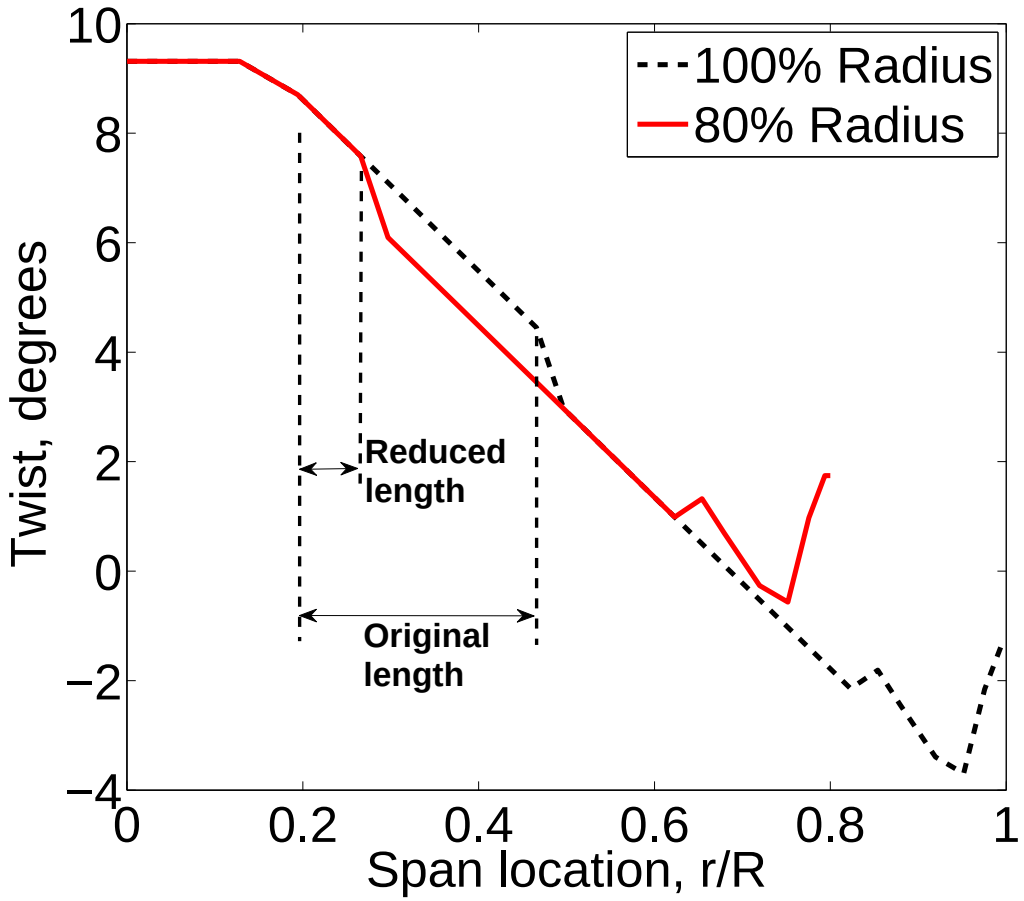

Figure 2.4: Variation of blade twist with radius – 100% and 80%.

The distribution of blade stiffness properties and other sectional properties can be treated differently to the mass distribution. A simple approach is taken here that assumes that the remaining sectional properties are unchanged by morphing for the morphing blade area concept, and are equal to the outer blade for the variable root cut-out concept. The blade twist does change with radius variation. Two possible

scenarios are that that twist rate is fixed so that the absolute twist varies with radius, or that the absolute twist is fixed and the twist rate varies over the morphing region. Both options are made available in UMARC as a user input, noting that if a fixed twist rate is desired, the blade twist must be linear in the region of radius variation to remain physical. Figure 2.4 shows the twist distribution that results assuming a fixed twist rate is maintained. Because the example twist distribution is has stepwise variations in twist rate, the radius variation has been confined to a region of linear twist in order to remain physical. Similarly, care must be taken when dealing with multiple airfoils along the span. The current method assumes that the airfoil does not change over a region of radius variation.

2.2 Variable Radius Model

2.2.1 Baseline UH-60A Rotor Model

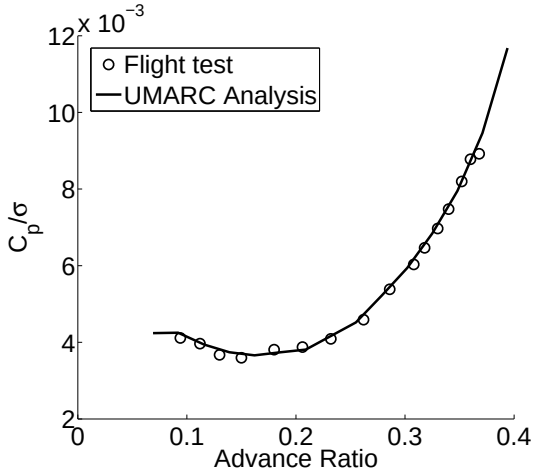

Figure 2.5: Validation of UMARC power prediction with UH-60A Black Hawk airloads data ($C_T/\sigma = 0.0783$).

The baseline rotor is a representative utility helicopter based on the UH-60A

Black Hawk because of the ready availability of the rotor description and important sectional properties which ensures a representative model. Extensive flight testing of the UH-60A has made available power measurements for validation of the analysis. The measured and predicted power versus airspeed for a steady, level flight is shown in fig. 2.5 for $C_T/\sigma = 0.08$, showing good agreement over the airspeeds of interest.

Table 2.1: Rotor properties.

Rotor properties	Value
Rotor type	Articulated
Number of blades	4
Radius	26.83 ft.
Twist	Non-linear (≈-16°)
Chord	1.73 ft.(nominal)
Rotor Speed (100%)	258 RPM
Solidity σ	0.0832
Lock number	6.33
Flat plate area, f	35 ft^{2†}

† Increased from 26 ft to reflect airloads program aircraft [106].

UH-60A rotor is described in table 2.1. The rotor aerodynamic description and structural properties and fuselage properties are available through the Airloads Program [57]. The rotor model uses the accepted airfoil distribution, the SC1095 airfoil between 20%–49% and 82%–100% radius and the SC1094r8 airfoil in the remaining station between 49%–82% radius. Airfoil tables are available for both airfoils. The measured twist distribution is used, although the tip sweep has not been modeled.

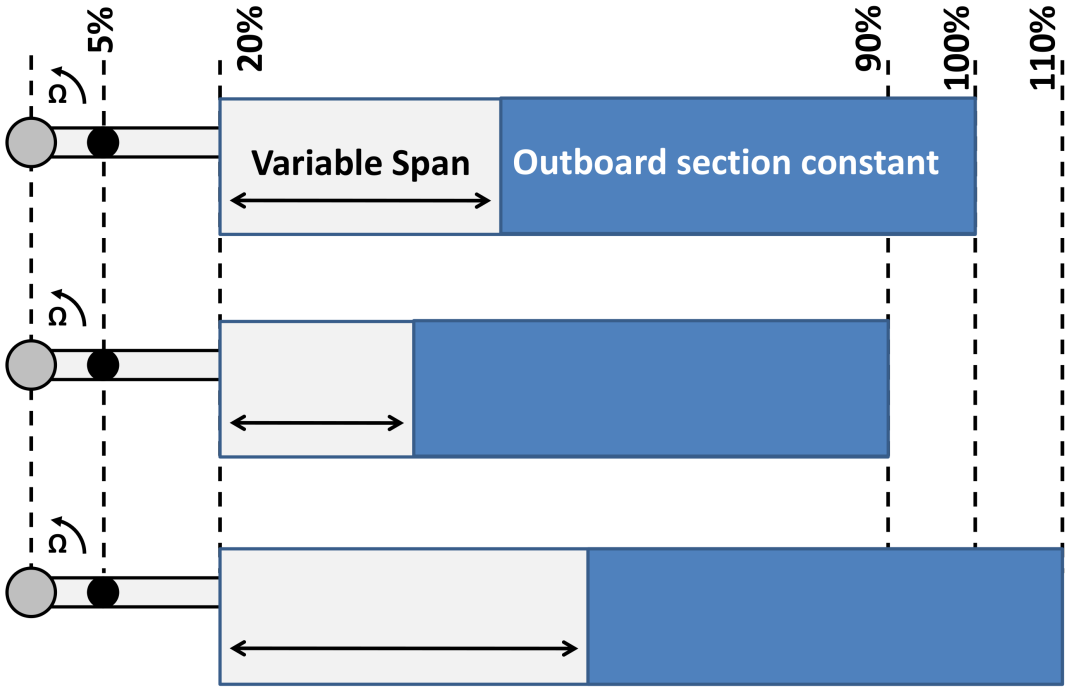

Figure 2.6: Schematic of variable radius concept with morphing blade area.

2.2.2 Description of Radius Variation Concept

The previous section introduced two concepts to radius variation that have been implemented in UMARC. The following results deal only with the morphing blade area concept, shown again in fig. 2.6. The alternate concept is investigated briefly at the conclusion of the results. The morphing area concept assumes a constant root cutout with a variable span lifting area. Because the baseline blade properties of the UH-60A rotor vary along the span, the variable radius concept assumes that the morphing area is between the root cut-out (20%) and the midspan (50%) to align with the constant twist rate, chord and airfoil in that region. It is assumed that the twist rate remains constant so that the absolute twist varies with

radius. Figure 2.4 shows how the aerodynamic twist variation looks for the baseline rotor and when the radius is reduced to 80%.

The blade stiffness properties are assumed to remain unchanged over the morphing region during radius change. There is no change in chord, center of lift, tension axis or c.g. offset (chordwise) to accommodate radius change. These assumptions are suitable for aerodynamic performance comparisons and first order dynamic comparisons.

Table 2.2: Variation of key aerodynamic properties

% Radius	100%	106%	94%	90%
Radius (ft)	26.83	28.44	25.22	24.15
Solidity	0.0817	0.0772	0.0869	0.907
C_W/σ	0.0693	0.0582	0.0835	0.0952
Lock No. (γ)	7.51	8.57	6.53	5.91
1^{st} Flap (/rev)	1.038	1.036	1.041	1.043
1^{st} Lag (/rev)	0.281	0.272	0.290	0.296
1^{st} Torsion (/rev)	4.251	4.150	4.361	4.439

Table 2.2 presents the variation in the key rotor properties with radius, fractions of 100%, 106%, 94% and 90% for a 16,000 lbs helicopter. The thrust weighted solidity (σ) increases with the radius reduction. The thrust coefficient (C_w) increases by $1/R^4$ for a constant weight. The Lock number is a function of the reducing radius and an inverse function of the flap inertia I_β, which decreases with radius, resulting in a net decrease with radius. The first blade flap, lag and torsion frequencies all increase slowly with a reduction in radius.

Airspeeds between 40 and 170 knots and gross weights between 14,000 lb and 20,000 lb (in 5 knot and 2000 lb increments respectively) are considered for a representative flight envelope. The radius is reduced in 2% steps until the changes

Table 2.3: Summary of variable radius cases evaluated

Thrust (lb)	14,000	–	20,000 (2,000 lb steps)
Airspeed (knots)	40	–	180 (5 knots steps)
Advance ratio	0.1	–	0.4
Radius ratio (% of baseline)	90	–	106 (2% steps).

in performance are no longer favorable at any airspeed for a targeted thrust (90% RPM was the minimum considered for the 14,000 lb rotor, and 106% radius was the maximum for the 20,000 lb rotor). The rotor speed remains fixed for this study so that tip speed varies linearly with radius. The flight conditions evaluated are summarized in table 2.3. Maintaining trim without auxiliary lift devices ensured that the advance ratio did not exceed $\mu = 0.4$ and reverse flow aerodynamics were not significant (but were included in the model).

The evaluation of performance assumes that there is no weight or efficiency penalty associated with achieving radius change. The performance presented here should be regarded as the performance of the rotor alone. Because the helicopter is trimmed to the same equilibrium, with the same propulsive force, propulsive power is unchanged. Therefore only induced and profile power are considered in the comparison.

2.3 Variable Radius Performance

The rotor power (sum of induced and profile power) for the baseline helicopter at 14,000 lb gross weight is shown in fig. 2.7a where the radius is varied in 2% steps between 102% and 90% of the baseline radius. At 40 knots, 90% and 92% radii require somewhat more power but otherwise the power is indiscernable from

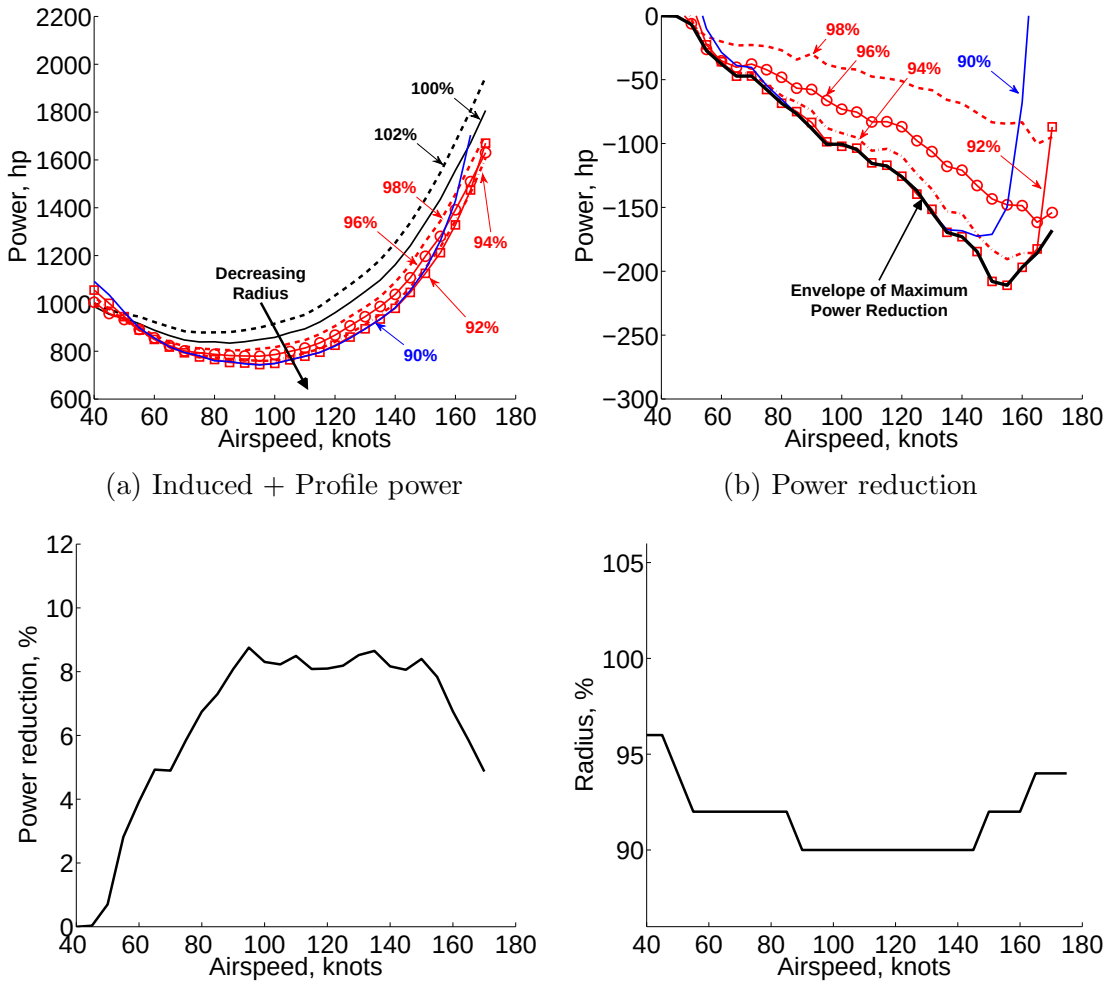

(a) Induced + Profile power

(b) Power reduction

(c) Maximum % Power reduction

(d) Radius schedule for minimum power

Figure 2.7: Variation of rotor power at 14,000 lb with varying rotor radius.

the baseline. For increasing speeds, the power gets reduced by radius reduction; while, increasing rotor radius always increases power. Radius reductions to less that 90% radius showed no additional improvement in performance. Both the 90% and the 92% radius rotors appear to stall above 150 and 160 knots respectively indicated by the more rapid increase in power at those speeds relative to the baseline. Figure 2.7b shows the difference between the baseline power and the power required for each variation in radius as a function of airspeed (only cases that decreased power are illustrated). For each radius, the difference in power increases with increasing airspeed before stall. The maximum reduction in power is 210 hp at 155 knots, which is followed by a sharp decrease in power reduction at higher speeds. At high airspeeds, the total power (excluding parasitic power) is predominately profile power. Reducing the rotor radius, reduces both the blade area and the maximum dynamic pressure (on the advancing tip) that bring about the large reduction in profile power. At low airspeeds, the induced power is the largest component of power. Induced power increases with reducing disc area and this counteracts the reduction in profile power. These two competing power terms appear to cancel at around 50 knots regardless of radius (true only for this thrust condition).

Figure 2.7c illustrates the maximum percentage reduction in power (total power including parasitic power) that can be achieved through radius variation for the 14,000 lb thrust case. The percentage power increases from 0% at 40 knots to 8.5% at 90 knots where it is nearly constant up to 160 knots before stall limits further improvement. Finally, the radius schedule that maximizes power reduction at each airspeed is shown in fig. 2.7d. A maximum reduction in radius to 90%

is required to maximize performance, although comparing the power reduction in fig. 2.7b suggests that 92% would perform almost as well.

Table 2.4: Aircraft blade loading coefficient with increasing gross weight

Gross Weight (lbs)	14,000	16,000	18,000	20,000
C_T/σ 100% Radius	0.0593	0.0698	0.0762	0.0847
C_T/σ 92% Radius	0.0762	0.0896	0.0980	0.1089

The impact of gross weight on the rotor power reductions due to radius variation is shown in fig. 2.8, which shows the power difference from baseline as the radius is varied for increasing gross weights between 16,000 and 20,000 lb. Table 2.4 shows the blade loading for each thrust at 100% and 92% radius. The 98% radius cases for the 16,000 lb and 14,000 lb thrust cases behave similarly, each case reducing power by 80 hp at 155 knots, indicating that both cases have the rotors operating away from stall. At 96% radius and 155 knots the power reduction remains similar, but for larger reductions in radius, the 16,000 lb rotor shows no further improvement in performance indicating that the rotor, operating at a higher blade loading, is becoming stalled. At 18,000 lb, the power reduction available at 98% radius is lower than for the lower thrust cases indicating that the higher blade loading rotor is already impacted by stall. Finally, at 20,000 lb, the change in power that can be achieved by radius reduction is marginal at any airspeed above 60 knots. The relative dominance of induced power at low airspeeds is seen by the performance improvement possible by increasing radius near 40 knots (and this is expected to grow for lower airspeeds). Both the 18,000 lb and 20,000 lb rotors show a large reduction in power at 40 knots with 2%-4% increase in radius. Finally, the results

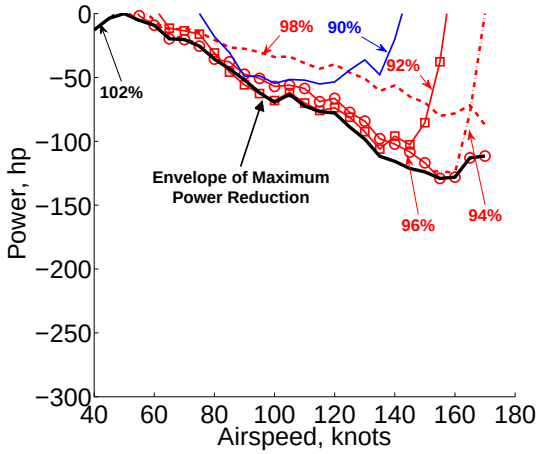

(a) Power reduction (16,000 lb)

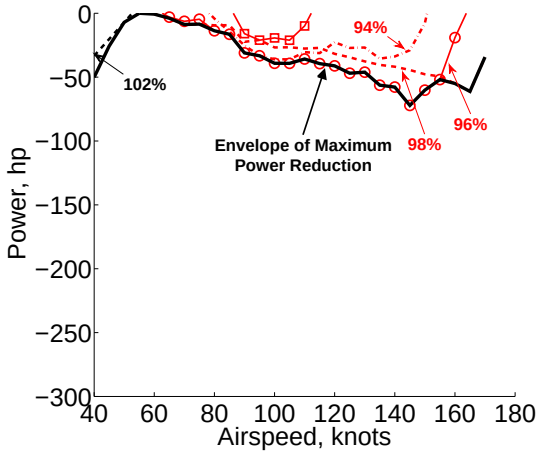

(b) Power reduction (18,000 lb)

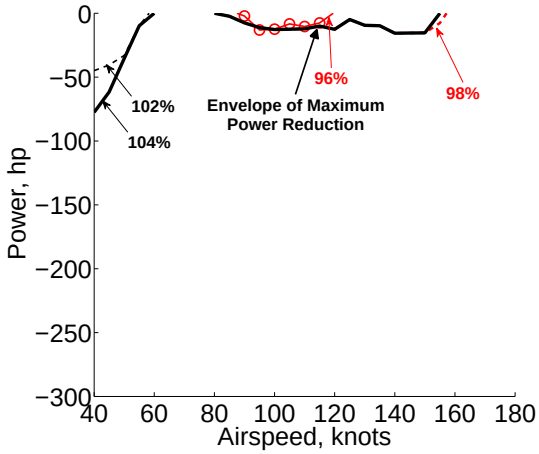

(c) Power reduction (20,000 lb)

Figure 2.8: Reduction of rotor power at 16,000 lb, 18,000 lb and 20,000 lb with varying rotor radius.

confirm that the baseline UH-60A helicopter runs out of stall margin at 20,000 lb and 160 knots, which agrees with the known limitations of the helicopter and further validates the analysis.

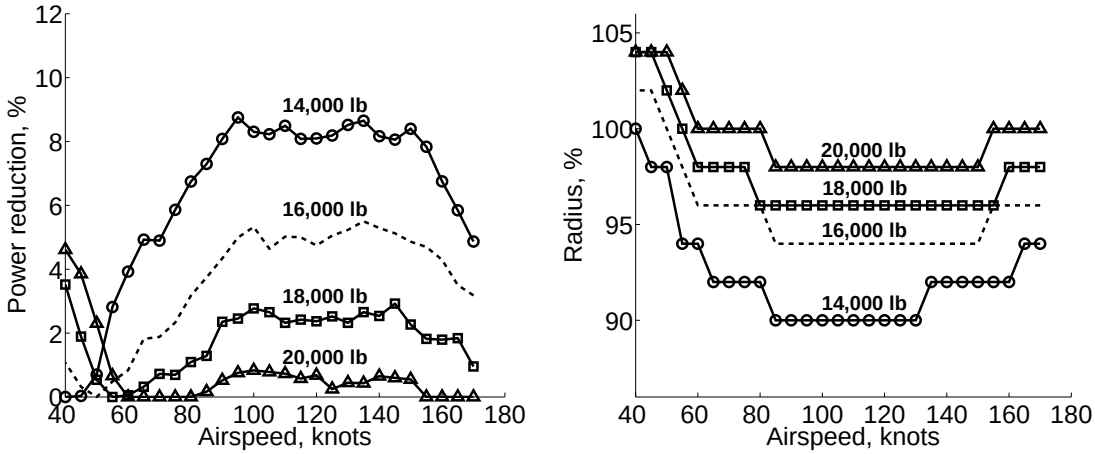

(a) Maximum % reduction in total power (b) RPM schedule for minimum power

Figure 2.9: Maximum % power reduction and associated radius schedule (14,000 lb - 20,000 lb).

The maximum reduction in power as a percentage of the total power, and the radius schedule that gave the result is shown in fig. 2.9b as a function of airspeed for 14,000 – 20,000 lb thrust. The trend is similar in each case, with an approximately constant percentage improvement in power (8.5%, 5%, 3% and 1% respectively) between 100 – 150 knots and decreasing rapidly thereafter. Both the 18,000 lb and 20,000 lb thrust cases show a consistent performance increase below 60 knots when increasing the radius. A range of radius between 90% – 104% would be required to minimize power for the range of thrusts and airspeeds considered. Assuming that reducing high speed power requirements is a priority, and noting that the difference in performance between 90% and 92% radius was small for 14,000 lb of thrust, a reasonable range of 92%–100% radius would maintain current capability as well as

significantly reducing power at high airspeeds for lower thrusting rotors.

2.4 Aerodynamic Analysis

This section breaks down the performance improvements available from radius variation into contributions from induced and profile power and investigates the impact of stall. The analysis focuses on a 18,000 lb thrust condition ($C_T/\sigma = 0.076$ for baseline radius) as being representative of a typical rotor.

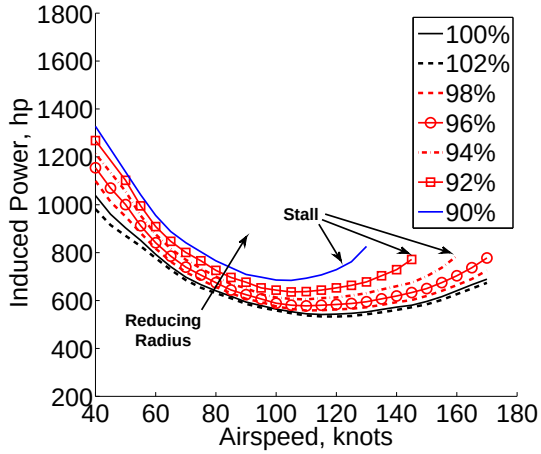

(a) Induced power vs. airspeed

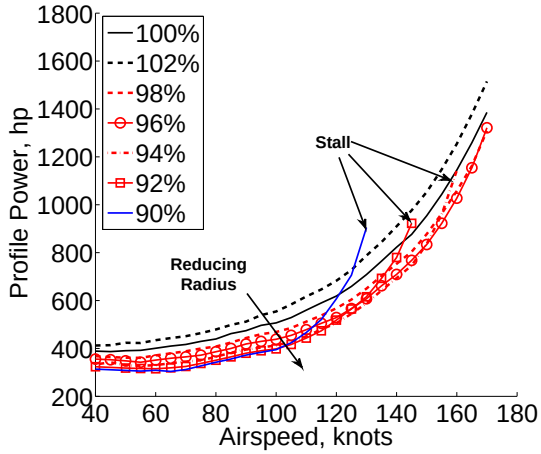

(b) Profile power vs. airspeed

Figure 2.10: Induced and profile power variation with reducing rotor radius (W = 18,000 lb)

Figures 2.10a and 2.10b show the impact of radius variation on the induced and profile power components with airspeed for a 18,000 lb helicopter. Reducing the radius (i.e., increasing disk loading) increases the induced power at all speeds; while, increasing the radius to 102% marginally decreases induced power. The result follows from the relationship between induced power, thrust and disc area while maintaining the same thrust on a smaller disc area implies higher induced velocities and thus higher induced power. The induced power is largest at low airspeeds, and reducing radius has the largest penalty at low airspeeds. The 90%, 92% and 94% radius cases show divergent induced power behavior near their respective maximum speeds that is due to increasing non-uniformity in the induced inflow due to stall.

The motivation for reducing rotor radius is shown in the change in profile power with radius for increasing airspeds fig. 2.10b. Reducing the rotor radius, reduces blade area and the dynamic pressure at the blade tip where drag power losses are greatest. This results in reduced profile power requirements at the cost of increased blade loading. Increasing blade loading does not incur a significant drag penalty if the sectional angles of attack do not approach stall. The reduction in profile power for the 98% radius case increases with airspeed and is greatest at the highest airspeed considered (170 knots). The profile power reduces more at higher airpseeds due to delaying compressibility effects at the advancing tip, which is captured through airfoil tables. At 96% radius, the decrease in profile power no longer grows continuously with airspeed and the profile power increases more rapidly at high airspeeds (above 150 knots) than the 98% or the baseline radius. The increased blade loading together with growing flow asymmetry (μ is higher

for the smaller radius at the same airspeed) promotes earlier stall on the retreating rotor resulting in a rise in profile and induced power. By the 90% - 94% radius cases, stall becomes more severe with the profile power exceeding the baseline rotor and finally resulting in limiting the flight envelope to lower airspeeds. The 90% shows no additional reduction in profile power over the 92% radius case. The blade loading at 90% radius ($C_T/\sigma \approx 0.1$) has been increased to the extent that the increased sectional drag overcomes the reduced blade area, and the profile power cannot be reduced further.

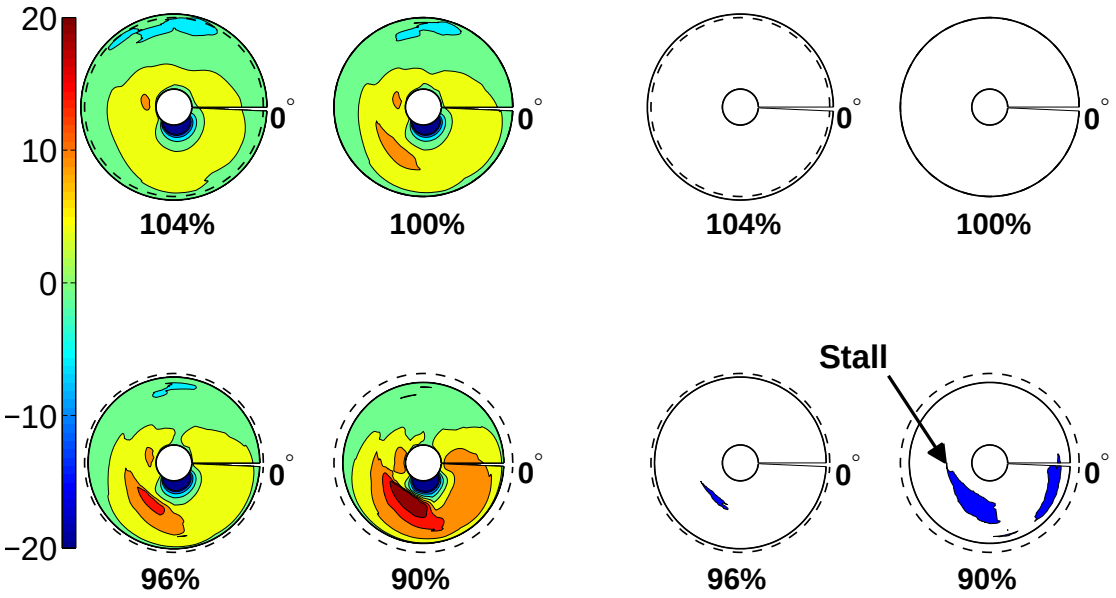

(a) [Angle of attack distribution (b) Stall distribution

Figure 2.11: Angle of attack and stall locus at 120 knots (W = 18,000 lb) (Disc area is scaled to represent the radius and the dashed circle indicates the baseline rotor)

The distribution of angle of attack for radii between 104% and 90% at 120 knots and a gross weight of 18,000 lb is shown in fig. 2.11a. Decreasing the radius,

resulting in increasing blade loading as indicated by increasing mean angle of attack. To maintain trim in forward flight, blade pitch is such that the angle of attack increases more rapidly on the retreating blade. Because the baseline rotor is highly twisted, the advancing tip is negatively loaded for the baseline rotor at this airspeed. Decreasing radius decreases the absolute blade twist because twist rate is assumed to remain constant for this concept (fig. 2.4), which in combination with increasing blade loading results in the negative tip loading disappearing with radius reduction to 90%. This effectively exacerbates the lift imbalance and requires larger still longitudinal cyclic to maintain roll balance, further increasing retreating side angle of attack. Figure 2.11b compares the sectional angle of attack to the break in the lift coefficient at the onset of stall to show regions of probable static stall (dark shading). At the root cut-out, a region of reverse flow exists with associated high angles of attack that exceed the stall limits but these are not important for performance due to very low dynamic pressures seen there. At 96% radius, corresponding to the radius for minimum power for this airspeed, the stall map indicates that outboard regions on the retreating blade are at the stall limit, which corresponds to the best efficiency of the airfoil. Reducing the radius further to 90% results in significant stall, increasing sectional drag and overall degraded performance (compared to 96% radius).

The normal force distribution for the 18,000 lb gross weight helicopter at 120 knots is shown in fig. 2.12a. As already mentioned, the negative lift on the advancing tip is effectively reduced as the radius is decreased and larger longitudinal cyclic pitch is required to ensure roll trim. For the rotor to produce enough thrust, lift must

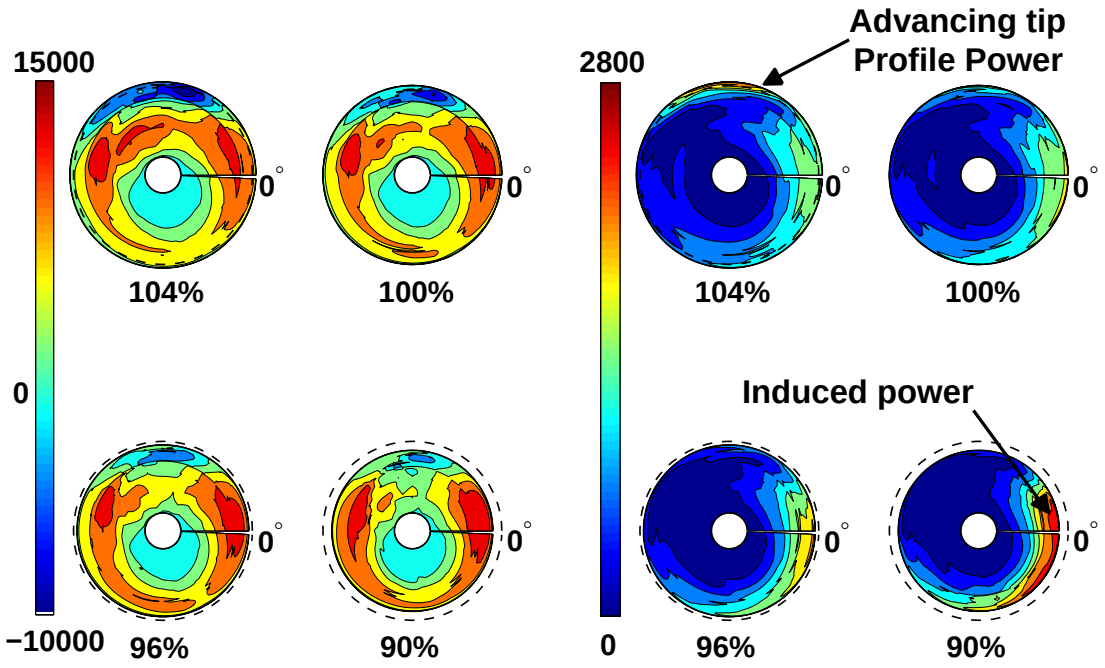

(a) Normal force (lb/ft)

(b) Total power (hp/ft)

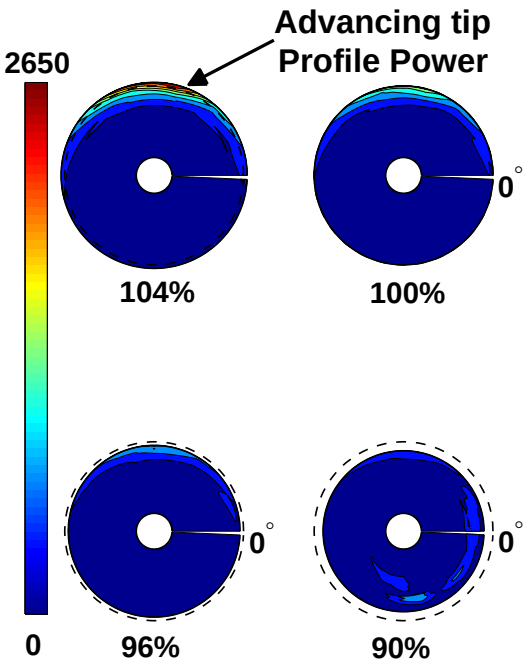

(c) Profile power (hp/ft)

Figure 2.12: Total and profile power locus at 120 knots (W = 18,000 lbs)

increase elsewhere and the fore and aft rotors are producing the majority of the lift. Reducing the radius causes the aft rotor to carry a larger share of the total lift.

The change in total rotor power with variation of radius for the same flight conditions is shown in fig. 2.12b. This illustrates the competing roles of profile and induced power. Reducing the radius negates the high dynamic pressures of the tip region, and reduces the overall blade area to return a reduction in profile power. Reducing the radius also increases blade loading and the airfoil sections operate at higher mean efficiency (in terms of $^{c_l}/_{c_d}$) resulting in some of the power savings in the second quadrant. The induced power is increasing on the aft rotor as the aft rotor carries more lift. When the rotor is stalled (90% radius for this airspeed) a much larger share of the lift is carried on the aft rotor giving rise to the large induced power penalty. Figure 2.12c shows just the profile component of the total power and confirms that profile power in the stalled regions contribute a relatively minor component of the total power, compared to the induced power on the aft rotor (the colors scales are similar for comparison).

2.5 Trim with Radius Variation

Figure 2.13 shows the variation of vehicle trim controls and orientation with airspeed for a gross weight of 18,000 lb. The rotor collective increases as the radius is reduced in order to maintain trimmed thrust on a smaller rotor. Longitudinal (θ_{1s}) and lateral (θ_{1c}) cyclic correct trim for the increasing collective and the effective reduction in twist, which both act to increase cyclic magnitude relative to the

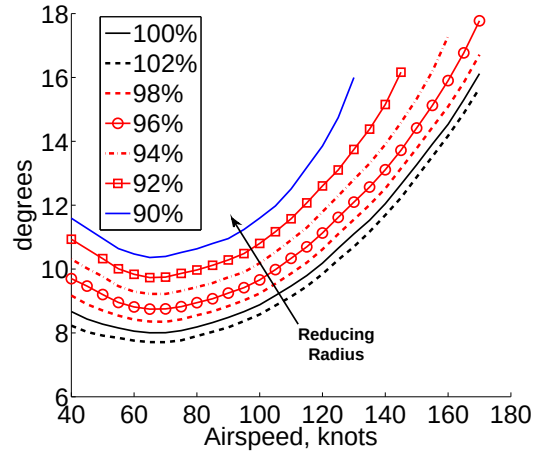

(a) Collective, θ_0

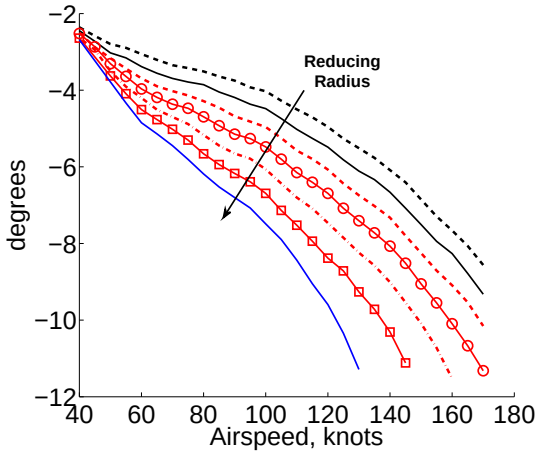

(b) Longitudinal cyclic, θ_{1S}

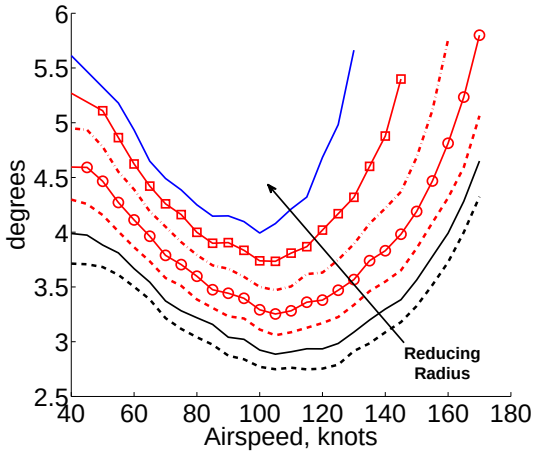

(c) Lateral cyclic, θ_{1C}

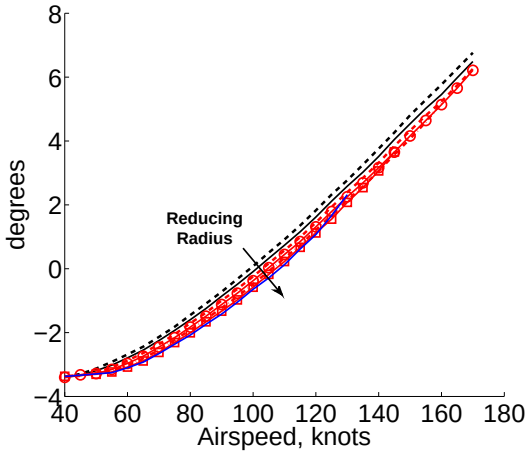

(d) Longitudinal shaft tilt, α_s

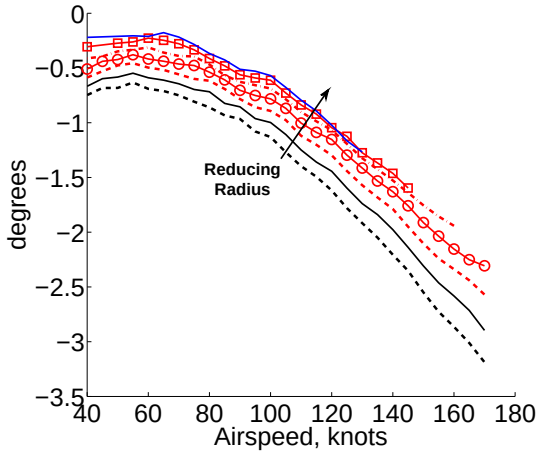

(e) Lateral shaft tilt, ϕ_s

Figure 2.13: Vehicle trim control and shaft orientation angles vs. airspeed at 18,000 lb with varying rotor radius

baseline. At stall, both cyclics increase (absolute values) more rapidly to achieve roll and thrust trim. The longitudinal cyclic looses authority with radius reduction, indicated by the increasing slope. At 90% radius, a larger change in longitudinal cyclic is required to effect a unit change in airspeed. Longitudinal and lateral shaft angles are not significantly impacted by radius variation with about 0.5° variation for the radii considered.

2.6 Vibratory Hubloads

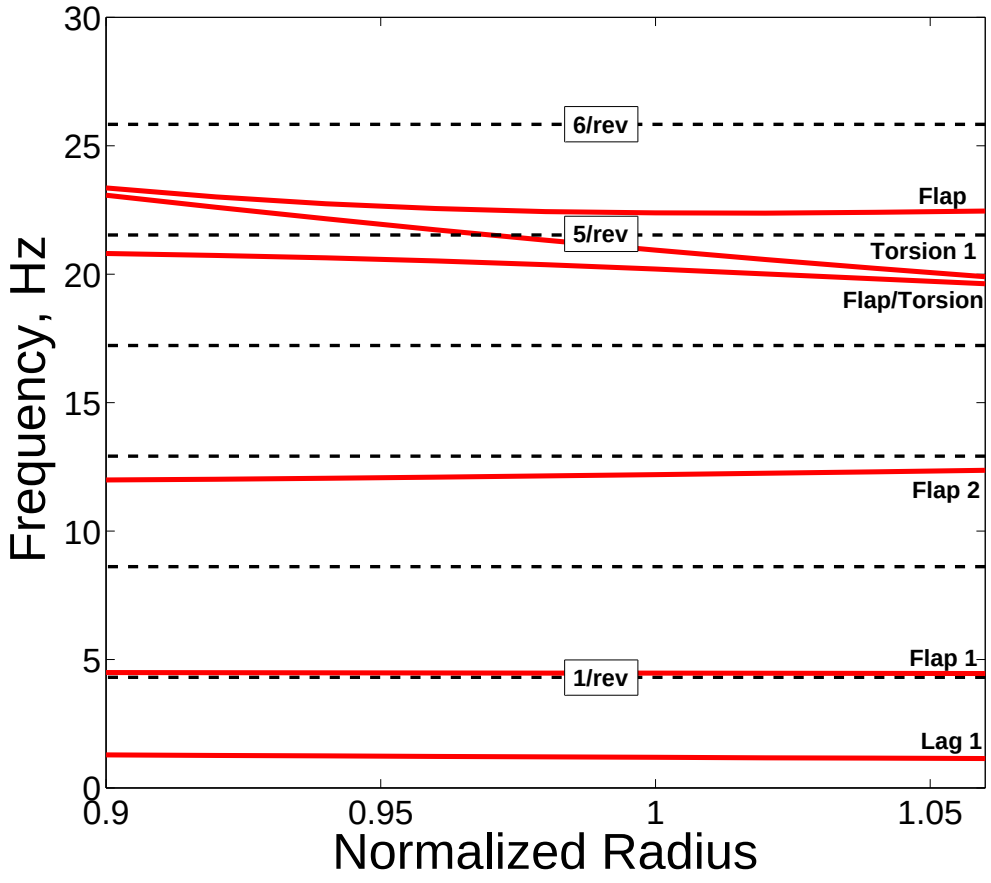

Figure 2.14: Variation of rotor frequencies with radius.

The variation of blade frequencies with radius is shown in fig. 2.14. For an articulated rotor the first flap and lag frequencies are not strong functions of radius ($\nu_\beta \approx \sqrt{1 + {}^{3\overline{e}}/_{2}}$, $\nu_\zeta \approx \sqrt{{}^{3\overline{e}}/_{2}}$, where $\overline{e}$ is the non-dimensional hinge offset). The higher blade frequencies increase with reducing radius primarily due to the reduced flap inertia of the contracted blade. This radius variation configuration has the fifth mode (torsion) crossing the 5/rev rotor passage frequency near 96% radius.

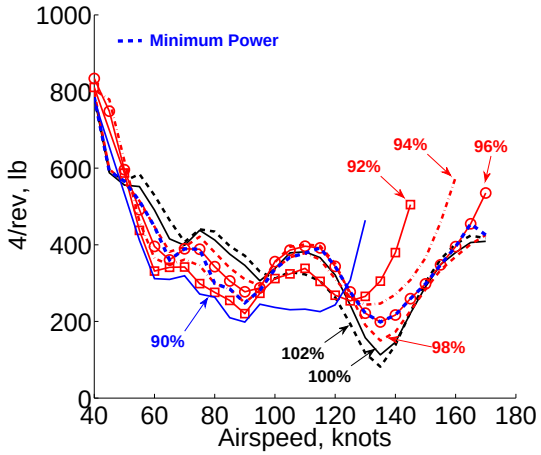

(a) Vertical shear force, F_z

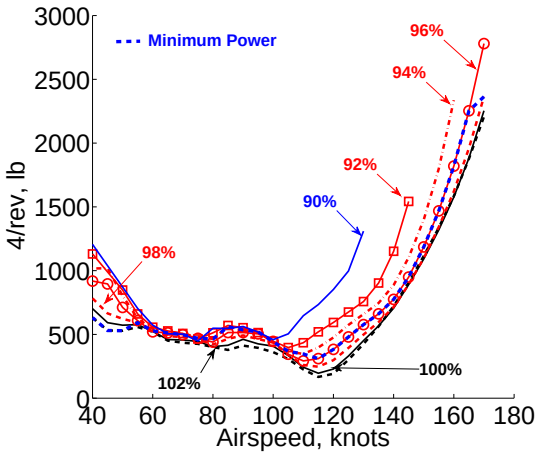

(b) In-plane shear force, $\sqrt{F_x^2 + F_y^2}$

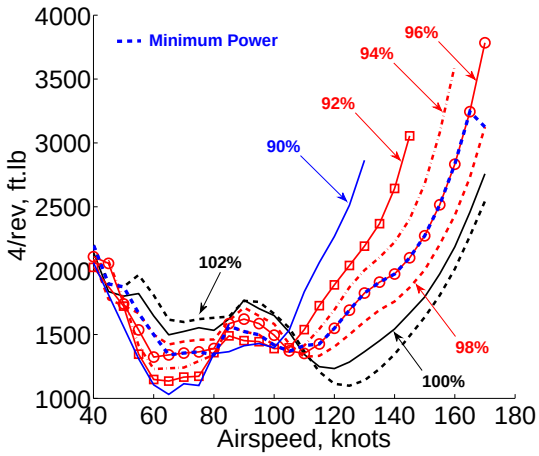

(c) In-plane moments, $\sqrt{M_x^2 + M_y^2}$

Figure 2.15: 4/rev hubloads vs. airspeed at 18,000 lb with varying rotor radius

The primary vibratory loads generated by the four bladed rotor are the 4/rev

fixed frame hubloads. These are the vertical shear load (F_z), the in-plane shear load ($\sqrt{F_x^2 + F_y^2}$), and the in-plane moment ($\sqrt{M_x^2 + M_y^2}$), shown for a 18,000 lb gross weight rotor at a selection of radii in fig. 2.15. Included in the figures are the expected hubloads that result for the rotor at its minimum power radius (dashed blue line). The 4/rev vertical hub shear is reduced by decreasing the radius at low to moderate speeds (less than 110 knots). At higher airspeeds, the reduced radius rotor would be penalized by higher vertical vibrations than the baseline rotor. The hubloads associated with minimum power are marginally lower than the baseline rotor at low speeds, and similar to the baseline at higher airspeeds. The in-plane vibratory forces for the reduced radius rotor are always larger than the baseline, but only significantly for larger radius reductions (90%) at higher airspeeds (above 100 knots). The in-plane shear force hubloads for minimum power will be higher than the baseline, but again not significantly so. The in-plane moments decrease for the reduced radius cases at low speeds but are much larger than the baseline at high airpseeds.

The 4/rev hubloads are plotted as functions of advance ratio (rather than airspeed) in fig. 2.16 that show that the trends are consistent with advance ratio and are not strongly influenced by the impact of radius variation or of advancing tip compressibility. There is also no evidence of increased hubloads near 96% radius, where the fanplot indicates the 1^{st} torsion can be excited in resonance. The increase in 4/rev loads seen in the in-plane shear and in-plane moments occurs consistently around $\mu = 0.27$ suggesting that flow asymmetry is the dominant cause. The somewhat dissimilar trend for the 90% radius case is due to significant stall giving rise

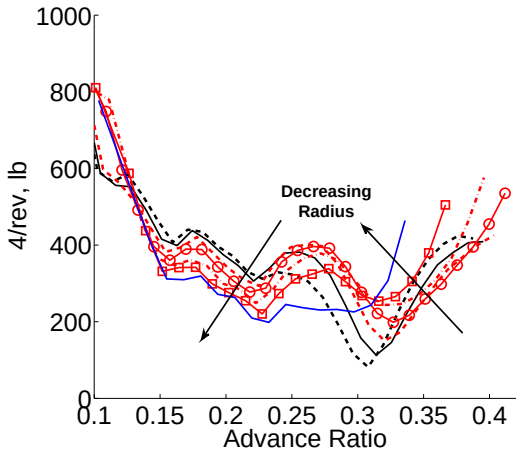

(a) Vertical shear force, F_z

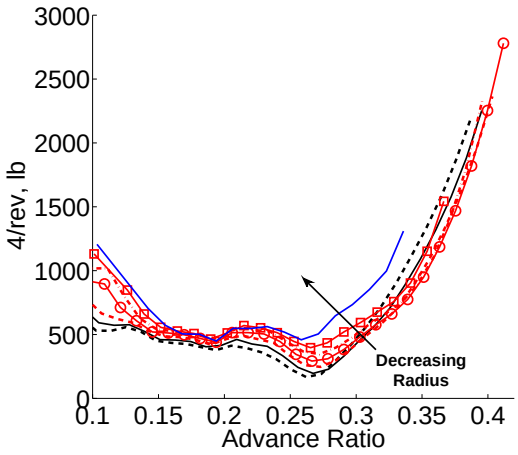

(b) In-plane shear force, $\sqrt{F_x^2 + F_y^2}$

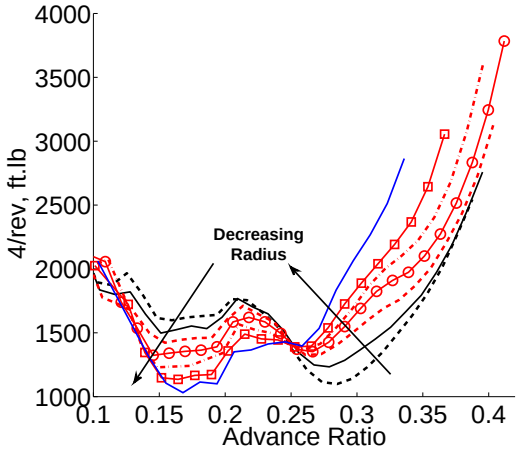

(c) In-plane moments, $\sqrt{M_x^2 + M_y^2}$

Figure 2.16: 4/rev hubloads vs. advance ratio at 18,000 lb with varying rotor radius

to higher vibrations at earlier advance ratios.

The vibration results must be viewed in light of the limitations of the analysis. Namely, above an advance ratio of 0.35 (for the 100% radius rotor) CFD-CSD is needed to capture the effects of compressibility on the advancing tip. Also, while the analysis has assumed a single tip vortex in the wake model (suitable for performance), a second wake trailer that captures the region of negative lift on the advancing side can be important for vibrations at high speeds.

2.7 Alternative Radius Variation Concepts

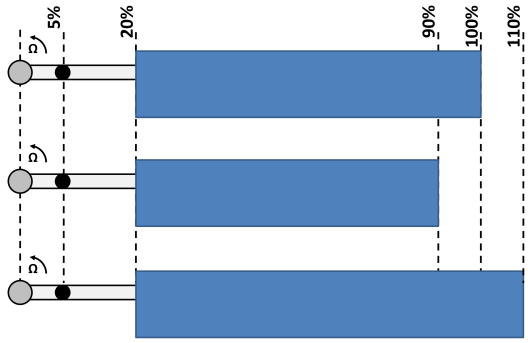

(a) Morphing blade area concept

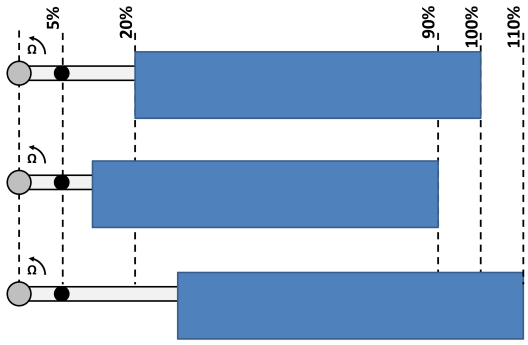

(b) Constant blade area concept

Figure 2.17: Alternative variable radius concepts

Figure 2.17 shows the baseline radius variation concept (fig. 2.17a) as well as an alternative concept that mimics the TRAC rotor design (derived from Telescoping Rotor AirCraft), shown in fig. 2.17b. The second concept varies the root cutout to accommodate radius variation and will highlight the importance of the root cutout to variable radius rotors. For a consistent comparison, drag in the root cutout must be included. It is assumed that root cut-out is an elliptical fairing with a drag coefficient of 0.02 and a chord of half that of the rotor blade.

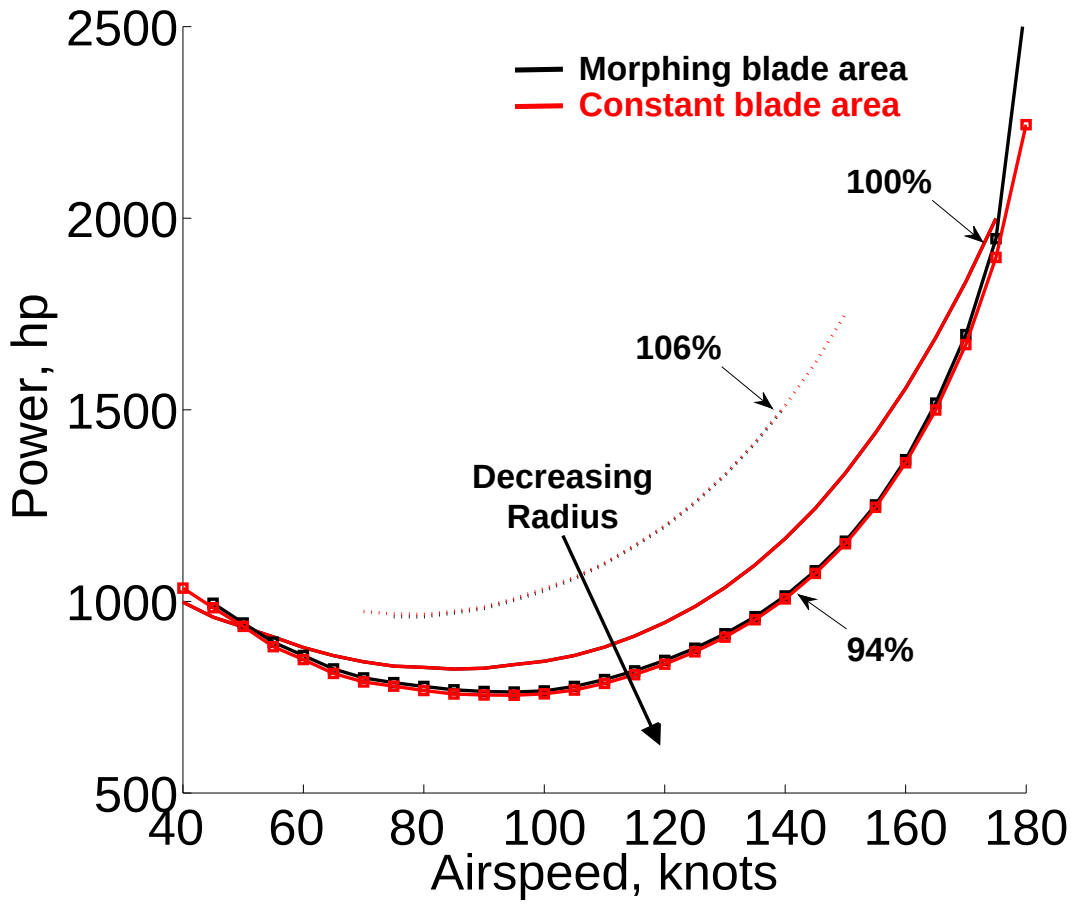

Figure 2.18: Comparison of power for alternative radius variation concepts at 14,000 lb.

Figure 2.18 shows the total of induced and profile power between the two pro-

posed concepts for a rotor at a gross weight of 14,000 lb at 106%, 100% and 94% radius. The power at 100% is indiscernible between the two concepts as expected. The difference in performance between the concepts is marginal for both the larger (106%) and smaller (94%) radius rotors with the constant blade area concept requiring slightly less power at 94% radius, but otherwise there is no visible difference. The constant blade area concept exchanges root cutout span, which has a relatively high drag coefficient ($C_d = 0.02$), with the blade which has a relatively low drag coefficient of the airfoil ($C_d \approx 0.01$). The dynamic pressures in the root cutout are low and keep the total power difference to a small value. The magnitude of the power difference is strongly influenced by the drag associated with the root cutout; however, for the range of thrusts and airspeed considered here, the differences between these models is small.

2.8 Chapter Summary

This chapter has evaluated the impact on performance and loads of a rotor capable of radius variation on a representative utility helicopter. The analysis was performed using the comprehensive code, UMARC. The model is based on a nominal UH-60A Black Hawk helicopter for a gross weight of 18,000 lb and trimmed in free level flight. A selection of alternate thrust conditions are also considered. Rotor radius was varied in 2% decrements until the performance degraded or the rotor could not achieve trimmed flight especially due to stall. The conclusions of this chapter are:

1. The performance of the baseline rotor at 18,000 lbs can be improved by reducing the radius in forward flight. The largest reduction in power is achieved at high speeds where power is reduced by about 70 hp (3% power reduction) at 150 knots with a 4% reduction in radius. The power was reduced consistently by about 3% for airspeeds above 100 knots.

2. Induced power increases for the reduced radius rotor due to higher inflow when the disc loading increases. Reducing the radius shifts higher lift onto the fore and aft of the rotor disk in order to maintain trim. High lift on the aft rotor results in increasing induced power that limits performance improvements from larger radius variation.

3. Profile power decreases for the reduced radius rotor by effectively reducing the dynamic pressure at the blade tip and by reducing total blade wet area. The reduction of profile power is largest at high airspeeds so long as the rotor does not begin to stall. At high speeds, reducing the radius delays compressibility effects to higher airspeeds.

4. Larger reductions in radius (greater than 4% for a 18,000 lb gross weight) cannot provide additional performance improvement because of the high blade loading and stall.

5. Thrust cases between 14,000 and 20,000 lbs are considered. The largest increase in performance is available for low thrust conditions at high speeds by reducing the radius. Above 20,000 lb, the change in induced and profile power

with radius variation almost cancel at all speeds and performance is largely insensitive to radius variation. For high thrusts, performance is significantly improved at low speeds (below 60 knots) by increasing the radius. At high speed and high thrust, stall limits the use of radius reduction.

6. Helicopter trim controls, collective (θ_0) and cyclics (θ_{1c}, θ_{1s}), increase in magnitude as rotor radius is reduced. Roll angle, ϕ_s, and longitudinal shaft angle, α_s, are not significantly affected by radius variation below stall.

7. The 4/rev vertical shear hubloads decrease with radius reduction below 110 knots but increase with radius reduction at higher speeds. In-plane vibratory forces are slightly increased at all airspeeds by reducing the radius. The in-plane moments behave similarly to the vertical shear loads. The trends of the 4/rev hubloads are determined by advance ratio and not radius. Above an advance ratio of $\approx$0.27, the 4/rev loads increase above the baseline for the reduced radius rotor.

In conclusion, variable radius rotors have a relatively small potential for performance improvements at high speeds, and then only when the thrust is low. The results do not include any penalty for the weight and complexity of a variable radius system, which would further reduce the modest improvements in performance available. The complexity of the mechanism for variable radius, as currently envisaged, is a strong deterrent to its practical implementation without more significant performance gains.

Chapter 3: Variable RPM for performance

In the last chapter, a variable radius rotor was discussed as an approach to varying tip speed for improved performance for a conventional rotorcraft configuration. The alternative approach to reducing tip speed is to vary rotor speed, which is discussed in this chapter.

The goal of investigating a variable speed rotor is to examine its potential for improved performance and to describe the important aerodynamic phenomena that are involved. It is also important to ensure that the impact of slowing the rotor on trim, hubloads and blade structural loads is understood. After describing the variable speed rotor model, the section investigates the scope for rotor performance improvement possible over a range of thrusts and airspeeds that represent the flight envelope of a utility helicopter. The key aerodynamic phenomena that describe the performance improvement are then described in detail. This is followed by highlighting the implications of the slowed rotor for trim, vibrations and blade loads. Before the final conclusions, system efficiency of a slowed rotor is briefly investigated by accounting for the impact of drive train efficiency on the overall performance.

3.1 Rotor Model

The University of Maryland Advanced Rotor Code (UMARC) [79, 105] was used as a baseline platform for this study to model a representative utility helicopter (based on the UH-60A Black Hawk). The description of the baseline rotor and key elements of UMARC and its modifications are already given in Chapter 2. Unlike the variable radius concept, varying the rotor speed does not require any modifications to the rotor key parameters and sectional properties other than ensuring that the non-dimensionalization is handled correctly.

Table 3.1: Summary of variable rotor speed cases evaluated

Thrust (lb)	14,000	–	20,000 (2,000 lb steps)
Airspeed (knots)	40	–	180 (5 knots steps)
Advance ratio	0.1	–	0.4
Rotor speed (% of baseline)	74	–	100 (2% steps).

This study intends to present the absolute gains and limitations of the variable rotor speed concept with a focus on performance. Airspeeds between 40 and 180 knots and gross weights between 14,000 lb and 20,000 lb (in 5 knot and 2000 lb increments respectively) are considered for a representative flight envelope. The RPM is reduced in 2% steps until the changes in performance are no longer favorable at any airspeed for a targeted thrust (74% RPM was the minimum considered for the 14,000 lb rotor). The flight conditions evaluated are summarized in table 3.1. Maintaining trim (lift and propulsive force) without auxiliary lift devices ensured that the advance ratio did not exceed $\mu = 0.4$ and reverse flow aerodynamics were not significant (but were included in the model).

The evaluation of performance assumes that there is no weight or efficiency penalty associated with achieving variable rotor speed. The performance presented here should be regarded as the performance of the rotor alone. A later section of this chapter briefly considers the effect of variable speed turbine engine efficiency on system performance but this is not a focus of this study.

3.2 Measure of Performance

The following sections refer to total power, induced power and profile power and these are defined in the same way as was introduced in Chapter 2. The parasitic power was found to be nearly independent of rotor speed, varying only as a very weak function of shaft pitch angle (α_s) which does not change significantly with RPM. Because the rotor is trimmed to the correct propulsive force in each case, the parasitic drag and the associated power are a function of airspeed only and nominally constant for varying RPM. The parasitic power has been subtracted from the total power in the discussion for clarity. Finally, the discussion of performance is meaningful in physical dimensions (hp, lb) rather than non-dimensional (C_P, C_T), for a variable speed rotor.

3.3 Slowed Rotor Performance

This section discusses the potential of rotor speed variation to decrease the power required in forward flight.

The rotor power (sum of induced and profile power) for a rotor trimmed to

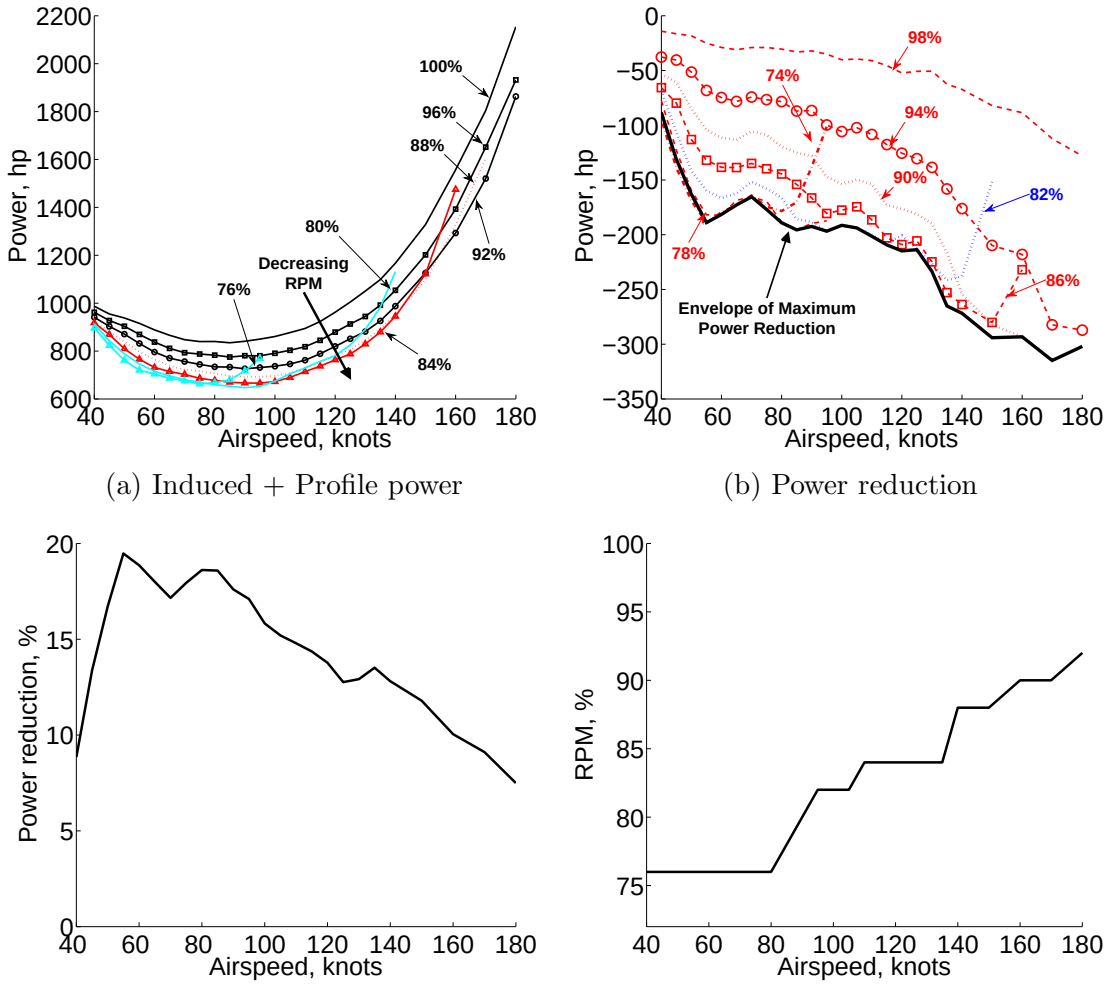

(a) Induced + Profile power

(b) Power reduction

(c) Maximum % Power reduction

(d) RPM schedule for minimum power

Figure 3.1: Variation of rotor power at 14,000 lb with varying RPM.

14,000 lb of thrust is shown in fig. 3.1a for reducing rotor speed. At 74% RPM, there was no additional improvement in performance over 76% RPM and the simulation was not continued further. For the range of airspeeds between 40 and 180 knots, the power is always reduced below the baseline rotor (100% RPM) with RPM reduction. Figure 3.1b shows the rotor power reduction at a selection of rotor speeds. For a small reduction in RPM (e.g., 98% RPM), the reduction in power grows gradually with airspeed from about 10 hp at 40 knots to about 100 hp at 180 knots. At high airspeeds, the rotor power is predominately from profile drag (ignoring parasitic power) and a small reduction in dynamic pressure, from reducing rotor speed, can result in large reductions in power. Decreasing the rotor speed further to 94% RPM returns nearly 300 hp at 180 knots. At 86% RPM, the rate of decreasing power with increasing airspeed is greater still, but the maximum power reduction occurs at a lower airspeed (150 knots) before the trend abruptly turns up, indicating stall. The profile power penalty due to retreating blade stall offsets the reducing profile drag on the advancing rotor resulting in less overall power reduction. For larger decreases in RPM, the peak power reduction occurs at earlier airspeeds and the incremental decrease in power required plateaus. By 74% RPM, there is no additional performance benefit compared to 76% RPM. At low airspeeds, the rotor power is dominated by induced power which is less affected by rotor speed variations. The relatively small contribution to total power made by profile power at low airspeeds means that larger variations in RPM result in smaller power reduction.

Figure 3.1c shows the maximum possible power reduction as a percentage of the total power (including parasitic power) at different forward speeds. The largest

percentage improvement in performance is available at lower speeds only because of the small contribution made by parasitic drag to the total power at lower airspeeds. The apparent lack of smoothness in the power reduction is in part due to the finite steps in RPM and airspeed but also from the rotor wake interacting with the rotor plane at consistent airspeeds (60-100 knots). Figure 3.1d shows the RPM schedule associated with the maximum power reduction. The RPM required for minimum power is continuously increasing with airspeed and the total range of RPM is between 76% and 92%.

The reduction in rotor power from decreasing rotor speed is shown in fig. 3.2 for rotor thrusts of 16,000, 18,000 and 20,000 lb. The reduction in power that can be achieved with RPM change reduces with higher thrust (or higher disk loading). Comparing the 98% RPM case for each thrust condition shows a similar behavior to the 14,000 lb result; the power reduction increases continuously with airspeed. The maximum reduction in power is decreasing with increasing thrust (100 hp – 50 hp – 40 hp for 16,000 lb, 18,000 lb and 20,000 lb respectively) on account of increasing blade loading. At higher blade loading, the profile drag penalty from increasing the mean rotor angle of attack (as a result of slowing the rotor) increases which in turn reduces the power reduction. Larger reductions in RPM progress in a similar way to the 14,000 lb case, but stall limits performance at earlier RPMs as the thrust increases. In this way, the benefits of RPM reduction decrease more rapidly at high speeds than at low speeds, for increasing thrust. At 60 knots, the power reduction decreases from 150 hp at 16,000 lb to 100 hp at 20,000 lb, while at 150 knots the power reduces from 230 hp to 70 hp respectively.

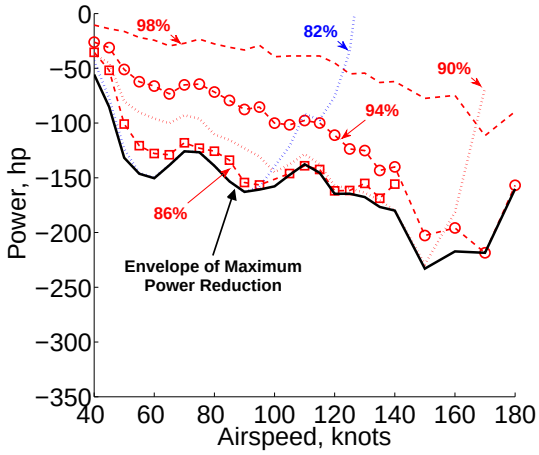

(a) 16,000 lb

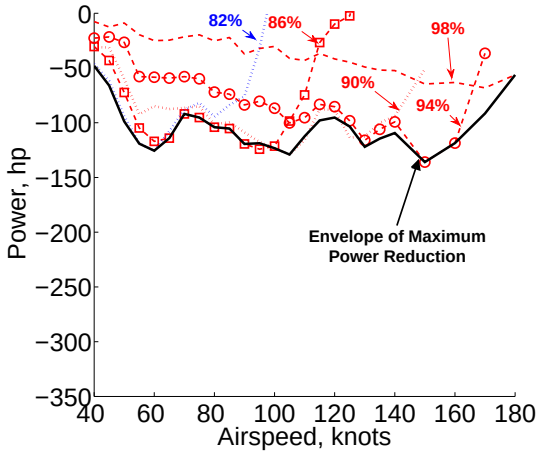

(b) 18,000 lb

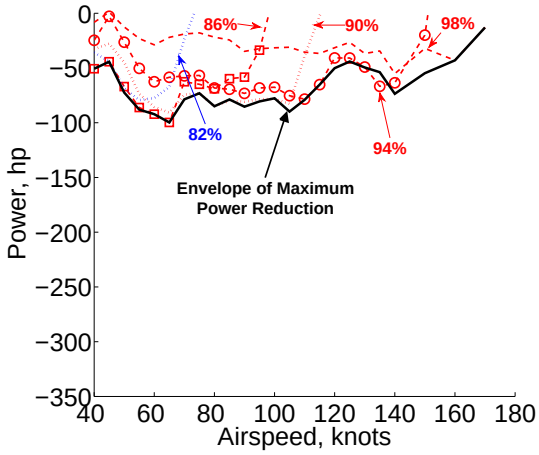

(c) 20,000 lb

Figure 3.2: Reduction of rotor power at 16,000 lb, 18,000 lb and 20,000 lb with varying RPM.

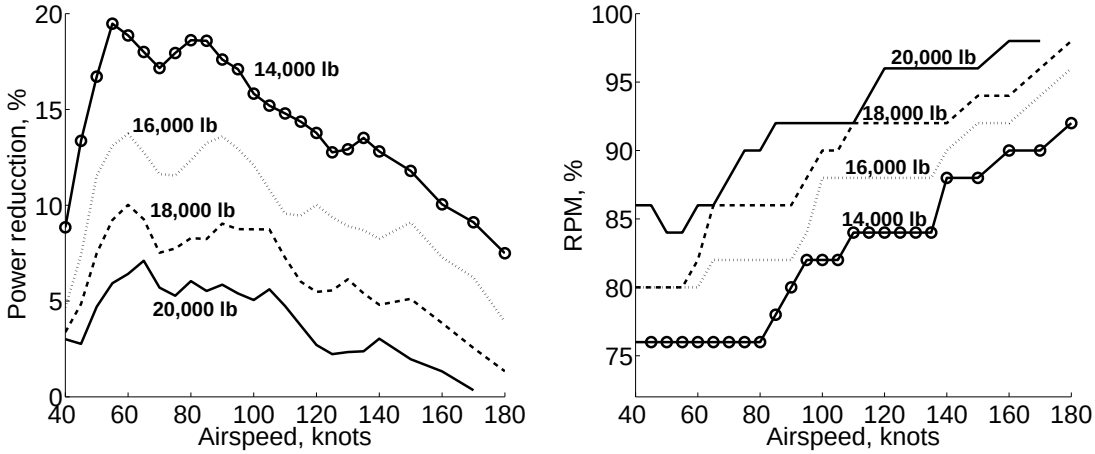

(a) Maximum % reduction in total power (b) RPM schedule for minimum power

Figure 3.3: Maximum % power reduction and associated RPM schedule (14,000 lb - 20,000 lb).

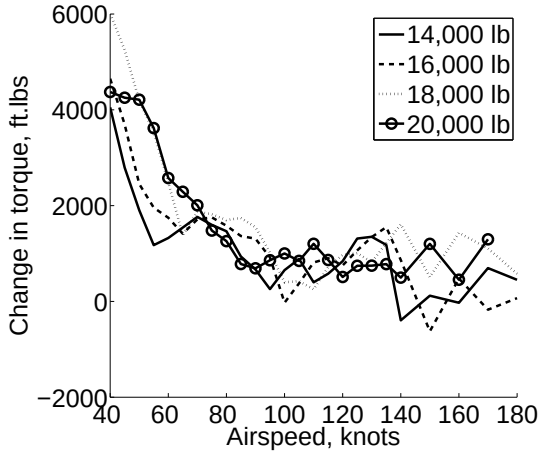

Figure 3.4: Change in torque for the minimum power RPM schedule (14,000 lb - 20,000 lb).

The maximum reduction in power as a percentage of the total power, and the corresponding RPM schedule is shown in fig. 3.3b as a function of airspeed for each thrust. The 14,000 lb rotor makes use of the largest RPM reduction, down to 76% RPM at low speeds that corresponds to a peak of 20% power reduction. Increasing airspeed is accompanied by increasing RPM to 92% at 180 knots. The higher thrust cases have the same trend requiring large RPM reductions near 40 knots and more modest reductions near 180 knots. The peak percentage power reduction decreases with increasing thrust to 14%, 10% and 7% for 16,000 lb, 18,000 lb and 20,000 lb respectively. The range between the maximum and the minimum rotor speeds is consistently about 16% RPM for each thrust, while the mean RPM increases with thrust.

Comparing fig. 3.3 for reducing RPM to fig. 2.9 for reducing radius shows that there is a much greater improvement in performance available by reducing rotor speed, and that the reductions in RPM are larger than those for radius. The difference arises from the effect on blade loading. Reducing RPM increases blade loading with $\frac{1}{\Omega_R^2}$, while reducing radius increases blade loading with $\frac{1}{\Omega_R^3}$. From this observation, reducing radius reduces the stall margin faster than reducing RPM does so that smaller radius variations can be achieved before stall limits further improvements in performance.

Accompanying a change in RPM is a change in rotor torque. Figure 3.4 shows that the torque increases for the minimum power RPM schedule, which is consistent for all thrust cases. The largest increase in torque is at low speeds where the reduction in RPM is largest. Above 100 knots, the torque difference is less than

2000 ft-lb over the baseline. At high speeds and thrusts, the transmission may be torque limited before being power limited, but this should not be an issue when targeting performance at low speed and cruise.

3.4 Analysis of Slowed Rotor Aerodynamics

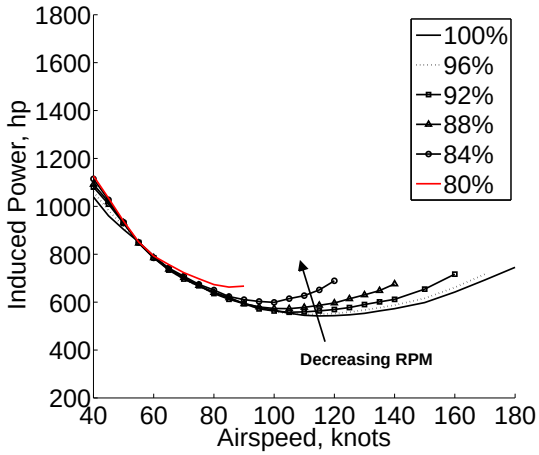

Figure 3.5: Induced power vs. airspeed at 18,000 lb with reduced RPM

Figure 3.5 shows the induced power contribution to the total power for the 18,000 lb thrust rotor with reducing RPM. The induced power, a function of rotor thrust, is unaffected by RPM variations at low airspeeds. At increased airspeeds, the induced power becomes larger for a slowed rotor than that for the baseline due to increasing non-uniformity in the inflow at increasing blade loading - a well-understood departure from Glauert's uniform inflow. The 84% and 80% RPM cases show larger increases in induced power at low speeds as a result of stall and increased inflow non-uniformity.

The source of the improved performance for a slowed rotor is the reduction of profile power, which is shown for 14,000 lb and 18,000 lb thrusts in fig. 3.6.

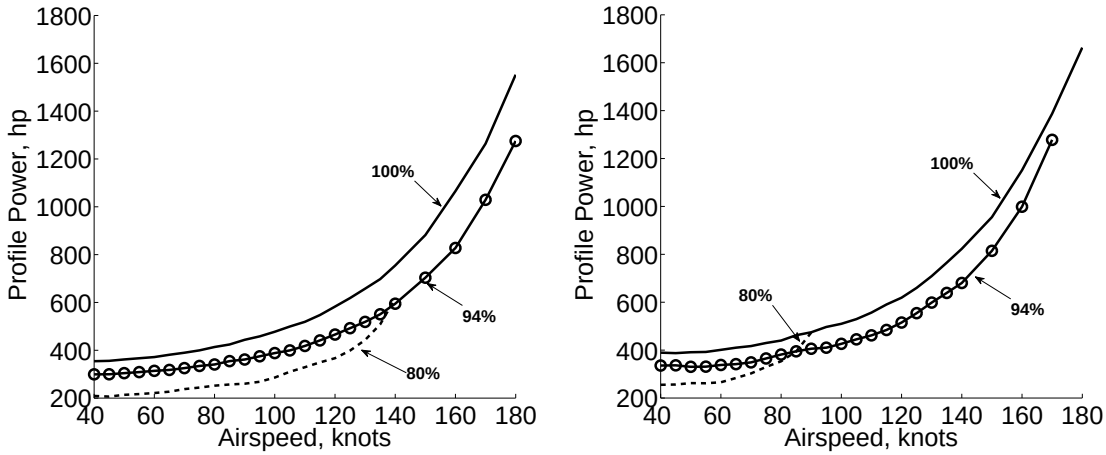

(a) 14,000 lb (b) 18,000 lb

Figure 3.6: Profile power vs. airspeed for reduced RPM

Decreasing the RPM reduces dynamic pressure which in turn reduces profile drag. Decreasing rotor speed comes at the expense of increased blade loading, or increasing angle of attack, which results in increasing airfoil drag coefficient. For 14,000 lb of thrust, reducing the rotor speed to 80% RPM decreases the profile power significantly between 40 and 120 knots before it increases dramatically at further higher airspeeds. For 18,000 lb, reducing the rotor speed to 80% RPM still produces larger profile power reduction at 40 knots but that immediately tapers off with increasing airspeed. This indicates that the benefit of reducing dynamic pressure is almost completely offset by increasing sectional drag coefficient. A rotor with a higher baseline blade loading (higher gross weight) has less margin for RPM reduction before the balance of decreasing dynamic pressure and increasing drag coefficient occurs. A result reflected in total power reduction available at low speeds (fig. 3.2).

Reducing the rotor speed to 94% RPM for the 14,000 lb case shows the reduction in profile power increases with airspeed. At high airspeeds, reducing the

dynamic pressure also delays compressibility on the advancing rotor (a large contributor to total power and vibrations). The same result is seen for the 18,000 lb rotor for airspeeds below 140 knots and thereafter the profile power reduction narrows relative to the baseline. Aerodynamic asymmetry at higher airspeeds promotes earlier stall and a large profile drag penalty which degrades performance. Stall impacts the higher thrust (higher blade loading) rotor earlier than the low thrust cases.

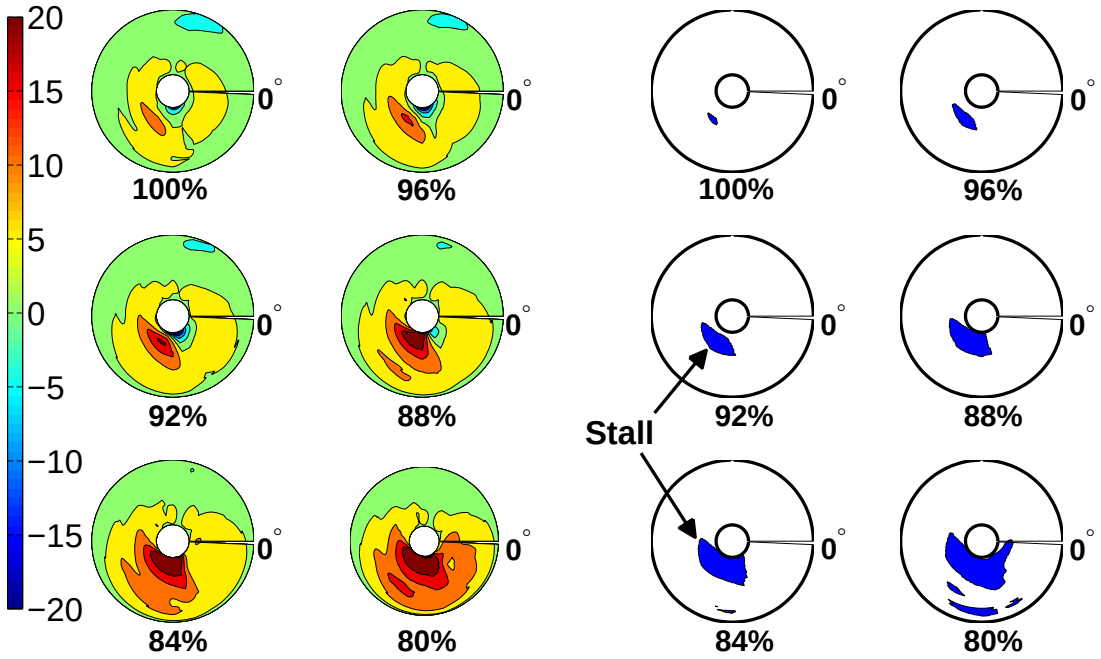

(a) Angle of attack distribution (b) Stall distribution

Figure 3.7: Angle of attack and stall locus for 18,000 lb thrust case at 80 knots with RPM variation.

Figure 3.7a shows the angle of attack distribution on the rotor disc for the reference 18,000 lb rotor thrust at a representative cruise speed of 80 knots while decreasing rotor speed from 100% to 80% in 4% decrements. As the RPM is reduced, the global angle of attack increases, with the most significant changes on the

retreating side of the rotor disk. At this speed, the retreating side incidence angles are not yet high enough to result in a significant stall region. Slowing the rotor reduces the dynamic pressure and the rotor requires larger pitch inputs to produce the thrust and roll moments for trim, disproportionately impacting the retreating side which can lead to stall. For the purpose of this analysis, static stall is defined for each available Mach number as the angle of attack where there is a break in the lift curve slope, determined from the airfoil tables. The stall regions of the rotor gradually expand as the rotor speed decreases and this is shown with the stall contours in fig. 3.7b. The impact of stall on performance is initially small because of the low dynamic pressure on retreating side. However, at 80% RPM, the stall is progressed sufficiently to include some of the outboard part of the rotor, and profile power increases dramatically.

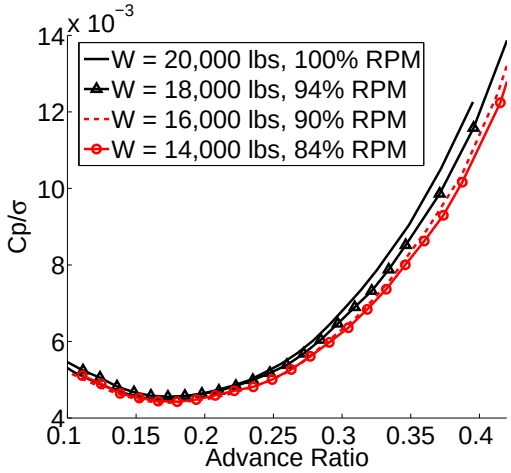

Figure 3.8: Non-dimensional total power (C_p/σ) vs. advance ratio at $C_T/\sigma \approx 0.084$.

It is instructive to consider the performance results in non-dimensional form to isolate higher order effects of slowing the rotor other than varying dynamic pressure (compressibility, stall, etc. any departure from linear aerodynamics). Figure 3.8

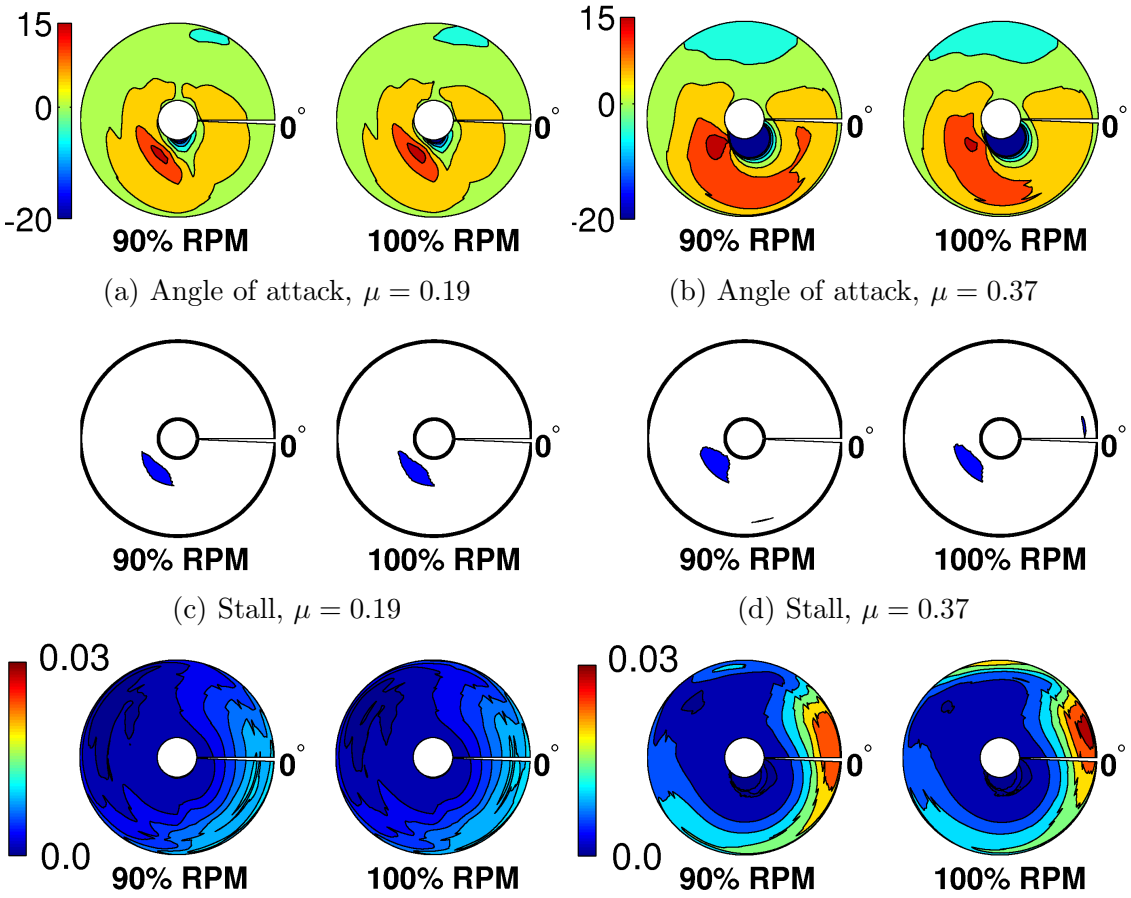

(a) Angle of attack, $\mu = 0.19$

(b) Angle of attack, $\mu = 0.37$

(c) Stall, $\mu = 0.19$

(d) Stall, $\mu = 0.37$

(e) Torque coefficient, $\mu = 0.19$

(f) Torque coefficient, $\mu = 0.37$

Figure 3.9: Low and high advance ratio aerodynamic environment, effect of RPM ($C_T/\sigma \approx 0.084$).

shows the non-dimensional power for four thrust levels and RPM combinations that result in the same non-dimensional thrust ($C_T/\sigma \approx 0.084$). At low advance ratio ($\mu < 0.2$) the power coefficient is nominally the same for each case which is expected for nominally linear aerodynamics. Increasing advance ratio shows that the power coefficient increases more for the higher thrust (higher rotor speed) case. Figure 3.9 considers the aerodynamic environment (angle of attack, stall and power distribution) at two advance ratios for the 16,000 lb rotor at 90% RPM and the 20,000 lb rotor at 100% RPM (constant C_T/σ). At $\mu = 0.19$, corresponding to indiscernible power coefficient between cases in fig. 3.8, the angle of attack distribution and stall maps are very similar and give indiscernible torque distributions. This is despite operating at different dimensional thrusts and airspeeds. The reduction in power at low airspeeds is primarily due to lowering dynamic pressure. At $\mu = 0.37$, where there is a spread of power coefficient, the angle of attack and stall plots remain similar but the advancing tip of the 100% RPM rotor shows increasing profile power due to compressibility. At high airspeeds, reduced compressibility effects and reduced dynamic pressure contribute to reducing the profile power of the slowed rotor.

The improved performance can also be viewed in terms of improving the rotor efficiency at the blade element level. The most efficient operating point for the airfoil section is at its maximum lift-to-drag angle of attack ($^{c_l}/_{c_d}$). Figure 3.10 shows the $^{c_l}/_{c_d}$ at the 75% span section for a 16,000 lb thrust rotor at 80 knots for 100%, 96% and 88% RPM. They are compared to the maximum lift-to-drag ratio of the airfoil (dashed lines - as a function of local Mach number). The reduced RPM rotors operate at higher efficiencies, particularly on the retreating side. The

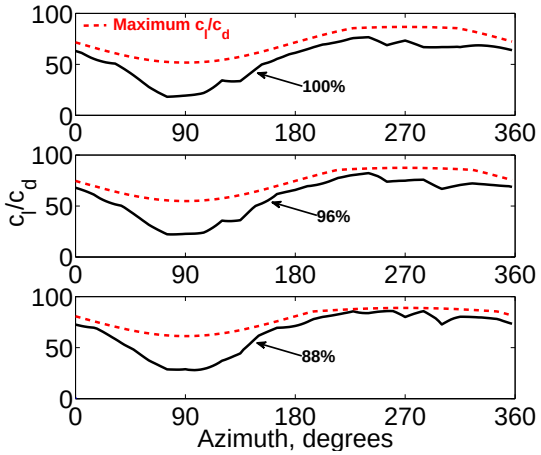

Figure 3.10: Sectional lift to drag ratio at 75% span and 80 knots (W = 16,000 lb).

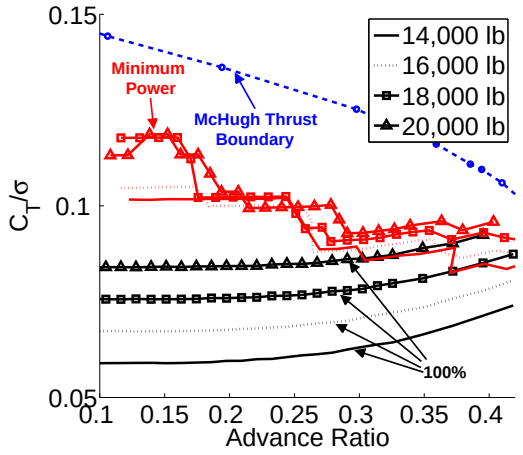

Figure 3.11: Comparison of the baseline and power-optimized non-dimensional thrust for each rotor thrust.

88% case is approaching the maximum efficiency of the airfoil section. Although not shown, further reductions in RPM start to show degraded efficiency as the rotor stalls. This improvement in efficiency is less apparent for increased rotor thrust, where the airfoil sections operate closer to their peak efficiencies and there is less margin for improvement via RPM reduction. An airfoil with a higher maximum $^{c_l}/_{c_d}$ would allow for larger reductions in rotor speed before stalling and a larger potential for power reduction.

Figure 3.11 shows the non-dimensional thrust vs. advance ratio at 100% RPM for the four thrust cases (14,000, 16,000, 18,000 and 20,000 lb). Note that the rotor thrust, in the shaft axis, is not constant with advance ratio because the rotor must produce increasing propulsive force due to parasitic drag. Also shown are the C_T/σ values for each thrust and airspeed (advance ratio) that resulted in the minimum power. The minimum power condition merges for the four thrusts onto a single trend line (within the resolution of the steps in RPM and airspeed). The trend line decreases as advance ratio increases. At an advance ratio of 0.4, the minimum power trend line approaches the 20,000 lb thrust condition and there is no further margin of performance improvement through RPM reduction at this thrust. Also shown is the McHugh thrust boundary [107] which is an indication of the useful thrust margin of a rotor. The minimization of power reduces the thrust margin (before stall), but does not negate it for advance ratios below 0.4. Beyond $\mu = 0.4$, it appears that there may not be thrust margin at the minimum power thrust level. This implies that unless the thrust is reduced considerably (14,000 lb is already less that the empty weight of the UH-60A helicopter), $\mu = 0.4$ is close to the maximum

advance ratio for which RPM variation is effective to improve performance for this configuration (single main rotor).

3.5 Slowed Rotor Trim

The trim angles for the 18,000 lb helicopter with decreasing RPM are shown in fig. 3.12. The amplitude of the collective (fig. 3.12a) and cyclics (figs. 3.12b and 3.12c) increase for the slowed rotor compared to the baseline, but they do not exceed the baseline limits before stall limits the maximum speed of the slowed rotor. This implies that the maximum stroke of the swashplate actuators remains within the bounds of the baseline rotor. The trend of the collective (θ_0) and lateral cyclic (θ_{1C}) remain similar for the slowed rotor whereas the slope of the longitudinal cyclic (θ_{1S}) increases as the rotor slows. From a control perspective, the slowed rotor will require a larger cyclic input to effect a unit change in airspeed compared to the baseline. A variable RPM rotor controller would have to account for the loss of control authority to alleviate pilot workload. The longitudinal shaft tilt (α_s) and lateral shaft tilt (ϕ_s), shown in figs. 3.12d and 3.12e, are less affected with variation of RPM.

3.6 Vibratory Hubloads

Before rotor speed variation can be implemented to improve performance, the impact on structural and vibratory loads must be understood. The starting point for this discussion is the fanplot in fig. 3.13. Care must be taken when designing

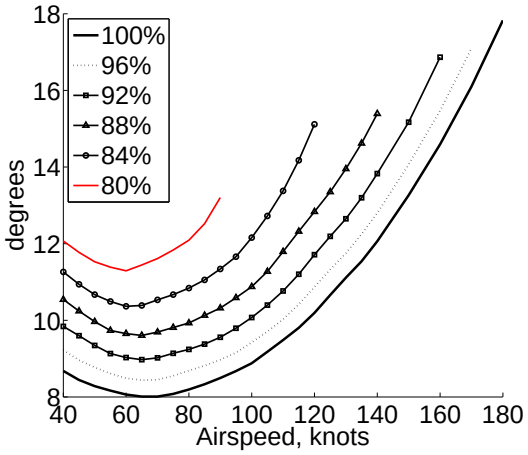

(a) Collective, θ_{75}

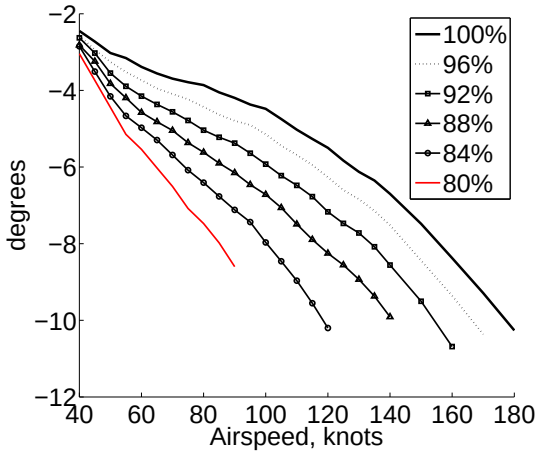

(b) Longitudinal cyclic, θ_{1S}

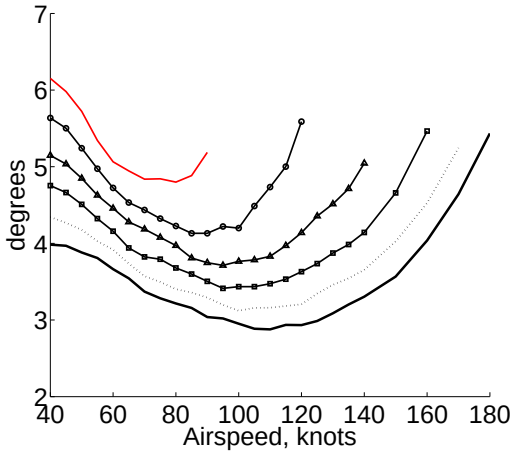

(c) Lateral cyclic, θ_{1C}

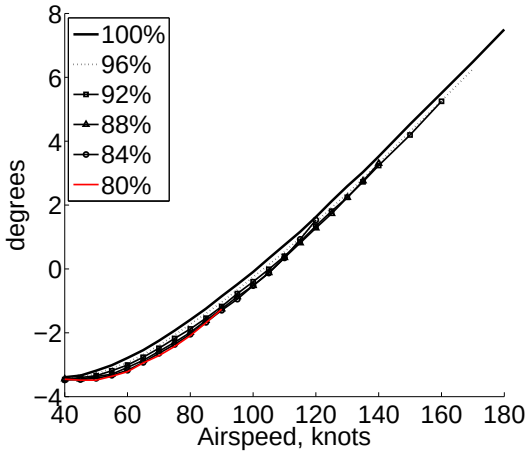

(d) Longitudinal shaft tilt, α_s

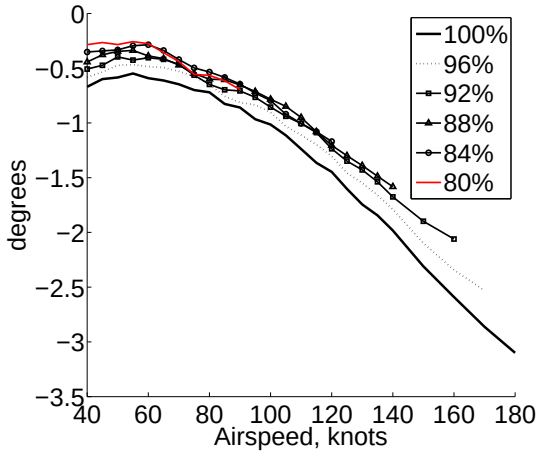

(e) Lateral shaft tilt, ϕ_s

Figure 3.12: Trim angles vs. airspeed at 18,000 lb with reduced RPM

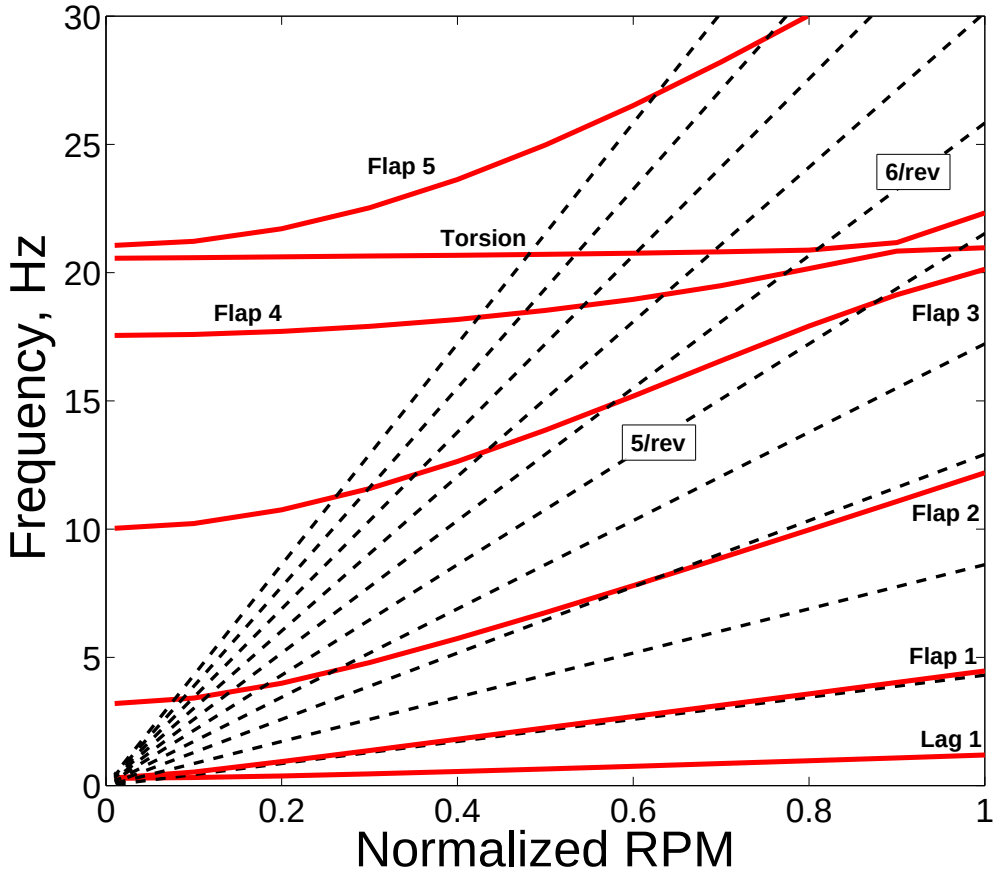

Figure 3.13: Fanplot for the UH-60A Blackhawk.

rotors for variable RPM to avoid resonance with rotor harmonics. The 4^{th} blade mode (3^{rd} flap) crosses the 5/rev rotor frequency at around 87.5% RPM, the 5^{th} mode crosses 5/rev near 97% RPM and 6/rev at 77% RPM and finally the 6^{th} mode crosses 6/rev at 81% RPM.

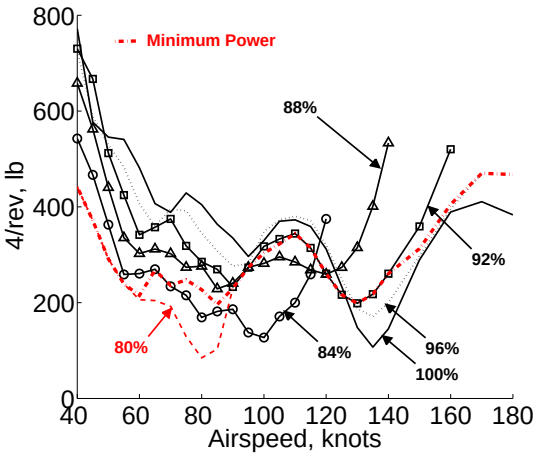

(a) Vertical shear force, F_z

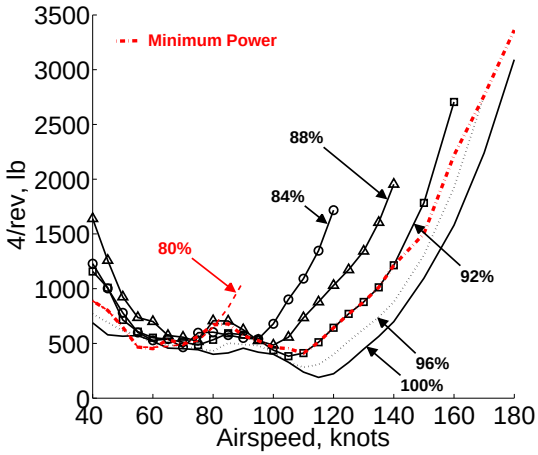

(b) In-plane shear force, $\sqrt{F_x^2 + F_y^2}$

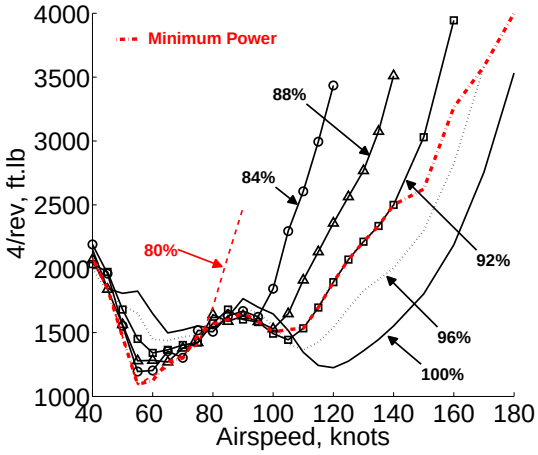

(c) In-plane moments, $\sqrt{M_x^2 + M_y^2}$

Figure 3.14: 4/rev hubloads vs. airspeed at 18,000 lb

The primary vibratory loads generated by the four bladed rotor are the 4/rev fixed frame loads. These are the vertical shear load (F_z), the in-plane shear load ($\sqrt{F_x^2 + F_y^2}$), and the in-plane moment ($\sqrt{M_x^2 + M_y^2}$). Figure 3.14 shows the three

resolved vibratory hubloads (4/rev magnitudes) with decreasing RPM for the 18,000 lb rotor. The 4/rev vertical shear loads are significantly and consistently reduced as the RPM is decreased for airspeeds below 115 knots. Above 115 knots, the slowed rotor vertical shear loads increase to become somewhat larger than the baseline. The in-plane shear forces are always larger than the baseline with slowing the rotor. The significant increase in the in-plane vibratory forces that occurs above 120 knots for the baseline case, begins at progressively earlier airspeeds as the rotor speed is reduced. This means that at high speeds, the in-plane loads of the slowed rotor can be much higher than the baseline rotor. The in-plane moments have a similar behavior to the in-plane forces at high airspeeds, although the slowed rotor loads are lower than the baseline below 80 knots. Figure 3.14 also highlights the vibratory loads that would result at the RPM schedule for minimum power. The vertical shear forces would be reduced at low speeds and cruise but marginally larger than the baseline above 130 knots. Both the in-plane shear forces and moments increase significantly above 100 knots. This may result in unacceptable vibration levels unless the increased vibrations can be mechanically isolated or actively controlled.

Figure 3.15 shows the percentage change from the baseline of each of the three 4/rev hubloads, as contour plots. This is of interest for minimizing hub vibrations, independent of power. The vertical shear force and the in-plane moment are each well behaved and have a single minima at each airspeed and the minimum vibrations rotor speed schedule nearly follows the schedule for minimum power for low airspeeds. The in-plane shear force has two minimums around 60 knots; however, the percentage decrease in hubloads that can be achieved is small ($\approx$0.8%) and

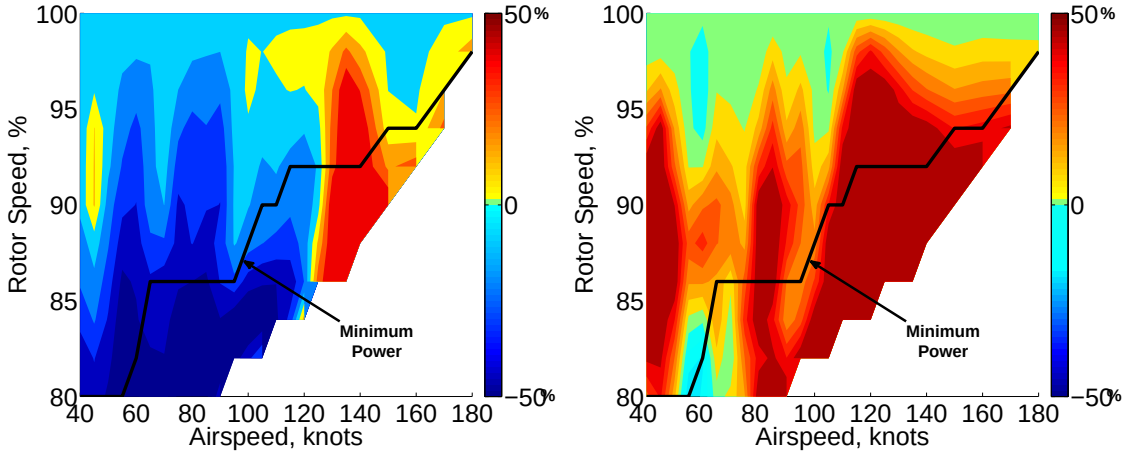

(a) Vertical shear force, F_z

(b) In-plane shear force, $\sqrt{F_x^2 + F_y^2}$

(c) In-plane moments, $\sqrt{M_x^2 + M_y^2}$

Figure 3.15: Contours of percent change in 4/rev hubloads as a function of rotor speed and airspeed at 18,000 lb (Max limited to ±50%)

can be ignored. At high speeds, slowing the rotor is consistently detrimental for vibratory hubloads.

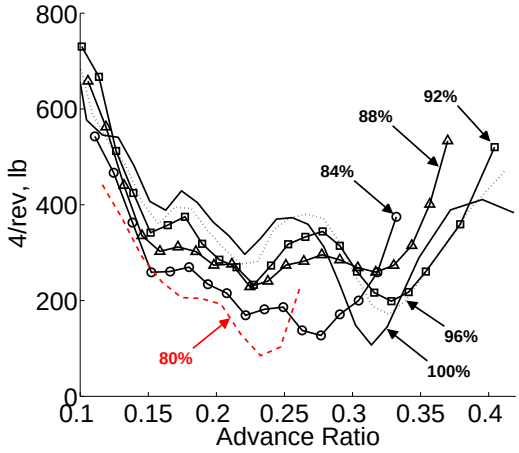

(a) Vertical shear force, F_z

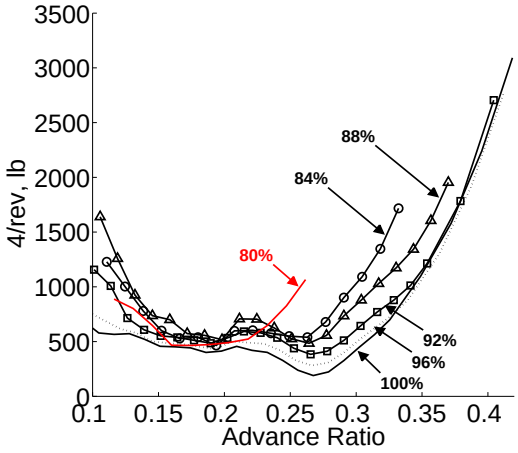

(b) In-plane shear force, $\sqrt{F_x^2 + F_y^2}$

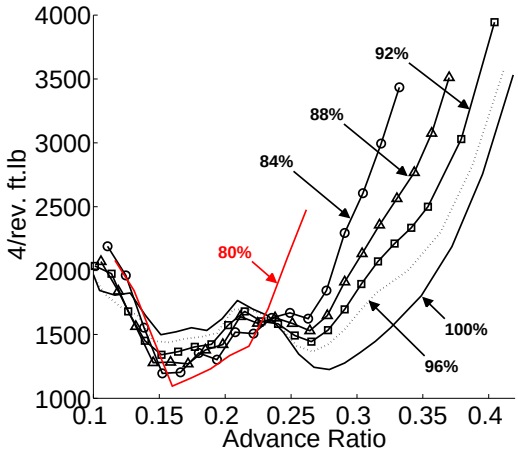

(c) In-plane moment, $\sqrt{M_x^2 + M_y^2}$

Figure 3.16: 4/rev vertical and in-plane shear forces and moments vs. advance ratio at 18,000 lb.

The 4/rev vertical and in-plane shear force and in-plane moment magnitudes are plotted as a function of advance ratio in fig. 3.16. The vertical shear forces have a consistent trend that follows the baseline for rotor speeds above about 88% RPM. For the 80% and 84% RPM rotor speeds, the trend does not remain consistent for

higher advance ratios and the airloads over those airspeeds suggest that lift stall plays a role. The in-plane shear forces and in-plane moments have a consistent trend with advance ratio and the increase in the vibratory loads takes place near $\mu = 0.27$ for all rotor speeds except 80% RPM. The consistency of this behavior with advance ratio, rather than airspeed, suggests that aerodynamic asymmetry plays a larger role than compressibility (which would be primarily a function of advancing tip speed). For 80% RPM, the loads are increasing from $\mu = 0.22$ due to extensive stall and does not follow the trend. The blade bending loads offer some insight into these trends at high advance ratio.

3.7 Blade Loads

Understanding the magnitude of the blade loads is critical for rotor blade design and for minimizing vibrations. The 4/rev vibratory loads showed that the in-plane forces and moments of the slowed rotor remained comparable to the baseline rotor until $\mu = 0.27$ and thereafter the slowed rotor loads increased significantly about the 100% RPM rotor. The following blade loads are compared at a) the combination of airspeed and rotor speed that match an advance ratio of $\mu = 0.27$; and at b) the highest airspeed for each RPM that a trim solution could be found (termed "Near stall").

Figure 3.17 compares the half peak-to-peak flap bending moments along the span for rotor speeds between 100% and 84% RPM at $\mu = 0.27$ and near stall. At $\mu = 0.27$, the half peak-to-peak flap bending is increasing with reducing rotor

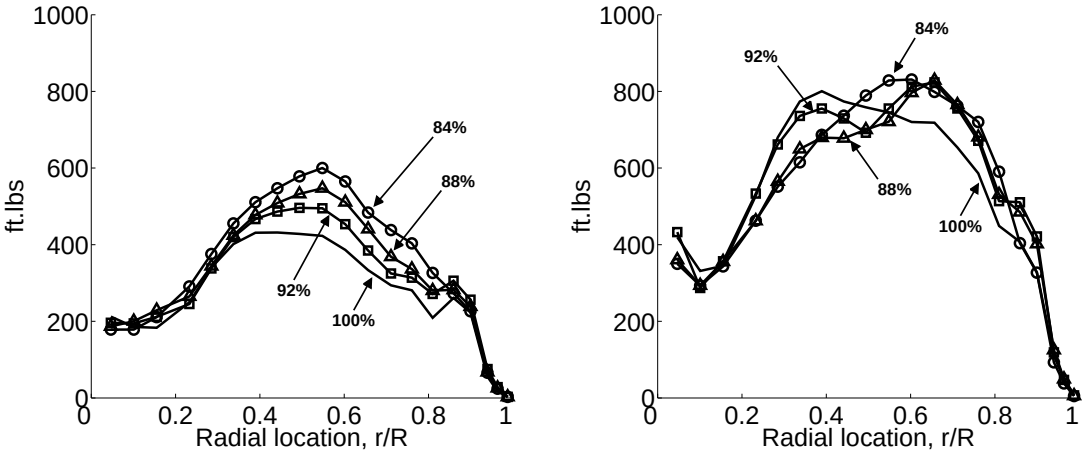

(a) $\mu \approx 0.27$ (b) Near stall

Figure 3.17: Half peak-to-peak flap bending vs. spanwise location at 18,000 lb.

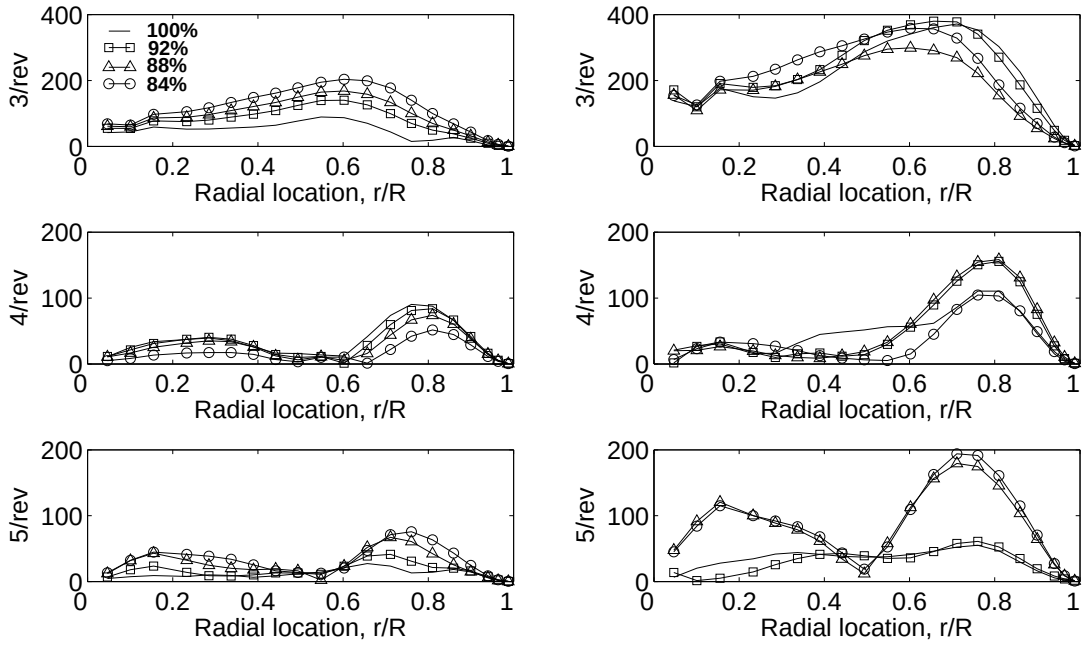

(a) $\mu \approx 0.27$ (b) Near stall

Figure 3.18: 3, 4 and 5/rev harmonics of flap bending vs. spanwise location at 18,000 lb.

speed. At airspeeds near stall for each rotor speed, the half peak-to-peak loads are similar for each case although the peak loading shifts outboard from near r/R = 0.4 to outboard of r/R = 0.6 for larger reductions in rotor speed. From this result, the maximum flap bending loads are not increased over the baseline by slowing the rotor.

The 3, 4 and 5/rev harmonics of the flap bending can help explain the 4/rev vibratory loads and are shown in fig. 3.18. Only 4/rev loads contribute to the vertical shear vibrations while the 3 and 5/rev harmonics contribute to the in-plane moment vibrations. At $\mu = 0.27$, the 4/rev vertical shear loads are decreasing with reduced RPM and this is consistent with the 4/rev blade loads. At the high speed case near stall, the magnitude of the 4/rev vertical shear loads are quite similar between the 84% RPM and the 100% RPM, as well as between the 88% RPM and 92% RPM which agrees with the 4/rev blade bending results. The fanplot shows that there are no blade frequencies near 4/rev rotor frequency which suggests that the source of the reduced vibrations at low speeds must come from reduced 4/rev aerodynamic forcing. Slowing the rotor speed increases the 3/rev flap bending loads above the baseline at $\mu = 0.27$. The fanplot shows that the 2^{nd} flap mode approaches 3/rev as the rotor speed is reduced, which may have a contribution to the blade loads. However, near their respective stall speeds, the 3/rev blade loads are similar for each rotor speed, which suggests that 3/rev aerodynamic forcing at stall is the dominant forcing again. The 5/rev blade loads increase significantly for the 88% and 84% RPM cases at high speeds due to the interaction of the 3^{rd} flap and the 5/rev rotor frequency (crossing near 87% RPM). However, the contribution of the 5/rev blade loads to the in-plane

moments appears to be small compared to the 3/rev bending loads.

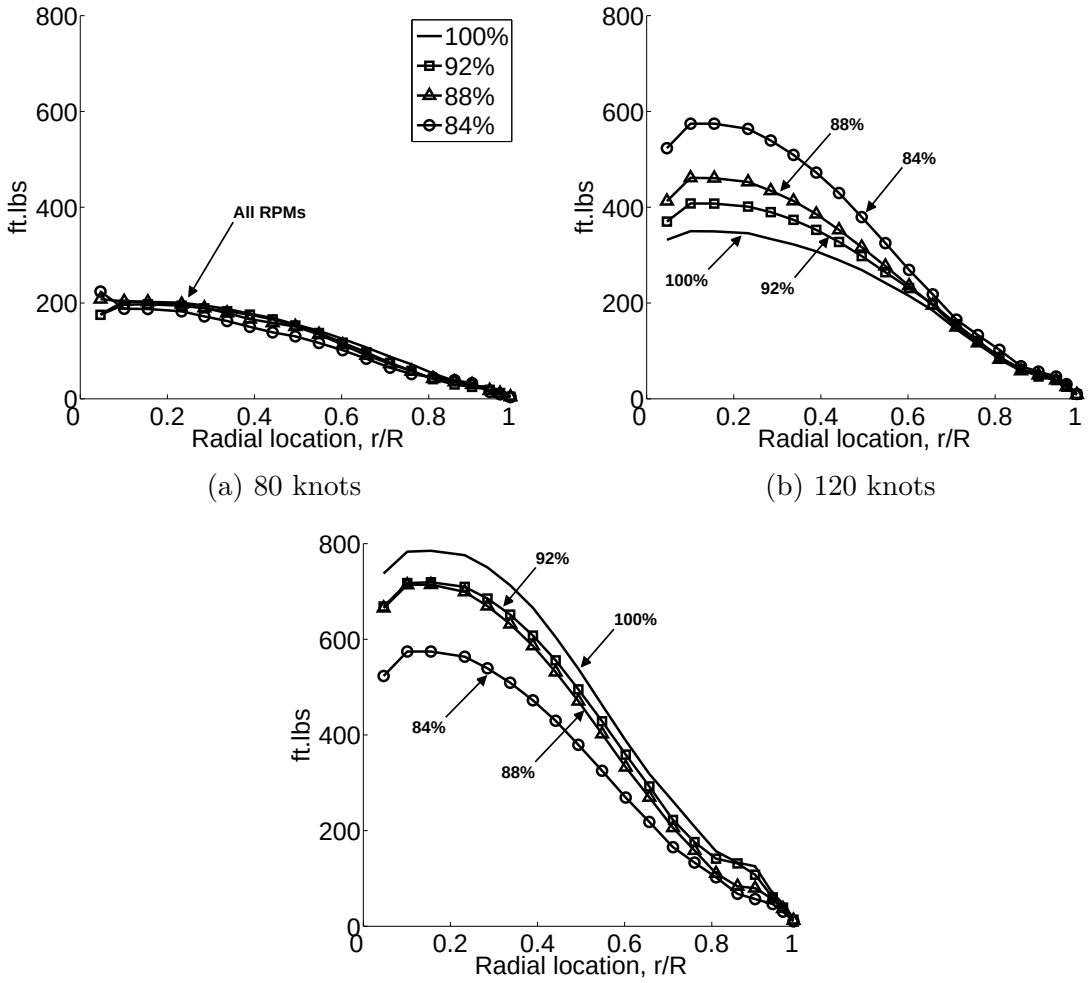

(a) 80 knots

(b) 120 knots

(c) Near stall

Figure 3.19: Half peak-to-peak torsion moment vs. spanwise location at 18,000 lb.

The half peak-to-peak torsion moments are shown in fig. 3.19. The torsion moment at the blade root correspond to the pitch link loads. The three cases considered are at a) 80 knots, before any of the cases approach stall, b) 120 knots, which corresponds to deep stall for the 84% RPM case and c) the highest airspeeds before stall for each RPM. At 80 knots, the four rotor speed cases considered have very similar torsion moments. At this airspeed, the four cases are not yet stalled and

compressibility effects are negligible. At 120 knots, the torsion moments increase for the slowed rotor cases and most significantly for the 84% RPM case which is because of stall driving up torsional loads. Finally, at the highest speeds before stall for each RPM, the torsional moments are highest for the full speed rotor at an airspeed of 180 knots. Compressibility effects at high speeds acts in addition to stall loads to increase the total blade torsion moments for the 100% RPM case. The slowed rotor cases stall at lower airspeeds (for a gross weight of 18,000 lb) and thus have reduced torsion loads at the limit of the flight envelope.

3.8 Turbine Efficiency

Chapter 1 introduced the importance of turbine efficiency in evaluating the total system efficiency of a variable rotor speed concept. Although this is not a focus of this dissertation, it will be briefly considered here.

The generic variation of SFC with both power output and turbine speed is shown again in fig. 3.20. For a first order analysis, the figure is digitized and interpolated to determine the fuel flow rates for combinations of turbine load (power) and shaft speed. To ensure that this approach is applicable to the UH-60A turbine engine (T700-GE-701C), it is compared with a result from Ballinn [108] who used the G.E. STATUS-81 model, made by General Electric specifically to model their engines. The variation of SFC with shaft power for the two approaches show good agreement at 100% turbine speed as shown in fig. 3.21. Ballin did not consider off-design turbine speed cases which limits further comparison; however, this simple

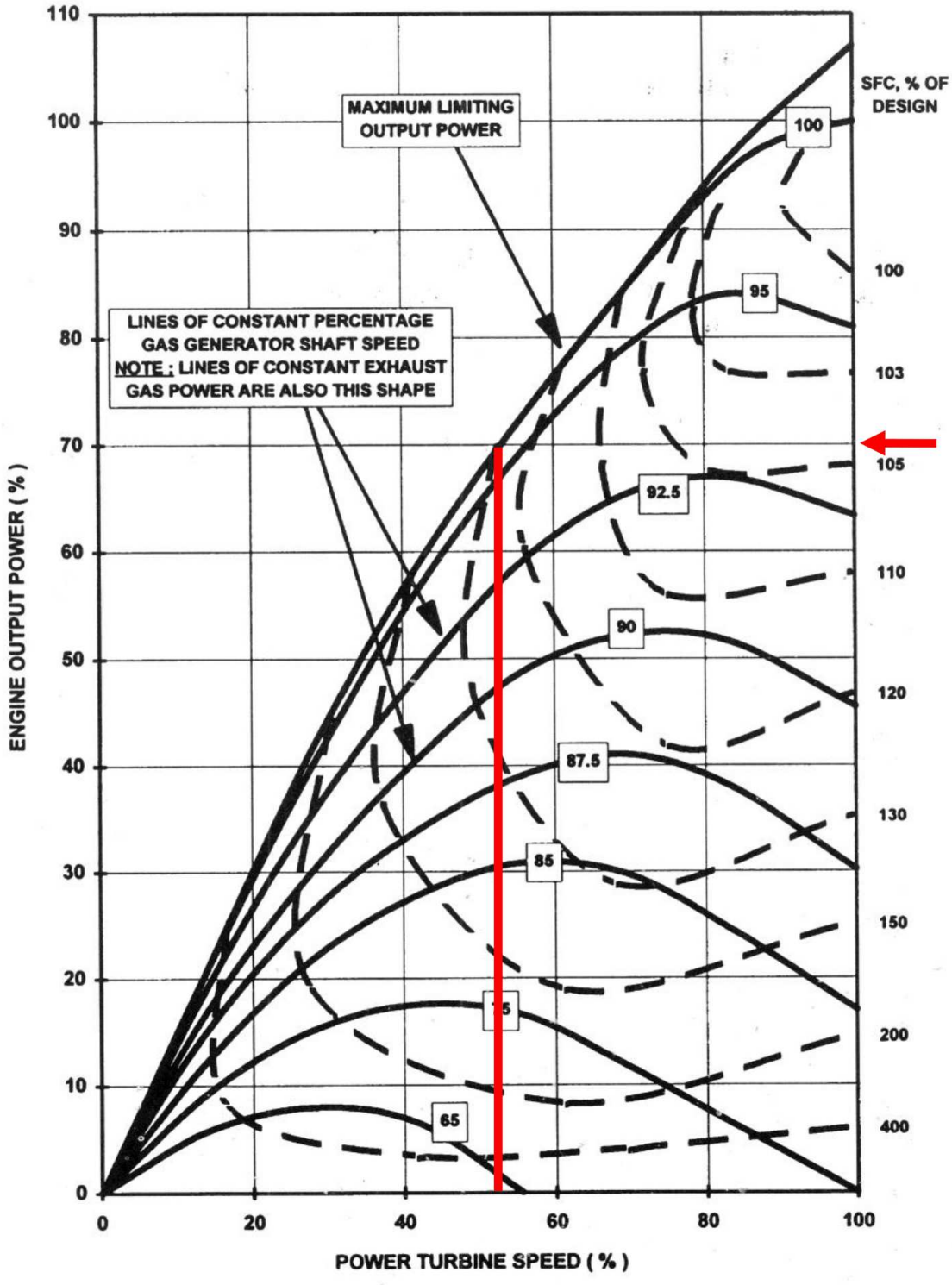

Figure 3.20: Typical variation of SFC with turboshaft speed [21].

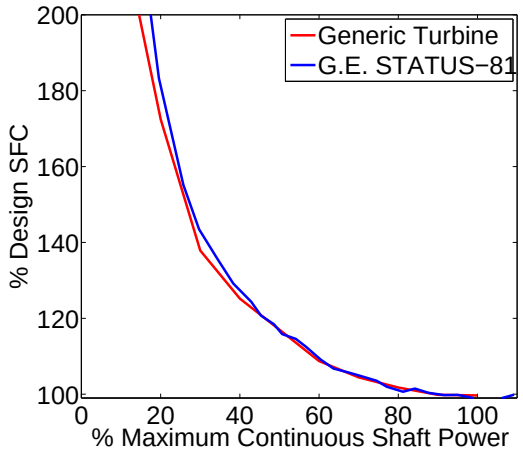

Figure 3.21: Variation of SFC with shaft power. Comparing generic turbine model [21] with T700-GE-701C model [108].

result provides confidence to continue with this method of analysis.

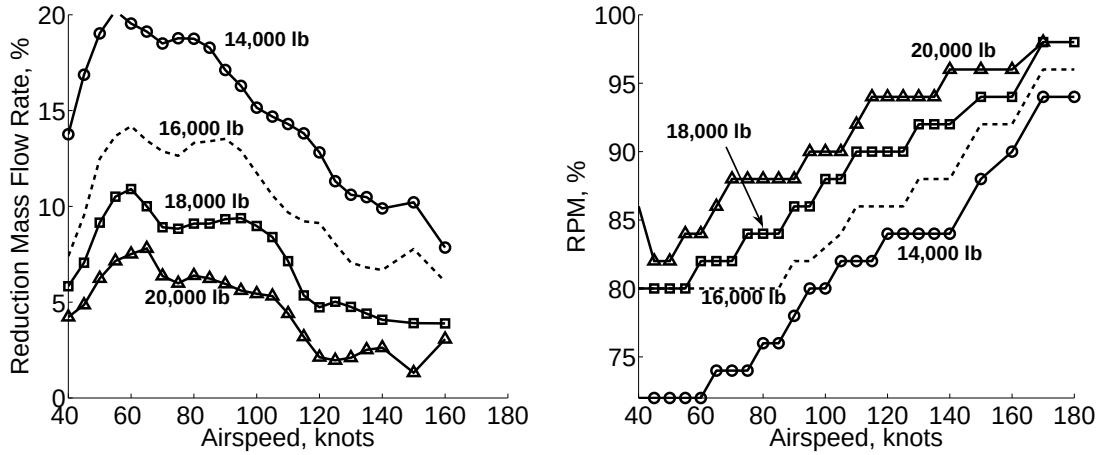

(a) Maximum % reduction in fuel flow rate (b) RPM schedule for minimum fuel flow rate

Figure 3.22: Maximum % fuel flow rate reduction and associated RPM schedule (14,000 lb - 20,000 lb)

The approach is to reevaluate the performance data, with the inclusion of a fuel flow correction based on fig. 3.20, to find the minimum fuel flow rate. Figure 3.22 shows the maximum percentage improvement in fuel flow rate and the associated rotor speed for each thrust condition. The result is very similar to the earlier result

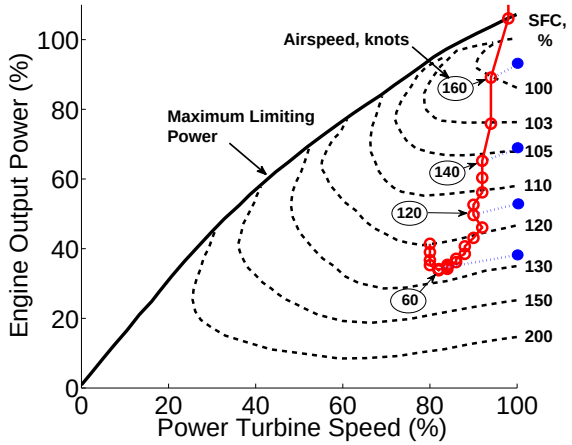

Figure 3.23: SFC for minimum fuel flow rate (red) compared to baseline rotor (blue) (18,000 lb)

that considered the rotor power in isolation. The fuel flow result is contrary to the expectation that turbine efficiency degrades at off-design speed, but is consistent with the assumed fuel flow map. Figure 3.23 plots the SFC required for minimum fuel flow rate (red) with selected points from the baseline (blue) for a sweep of airspeeds (40 - 170 knots) at 18,000 lb of thrust. Compared to the baseline case, the SFC of the slowed rotor increases at high airspeeds (140 and 160 knots), is similar near 120 knots and tends to decrease slightly at low speeds (near 60 knots). However, these small changes in SFC are greatly outweighed by the reduced rotor power that is achieved. To see a larger impact of the turbine efficiency, the turbine speed would have to be reduced further (below 70%) or the differential rotor power must be larger. The requirement for the helicopter to maintain trim, without auxiliary thrust or lift, precludes this situation from arising.

3.9 Chapter Summary

This chapter has evaluated the impact on performance and loads of rotor speed variation (70%-100% of baseline) on a representative utility helicopter up to 180 knots ($\mu = 0.4$). The analysis was performed using UMARC. The model is based on a nominal UH-60A Black Hawk helicopter generating 18,000 lb of thrust and trimmed in free flight. Rotor speed was varied in 2% decrements until the performance degraded or the rotor could not achieve trimmed flight especially due to stall. The impact of disc loading is investigated by varying the thrust level between 14,000 and 20,000 lb. The key conclusions of this chapter are:

1. For an 18,000 lb thrust, a mean reduction of 100 hp across the flight envelope can be realized by tailoring the rotor speed between 80% and 96% RPM. Further reductions in RPM result in stall and an increase in power over the baseline.

2. At lower thrusts, the maximum power reduction increases with airspeed, while at higher thrusts, the power reduction decreases with airspeed. The largest reduction in RPM is necessary at low speeds and as such a range of about 16% RPM was required to achieve the maximum power reduction for each thrust.

3. For minimum power, the rotor torque is increased over the baseline. The increase in torque is less than 2000 ft-lb at high speeds for all thrusts considered. The highest torque increase occurs at low speeds (60 knots) where the maximum RPM reductions are required.

4. The rotor collective and cyclics increase to maintain the trim state for the slowed rotor, but do not exceed the limits of the baseline rotor. The longitudinal cyclic requires larger inputs to effect a change in airspeed for the slowed rotor. The vehicle shaft angles (α_s and ϕ_s) are not significantly affected by RPM variation.

5. The induced component of power is not impacted by slowing the rotor until stall, when the induced power increases. The profile power is the source of all of the power reduction when slowing the rotor and is a result of reduced dynamic pressure and reduced compressibility drag. For large reductions in rotor speed, high pitch angles result in increasing drag coefficients and limit further reductions in profile power.

6. The minimum power for this rotor is defined by the optimum C_T/σ as a function of advance ratio. The C_T/σ for minimum power is a reduction in the stall margin of the rotor, but does not come close to the McHugh stall boundary before an advance ratio of 0.4. For 20,000 lb thrust, the required thrust is coincident with the C_T/σ for minimum power at an advance ratio of 0.4. Improving performance at higher advance ratios requires decreasing the rotor thrust.

7. The vertical shear vibratory loads are less affected for a slowed rotor. The in-plane forces and moments increase significantly over the baseline rotor values at high speeds. The increase in loads is a function of advance ratio and occurs near an advance ratio of 0.28 regardless of RPM unless the rotor is stalled.

The loads for the stalled rotor increase prematurely. The minimum power rotor will incur a vibrations penalty at high speeds.

8. Contour surfaces of the hubloads for reducing rotor speed showed that the vertical shear force and the in-plane moments have unique minimums for each airspeed and a significant reduction in these hubloads is possible at low speeds. The in-plane shear force can be reduced by less than 1% at low speeds. All of the hubloads are uniformly and significantly increased over the baseline at high airspeeds when the rotor is slowed.

9. Blade flap bending moments are larger than the baseline for the slowed rotor. In the limiting case of stall, the slowed rotor and the baseline half peak-to-peak flap bending loads are similar but the peak moves outboard for the slowed rotor. Stall drives up the 3/rev harmonics of flap bending for the slowed rotor at high speeds. The 5/rev harmonics of flap bending are much larger than the baseline for the 88% and 84% RPM rotors due to 5/rev excitation of the 3^{rd} blade flap mode.

10. Half peak-to-peak torsional moments are not significantly affected by rotor speed below stall. For the same airspeed, the torsional moments of the slowed rotor increase over the baseline as it approaches stall; however, peak torsional moments are determined by compressibility at high airspeeds which has a greater impact than stall.

11. There is minimal impact of reduced turbine efficiency on the performance of

the rotor system due to the relatively small differential in rotor power for the variable speed rotor system and the small (less than 30%) reductions in rotor speed investigated.

Concluding chapters 2 and 3, variable rotor speed appears to be the more attractive option to improve the performance of convention edgewise rotorcraft. Variable rotor speed offers a larger improvement in performance at moderate to high speeds than from variable radius alone. At low speeds near hover (below 50 knots), variable radius offers an advantage if the radius can be increased, although there are practical design trades and limitations to this. The complexity of implementing the two approaches to variable tip speed heavily favor rotor speed variation over radius variation.

Challenges for rotor speed variation are in avoiding blade mode crossings during speed changes and achieving efficient power transmission at multiple rotor speeds. Stiff, light weight rotors that are resistant to resonance during RPM changes have already been built and tested and composite construction techniques should allow greater control and tailoring of this in the future. For the relatively modest changes in rotor speed considered for the UH-60A helicopter (20%–30% reduction) turbine efficiency reduction with reducing turbine speed is small compared to the normal variation of turbine efficiency across the flight envelope. Advancements to gas turbine technology will improve the performance of rotor speed variation further.

Variable radius concepts require complex mechanisms to change the blade radius in flight. Technology to achieve this has been shown in wind tunnel tests with

some success, but has never transitioned to flight tests. The robustness of the proposed mechanisms is a huge concern, as is the parasitic weight introduced. The increased complexity and weight in the rotating frame will result in overall vehicle weight penalties that will further degrade the modest potential for performance improvement. The increased complexity implies increased parts count and higher maintenance and cost. In summary, the obstacles to variable radius seem insurmountable in the foreseeable future unless larger performance gains can be achieved to warrant further investigation.

Chapters 4 and 5 goes on to investigate the variable rotor speed concept at high advance ratios, with comparison to wind tunnel test data.

Chapter 4: Investigation of the UH-60A Rotor at High Advance Ratios

This and the following chapter present the prediction and validation of performance and loads for a rotor in high advance ratio flight. High speed rotorcraft are limited by compressibility at the advancing rotor tip. Compressibility becomes important as the incident flow speeds approach the speed of sound (usually by $M_{ADV} = 0.8$–0.85) and results in high power requirements and unacceptable vibration levels that become limiting to flight. The solution to reducing tip compressibility is to reduce the tip speed by either reducing the rotor radius or the rotor speed. Chapters 2 and 3 introduced both approaches as applied to the UH-60A Black Hawk helicopter in free flight. Both showed the potential to improve performance at typical flight speeds and thrusts, but the larger improvement was shown possible by reducing the rotor speed, while also being the technologically simpler solution. There has also been recent interest in slowed rotor helicopters resulting in new, high quality data with which to correlate analyses. For these reasons, the study of high speed rotors will progress considering reduced speed rotors only.

High speed flight with reduced rotor speed implies high advance ratios. At

high advance ratios, the rotors ability to produce thrust and control authority to trim becomes diminished as the flow becomes more asymmetric. The retreating side is required to operate with large regions in reverse flow (from trailing edge to leading edge), which is a complex flow environment. In order to design the next generation of high speed rotorcraft, it is important to understand and to be able to predict both the performance and the limiting loads at high advance ratios. The goal of this chapter is to validate the predictions of the modified comprehensive analysis UMARC, to highlight key modeling requirements and to identify what shortcomings remain within the scope of a comprehensive analysis at high advance ratios. This is achieved by correlation with high quality wind tunnel test data at high advance ratios.

There have been two recent efforts to collect a comprehensive data set at high advance ratios. These are the slowed rotor testing of the UH-60A rotor carried out by NASA-Ames/Army-AFDD that achieved an advance ratio of 1.0, and a series of wind tunnel tests on a Mach-scaled rotor by the University of Maryland that have reached an advance ratio of 1.5. These two sets of data stand apart from earlier tests because of the scope of the instrumentation that includes fixed frame loads and torque, vibratory loads, pitch link loads, trim controls as well as blade bending moment and airload measurements.

This chapter deals with the UH-60A rotor. The UH-60A rotor is the same as that flight tested in the airloads program [57] and is the most studied modern rotor. The rotor description and blade properties are generally agreed upon, allowing for direct comparison between different analyses. The UH-60A rotor is also an

articulated rotor including multiple airfoils, a high twist rate, trim tabs and tip sweep. The complexity of the rotor allows a realistic assessment of analytically models against realistic future rotors; however, the complexity also means that it can be quite difficult to isolate different aspects of the rotor system when identifying limitations of the analyses. For this reason, the University of Maryland has tested a simpler Mach-scaled rotor that has uniform blade properties and planform, is untwisted and has a simple NACA0012 airfoil. This test data is validated in chapter 5.

This chapter describes modifications made to UMARC that can be important for resolving the performance and loads at high advance ratios. These include a fuselage model, aerodynamics of the root cut-out, and radial flow corrections. The modification are evaluated by validation with the UH-60A slowed rotor wind tunnel tests. In addition, the sensitivity of the analysis to modeling refinements is investigated. This includes wake model refinement and treatment of the nearwake in reverse flow.

Data available from the UH-60A slowed rotor wind tunnel tests include performance measurements for a range of collective at increasing advance ratio, predominantly at 0° shaft angle, and a few selected cases where airloads measurements (normal force and pitching moment) and blade bending loads and pitch links loads are available. The approach will be to determine the baseline correlation before investigating which model refinements are important to achieve a good correlation. Once the performance predictions are established, the details of the sectional airloads and blade bending moments will be investigated in some detail.

4.1 UMARC Modifications

The modified University of Maryland Advanced Rotorcraft Code, as described in chapter 2, was used in this study. This section describes the important modifications and refinements made to UMARC that were relevant at high advance ratios. Before describing each modification, the treatment of the unsteady airloads at high advance ratios must be explained.

The earlier analysis of variable rotor speed and variable radius concepts included the Leishman-Beddoes unsteady models for attached flow. However, the unsteady models (as implemented in UMARC) are not suitable for the reverse flow. At the reverse flow boundary, the airfoil sees large angles of attack, high pitch rates and a change in flow direction resulting in large and seemingly non-physical lift and pitching moment impulses. The resulting unsteady impulses excite a large blade response and the rotor analysis could not find a steady trimmed solution. Neglecting the unsteady airloads in the reverse flow at low advance ratios is assumed to have little impact on the result due to low dynamic pressures seen there. However, as will be shown in this and the following chapters, unsteady airloads may be important for predicting lift and pitching moment at high advance ratios (near 1.0) as the dynamic pressure in the reverse flow becomes large. Validating these unsteady models for the extreme conditions in the reverse flow requires careful wind tunnel testing and is the subject of ongoing research elsewhere [109].

In the current analysis, non-circulatory lift is included in the reverse flow with Theodorsen's quasi-steady model while the higher order Leishman-Beddoes attached

and dynamic stall models are used only outboard of the reverse flow, but show little impact there.

The following section describes the important modifications made to UMARC that were relevant at high advance ratios.

4.1.1 Trim procedure at High Advance Ratios

One of the biggest challenges of studying high advance ratio with an analysis like UMARC is solving the trim equations. Trim is found in UMARC by building a Jacobian matrix from the trim equations before minimizing the trim equation residuals until satisfactory convergence is reached. In addition, the change in blade deflections between iterations must be suitably converged.

At normal advance ratios (< 0.4), the well established procedure in UMARC is that the Jacobian is generated once, during the first $n + 1$ iterations where n is the number of degrees of freedom in the trim solution. The Jacobian is built before the non-linear influence of airfoil tables, unsteady airloads, nearwake or farwake are turned on in the analysis. The quality of the Jacobian is determined by the quality of the initial guess of the trim angles (θ_0, θ_{1c}, θ_{1s}, α_s and ϕ_s) and the initial value of inflow (λ), derived from the desired rotor thrust. Two methods were available to create the initial conditions, either by user input or solving the rigid blade equations of the helicopter. The later approach is generally reliable unless trimming to high speeds or high thrusts when assumptions in the rigid blade calculations break down and an educated initial guess gives better convergence rates.

For the high advance ratio studies, rotor thrust is not a trim target, which left inflow undefined. An optional input argument **IG_inflow** was added to the input routine (defaulting to 0.05 unless a target thrust is specified). At moderately high advance ratios (0.4 – 0.8), initial guesses for the trim controls and inflow were generally required to find a trim solution. The initial values can be determined intelligently by incrementally increasing advance ratio from a known trimmed solution. Over this range of advance ratios, the trim solution is somewhat forgiving to the initial guess although better guesses can decrease the number of iterations considerably.

At high advance ratios approaching and exceeding 1.0, the solution procedure becomes increasingly sensitive to the initial conditions. Above an advance ratio of about 0.9, the baseline trim procedure could not consistently find trim solutions, regardless of the initial conditions. As will be shown in this chapter, the stall behavior of the rotor is very influential on the rotor trim condition at high advance ratios. The Jacobian, constructed without airfoil tables, used linear lift coefficients without stall and resulted in a poor quality Jacobian. To remedy this, an option has been added to the analysis to include the airfoil tables in the Jacobian calculation. The drawback of this approach is that the initial guess of the trim controls and inflow must be reasonably good otherwise the solution quickly diverges. However, with incremental increases in advance ratio (0.1) and collectives (1°) the trim is reliable beyond an advance ratio of 1.2 (the limit investigated in chapter 5). For advance ratios above the point of thrust reversal (discussed in this chapter) the guess for inflow must generally be negative for positive collectives to reflect the negative

thrust of the rotor.

4.1.2 Table Look-Up in Reverse Flow

The sectional angle of attack, α, is defined by the velocity components tangent to the chord, u_t, and perpendicular to the chord, u_p, so that the angle of attack in the table look up to determine the airfoil coefficients c_l, c_d and c_m is given by:

$$\alpha = \begin{cases} \arctan(-u_p/u_t) & : -u_t > 0 \\ \arctan(-u_p/u_t) + \pi & : -u_p \geq 0, u_t < 0 \\ \arctan(-u_p/u_t) - \pi & : -u_p < 0, u_t < 0 \\ \frac{\pi}{2} & : -u_p > 0, u_t = 0 \\ -\frac{\pi}{2} + \pi & : -u_p < 0, u_t = 0 \end{cases}$$

For small angles of attack, α, it was convenient to express the lift, drag and moment coefficients as linear functions of α

$$c_l = c_0 + c_1\alpha \tag{4.1}$$

$$c_d = d_0 + d_1\alpha \tag{4.2}$$

$$c_m = f_0 + f_1\alpha \tag{4.3}$$

From the airfoil coefficients, the chord force (L_v positive towards the leading edge), normal force (L_w) and pitching moments (M_ϕ) are described by:

$$L_v = \frac{\gamma V^2}{6a}(c_l(\alpha)\sin(\alpha) - c_d(\alpha)\cos(\alpha)) \tag{4.4}$$

$$L_w = \frac{\gamma V^2}{6a}(c_l(\alpha)\cos(\alpha) + c_d(\alpha)\sin(\alpha)) \tag{4.5}$$

$$M_\phi = \frac{\gamma V^2 \bar{c}}{6a} c_m(\alpha) \tag{4.6}$$

The nonlinear trim solution in steady level flight is found using finite elements in space and time. The aerodynamic forcing terms are non-linear functions of the blade deflections. To ensure stable solutions, the linear contributions to the forcing terms are moved the left hand side of the solution as effect stiffness and damping terms, while the constant and non-linear (linearized about the current state) terms remain on the right hand side. The angle of attack is assumed to be small and u_t is large compared to u_p so that:

$$\begin{aligned} V \approx & u_t \\ \alpha \approx & {}^{-u_p}/_{u_t} \\ cos(\alpha) \approx & 1 \\ sin(\alpha) \approx & \alpha = \frac{-u_p}{u_t} \end{aligned} \tag{4.7}$$

So that the chord force, normal force and pitching moment expressions become:

$$L_v = \frac{\gamma V^2}{6a}(-d_0 u_t^2 - (c_0 - d_1) u_p u_t + c_1 u_p^2) \tag{4.8}$$

$$L_w = \frac{\gamma V^2}{6a}(c_0 u_t^2 - (c_1 + d_0) u_p u_t + d_1 u_p^2) \tag{4.9}$$

$$M_\phi = \frac{\gamma V^2 \bar{c}}{6a}(f_0 u_t^2 - f_1 u_p u_t) \tag{4.10}$$

The error introduced to the analysis from the small angle assumption on α is small for α less than about 20°, which is satisfactory for normal rotorcraft analysis. However, the small angle assumption on α introduces errors that are important at high advance ratios where there is a large region of reverse flow. The first error is illustrated in fig. 4.1, which shows the angle of attack (α), $\sin(\alpha)$ and the normal force ($C_N M^2$) distributions around the azimuth at a radial station within the reverse flow for an arbitrary trim condition. The figures include the exact calculation of α and the small angle assumption result. The angle of attack result shows a discontinuity in the small angle results when u_t goes to 0 and that the small angle approximation is 180° out of phase. To avoid an error in the table look up, the exact angle of attack is used in UMARC to find the airfoil coefficients. However, taking the sin of the angle of attack, needed to rotate the lift and drag into the airfoil fixed frame, results in a sign error so that the lift ($C_N M^2$) in the reverse flow has the wrong sign. Note that the small angle assumption does not introduce any perceptible error under normal (forward) flow conditions. To correct this error, the normal and chord forces must be multiplied by the sign of u_t to give:

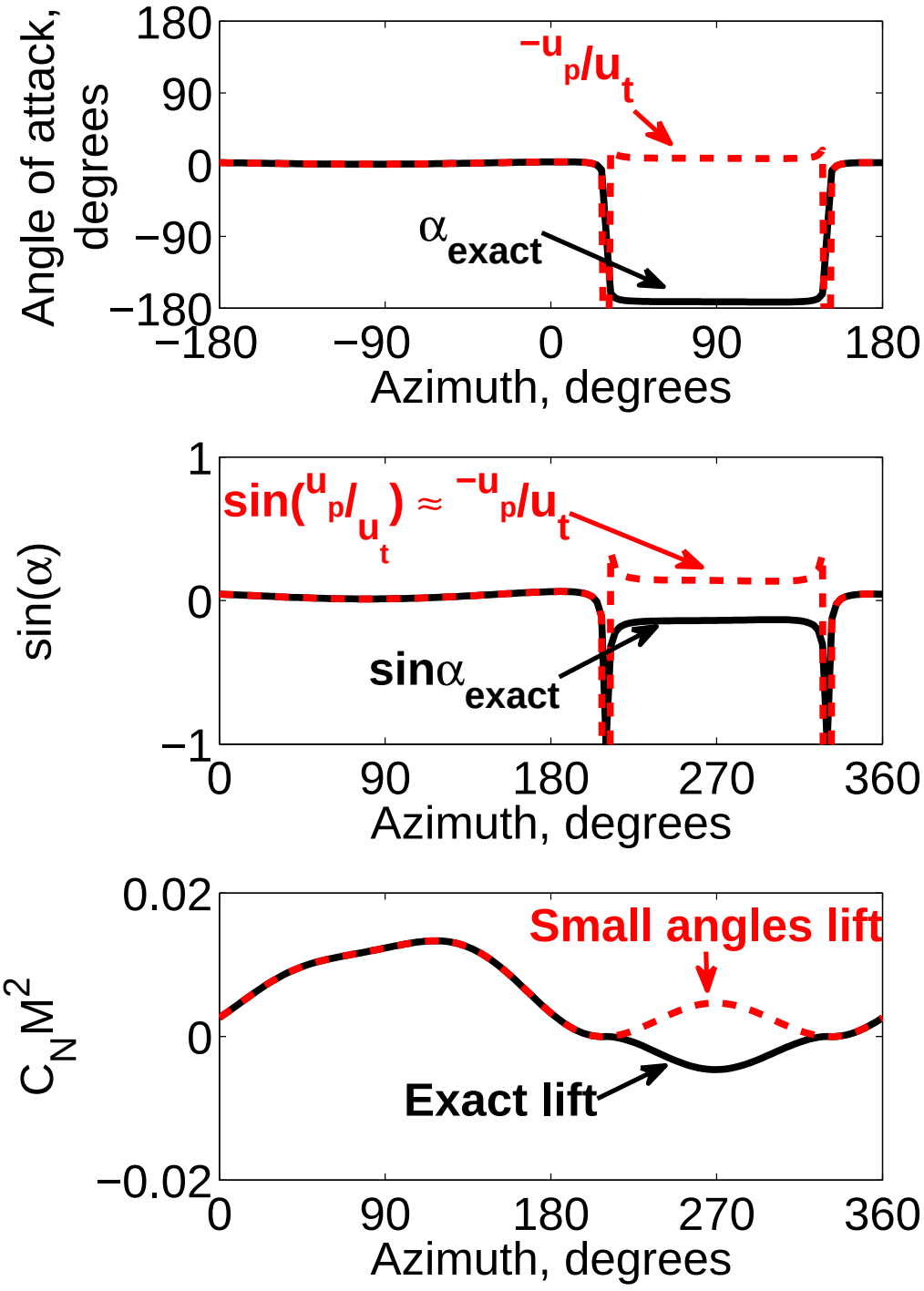

Figure 4.1: Error in normal force from small angle approximations.

$$L_v = \frac{\gamma V^2}{6a}(-d_0 u_t^2 - (c_0 - d_1)u_p u_t + c_1 u_p^2) sgn(u_t) \tag{4.11}$$

$$L_w = \frac{\gamma V^2}{6a}(c_0 u_t^2 - (c_1 + d_0)u_p u_t + d_1 u_p^2) sgn(u_t) \tag{4.12}$$

$$M_\phi = \frac{\gamma V^2 \bar{c}}{6a}(f_0 u_t^2 - f_1 u_p u_t) \tag{4.13}$$

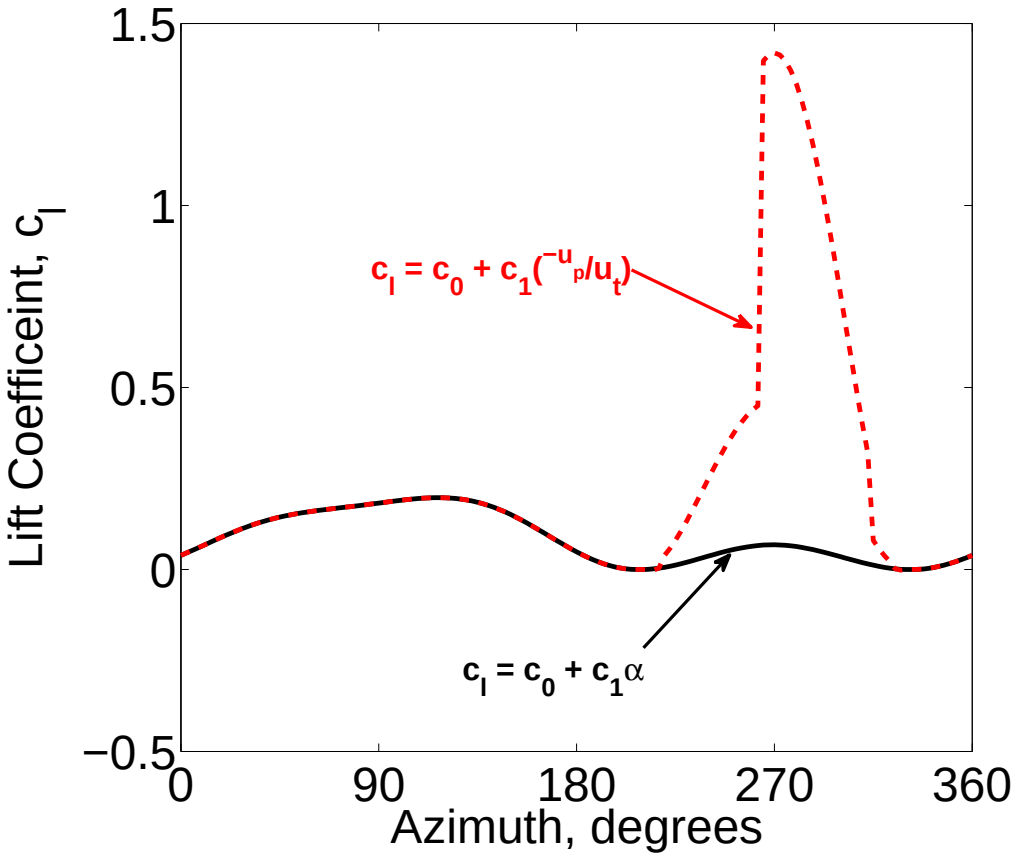

Figure 4.2: Error in lift from small angle approximations in table look-up.

The small angle assumption also creates an error from the table look-up despite using the exact angle of attack. The lift coefficients are linearized about α (exact) to find c_0, c_1, d_0, etc., so that $c_l = c_0 + c_1\alpha$ (eq. (4.1); however, from eq. (4.8), the

linearized coefficients are actually evaluated at ${}^{-u_p}/_{u_t}$. The error that is introduced to the lift coefficient by this disconnect is shown in fig. 4.2, which shows the lift coefficient around the azimuth at a radial station including reverse flow. The error is only present in the reverse flow region, but results in the lift and drag coefficients being orders of magnitude too large. The correction made to UMARC is to find the airfoil coefficients using the exact angle of attack, and then correct the linear coefficients to be evaluated at the small angle such that:

$$\begin{aligned} c_l(\alpha) &= c_0 + c_1(\alpha) \\ &= c_0 + c_1(\alpha) + c_1({}^{-u_p}/_{u_t}) - c_1({}^{-u_p}/_{u_t}) \\ &= c_0^* + c_1({}^{-u_p}/_{u_t}) \end{aligned} \tag{4.14}$$

where

$$c_0^* = c_0 - c_1({}^{-u_p}/_{u_t})$$

and repeating the process for the drag and moment coefficients. The corrected normal force, chord force and pitching moments become:

$$L_v = \frac{\gamma V^2}{6a}(-d_0^* u_t^2 - (c_0^* - d_1)u_p u_t + c_1 u_p^2) sign(u_t) \tag{4.15}$$

$$L_w = \frac{\gamma V^2}{6a}(c_0^* u_t^2 - (c_1 + d_0^*)u_p u_t + d_1 u_p^2) sign(u_t) \tag{4.16}$$

$$M_\phi = \frac{\gamma V^2 \bar{c}}{6a}(f0 u_t^2 - f1 u_p u_t) \tag{4.17}$$

The above two corrections to UMARC are valid for all flight conditions that

include a region of reverse flow; however, the corrections do not make a meaningful difference to the rotor performance at low advance ratios (below $\mu = 0.4$) because of the low dynamic pressures in the reverse flow. The corrections only become important at high advance ratios when the airloads of the reverse flow region start to influence the rotor trim state.

4.1.3 Fuselage Model

Figure 4.3: NASA's Large Rotor Test Apparatus (LRTA) fuselage.

Initial results for the UH-60A rotor showed that the rotor thrust was generally under-predicted by the analysis with similar results shown by Yeo [100] and Ormiston [101] using comprehensive analyses (lifting line analyses) and the CFD results

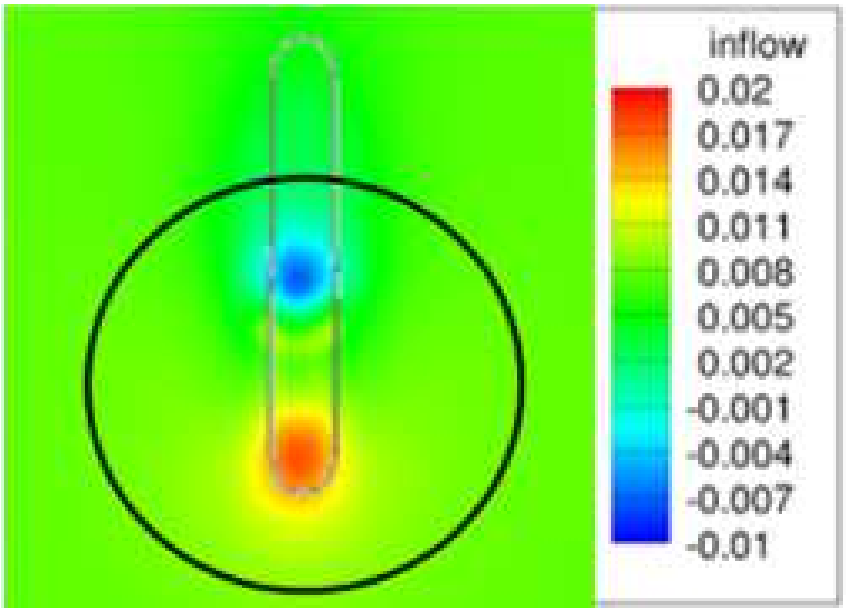

Figure 4.4: Inflow at the rotor plane due to HART fuselage, $\mu = 0.15$, 4.5° shaft tilt.

from Potsdam et al. [102]. The UH-60A rotor was tested above the large rotor test apparatus (LRTA), which includes a fairing as shown in fig. 4.3. The motivation to investigate the effect of the fuselage on rotor thrust at high advance ratios came from early thrust measurements of the University of Maryland high advance ratio tests, which suggested that the exclusion of the test stand fairing (fuselage) decreased the measured thrust in the presence of a spinning rotor.

The two interactions possible from the fuselage are with the wake and by disturbing the freestream. At high advance ratios, the wake is swept aft and is not expected to interact with the fuselage. However, the freestream fuselage disturbance is expected to grow at high advance ratios. Figure 4.4 shows a CFD result by Amiraux et al. [110] showing the velocity induced at the rotor plane by the HART fuselage, which is predominantly a region of upwash over the fuselage nose and a reciprocal downwash over the tail. The velocities are small, but could be large

relative to the induced inflow for rotors producing little to no thrust at high advance ratios. The simplest model of the fuselage is to model it as a source–sink pair to create a Rankine Ovaloid.

4.1.3.1 Rankine Ovaloid

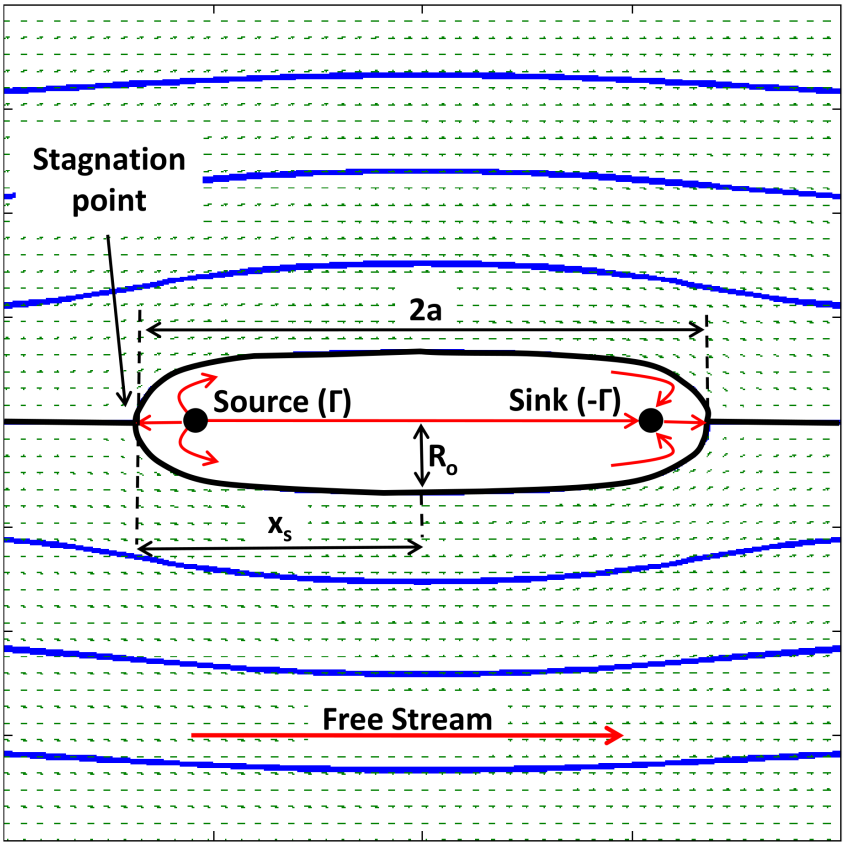

Figure 4.5: Rankine Oval in 2D.

The Rankine oval is a result of a source and sink pair of equal strengths in a uniform flow. Where the stream function of the resulting flow is equal to zero, and describes the Rankine body as shown in fig. 4.5. The shape of the body is defined by the stagnation point, x_s, and the radius, R_o, in terms of the unknown mass flux, Γ, and the separation, $2a$, of the source–sink pair.

Solving for the mass flux and the source–sink separation distance requires two equations. These are:

1) The flow velocity in the x direction, u, must be zero at the stagnation point,

$$u = \frac{\partial \phi}{\partial x} = U + \frac{\Gamma}{4\pi}\left[\frac{x+a}{((x+a)^2+y^2+z^2)^{3/2}} - \frac{x-a}{((x-a)^2+y^2+z^2)^{3/2}}\right]$$

$$u|_{y=z=0} = 0 = U - \frac{\Gamma}{\pi}\frac{a x_s}{(x_s^2-a^2)^2} \tag{4.18}$$

2) The mass flux at the half body must equal the mass flux of the source/sink.

$$\Gamma = 2\pi \int_0^{R_o} uR \, \mathrm{d}R \tag{4.19}$$

where

$$u = U + \frac{\Gamma}{4\pi}\frac{2a}{(a^2+R^2)^{3/2}}$$

$$R = y^2 + z^2$$

The disturbed flow at the rotor plane can be calculated for a known geometry and wind speed after solving for Γ and a. From a description of the LRTA fuselage shown in fig. 4.6a, it is approximated as 384 inches long ($x_s = 192$ inches) with a diameter of 100 inches ($R_o = 50$ inches) and the rotor plane is 80 inches above the center of the fuselage (h). The predicted upwash at the rotor plane for the approximate LRTA fuselage is shown for an advance ratio of 0.3 in fig. 4.6b and for an advance ratio of 1.0 in fig. 4.6c.

A simple modification is to assume that the wake behind the rotor hub disrupts

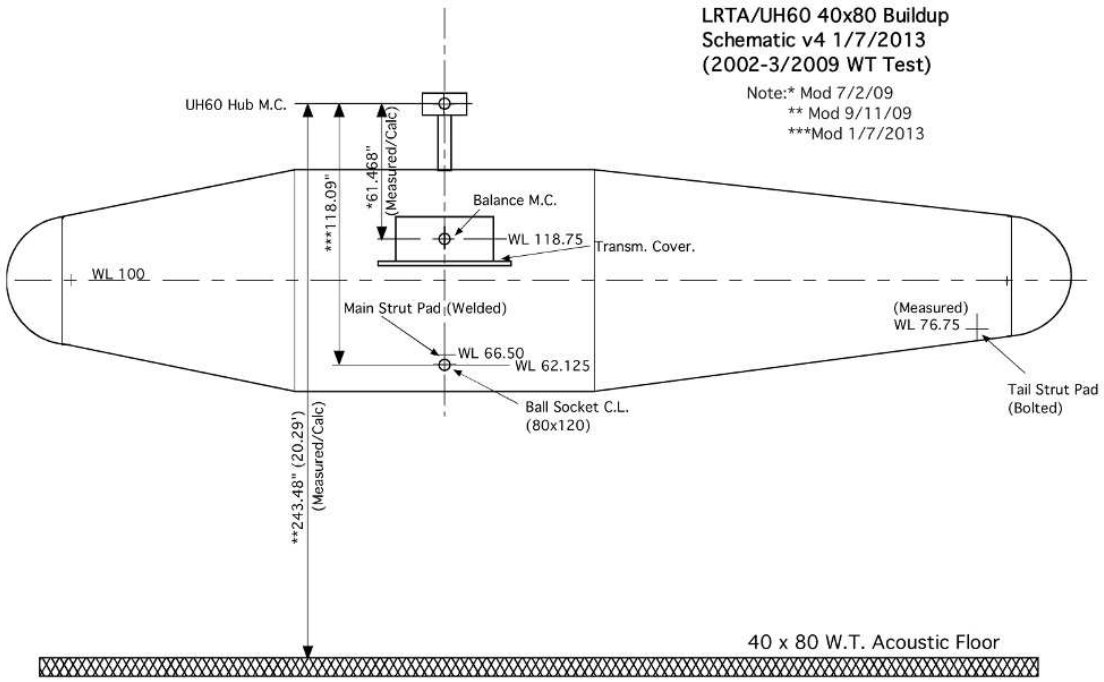

(a) Sketch of LRTA fuselage.

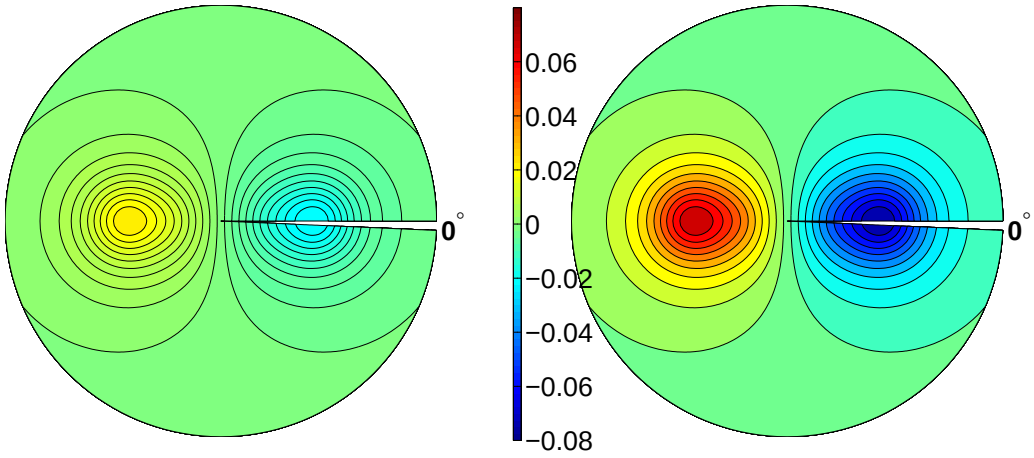

(b) $\mu = 0.3$ (c) $\mu = 1.0$

Figure 4.6: Sketch of LRTA fuselage with the induced upwash at advance ratios of 0.3 and 1.0.

the downwash on the rear of the rotor disk so that only the upwash over the nose is included.

4.1.4 Trailed Wake Models

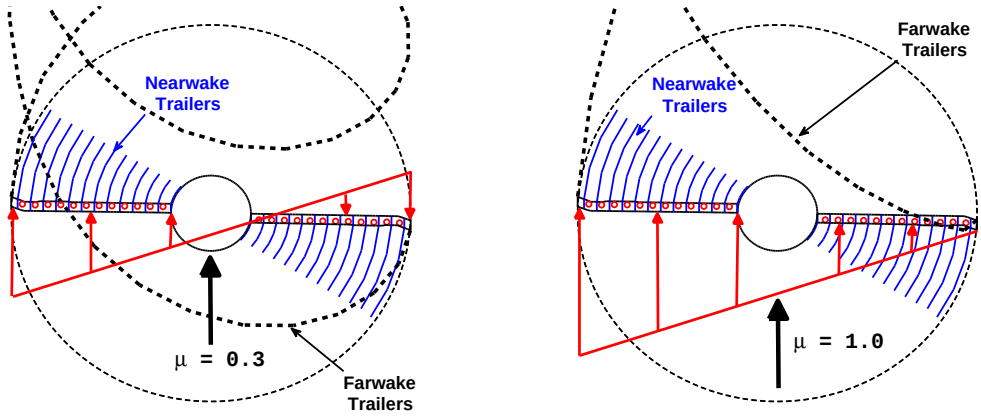

(a) $\mu = 0.3$ (b) $\mu = 1.0$

Figure 4.7: Trailed near and far wake geometry.

The trailed wake system is modeled by a farwake model that tracks the rolled-up, tip trailer, and a nearwake model that represents the near trailed wake. It is common practice to treat the nearwake as a planar sheet of trailed vorticity behind the blade. The roll up is represented by a tip weighted triangular distribution of the nearwake. The geometry of this model is shown for an advance ratio of 0.3 in fig. 4.7a and an advance ratio of 1.0 in fig. 4.7b. At $\mu = 0.3$, there is a small inconsistency between the nearwake model and the farwake on the retreating side but this is assumed unimportant relative to the simplicity of the model. However, at an advance ratio of 1.0, the rigid nearwake model does not represent the flow direction nor does it align with the position of the farwake vortex.

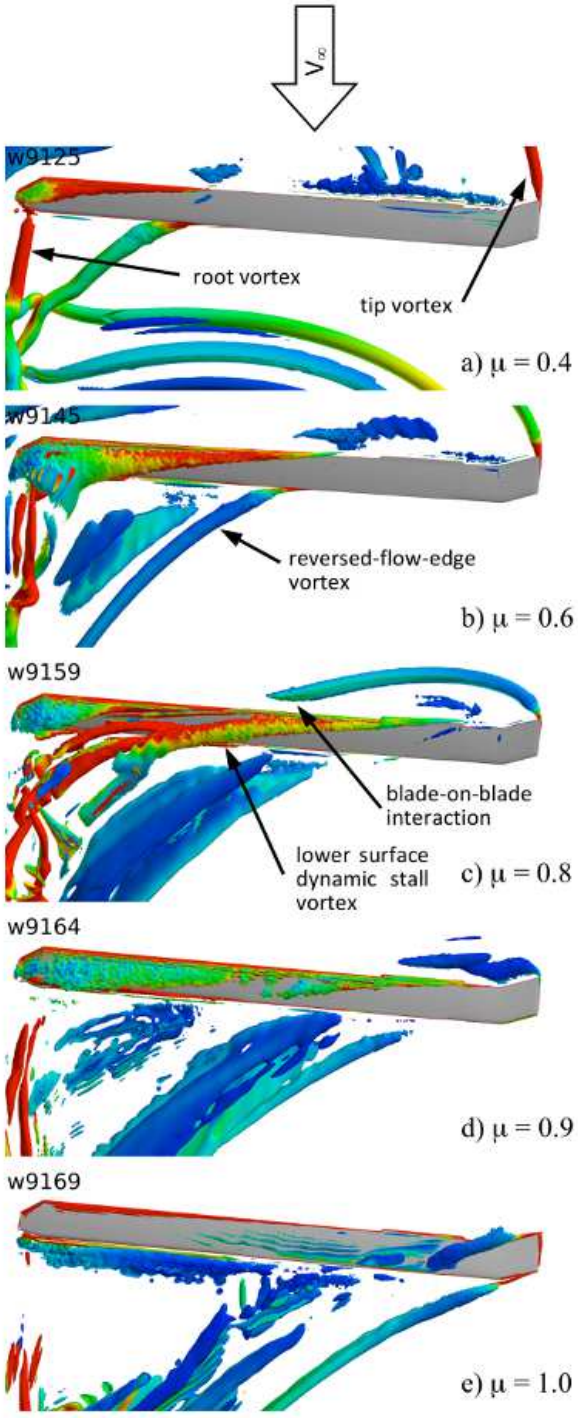

Figure 4.8: CFD wake visualization of underside of retreating blade at increasing advance ratios showing the formation of multiple trailers [68].

The roll up of the trailed wake is expected to follow the freestream, which is supported by CFD wake visualization of high advance ratio flows conducted by Potsdam et al. [68] and shown in fig. 4.8. The CFD result shows vorticity, from the point of view below the retreating blade for increasing advance ratios. The complex flow shows evidence of leading and trailing edge tip vortices, a wake vortex from the edge of the reverse flow and a root vortex that leads the blade. Because the aerodynamics of the reverse flow grows in importance at high advance ratios, correctly modeling the multiple trailer system and the nearwake may be important for loads correlation. These are investigated in the following section.

4.1.4.1 Weissinger-L like Nearwake Models

The Weissinger-L nearwake model has been implemented in UMARC to solve for the nearwake inflow, V_{NWK_i}, and circulation strength, Γ_j, along the span at each azimuthal location. The blade is represented by a series of spanwise horseshoe vortex elements. The bound vortex is at the $^1/_4$ chord location and flow tangency is imposed at the $^3/_4$ chord location, consistent with thin airfoil theory. The nearwake inflow is found from imposing flow tangency for each spanwise element, i:

$$V_{b_i} = -(u_{p_i} + V_{NWK_i}) \tag{4.20}$$

where, V_{b_i} is the velocity induced by the bound vortex system and u_{p_i} is the normal velocity composed of the freestream, blade deflections and the farwake inflow. The bound and trailed induced velocity are described in terms of influence coefficients

($I_{j,i}$ from Biot-Savart) and the bound vortex strengths (Γ_j):

$$V_{b_i} = \sum_{j=1}^{N} I_{b_{j,i}} \Gamma_j \tag{4.21}$$

$$V_{NWK_i} = \sum_{j=1}^{N} I_{NWK_{j,i}} \Gamma_j \tag{4.22}$$

There are two approaches that can be followed to find Γ. The first is to form and solve the algebraic equation for the bound vortex strength as given by:

$$\sum_{j=1}^{N} \{I_{b_{j,i}} + I_{NWK_{j,i}}\} \Gamma_j = -u_{p_i} \tag{4.23}$$

This is strictly the Weissinger-L approach, giving a linear equation to solve for Γ. The alternative is a Weissinger-L like approach, otherwise called a non-linear lifting-line approach, which is to find Γ_j based on the lift distribution directly,

$$\Gamma_i = \frac{l_i}{\rho V} \tag{4.24}$$

Once the bound vortex strength is known, the velocity induced by the nearwake system, V_{NWK_i}, is determined and an effective angle of attack, α_e, is calculated and used to lookup the airfoil coefficients:

$$\alpha_e = \arctan(\frac{-(u_{p_i} + V_{NWK_i})}{u_{t_i}}) \tag{4.25}$$

The second approach, requires sub-iterations to ensure that the lift is consistent with the effective angle of attack (usually 10 iterations is sufficient), but does not require inverting the influence matrix. The second approach has proved more robust in the reverse flow where the angles of attack are large and exceed stall and was adopted for this work.

The nearwake inflow depends on the nearwake geometry through the influence coefficients $I_{b_{j,i}} + I_{NWK_{j,i}}$. The following investigates the influence of the shape of the nearwake geometry at high advance ratio predictions.

4.1.4.2 Fixed Geometry Nearwake

The first modification to the baseline analysis is the inclusion of the rigid nearwake inflow in the reverse flow. The baseline model neglected nearwake inflow in the reverse flow due to issues related to small angle assumptions (discussed earlier), which have since been resolved. For the large reverse flow region at high advance ratios, the reverse flow nearwake should not be neglected.

Figure 4.9a shows the effective angle of attack compared with the angle of attack excluding the nearwake (but including farwake) inflow at an advance ratio of 1.0. The inclusion of the nearwake inflow reduces the effective angle of attack at the root cut-out from -9° to -3° (relative to the wind), with diminishing effects moving outboard. The effect is to reduce the negative lift in the reverse flow region, and delay stall. Figure 4.9b shows the circulation distribution. Notice that the entire circulation is negative, and the peak circulation is near the blade root (where the dynamic pressure is highest). The circulation distribution suggests a dominant root

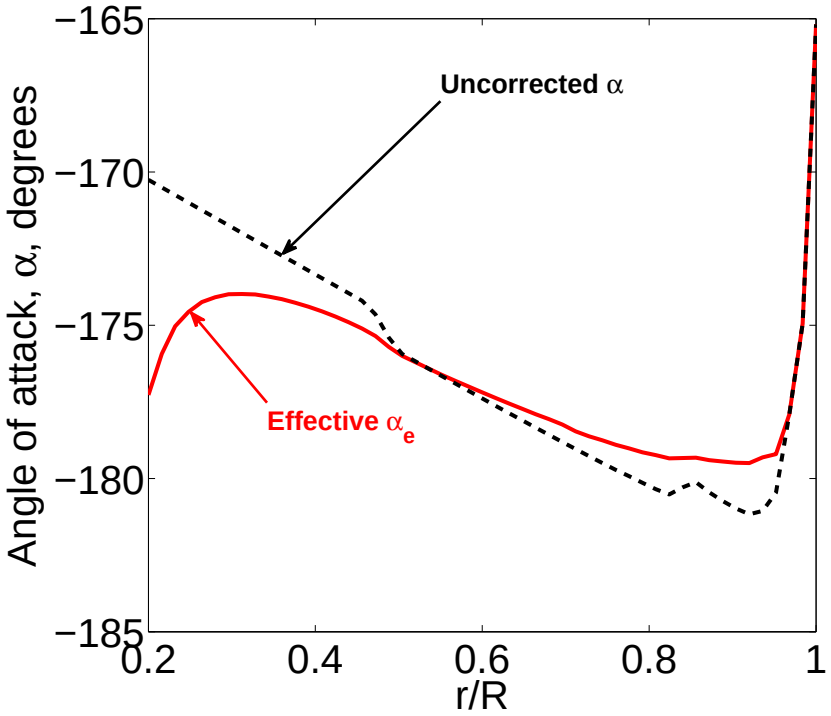

(a) Effective angle of attack in reverse flow, α_e.

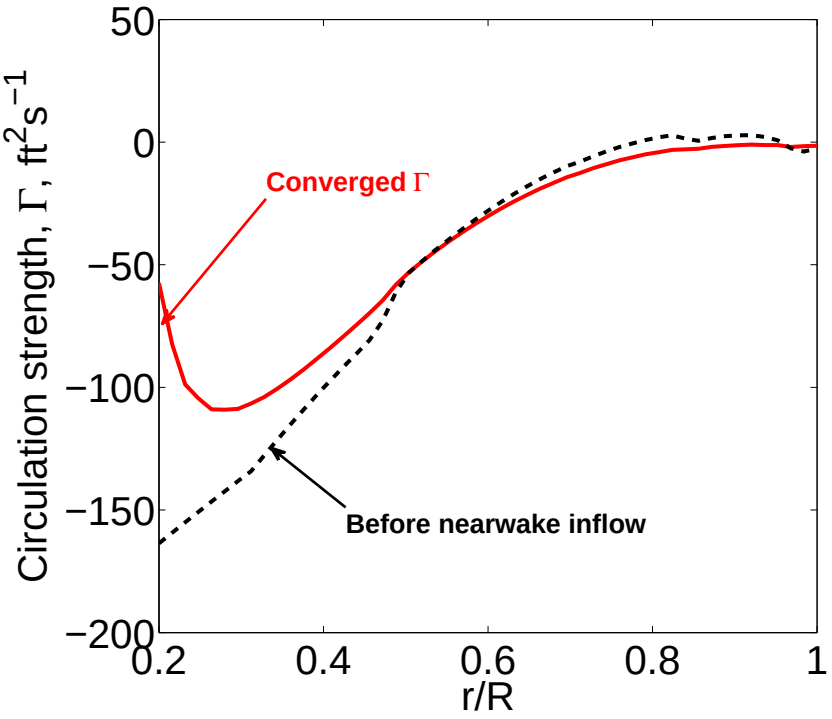

(b) Circulation strength in the reverse flow.

Figure 4.9: Effective angle of attack and circulation strength at $\mu = 1.0$, fixed geometry nearwake, $\theta_0 = 0°$, $\psi = 270°$.

vortex and a relatively weak tip vortex.

4.1.4.3 Free Geometry Nearwake

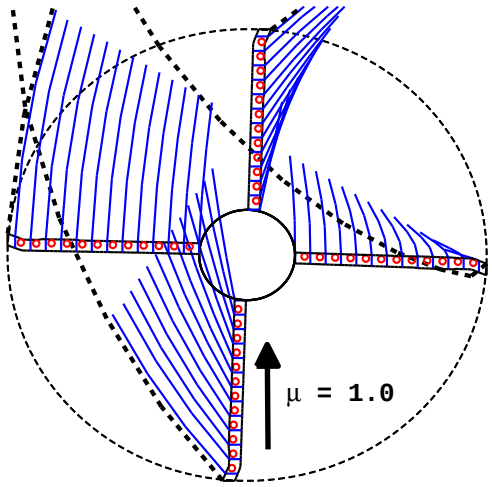

Figure 4.10: Nearwake geometry deformed with the free stream at $\mu = 1.0$.

A potential improvement to the nearwake modeling is to allow the nearwake to deform with the freestream. This approach tries to represent the wake roll up shown in the CFD to give better agreement between the far and near wake markers. It also appears acceptable to assume from thin airfoil theory that in reverse flow, the bound vortex moves to the $^3/_4$ chord position and flow tangency is imposed at $^1/_4$ chord location. A vortex core size equal to $0.1c$ is included in the model to remove singularities. It is also assumed that the nearwake trailers do not cross over the blade so that the trailer is entirely either in front of or behind the blade depending on the flow direction. The free geometry nearwake is shown in fig. 4.10 at an advance ratio of 1.0. The nearwake aligns well with the farwake except on

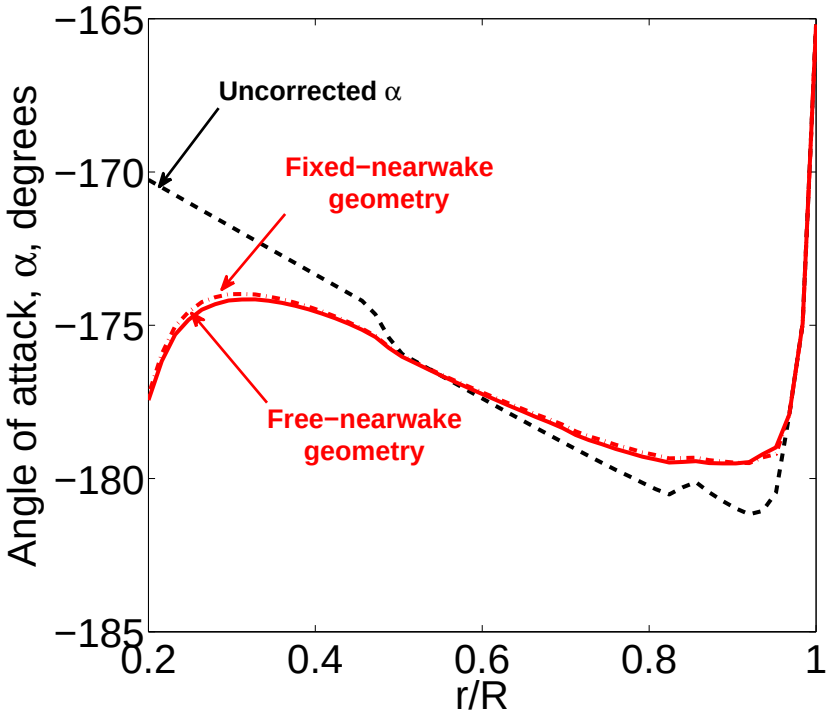

(a) Effective angle of attack, α_e.

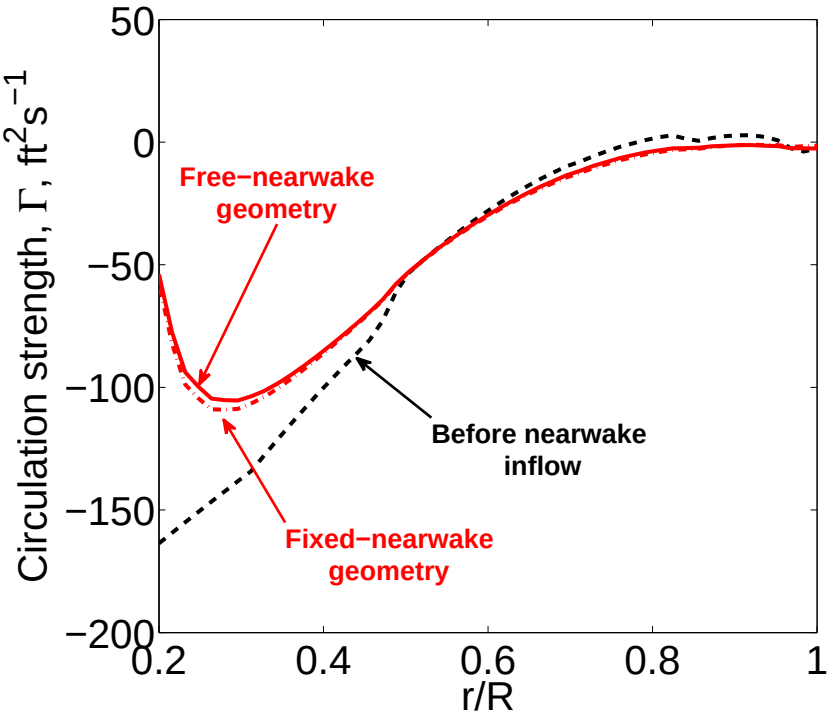

(b) Circulation strength.

Figure 4.11: Effective angle of attack and circulation strength at 270° azimuth, $\mu = 1.0$, free geometry nearwake, $\theta_0 = 0°$, $\psi = 270°$.

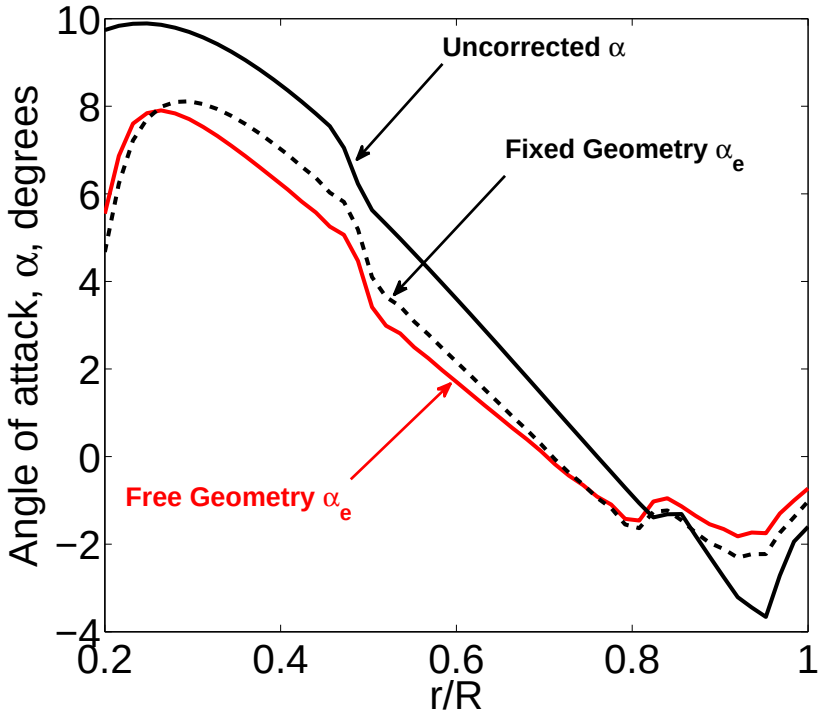

(a) Effective angle of attack, α_e.

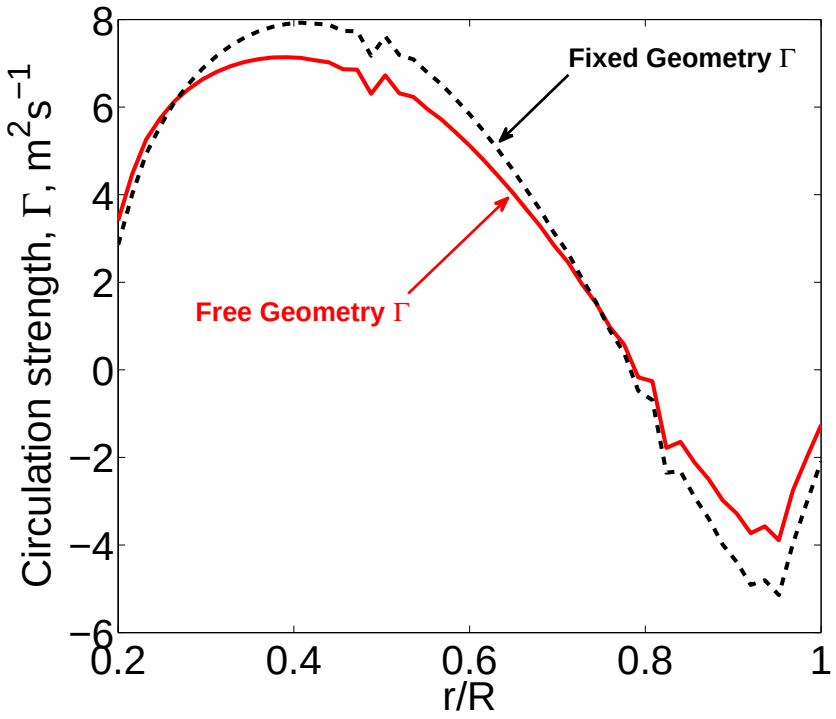

(b) Circulation strength.

Figure 4.12: Effective angle of attack and circulation strength at 180° azimuth, $\mu = 1.0$, free geometry nearwake, $\theta_0 = 0°$, $\psi = 180°$.

the advancing rotor. A small discrepancy remains in the reverse flow that arises from the stipulation that the nearwake does not cross over the blade, but this still represents an improved physical description of the nearwake.

The resulting angle of attack and circulation strength in the reverse flow are shown in fig. 4.11 and there is negligible difference from the deformed wake geometry. The difference in circulation is influenced by the length of the tracked nearwake (30° in this case) and is not significant. A larger impact of the free wake geometry is apparent over the front of the rotor shown at 180° azimuth in fig. 4.12. In this case, the deformed wake trailers are running nearly parallel to the blade control points (especially near the root), increasing the nearwake inflow and decreasing the effective angle of attack.

In conclusion, nearwake inflow should be included in the reverse flow region. The nearwake inflow acts to decrease the reverse flow effective angle of attack (relative to the wind), which reduces lift and delays stall. Allowing the nearwake to deform with the freestream has only a small effect in the reverse flow at 270° for an advance ratio of 1.0, but can have a significant impact when the deformed wake trailers are swept in closer proximity to the control points.

4.1.4.4 Farwake Trailers

The farwake induced inflow is calculated using the Bagai-Leishman free wake method [73]. The wake model has the option for multiple wake trailers, but the baseline analysis usually assumes a single wake trailer from the rotor tip. The single tip vortex model assumes that the trailed wake entirely roles up at the blade tip.

The strength of the vortex at each azimuth is defined by the maximum circulation strength along the span. For highly twisted rotors, two wake trailers that represent negative tip loading (positive inboard) have been shown to be important [76] to model the phase of advancing side lift. For the dual-wake trailer model, a vortex is shed at the tip with a strength equal to the minimum circulation near the tip and a second vortex is shed from the point of zero circulation with a strength equal to the sum of the maximum and minimum circulation strength along the blade. The CFD results of Potsdam et al. in fig. 4.8 show the potential for an additional two trailers, from the inboard blade at the root cut-out (root trailer) and from the edge of the reverse flow.

The baseline azimuthal resolution of the wake is 15° and this is used for the majority of the study looking at global performance measures. When comparing sectional airloads, the resolution of the wake is increased until the predicted airloads converged. Increasing the wake resolution does not have a significant effect on steady hub forces, moments or power predictions.

4.1.5 Yawed Flow Corrections

Figure 4.13 shows a section of a rotor blade with the in-plane velocity components. In general, the rotor blade is swept by an angle Λ to the freestream. The independence principle states that only the velocity components perpendicular to the blade span axis define the aerodynamic characteristics of the section, such as angle of attack, Mach number and Reynolds number. This is the baseline model in

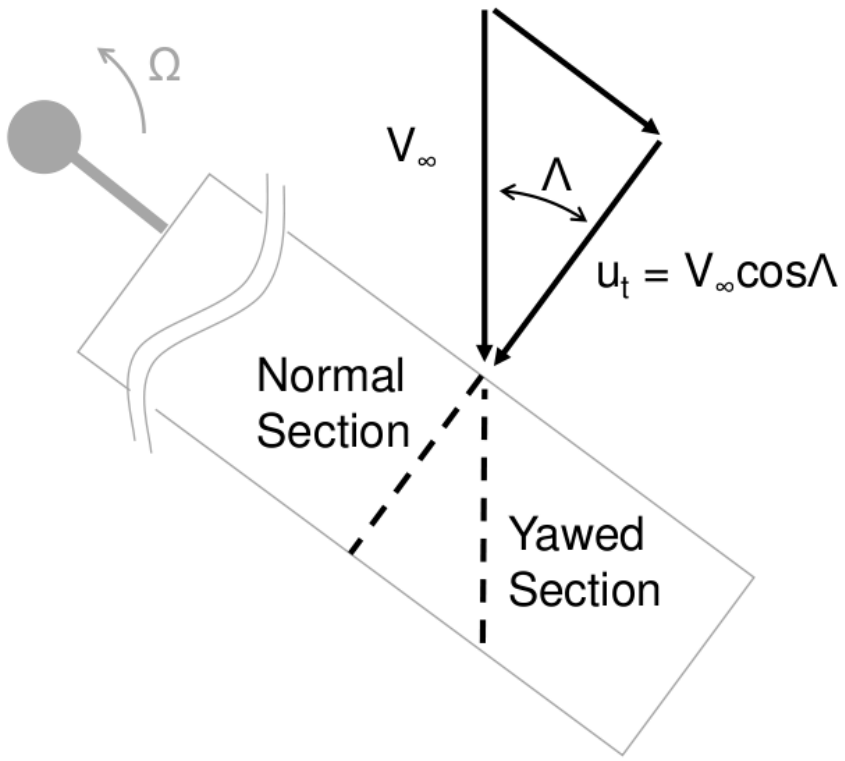

Figure 4.13: Geometry of yawed flow across a blade. Adapted from Johnson [111].

UMARC with an additional approximation for spanwise drag c_r to give:

$$c_l = c_{l_{2D}}(\alpha, M) \tag{4.26}$$

$$c_d = c_{d_{2D}}(\alpha, M) \tag{4.27}$$

$$c_m = c_{m_{2D}}(\alpha, M) \tag{4.28}$$

$$c_r = tan\Lambda c_{d_{2D}}(\alpha, M) = \frac{u_r}{u_t} c_{d_{2D}}(\alpha, M) \tag{4.29}$$

where subscript $2D$ indicates 2D sectional airfoil properties and α is found perpendicular to the blade axis. This approach ignores any effect of spanwise flow on the airfoil coefficients. However, it has been shown experimentally that for large yaw angles, the sectional drag coefficient increases and stall is delayed. Figure 4.14 shows the yaw angles around the azimuth for low and high advance ratios. The impact of yawed flow is small at $\mu = 0.3$ but could have a significant effect at $\mu = 1.0$ when yaw angles reach 90° at the root.

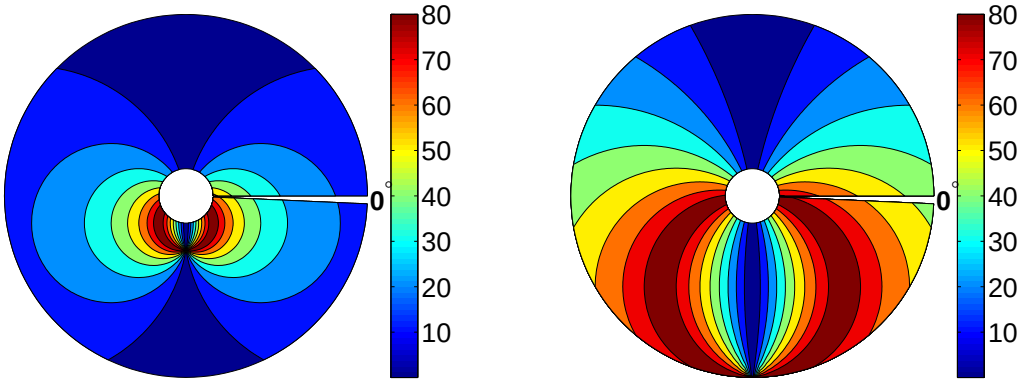

(a) $\mu = 0.3$ (b) $\mu = 1.0$

Figure 4.14: Radial flow angles (degrees) around the azimuth at high advance ratio.

The correction for yawed flow is found from equivalence with swept wings and is derived by Harris [112]. It is assumed that the lift for the un-yawed section is the same as for the yawed section (subscript y) and that the drag of the yawed section can be found from un-yawed airfoil characteristics so that:

$$c_l(\alpha) = c_{l_{2D}}(\alpha) \tag{4.30}$$

$$c_{d_y}(\alpha_y) = c_{d_{2D}}(\alpha_y) \tag{4.31}$$

$$\tag{4.32}$$

From the geometry of the swept blade, $q_y = q\cos\Lambda$ and $\alpha_y = \alpha\cos\Lambda$, which gives the yawed flow corrections:

$$c_l(\alpha) = \frac{L}{qS} \qquad = \frac{L_y}{q_y\cos^2(\Lambda)S} = \frac{c_{l_y}(\alpha_y)}{\cos^2(\Lambda)} \qquad = \frac{c_{l_{2D}}(\alpha\cos^2\Lambda)}{\cos^2(\Lambda)} \tag{4.33}$$

$$c_d(\alpha) = \frac{D}{qS} \qquad = \frac{D_y\cos(\Lambda)}{q_y\cos^2(\Lambda)S} = \frac{c_{d_y}(\alpha_y)}{\cos(\Lambda)} \qquad = \frac{c_{d_{2D}}(\alpha\cos\Lambda)}{\cos(\Lambda)} \tag{4.34}$$

Notice that the final expression for c_l comes from noting that below stall the lift curve slope is a and,

$$c_l(\alpha) = a\alpha = \frac{a_y\alpha_y}{\cos^2(\Lambda)} = \frac{a_y\alpha}{\cos(\Lambda)} \tag{4.35}$$

$$c_{l_y}(\alpha_y) = \alpha\cos^2(\Lambda) \tag{4.36}$$

The yawed flow corrections have shown reasonably agreement with CFD and

experiment [112, 113] for incompressible flows below stall and for yaw angles below 60°. Notice that there is no effect of the yawed flow corrections on lift below stall, but it tends to delay stall. The drag coefficient is increased below stall and decreased somewhat above stall. The validity of the models above stall has not been established while Johnson [111] suggests that the radial flow corrections be washed out as the normal angle of attack approaches 90°. In this implementation, the yawed flow correction smoothly decays for angles of attack above stall (15°) until 45°.

4.1.6 Root Cut-Out Aerodynamics

UMARC follows the general convention that the aerodynamics of the root cut-out are ignored. The root cut-out is, at a minimum, a circle prescribed by the blade attachment to the shaft, but can be enlarged for aerodynamic reasons in the reverse flow. Drag from the hub is usually included in the flat plate area of the fuselage, and there is no lift attributed to this region. Figure 4.15 shows a sketch of the planform and an image of the blade shank (8%-13% radius) from the UH-60A wind tunnel tests. Between 13% radius and 20% radius, the blade grip transitions smoothly into the airfoil section and this is considered non-aerodynamic. The clean airfoil sections begins at 20% radius. The root cut-out for the UH-60A is normally defined to extend to 20% radius. The wind tunnel test included taking tares of the stand (LRTA) that included the blade root attachments up to 8% radius. The blades include a region called the blade shank, which defines the region from the root attachment at 8% radius, to the beginning of the clean airfoil at 20% radius. The region inside of

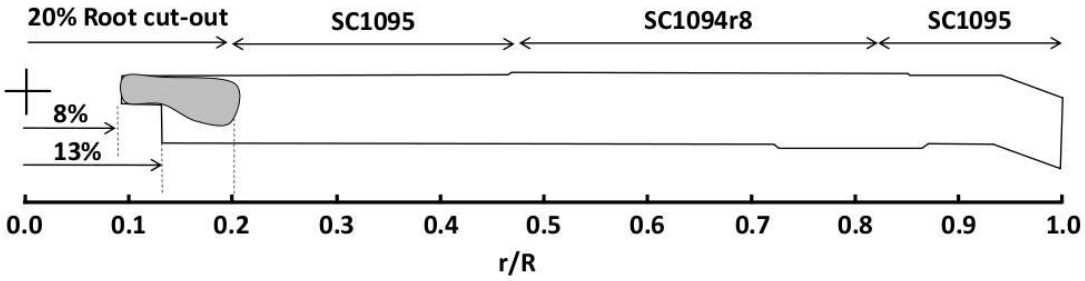

(a) UH-60A blade planform.

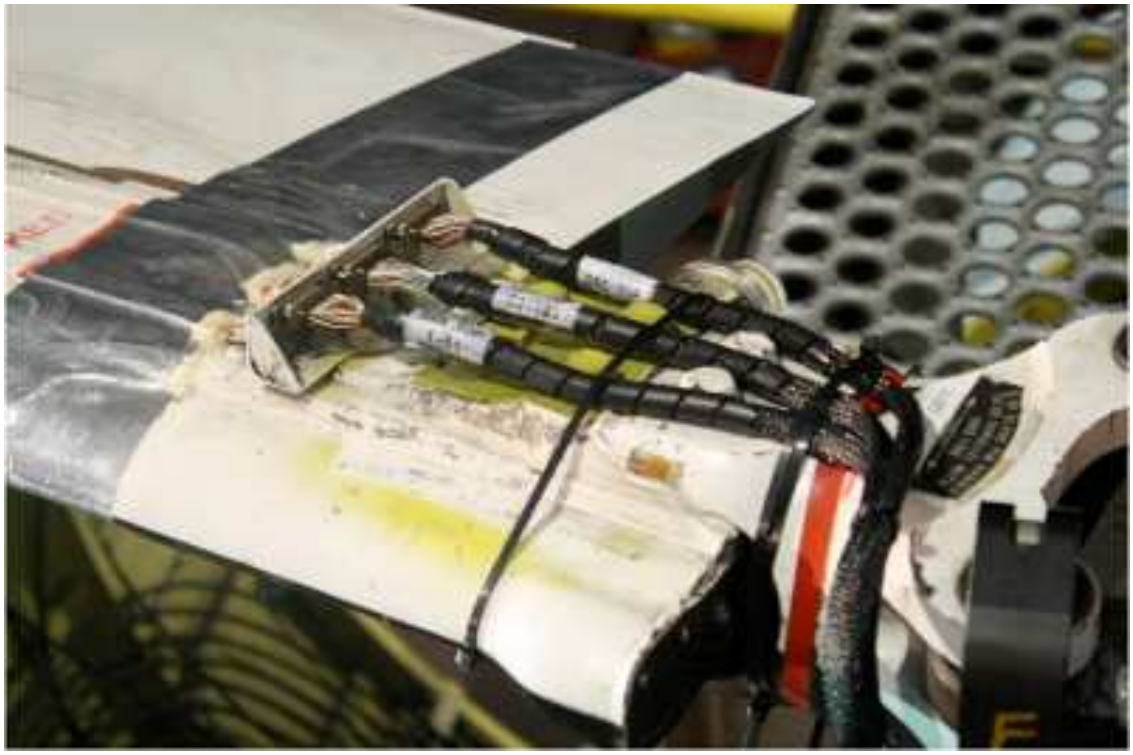

(b) UH-60A instrumented blade shank.

Figure 4.15: UH-60A root geometry.

20% radius is considered the root cut-out and the aerodynamics (lift and drag) are normally (advance ratios below 0.4) neglected in analyses owing to the low dynamic pressures present. The blade shank comprises bluff, unfaired structures from 8% to 13& radius followed by a nominally smooth transition to the airfoil section at 20% radius. The region from 13% to 20% included wiring and electrical hardware for instrumentation that was surface mounted. Harris [56], investigating the older H-34, UH-1 and PCA-2 high advance ratio rotor tests, and showed that all analyses under-predicted rotor drag force significantly, which could be corrected by assigning drag to the blade shank region. Yeo [100] and Ormiston [101] saw similar deficiencies comparing CAMRAD II and RCAS respectively with the UH-60A slowed rotor tests. Yeo found that assigning the shank region a drag coefficient ($c_{d_{shank}}$) of = 0.4 between 8% – 13% and 0.01 between 13% – 20% gave reasonable correlation, while Ormiston assigned it 1.5 (further details not given). Both values are assumed based on the correlation with test data. Potsdam [68] has modeled the blade shank using a first principles approach, although this does not appear to have included the exposed wiring. These results suggest drag coefficients of the shank between 0.14–0.18. Drag on the non-aerodynamic blade could not be determined. The CFD also showed that the non-aerodynamic region contributed 50%–80% of the lift of the adjacent clean airfoil section (20% radius). This has implications for predicting thrust at high advance ratios where the lift at the blade root, particularly in reverse flow, is important. This also affects the location of the blade root vortex (if it exists), by shifting the starting location from 20% to 13% corresponding to the physical end of the blade chord (fig. 4.15a).

The root cut-out region in UMARC now accounts for root drag and lift, based on the CFD results, as follows:

$$
\begin{aligned}
0\% \rightarrow 8\% &: \text{Removed in tare} \\
8\% \rightarrow 13\% &: Drag = c_{d_{shank,1}} = 0.4 \\
&: Lift = 0.0 \\
13\% \rightarrow 20\% &: Drag = c_{d_{shank,2}} = 0.4 \\
&: Lift = 0.5 c_{l_{\text{clean airfoil}}}
\end{aligned}
$$

where the shank drag coefficients ($c_{d_{shank,1,2}}$) have been determined by best fit of rotor drag predictions at 0°.

4.2 Description of UH-60A Test

The UH-60A rotor was tested in the NASA Ames National Full-Scale Aerodynamics Complex (NFAC) 40- by 80- ft wind tunnel in 2010. The test had several phases designed to provide good quality test data for correlation with analyses and to better understand the aeromechanic interactions at high advance ratios. The last phase of the test was to investigate high advance ratios. The motivation of the high advance ratio tests was to collect detailed measurements of the hub forces and moments, blade loads and pressures at a resolution that was not achieved with the earlier high advance ratio tests. The UH-60A rotor was chosen for this test because it has already been modeled in detail for normal flight conditions and it is expected

to provide insights on the important aspects of high advance ratio flows. A detailed description of the hardware, measurement systems, data acquisition systems and an overview of the test program is given by Norman et al. [58] and a more detailed description of the high advance ratio tests by Datta et al. [59]. The following is a brief summary.

Table 4.1: UH-60A blade properties.

100% RPM	258
Radius (ft)	26.833
Solidity	0.0826
Lock No. (γ)	7.0
Airfoil	SC1095 SC1094r8
Twist	-16°
Sweep	20° at 93%

The UH-60A rotor was mounted on the NFAC Large Rotor Test Apparatus (LRTA) as shown in fig. 4.3. The instrumented rotor blades were the same as those used during the airloads flight tests of the UH-60A Black Hawk [57] although they were refurbished for the wind tunnel test. Important properties of the rotor are listed in table 4.1 and a plan view has already been shown in fig. 4.15a. The instrumentation included; hub forces and moments and shaft power; pressure transducers placed between 22.5% and 99% spanwise stations (only the 22.5%, 86.5% and 92% stations survived the test); strain gauges were placed between 13.5% and 90% stations to gather blade bending information and pitch link loads were measured.

The rotor was set to 100%, 65% and 40% of nominal operating rotational speed (258 RPM) to achieve tip Mach number of 0.65, 0.42 and 0.26 respectively. The maximum tunnel speed was 175 knots to provide an advance ratio of 1.0 for

the 40% RPM cases. The rotor shaft angle was set to 0°, 2° and 4° (positive aft). For each test condition, the collective was set and the cyclics were used to trim the rotor to zero first harmonic flapping at the blade root. From the tunnel dimensions a shaft angle correction was derived to account for wind tunnel blockage given by Datta et al. as:

$$\Delta\alpha_s = 8.6101(C_N/\mu^2) \text{ deg} \tag{4.37}$$

The tunnel correction is positive aft and has been applied to the analysis based on the measured, rather than predicted, rotor normal force (C_N).

Table 4.2: Test conditions for the UH-60A tests.

Rotor	UH-60A
RPM Variation	40%
Tunnel runs	91 (0° shaft tilt) and 93,95(4° shaft tilt)
Shaft Angle (Degrees)	0°, 4° (aft)
Wind Speed (knots)	50-175
Advance Ratio	0.3-1.0

Table 4.3: Airload and bending moment comparison points.

Run No.	α_s	μ	θ_0	θ_{1C}	θ_{1S}	C_T/σ	BM	Airloads	PL
9116	0°	0.3	4.0°	1.55°	-3.99°	0.062	50%	92%	×
9125	0°	0.4	6.0°	1.70°	-6.50°	0.072	×	✓	×
9133	0°	0.5	6.0°	0.87°	-7.35°	0.062	50%	92%	×
9145	0°	0.6	7.93°	0.27°	-10.10°	0.062	50%	92%	×
9162	0°	0.9	0.0°	-3.65°	-0.30°	0.020	×	✓	×
9175	0°	1.0	1.94°	-5.11°	-2.73°	0.022	50%	92%	✓
9318	4°	0.4	1.96°	0.65°	-4.02°	0.062	✓	✓	✓
9325	4°	0.5	1.96°	0.13°	-4.81°	0.062	✓	✓	×
9518	4°	0.7	2.96°	-0.82°	-6.85°	0.061	✓	✓	×
9528	4°	0.9	6.16°	-3.12°	-11.62°	0.063	✓	✓	✓

Only a portion of the test data is publicly available, limited to the 40% RPM rotor speed at 0° shaft tilt with a few points at 4° shaft angles. The test conditions

are shown in table 4.2. For these test points, a limited set of performance and trim values are available. Airloads, blade bending moments (BM) and pitch link loads (PL) are available only for the specific cases listed in table 4.3 (✓: indicates 22.5%, 86.5% and 92% stations for the airloads and every 10% for the blade loads). The test points were chosen to match thrust coefficients of $C_T/\sigma \approx 0.062$.

4.3 Performance Results

This section concerns the prediction of rotor performance in terms of thrust, power and drag coefficients and the vehicle trim angles. Once the baseline predictions have been established, the influence of the modifications and corrections to UMARC are investigated. Recall that the baseline analysis includes a single wake trailer at the blade tip, nearwake inflow has a fixed geometry (30° behind the blade) and is ignored in the reverse flow, the root cut-out is at 20% radius, there are no yawed flow corrections and no fuselage to disturb the flow.

4.3.1 Baseline Results

Figure 4.16 shows the comparison of the measured and predicted thrust ($^{C_T}/_{\sigma}$), axial force ($^{C_H}/_{\sigma}$) and power ($^{C_P}/_{\sigma}$) coefficients versus collective and the trim cyclics (θ_{1C}, θ_{1S}) versus thrust for increasing advance ratios (μ = 0.3–1.0). The thrust in fig. 4.16a is under-predicted by the analysis for all advance ratios, although the trends are reasonably well predicted. The thrust sensitivity to collective ($\Delta C_T/\Delta\theta_{75}$) around small collectives is shown in fig. 4.16b. The analysis over predicts the thrust

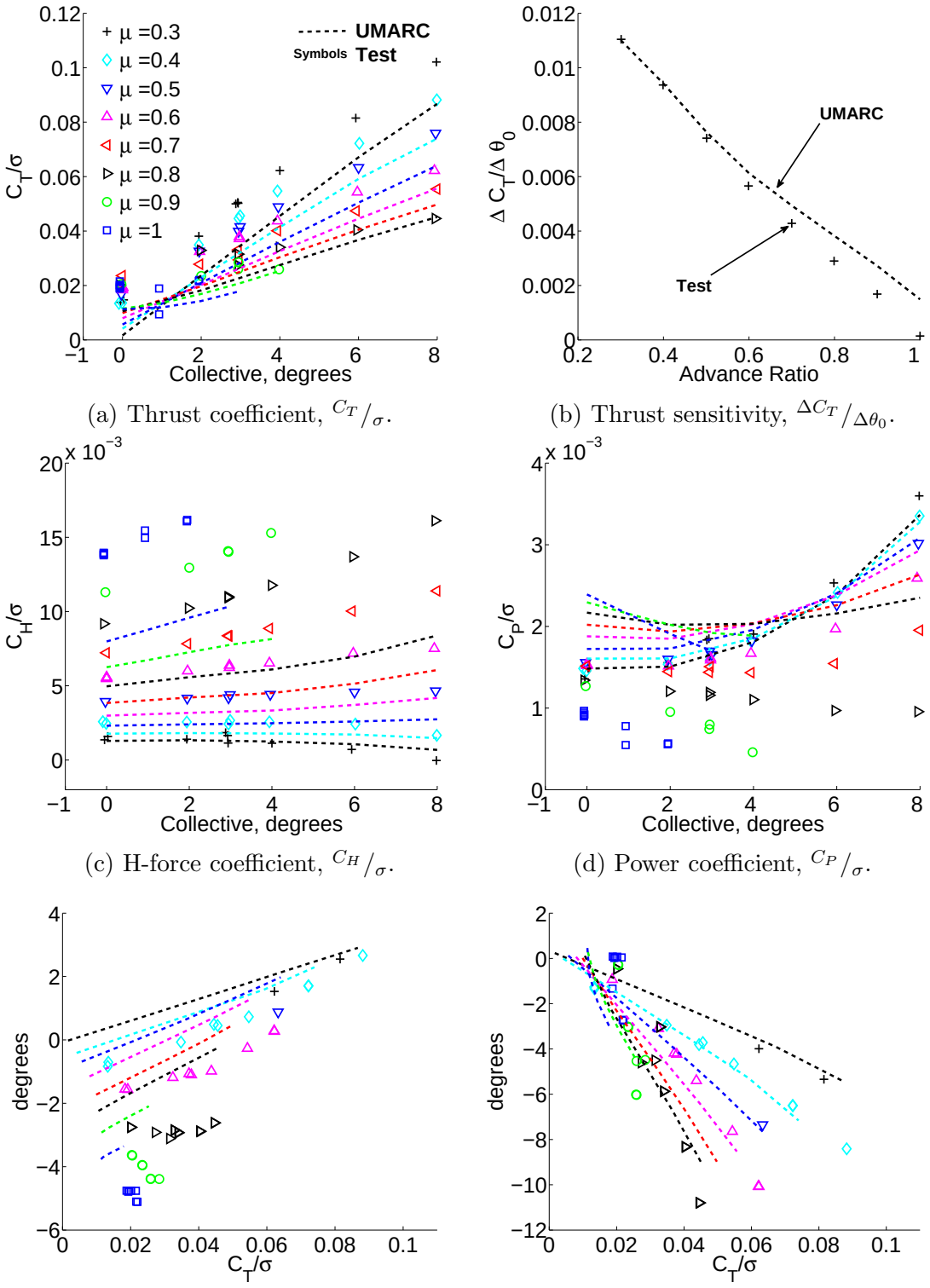

(a) Thrust coefficient, $^{C_T}/_{\sigma}$.

(b) Thrust sensitivity, $^{\Delta C_T}/_{\Delta\theta_0}$.

(c) H-force coefficient, $^{C_H}/_{\sigma}$.

(d) Power coefficient, $^{C_P}/_{\sigma}$.

(e) Lateral cyclic, θ_{1C}.

(f) Longitudinal cyclic, θ_{1S}.

Figure 4.16: Baseline rotor performance and predictions for increasing advance ratio, $M_{tip} = 0.26$, 0° shaft angle (Symbols: Test, - - Analysis).

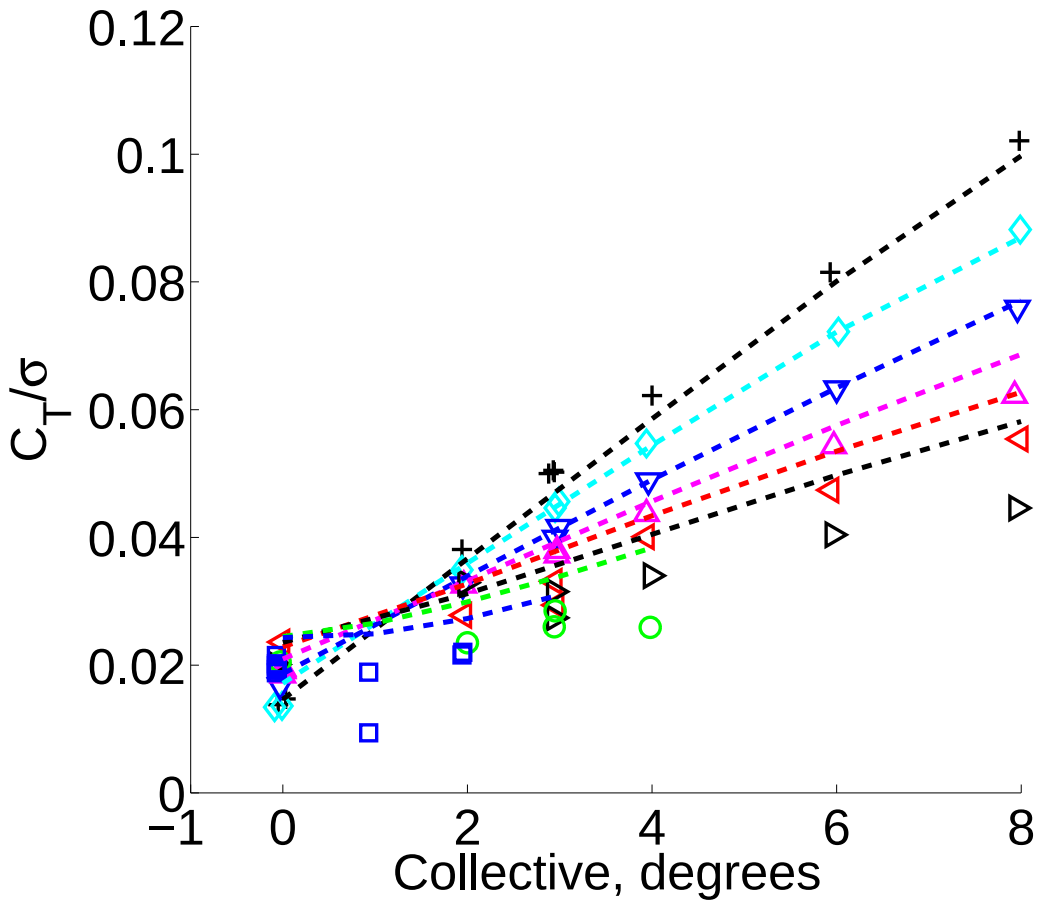

Figure 4.17: Thrust coefficient corrected for offset ($\Delta^{C_T}/_{\sigma} = 0.013$).

sensitivity starting from $\mu = 0.6$ and does not predict the zero sensitivity of thrust to collective at an advance ratio of 1.0. The reason for the thrust offset is not obvious, although this is one of the motivations to investigate the influence of a fuselage on the thrust. Figure 4.17 repeats the thrust prediction with a constant offset added to the analysis of $\Delta^{C_T}/_{\sigma} = 0.013$ (485 lb) to match thrust at 1° collective. With the offset, the thrust for advance ratios 0.3 – 0.5 agree well, but at higher advance ratios the predicted thrust is higher than the test.

The axial force coefficient (C_H) is shown in fig. 4.16c. Other than at $\mu = 0.3$, where the prediction is quite good, the axial force is under-predicted for increasing advance ratios by as much as 30% at $\mu = 1.0$. The trend of the axial force with increasing collective is well predicted including at high advance ratios. The predicted power (fig. 4.16d) agrees well at $\mu = 0.3$ only. For increasing advance ratios, the predicted power shows the correct trend, but there is a significant deviation in magnitude. In particular the measured power at 0° collective decreases slightly with increasing advance ratio, but the analysis predicts increasing power. At advance ratios of 0.9 and 1.0, the power is decreasing with increasing collective but autorotation is not achieved. The poor prediction of power at high advance ratios is a significant issue that has been shown other analyses, both comprehensive analysis ([100, 101]) and CFD-CSD ([68]). The lateral cyclic is predicted with a small offset at $\mu = 0.3$ and 0.4 but the analysis does not predict the change in slope at high advance ratios. Longitudinal cyclic is well predicted as a function of thrust at all advance ratios.

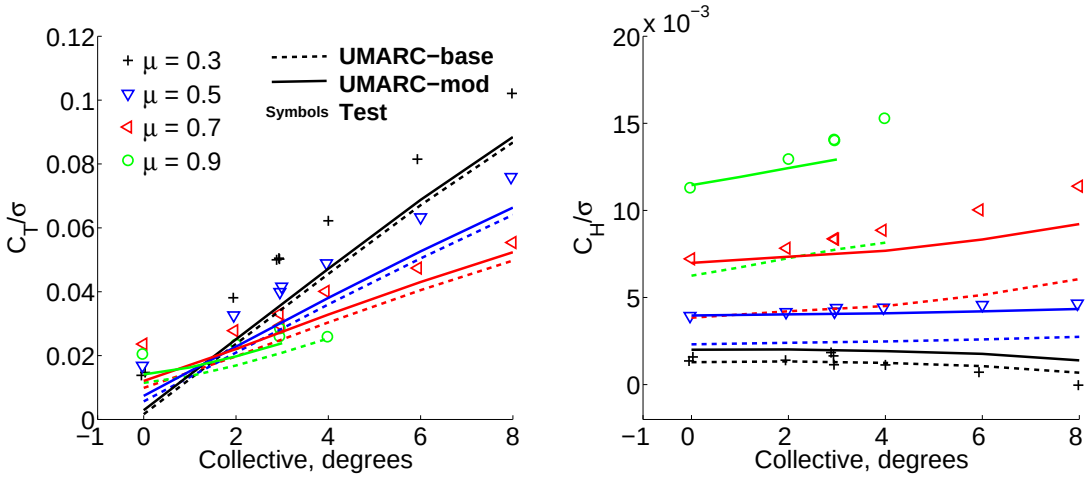

(a) Thrust coefficient, C_T/σ.

(b) H-force coefficient, C_H/σ.

(c) Power coefficient, C_P/σ.

Figure 4.18: Effect of root cut-out model on performance predictions, $M_{tip} = 0.26$, 0° shaft angle (Symbols: Test, - - Baseline analysis, – Modified analysis).

4.3.2 Root Cut-Out Model

The effect of the root cut-out model on performance is shown in fig. 4.18. A drag coefficient of $c_d = 0.4$ was used between 8% – 20% blade radius based on best fit at 0° collective. The lift coefficient on the non-aerodynamic blade between 13% – 20% was corrected to 50% of the table look-up value. An improved axial force correlation is achieved as expected; although, this is primarily at 0° collective and the trend with increasing collective has a small under-prediction. There is a small effect of the root cut-out model on the thrust that grows more apparent at high advance ratios. The trim condition is nominally unchanged by the extra blade area. Moving the blade root further inboard, reduces the edge effects (downwash) from the inboard blade edge allowing increased lift on the inboard blade (this is discussed further in the discussion of sectional loads). The edge effects of the blade is captured with the nearwake model as a result of the blade root at 13% radius instead of 20% radius. The predicted shaft power increases somewhat because of the increased drag and the discrepancy with test remains unresolved. Overall, the drag in the root cut-out is an important element in determining axial force and results in higher lift prediction at high advance ratios.

4.3.3 Fuselage Model

Figure 4.19 shows the performance impact of including the fuselage model below the rotor. The left hand results include only the upwash over the nose assuming that the hub disrupts downwash behind the rotor. The right hand results are in-

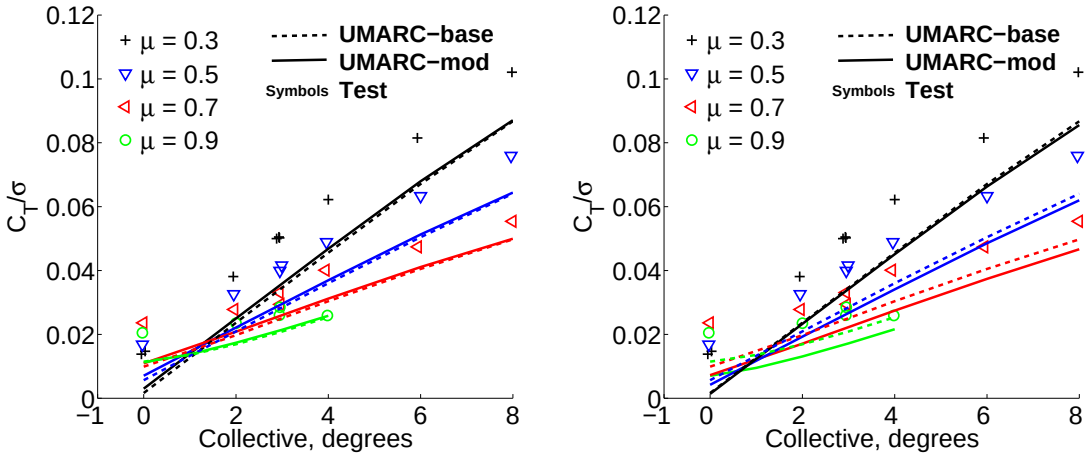

(a) Thrust coefficient, $^{C_T}/_{\sigma}$.

(b) Thrust coefficient*, $^{C_T}/_{\sigma}$.

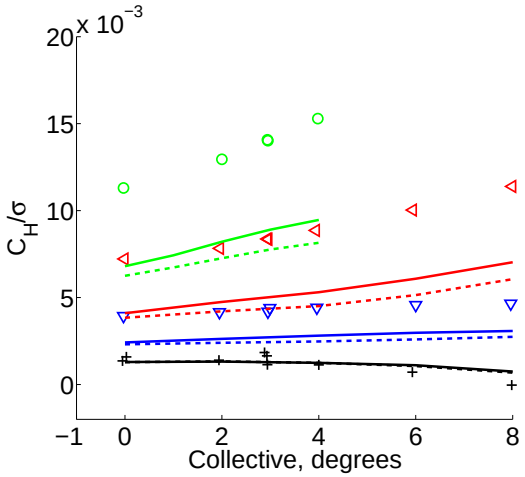

(c) H-force coefficient, $^{C_H}/_{\sigma}$.

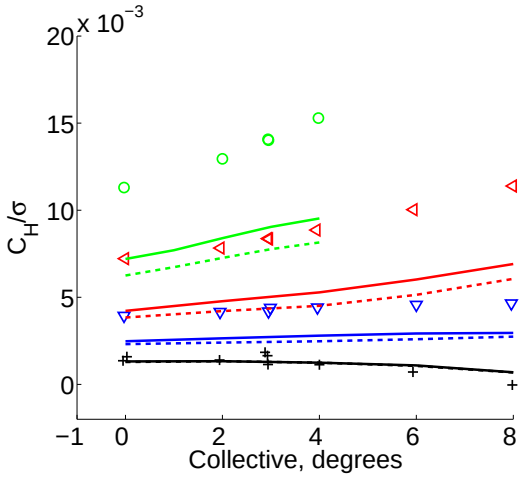

(d) H-force coefficient*, $^{C_H}/_{\sigma}$.

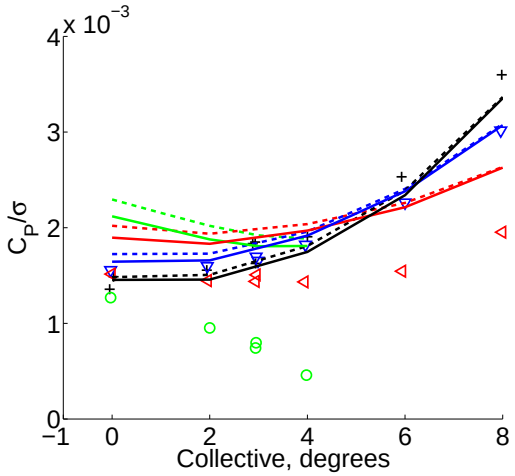

(e) Power coefficient, $^{C_P}/_{\sigma}$.

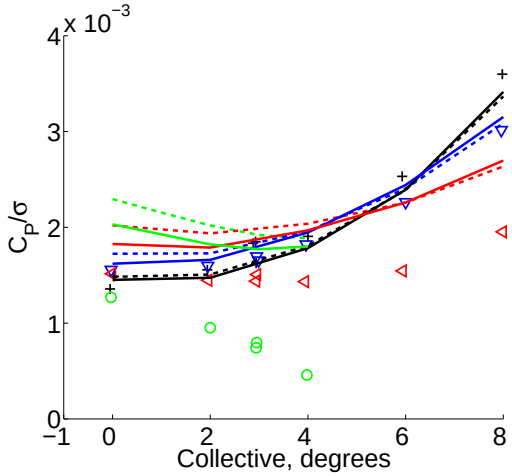

(f) Power coefficient*, $^{C_P}/_{\sigma}$.

Figure 4.19: Effect of fuselage on performance predictions, $M_{tip} = 0.26$, 0° shaft angle (Symbols: Test, - -: Baseline analysis, –: Modified analysis, left-hand figures are upwash only (front of rotor), right-hand figures (*) are complete fuselage model).

(a) Angle of attack, degrees.

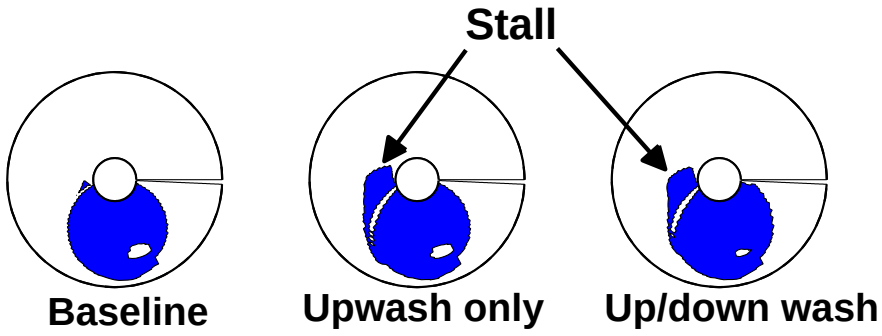

(b) Lift stall.

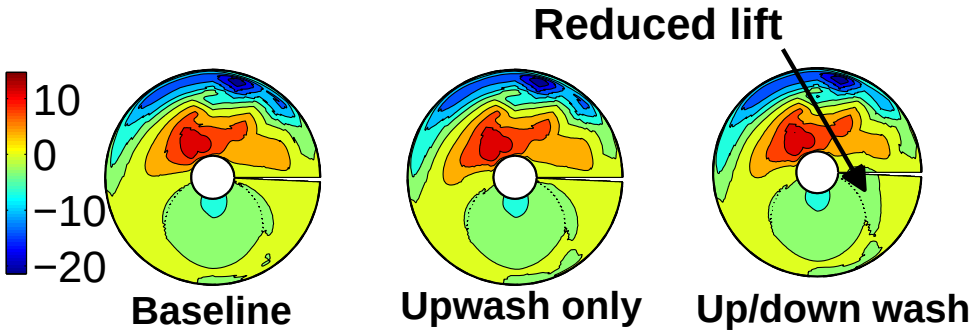

(c) Normal force, $\mathrm{lb.s^{-1}/ft}$.

Figure 4.20: Contours of the effect of the fuselage on angle of attack and power (upwash only), $\mu = 0.9$, 4° collective, 0° shaft angle).

cluding the complete fuselage model. The motivation for including the fuselage is to improve thrust prediction; however the effect on thrust is negative and small at low advance ratios for the full fuselage model. At $\mu = 1.0$, the full fuselage model significantly decreases thrust compared to the baseline. The axial force and the slope with increasing collective increase somewhat, but full fuselage model shows no additional effect. The power decreases for small collectives, but the difference tends to be negligible as the collective increases. The decrease in power is somewhat larger for the full fuselage model, but a discrepancy with measurements remains at high advance ratios.

The fuselage upwash acts to increase the angle of attack over the front of the rotor and decrease it on the aft rotor. Figure 4.20 shows the angle of attack, stall and normal force contours for the baseline, upwash only and full fuselage models. The angle of attack on the front rotor increases due to the upwash; however, lateral cyclic corrects for this to maintain trim (θ_{1C} = -2.09 $\rightarrow$ -1.71 $\rightarrow$ -1.29 respectively) and the change in angle of attack and lift is minimized. Near the root, the blade stalls due to the low dynamic pressure and high twist. The full fuselage model also has downwash on the aft rotor, which decreases angle of attack and reduces lift. Downwash on the aft rotor determines the final thrust response of the rotor. The power reduction is because the rotor is producing less lift on the aft rotor.

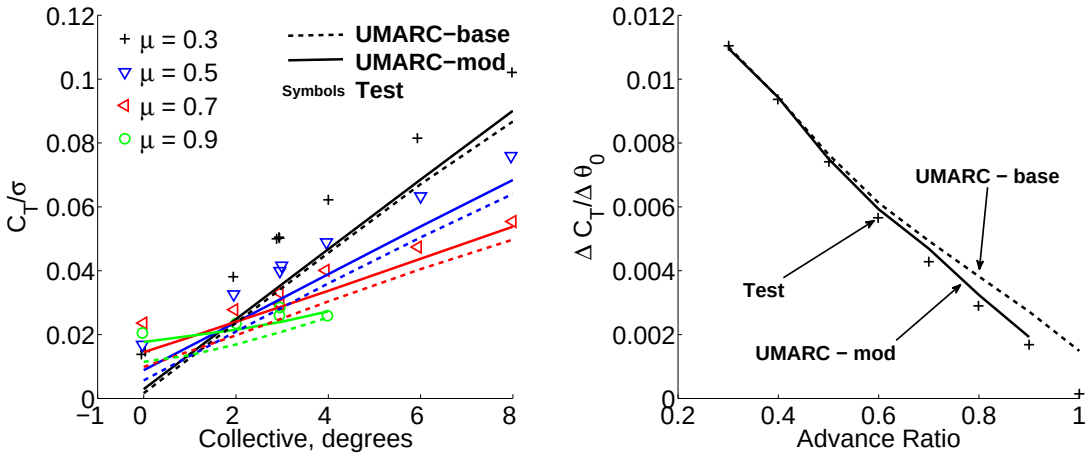

(a) Thrust coefficient, C_T/σ.

(b) Thrust sensitivity, $\Delta C_T/\Delta\theta_0$.

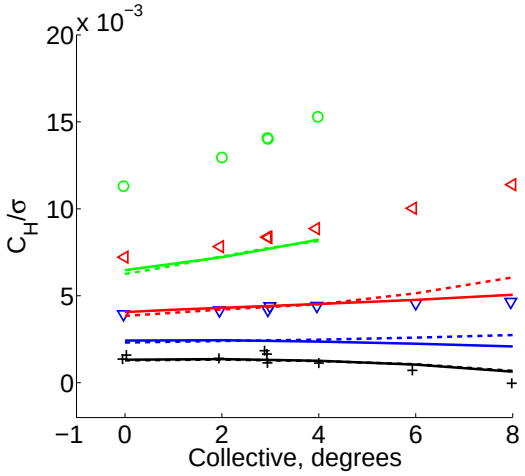

(c) H-force coefficient, C_H/σ.

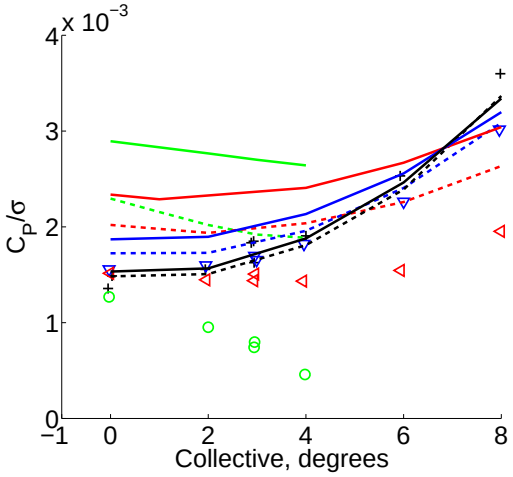

(d) Power coefficient, C_P/σ.

Figure 4.21: Effect of yawed flow corrections on performance predictions, $M_{tip} = 0.26$, 0° shaft angle (Symbols: Test, - -: Baseline analysis, –: Modified analysis).

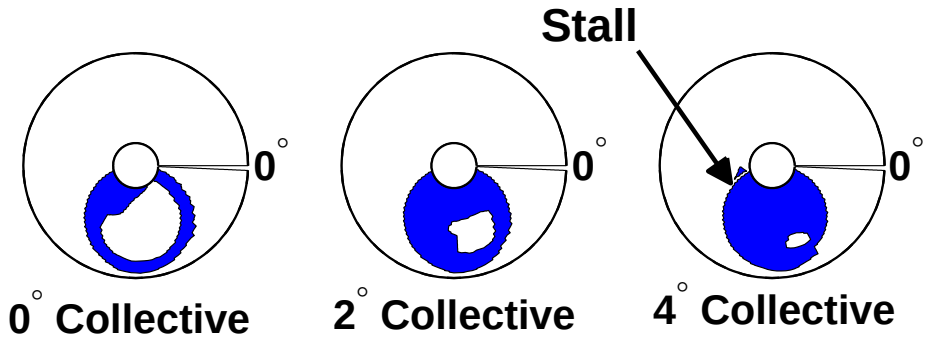

(a) Baseline analysis.

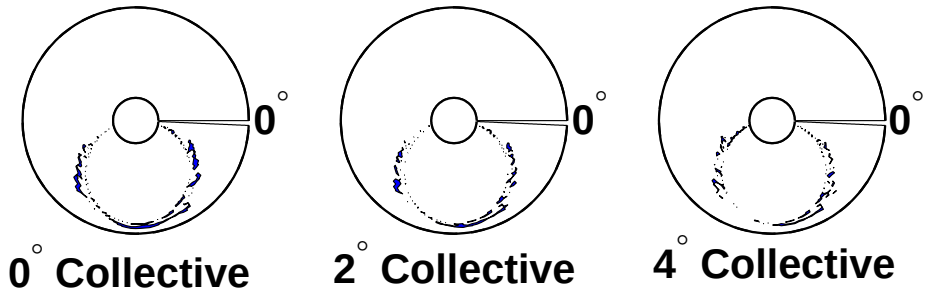

(b) Stall delayed by yawed flow correction.

Figure 4.22: Contours of the effect of the yawed flow corrections on stall, $\mu = 0.9$, 0°–4° collective, 0° shaft angle).

4.3.4 Yawed Flow Corrections

The influence of the yawed flow correction on performance predictions is shown in fig. 4.21. Large radial flow angles are a high advance ratio phenomena and this is shown in the results. The thrust prediction is unaffected at $\mu = 0.3$ but the predicted thrust increases relative to the baseline with increasing advance ratio because of yawed flow corrections. The motivation for the yawed flow corrections was to delay stall at high advance ratio (approaching 1.0) and improve the prediction of thrust sensitivity to collective. Figure 4.21b shows that the thrust sensitivity at high advance ratios is now well predicted with the yawed flow model. Figure 4.22 shows the stall contours for increasing collective with and without yawed flow corrections at $\mu = 0.9$. The reverse flow region remains unstalled at each collective. Reverse flow stall determines the thrust slope at high advance ratios and is crucial in determining thrust reversal (negative thrust for increasing collective), which is discussed in further detail in the next chapter.

Rotor axial force is not significantly changed because the yawed flow corrections to drag are approximately symmetric. Predicted shaft power increases significantly due to the increased drag coefficients on the yawed sections.

4.3.5 Nearwake in Reverse Flow

Including the nearwake inflow in the analysis, shown in fig. 4.23, has minimal effect until high advance ratio, $\mu > 0.9$. It has already been shown that the nearwake inflow decreases the angle of attack in the reverse flow at the blade root. The lift in

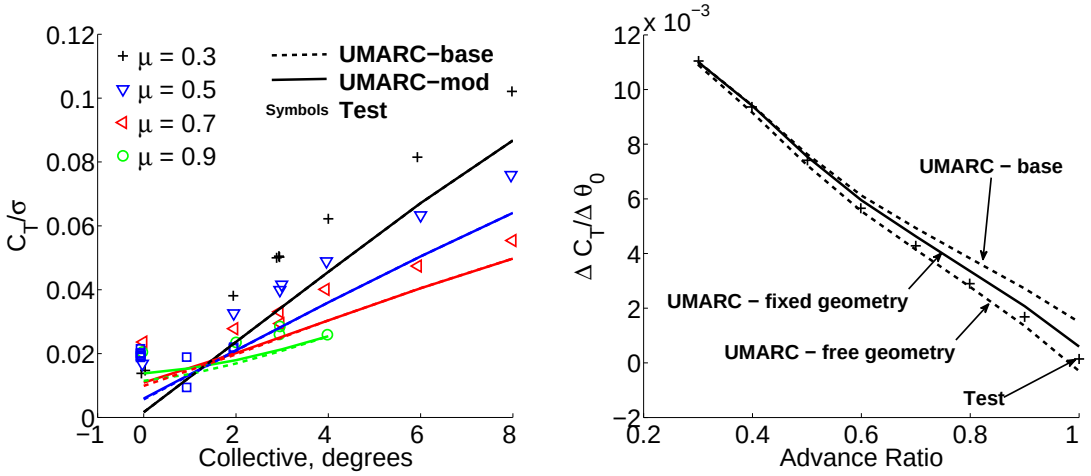

(a) Thrust coefficient, C_T/σ.

(b) Thrust sensitivity, $\Delta C_T/\Delta\theta_0$.

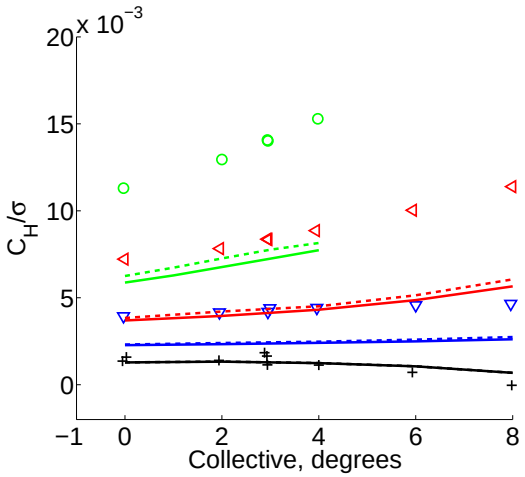

(c) H-force coefficient, C_H/σ.

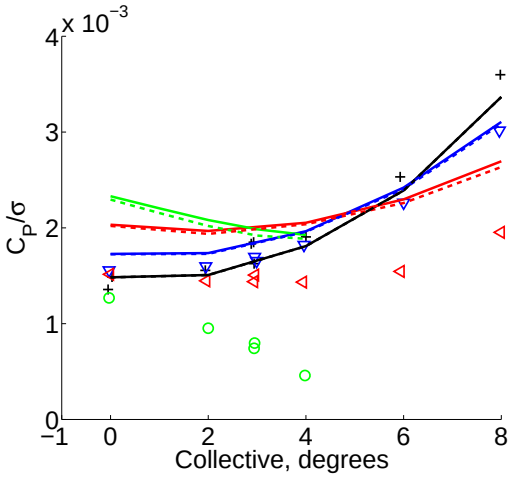

(d) Power coefficient, C_P/σ.

Figure 4.23: Effect of reverse flow nearwake inflow on performance predictions, M_{tip} = 0.26, 0° shaft angle (Symbols: Test, - -: Baseline analysis, –: Modified analysis).

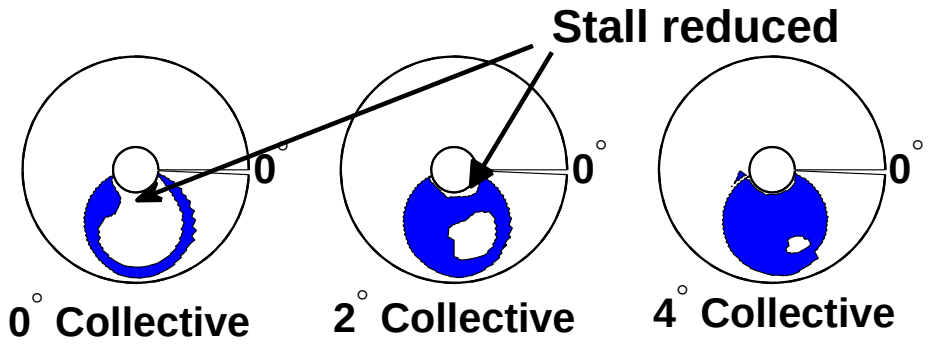

(a) Fixed nearwake geometry in the reverse flow.

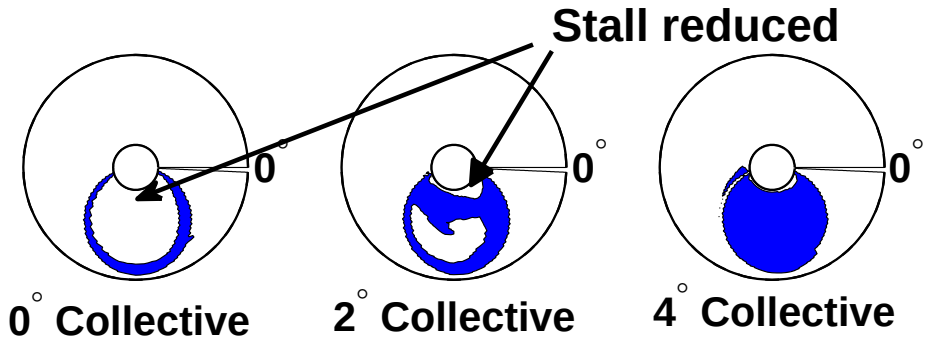

(b) Reverse flow nearwake deformed by freestream.

Figure 4.24: Contours of the effect of nearwake in the reverse flow on stall, $\mu = 0.9$, 0°–4° collective, 0° shaft angle).

the reverse flow, and hence the circulation and inflow, is small until a high enough advance ratio is reached for it to affect rotor thrust. This occurs around $\mu = 0.8$. Decreasing the angle of attack in the reverse flow region reduces stall and the thrust sensitivity to collective gives better correlation with the test (fig. 4.23b). The change in thrust slope is primarily affected for 0° and 2° collective, thereafter the rotor continues to stall as before. Figure 4.23b shows the thrust sensitivity for both the fixed nearwake geometry and the nearwake deformed by the freestream. The deformed nearwake model compares better to the test. The stall maps in fig. 4.24 (compared to the baseline in fig. 4.22a) show that the deformed nearwake reduces the stall region more than the fixed nearwake, particularly when the blade enters the reverse flow. This is because the nearwake trailers sweep acutely to the blade and have an increased influence on the blade loads. Both the fixed geometry and deformed nearwake are fully stalled by 4° collective. There is nearly no effect of reverse flow nearwake on the axial force and the discrepancy in the power prediction remains.

4.3.6 Wake Trailers

4.3.6.1 Dual Wake Trailers

Dual wake trailers are important when there is a change in sign of lift along the span, such as negative lift near the blade tip on twisted blades. Instead of assigning the peak blade circulation (outboard of 50% radius) to the blade tip wake, the dual trailer model assigns only the negative circulation to the tip wake and sheds the

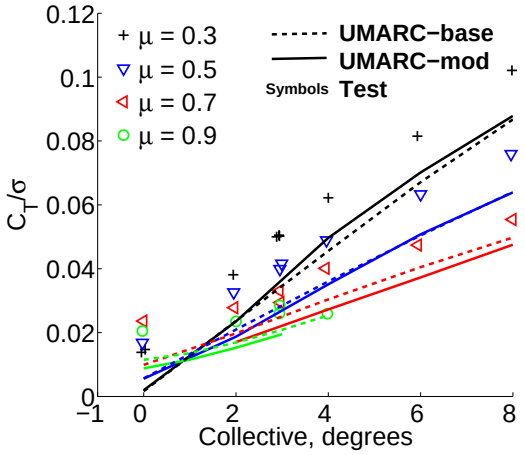

(a) Thrust coefficient, C_T/σ.

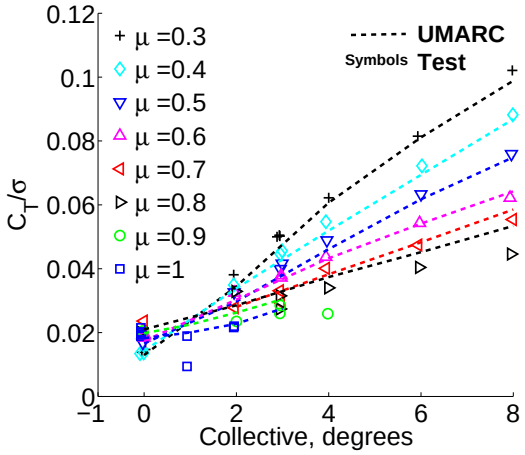

(b) Thrust coefficient + $\Delta C_T/\sigma = 0.011$.

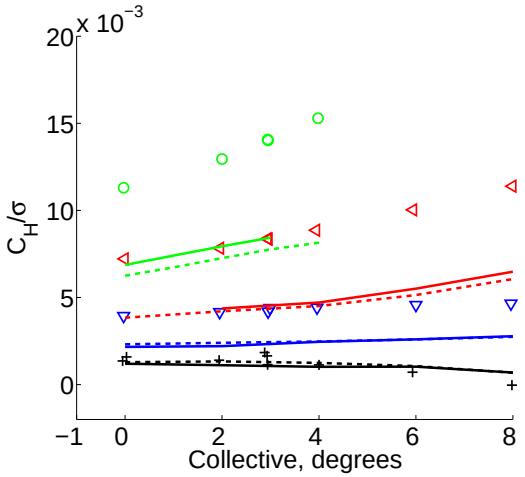

(c) H-force coefficient, C_H/σ.

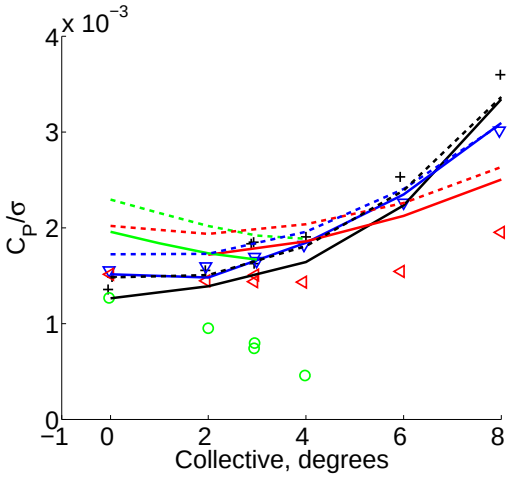

(d) Power coefficient, C_P/σ.

Figure 4.25: Effect of dual wake trailers on performance predictions, $M_{tip} = 0.26$, 0° shaft angle (Symbols: Test, - -: Baseline analysis, –: Modified analysis).

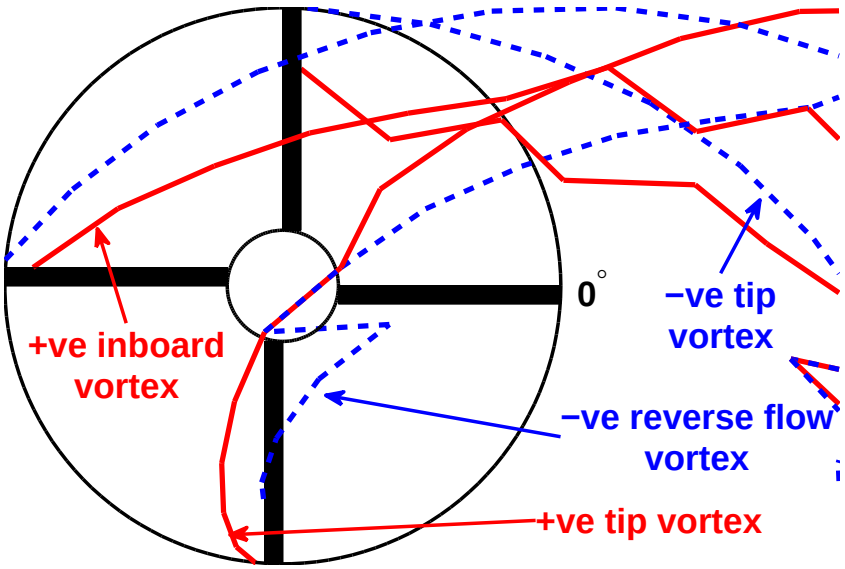

(a) Dual trailer wake system.

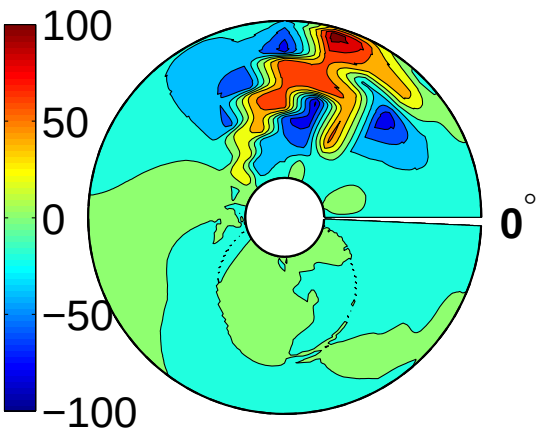

(b) Change in normal force, lb/ft.

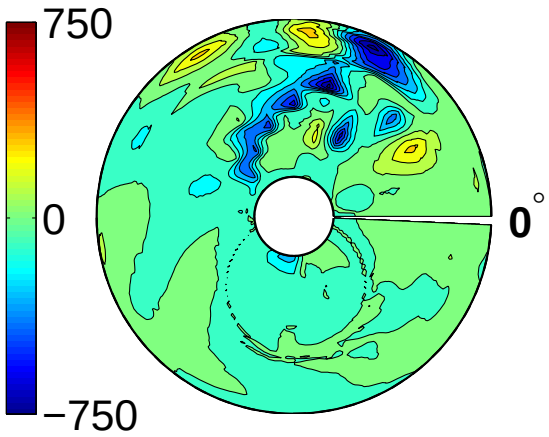

(c) Change in power, ft.lb.s^{-1}/ft.

Figure 4.26: Dual wake system and contours of the change in normal force and power from dual wake trailer system, $\mu = 0.7$, 4° collective, 0° shaft angle).

inboard circulation (positive) at the point when the circulation is zero. Dual wake trailers are important for predicting the sectional airloads, shown later.

Performance predictions using the dual wake trailer are shown in fig. 4.25. The effect of dual trailers on the predicted thrust is small but the trend with increasing collectives is generally improved. Comparison to the test data (with the offset, $\Delta^{C_T}/_{\sigma} = 0.011$) is shown in fig. 4.25b and shows significant improvements compared to the baseline. Axial force is not significantly affected. The dual trailer model predicts lower shaft power and gives better agreement with the test but still not satisfactory. Figure 4.26 shows the dual wake trailer system and contours of the change in thrust and power. The trailer system is complex and impacts most strongly on the advancing rotor. The change in normal force is predominately a shift of lift onto the advancing rotor tip region. This is caused by the counter rotating trailed wake from the leading blade at 180° azimuth. The longitudinal cyclic is more negative for the dual trailer model (-4.5° to -4.8°) to maintain trim and results in a net decrease in thrust on the advancing rotor. The change in power follows the pattern of the change in lift and suggests that the induced contribution to power is reduced for low advance ratios. The effect of including a trailer from the edge of the reverse flow had no impact on performance because the retreating side trailers are swept aft before interacting with the rotor.

4.3.6.2 Dual Wake Trailers and Root Trailer

The root trailer is modeled together with the dual wake trailers for the performance predictions in fig. 4.27. The thrust prediction increases significantly with

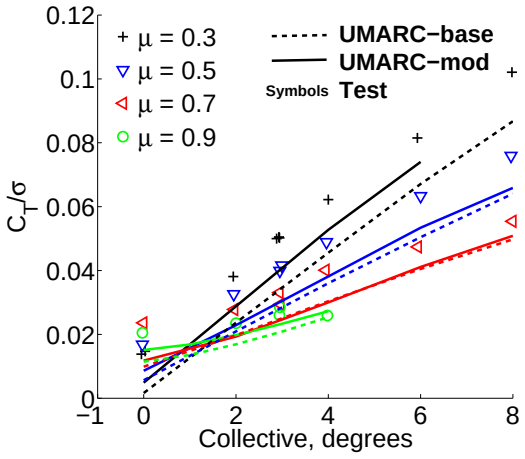

(a) Thrust coefficient, C_T/σ.

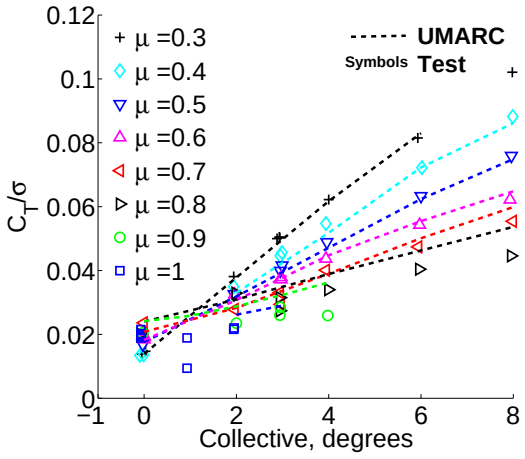

(b) Thrust coefficient + $\Delta C_T/\sigma = 0.009$.

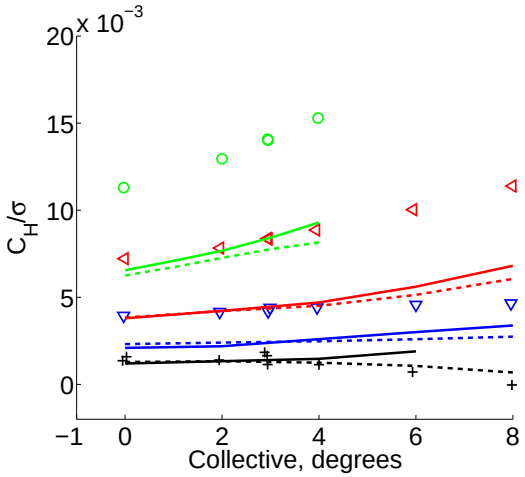

(c) H-force coefficient, C_H/σ.

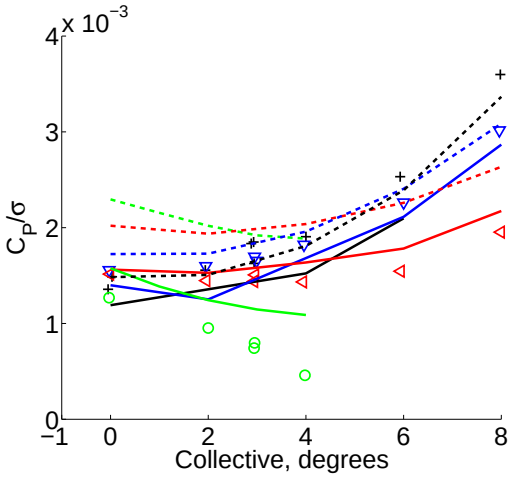

(d) Power coefficient, C_P/σ.

Figure 4.27: Effect of dual wake trailers and root trailer on performance predictions, $M_{tip} = 0.26$, 0° shaft angle (Symbols: Test, - -: Baseline analysis, –: Modified analysis).

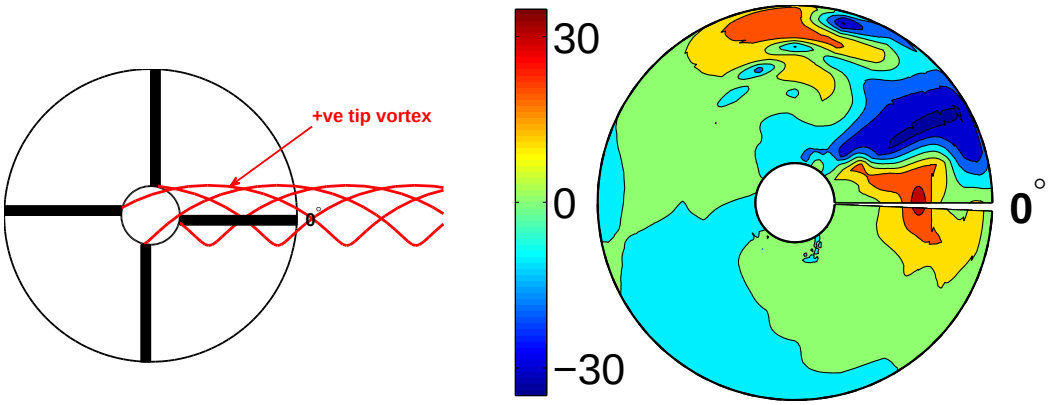

(a) Root trailer wake system (Tip wake hidden).

(b) Change in normal force, lb/ft.

Figure 4.28: Root wake system and contours of the change in normal force, $\mu = 0.3$, 4° collective, 0° shaft angle).

the addition of the root trailer, predominantly at low advance ratios, reducing to no change at $\mu = 0.7$. The global effect on thrust is to decrease the thrust offset to about 330 lb from 500 lb for the baseline. The axial force is increased over the baseline at higher collectives. The shaft power is significantly reduced and gives an overall improved correlation with the test, which is a significant improvement.

The root wake trailers and a contour of the change in normal force (relative to the dual wake trailer system) are shown in fig. 4.28 for the low advance ratio case ($\mu = 0.3$) where the largest increase in thrust is shown. The change in normal force is an increase on the aft rotor near the advancing tip and a decrease around 30° azimuth. Because of high twist, the advancing inboard rotor produces the majority of advancing side lift, which results in a high circulation strength of the root trailer. The trailer interacts with the aft blade to cause the reduction in lift around 30° azimuth. The net increase in rotor thrust is because less longitudinal cyclic (-4.4° to -2.7°) is required to trim lateral moments, allowing for more advancing side lift.

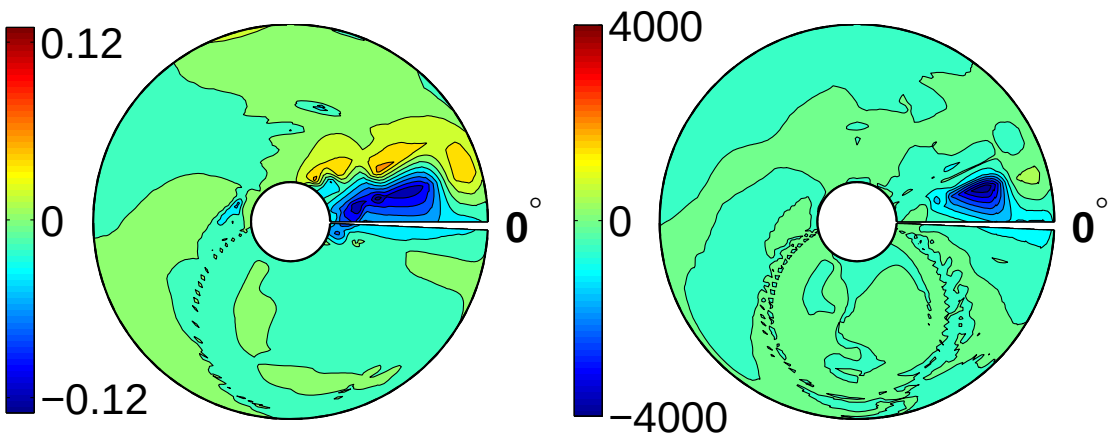

(a) Change in inflow velocity ($\Lambda\Omega R$). (b) Change in shaft power, ft.lb.s^{-1}/ft.

Figure 4.29: Contours of the change in normal force and power from dual wake trailer system, $\mu = 0.9$, 4° collective, 0° shaft angle)

The significant improvement in shaft power prediction comes from a reduction in induced power on the rear of the rotor disk. Figure 4.29 shows the changes in both the inflow distribution and the shaft power distribution after the addition of the root wake trailer model (the reference is now the dual tip trailer model rather than the original baseline). The root vortex system creates an upwash (negative inflow means upwash) on the rear of the rotor disk (fig. 4.29a), which brings about the reduction in induced power and shaft power in that immediate region while minimizing any changes elsewhere.

Table 4.4: Summary of UMARC modifications for the UH-60A test.

Root cut-out Drag	8%–13%: $C_D = 0.4$, 13%–20%: $C_D = 0.3$
Root cut-out Lift	13%–20%: $L_{shank} = 0.5 L_{\text{clean section}}$
Fuselage model	$R_0 = 0.06$R, a = 0.5R, h = 0.25R
Yawed flow	not included
Nearwake	Deformed by freestream, included in reverse flow
Wake trailer	Dual, including from edge of reverse flow
Root wake trailer	Yes, from 13%R

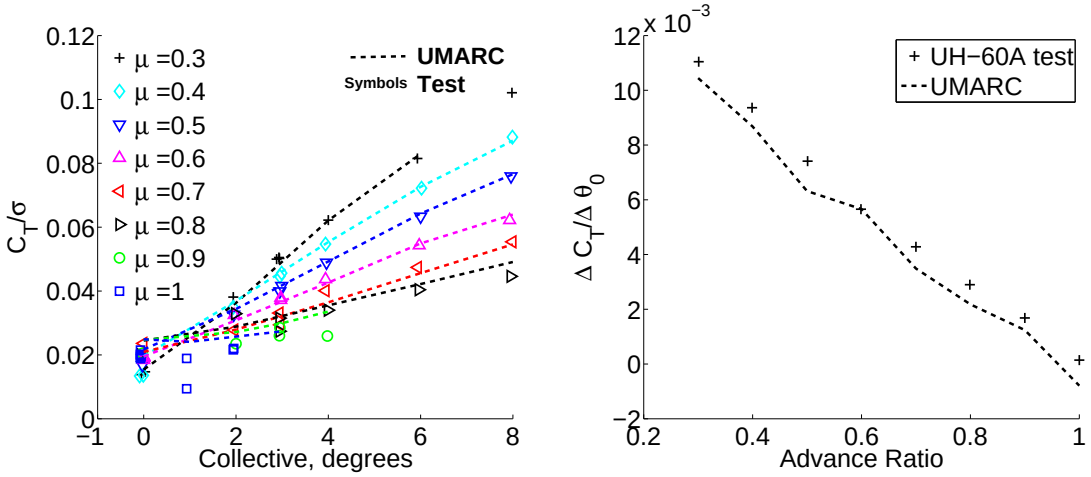

(a) Thrust coefficient, C_T/σ.

(b) Thrust sensitivity, $\Delta C_T/\Delta\theta_0$.

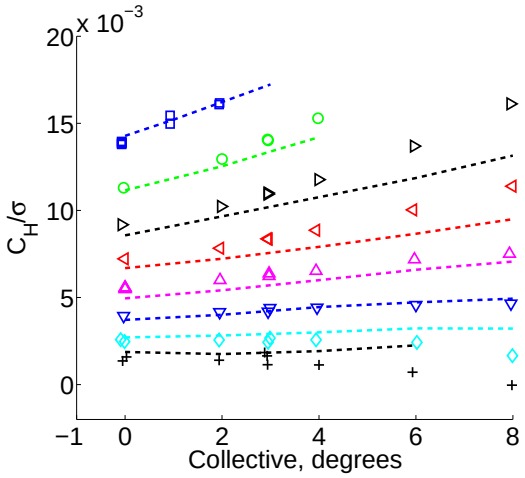

(c) H-force coefficient, C_H/σ.

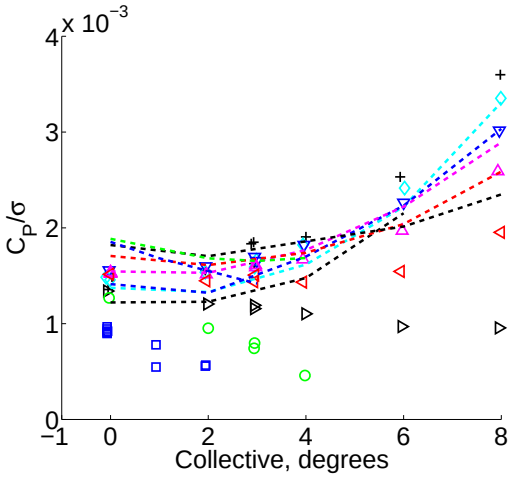

(d) Power coefficient, C_P/σ.

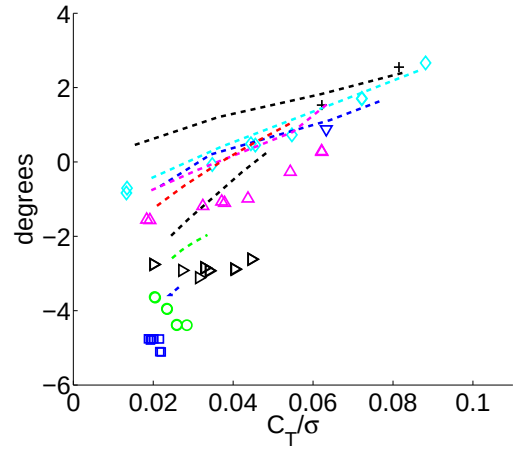

(e) Lateral cyclic, θ_{1C}.

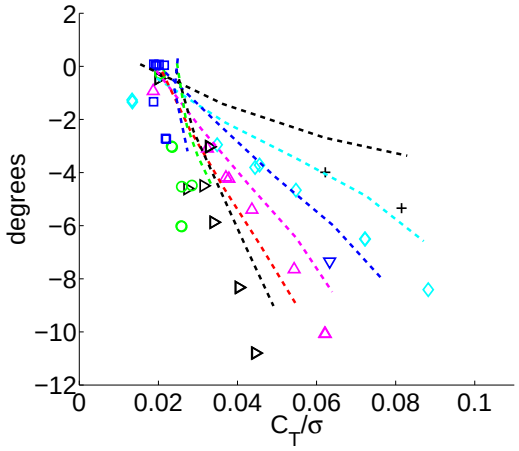

(f) Longitudinal cyclic, θ_{1S}.

Figure 4.30: Rotor performance and predictions with UMARC modifications, for increasing advance ratio, $M_{tip} = 0.26$, 0° shaft angle (Symbols: Test, - - Analysis).

4.3.7 Summary of Performance Prediction

The final performance predictions in fig. 4.30 include all of the modifications to UMARC (excluding yawed flow corrections). These are summarized in table 4.4. None of the modifications accounted for the general under-prediction of thrust and a uniform increment to thrust of $\Delta^{C_T}/_{\sigma} = 0.011$ has been added to the all the predictions. Compared to the baseline results (see fig. 4.16), the prediction of thrust, axial force and power are all improved, while the trim cyclic prediction is somewhat worse. Modeling the root cut-out drag is important for predicting axial force; although, a physical model rather than an empirical fit is warranted. The fuselage has negligible effect on thrust and axial force but the fuselage upwash could reduce shaft power somewhat. Yawed flow corrections improved the slope of thrust against collective at high advance ratios by delaying retreating side stall but it also significantly increased power required. The yawed flow corrections could not be consistently trimmed together with the remaining UMARC modifications and is not included. Including nearwake in the reverse flow improves high advance ratio thrust prediction by reducing reverse flow stall, particularly at the root cut-out. Allowing the nearwake to deform with the freestream gave a small improvement in thrust slope at high advance ratios. Modeling the dual wake trailers was important for capturing the thrust trends at high collectives for all advance ratios. Including root trailers significantly reduced the predicted power (in better agreement with the test) and generally improved predicted thrust. However, the root trailers are the cause for degraded longitudinal cyclic prediction at low advance ratios. The final prediction

of power remains unsatisfactory, despite the improvements available from adding the root wake. This is because the effects of the root trailer are overcome by the increased power predicted by the yawed flow corrections.

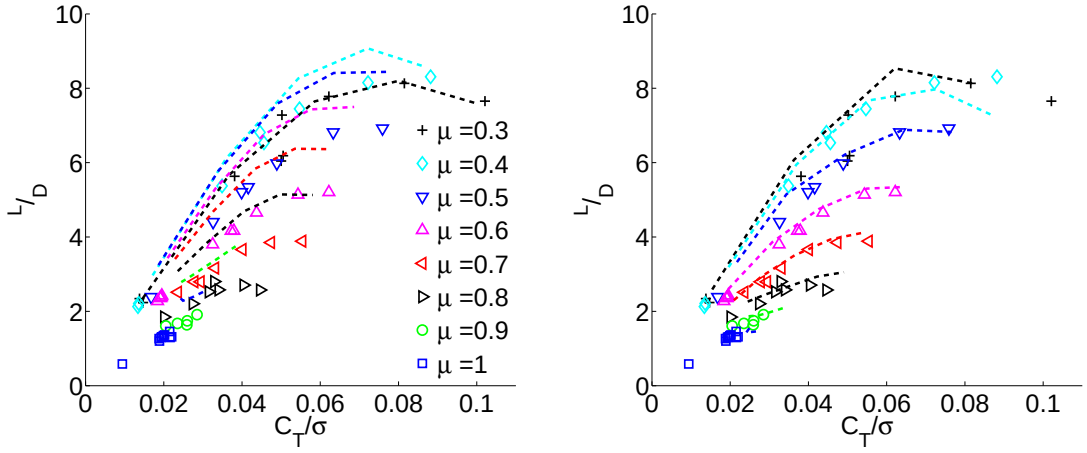

(a) Baseline UMARC prediction, $\Delta^{C_T}/_{\sigma}$ = 0.013.

(b) Modified UMARC prediction, $\Delta^{C_T}/_{\sigma}$ = 0.011.

Figure 4.31: UH-60A lift-to-drag ratio with baseline and modified predictions, M_{tip} = 0.26, 0° shaft angle (Symbols: Test, - - Analysis).

Finally, the rotor lift-to-drag ratio with the UMARC prediction is compared in fig. 4.31 for the baseline and modified analysis. The lift-to-drag ratio combines the influence of thrust, axial force and shaft power to describe the overall rotor efficiency. This result summarizes the improvements from the newly implemented UMARC modifications. Both predictions include a thrust offset based on best correlation at 1° collective. The modifications to UMARC give a very good prediction of rotor efficiency at all advance ratios. The modifications to UMARC also summarize the minimum model fidelity required to accurately predict high advance ratio performance. Assumptions about the root drag are key to validating the result, and the source of the thrust offset is not yet identified. However the improvements in

the predicted thrust trends and shaft power prediction remain significant.

4.4 Airloads Prediction

The UH-60A slowed rotor test to high advance ratios is unique from previous high advance ratio tests because of airloads measurements from pressure transducers installed at several radial stations along the span. The previous section discussed the global performance of the rotor at high advance ratios, which can be somewhat insensitive to the details of the airloads. The airloads are useful both for validating the details of the aerodynamic model and for understanding the blade bending loads and the vibratory loads transferred to the fixed frame. The blade loads are discussed in the final section.

There are a limited number of test conditions for which the airloads data is available, listed in table 4.3. Comparisons are made for selected cases where the analysis is trimmed to match collective, but the cyclics and rotor thrust generally differ as determined by trim. The approach is to introduce the baseline predictions using the simplified UMARC analysis before introducing the modeling improvements important at high advance ratios by studying specific test points.

4.4.1 Baseline Sectional Airloads

The sectional normal force at 92% radial station at a selection of advance ratios and shaft angles are shown in fig. 4.32, and at 22.5% radius in fig. 4.33. The force coefficients are scaled by the local Mach number squared to account for

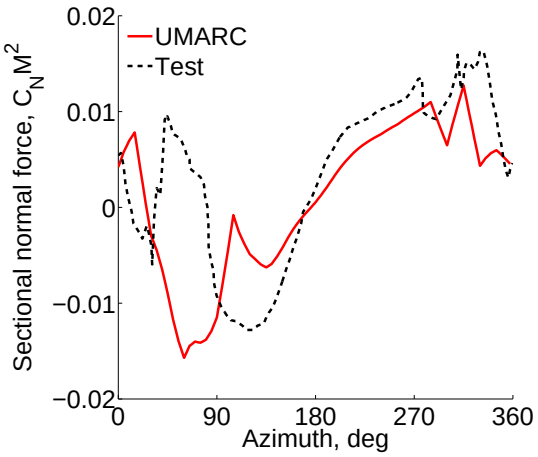

(a) $\mu = 0.3$, $\theta_0 = 4.0°$, $\alpha_s = 0°$.

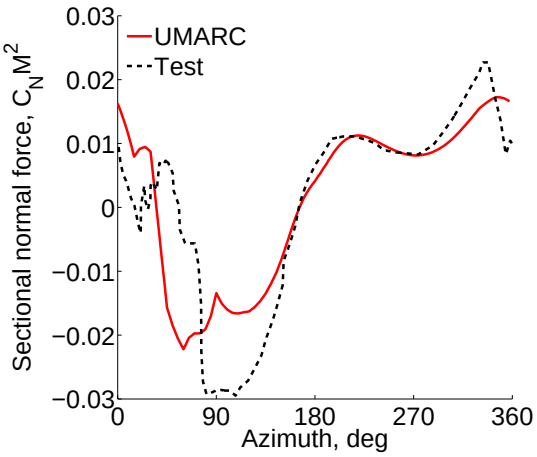

(b) $\mu = 0.5$, $\theta_0 = 6.0°$, $\alpha_s = 0°$.

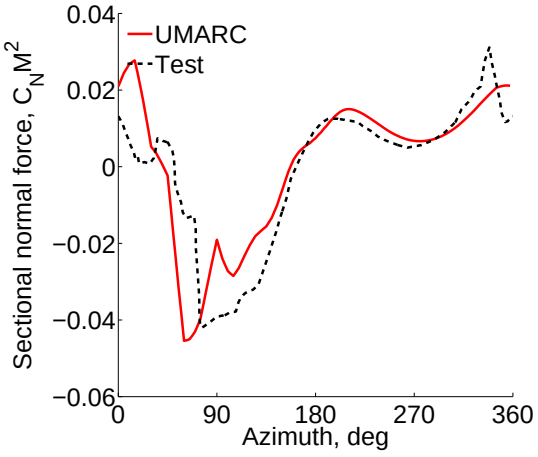

(c) $\mu = 0.6$, $\theta_0 = 7.93°$, $\alpha_s = 0°$.

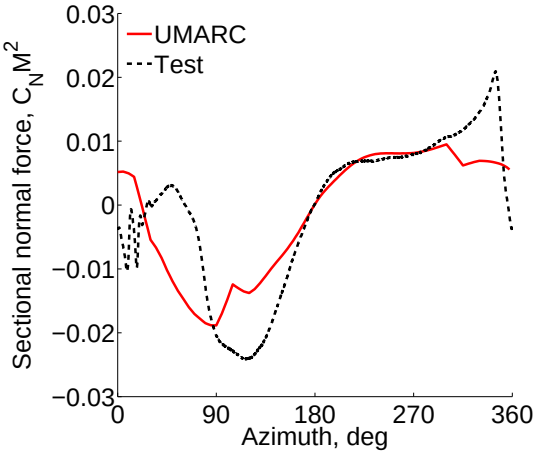

(d) $\mu = 0.4$, $\theta_0 = 1.96°$, $\alpha_s = 4°$.

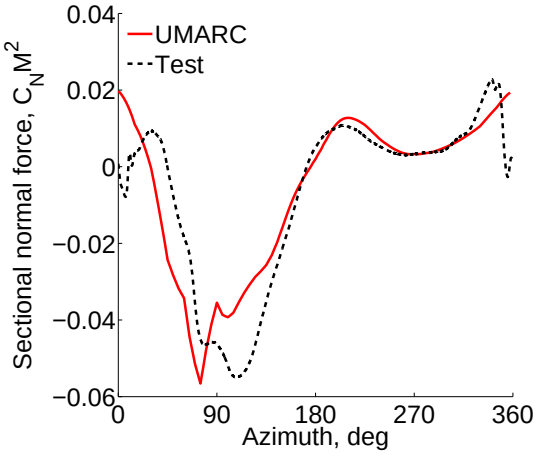

(e) $\mu = 0.7$, $\theta_0 = 2.96°$, $\alpha_s = 4°$.

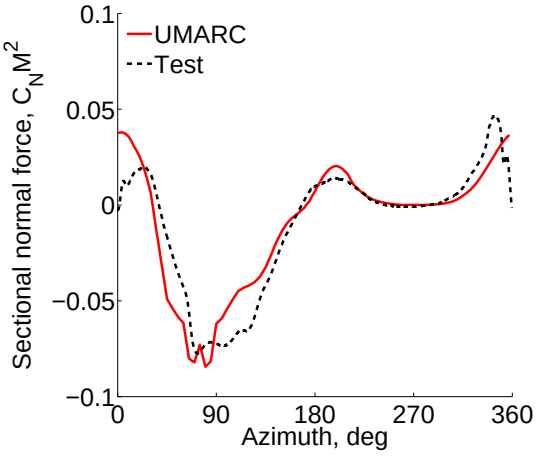

(f) $\mu = 0.9$, $\theta_0 = 6.16°$, $\alpha_s = 4°$.

Figure 4.32: Sectional normal force ($C_N M^2$), r/R = 92%. $C_T/\sigma_{test} = 0.062$.

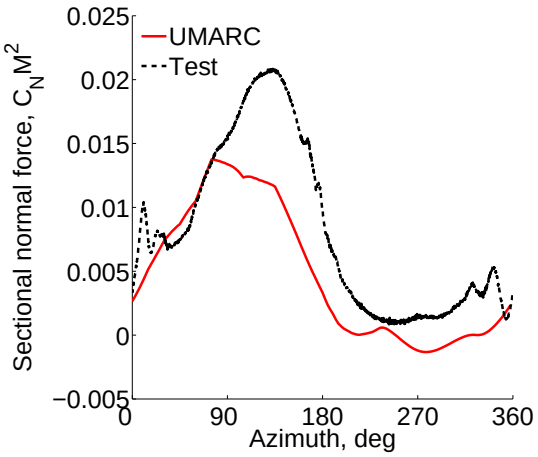

(a) $\mu = 0.4$, $\theta_0 = 1.96°$, $\alpha_s = 4°$.

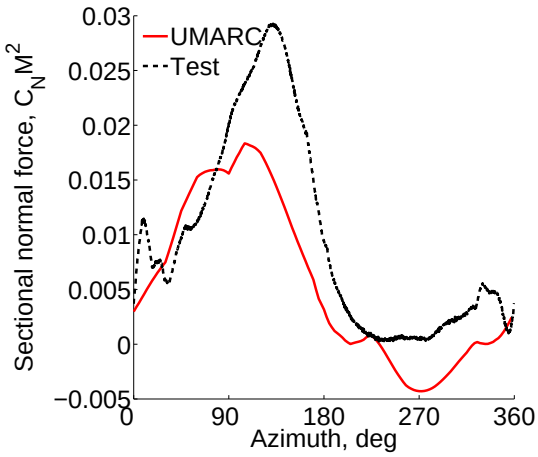

(b) $\mu = 0.5$, $\theta_0 = 1.96°$, $\alpha_s = 4°$.

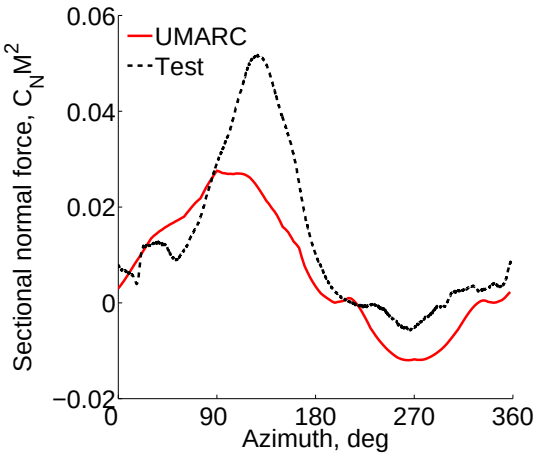

(c) $\mu = 0.7$, $\theta_0 = 2.96°$, $\alpha_s = 4°$.

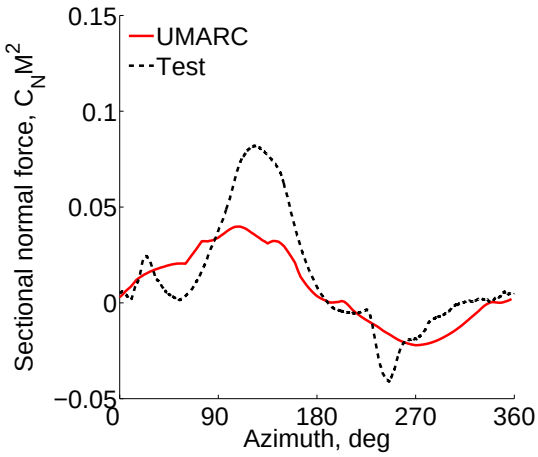

(d) $\mu = 0.9$, $\theta_0 = 6.16°$, $\alpha_s = 4°$.

Figure 4.33: Sectional normal force ($C_N M^2$), r/R = 22.5%. $C_T/\sigma_{test} = 0.062$.

the dynamic pressure. The baseline analysis is the same as used for the initial performance predictions and does not include the dual wake and root wake trailers, which are investigated in a later section.

The normal force predictions at 92% radius show significant error on the advancing side lift and on the aft rotor, while the retreating side is generally well predicted. The measured normal force on the advancing side is dominated by a negative lift impulse around 90° azimuth. The negative lift results from high installed twist and large longitudinal cyclics required for trim. The baseline analysis under-predicts the magnitude of the impulse worst at low advance ratios and for 0° shaft angle, improving at higher advance ratios and for aft shaft angles. Above an advance ratio of 0.3, lift is well predicted from 180° azimuth and over most of the retreating side. At $\mu = 0.3$, the lift is somewhat under-predicted, but the blade vortex interaction near 300° azimuth is captured well. For higher advance ratios, the wake is swept aft of the rotor before interacting with the retreating blade and the retreating side correlation is quite good. On the aft rotor, there is a lift peak near 330° azimuth that is consistent for all advance ratios but not predicted by the analysis. Lift in the first quadrant is poorly predicted for the low advance ratios cases (0.3 and 0.4) independent of the shaft angle, but the lift magnitude is otherwise generally captured. The first quadrant prediction error is significantly reduced after the introduction of addition wake trailers shown in the following sections.

At 22.5% radius, shown in fig. 4.33 for 4° shaft angles only, the section is just outside of the traditional root cut-out (20%) and highlights the reverse flow dynamics. The prediction generally captures the trends, but the lift magnitude on

the advancing side is under-predicted by up to 50% and the negative lift in the reverse flow is highly over-predicted, but the magnitudes are generally small. The inboard station lift is much higher than the tip region due to twist. Under-predicting the lift at 22.5% radius likely is responsible for the global under-prediction of thrust shown in the previous section. The spike in the measured force on the aft rotor at low advance ratios is not predicted. At 0.9 advance ratio, there is clear evidence of dynamic stall in the reverse flow, as pointed out by Datta et al. [59]. The analysis does not model dynamic stall in the reverse flow so that this will not be captured.

The sectional pitching moments are shown in fig. 4.34 for the 92% station and in fig. 4.35 for the 22.5% station for the same test conditions used for the normal force. The mean pitching moment has been removed in both measured and predicted values. For the tip region, the pitching moment is not well resolved. A weak 1/rev is captured by the analysis by the details of the pitching moment around the azimuth and the magnitudes are not predicted. The best correlation is at the highest advance ratio, $\mu = 0.9$, which somewhat resolves the advancing side pitching moment. At 22.5% radius, the pitching moment prediction is generally improved and the general shape is predicted well at all advance ratios. At higher advance ratios, the pitching moment is dominated by the reverse flow. In the reverse flow, the lift moves to the $^3/_4$ chord location resulting in a large pitching moment. The analysis over-predicts the reverse flow pitching moment, consistent with the over-predicted lift in that region. The similar peak magnitudes at $\mu = 0.9$ is misleading because of dynamic stall which is not present in the analysis.

The poor pitching moment prediction, particularly at 92% station, is not well

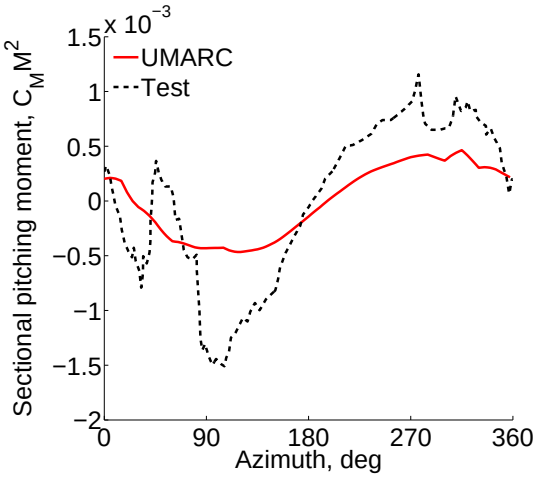

(a) $\mu = 0.3$, $\theta_0 = 4.0°$, $\alpha_s = 0°$.

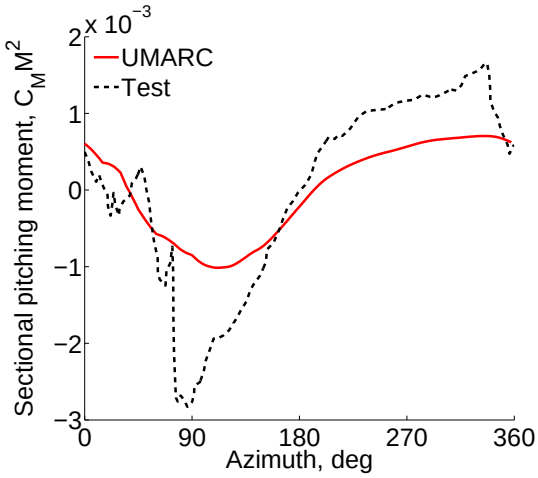

(b) $\mu = 0.5$, $\theta_0 = 6.0°$, $\alpha_s = 0°$.

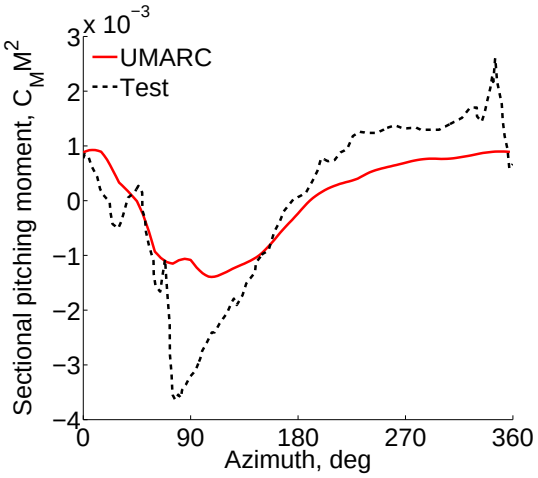

(c) $\mu = 0.6$, $\theta_0 = 7.93°$, $\alpha_s = 0°$.

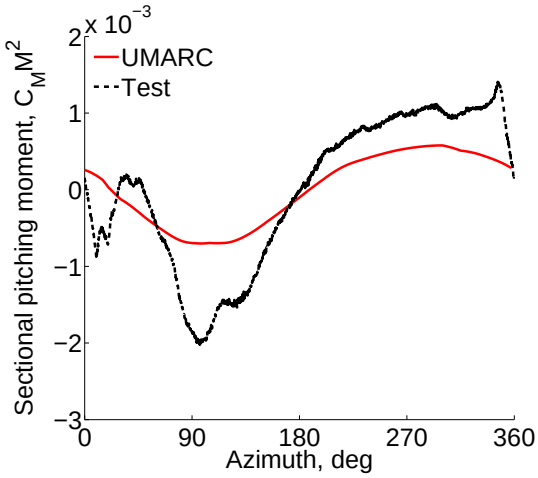

(d) $\mu = 0.4$, $\theta_0 = 1.96°$, $\alpha_s = 4°$.

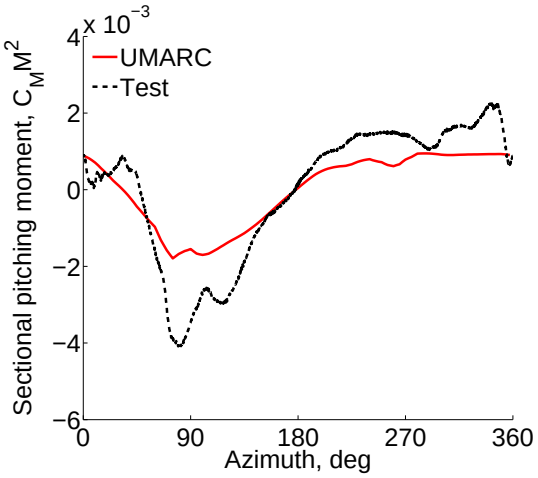

(e) $\mu = 0.7$, $\theta_0 = 2.96°$, $\alpha_s = 4°$.

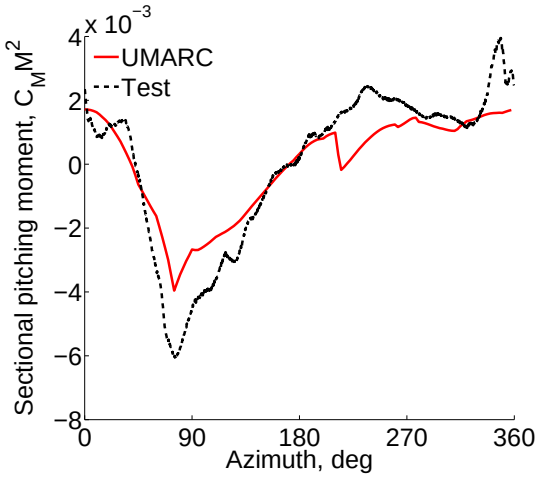

(f) $\mu = 0.9$, $\theta_0 = 6.16°$, $\alpha_s = 4°$.

Figure 4.34: Sectional pitching moment ($C_M M^2$), r/R = 92%. $C_T/\sigma_{test} = 0.062$.

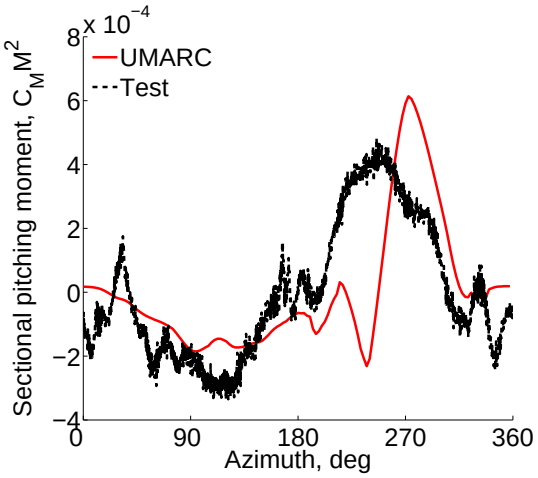

(a) $\mu = 0.4$, $\theta_0 = 1.96°$, $\alpha_s = 4°$.

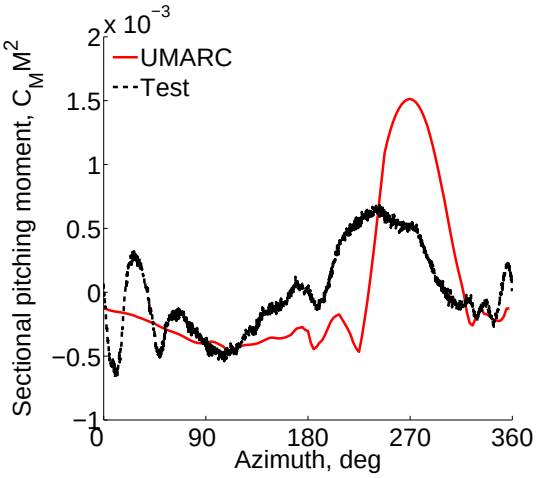

(b) $\mu = 0.5$, $\theta_0 = 1.96°$, $\alpha_s = 4°$.

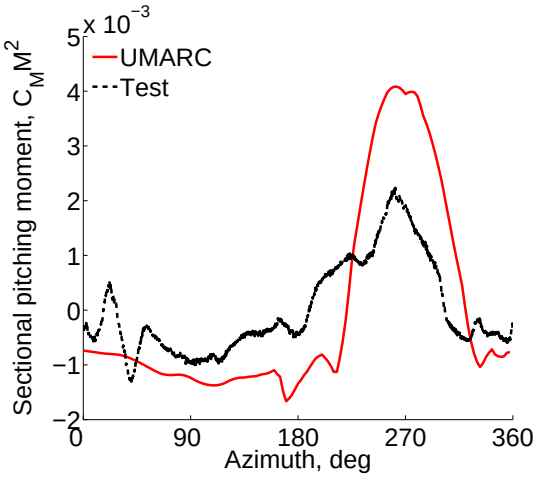

(c) $\mu = 0.7$, $\theta_0 = 2.96°$, $\alpha_s = 4°$.

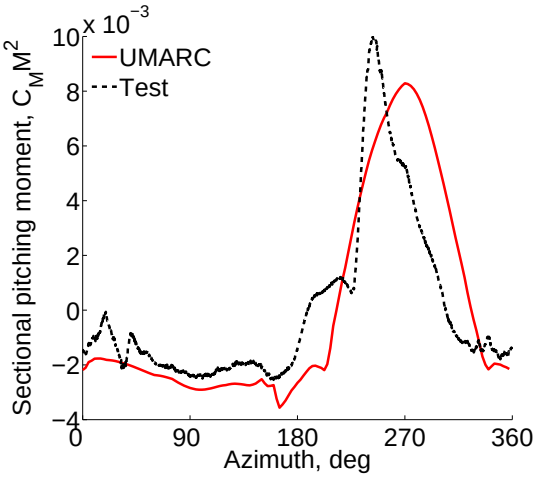

(d) $\mu = 0.9$, $\theta_0 = 6.16°$, $\alpha_s = 4°$.

Figure 4.35: Sectional pitching moment ($C_M M^2$), r/R = 22%. $C_T/\sigma_{test} = 0.062$.

understood. Similar poor predictions have been shown with CAMRAD II, RCAS and Helios (CFD-CSD) [68], despite each showing good correlation for normal rotor speeds in level flight. The low tip speeds and Mach numbers mean that the pitching moment for the slowed rotor should be benign. Potsdam et al. [68] and Norman [114] have each investigated the discrepancy and have not found an error in the pitching moment integration, nor do differences in trim (θ_{1S}) explain the difference. The elastic twist response of the blade is unknown but could result in a pitch difference if not well predicted. None of the modifications to UMARC have a significant improvement on the trends and they are not considered further.

4.4.2 Modified UMARC results

4.4.2.1 Dual Wake Trailers

The results of the performance analysis showed that dual wake trailers are important for predicting thrust, particularly at lower advance ratios. The effect of dual wake trailers on the sectional tip normal force is shown in fig. 4.36 including the effect of wake resolution ($15^\circ \rightarrow 10^\circ$). The largest impact is for low advance ratios where the dual wake model improves the magnitude and phase of the normal force at 90° azimuth. The improved correlation on the retreating side at $\mu = 0.3$ is in response the new trim state of the rotor. The impulse in the first quadrant is somewhat improved as well. The reason for the improvement is that the with the negative vortex at the tip, the larger inboard vortex is released with the right trajectory to interact with the following blade correctly. For 0.4 and 0.9 advance

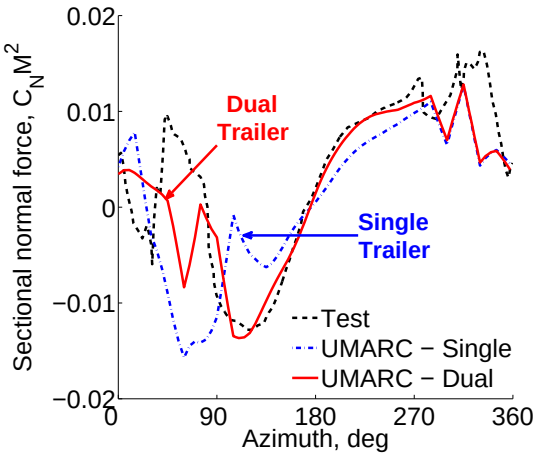

(a) $\mu = 0.3$, $\theta_0 = 4.0°$, $\alpha_s = 0°$.

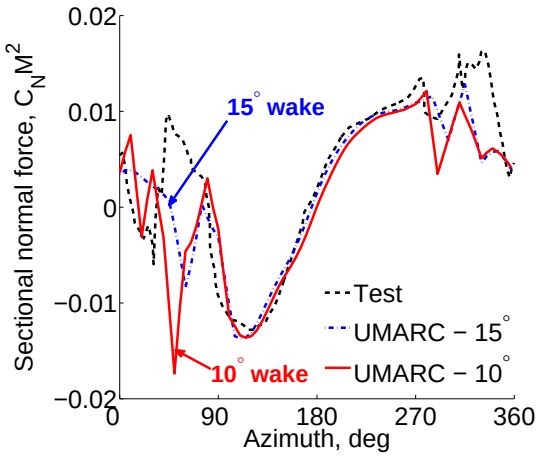

(b) $\mu = 0.3$, $\theta_0 = 4.0°$, $\alpha_s = 0°$ (10° wake).

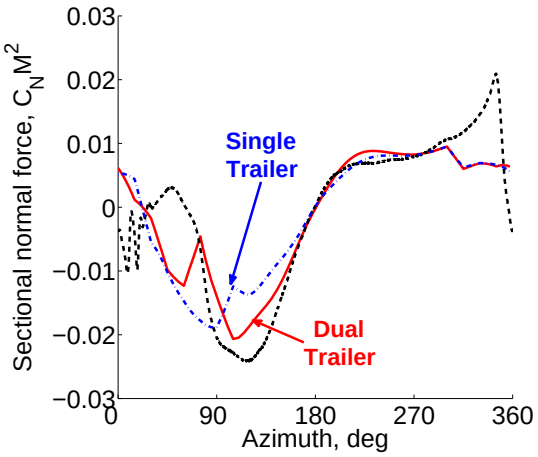

(c) $\mu = 0.4$, $\theta_0 = 1.96°$, $\alpha_s = 4°$.

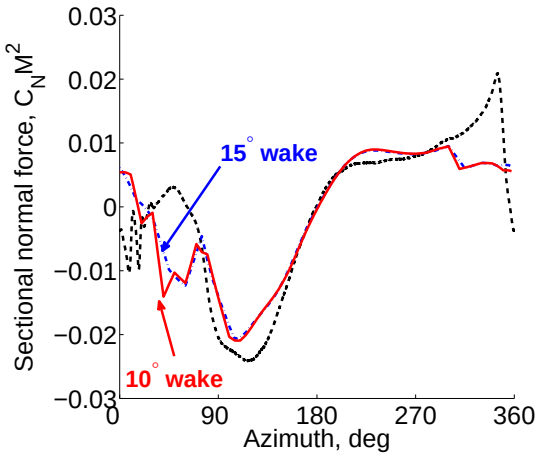

(d) $\mu = 0.4$, $\theta_0 = 1.96°$, $\alpha_s = 4°$ (10° wake).

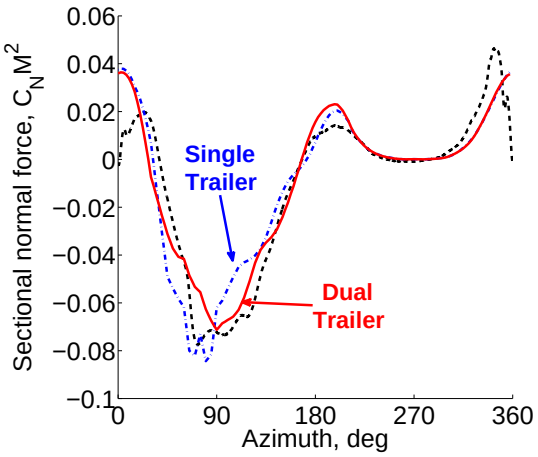

(e) $\mu = 0.9$, $\theta_0 = 6.16°$, $\alpha_s = 4°$.

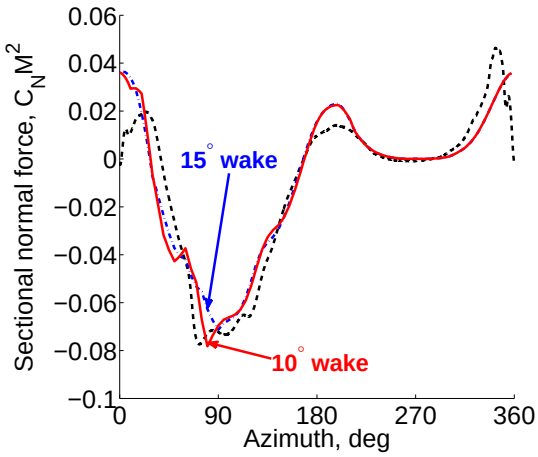

(f) $\mu = 0.9$, $\theta_0 = 6.16°$, $\alpha_s = 4°$ (10° wake).

Figure 4.36: Sectional normal force with dual wake trailers ($C_N M^2$), r/R = 92%. $C_T/\sigma_{test} = 0.062$.

ratios, the shaft is 4° aft, which reduces wake interaction and the dual trailer model has less effect but still improves the advancing side correlation. The retreating side is largely unchanged. To ensure that the wake resolution is adequate, the same dual wake trailer case was run with 10° azimuthal resolution (baseline was 15°). Once again, only the lower advance ratio case shows a significant effect of wake resolution and only in the first quadrant where it can be important for blade wake interactions. There is no effect of the wake trailers on the root force predictions and there is no significant change to the pitching moments. The remaining results continue with the dual wake trailers with 15° azimuthal resolution as the baseline.

4.4.2.2 Root Modeling

Figure 4.37 shows the effect of the root trailer on the tip (92%) and root (22%) stations. At 92% radius (fig. 4.37a), the root vortex is responsible for the peak in normal force near 300° azimuth as well as improving the predictions of the wake interactions generally on the aft rotor. Two results are shown for the inboard station, the first is releasing the trailer from the traditional root cut-out at r/R = 20% (fig. 4.37b) and the second is releasing the trailer at r/R = 13% corresponding to the physical end of the blade (fig. 4.37c). Released from 20% radius, the root trailer disrupts the normal force on the advancing side and somewhat improves the retreating side lift prediction. At 13% radius, the root trailer captures the spike in normal force around 20° azimuth caused by the blade interacting with the root vortex. The root trailer appears to improve advancing side lift prediction. The increase in lift is caused by moving the effective end of the lifting blade further

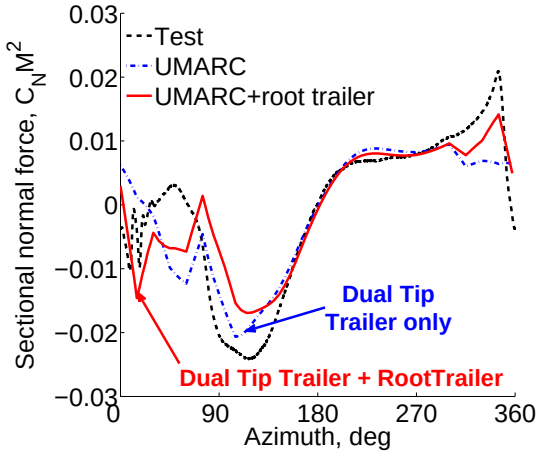

(a) r/R = 92%.

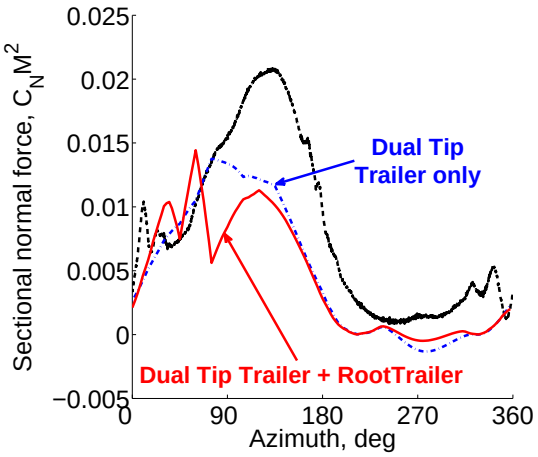

(b) r/R = 22.5%, root trailer at 20%.

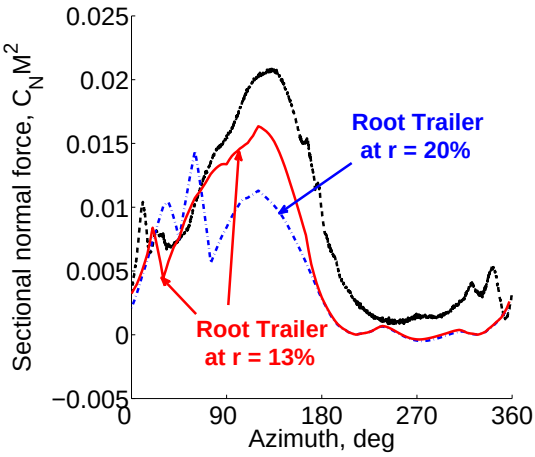

(c) r/R = 22.5%, root trailer at 13%.

Figure 4.37: Sectional normal force with dual wake trailers ($C_N M^2$), $\mu = 0.4$, $\theta_0 = 1.96°$, $\alpha_s = 4°$.

inboard from the 22% station to the 13% station. This reduces the downwash on the inboard blade and increases thrust. It is possible that the blade shank disrupts and disperses the advancing side root vortex, which could improve thrust prediction further. Evidence of the shank disrupting the root vortex was shown with CFD by Potsdam et al. [102], but it was not pursued.

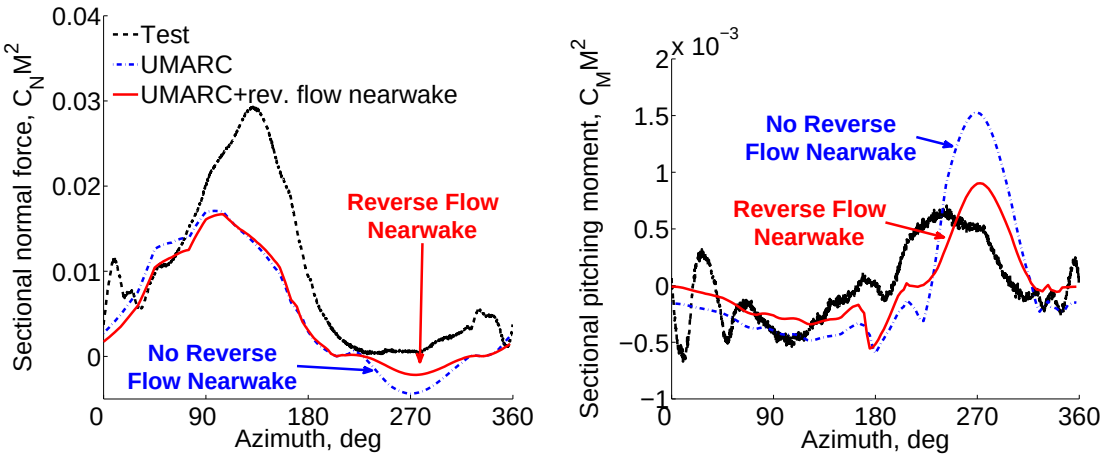

(a) Normal force. (b) Pitching moment.

Figure 4.38: Effect of reverse flow nearwake on normal force and pitching moment,r/R = 22.5%, $\mu = 0.5$, $\theta_0 = 1.96°$, $\alpha_s = 4°$.

4.4.2.3 Nearwake

The effect of the nearwake in the reverse flow is small and isolated to the root cut-out region of the reverse flow. Figure 4.38 shows a small decrease in the reverse flow lift and pitching moment due to the nearwake inflow. There was no difference between the fixed or freestream-deformed nearwake at this radial station.

4.4.3 Airloads Summary

Modeling the wake with sufficient trailers results in a significant improvement in sectional force prediction. Dual wake trailers that model negative lift on the advancing rotor are important for the magnitude and phase of the advancing side lift impulse, but its impact decreases as the advance ratio approaches 1.0. A wake trailer from the edge of the reverse flow showed no significant change in the results. The root trailer determines the blade–wake interactions on the aft rotor. Trailing the root trailer from the physical blade edge at 13% improves both the advancing side thrust (near the root) and the phase of the blade–wake interactions at inboard stations. Including the nearwake in the reverse flow resulted in a small decrease in the reverse flow lift and pitching moment, which improved correlation. Effects from the fuselage were not seen at the available radial stations (expected 30%–50%), nor were any impact from yawed flow corrections.

The normal force for the final model is well predicted near the tip at all advance ratios, including the peak-to-peak magnitudes and the phase of dominant phenomena. At inboard stations, the lift remains under-predicted on the advancing side, although it is improved by the appropriate blade root modeling. Pitching moments at the tip are not predicted well and the predictions are not improved with any modeling refinements. At the blade root, the pitching moment is somewhat predicted, but over predicted by the analysis in the reverse flow. Accounting for nearwake inflow and root trailer reduce the difference. At 0.9 advance ratio, the reverse flow region shows signs of dynamic stall which is not modeled in the analysis.

4.5 Blade Loads Predictions

This section presents the blade bending loads measurements and predictions. The development of the analysis is not repeated, instead the final analysis configuration is used for all the results. The wake model includes dual tip trailers and a root trailer. The root trailer is trailed from 13% radial station. The fixed geometry nearwake is included in the nearwake. Fuselage upwash and radial flow effects are neglected.

Table 4.5: Blade frequency variation at 100% and 40% RPM.

	100% (/rev)		40% (/rev)	
1^{st} Mode	0.276	(L)	0.312	(L)
2^{nd} Mode	1.037	(F)	1.047	(F)
3^{rd} Mode	2.83	(F)	3.31	(F)
4^{th} Mode	4.38	(T)	10.76	(T)
5^{th} Mode	4.68	(F/L/T)	7.30	(F)
6^{th} Mode	5.18	(F)	10.54	(F/L/T)
7^{th} Mode	7.88	(F)	13.66	(F)
8^{th} Mode	11.46	(F)	22.32	(F)

The first 6 blade frequencies for the UH-60A rotor are listed in table 4.5 for the baseline (100% RPM) and the slowed rotor (40% RPM). The first torsion frequency changes significantly from 4.44/rev to near 11/rev and the 5^{th} Flap/Lag coupled mode increases to 7.6/rev leaving only the second flap in the region of 4/rev with its frequency at 3.39/rev.

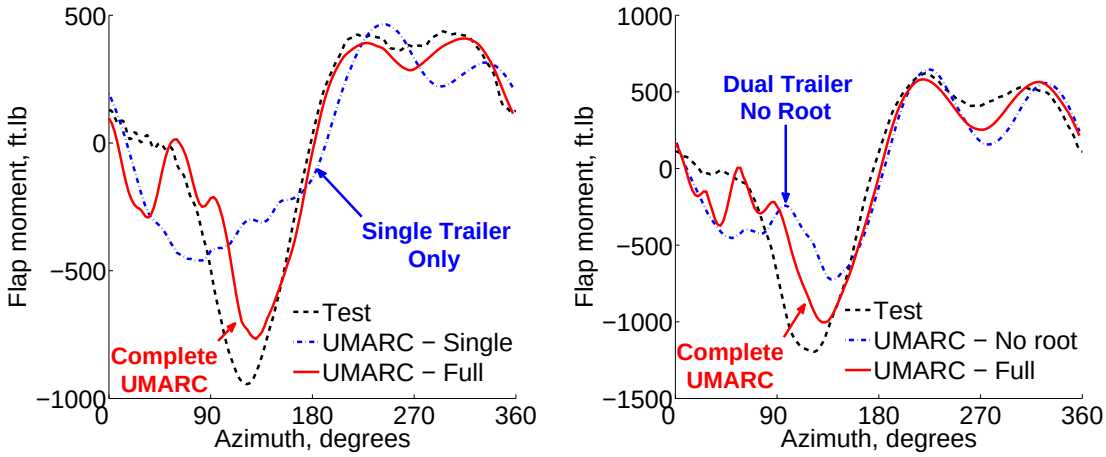

(a) $\mu = 0.4$ (b) $\mu = 0.5$

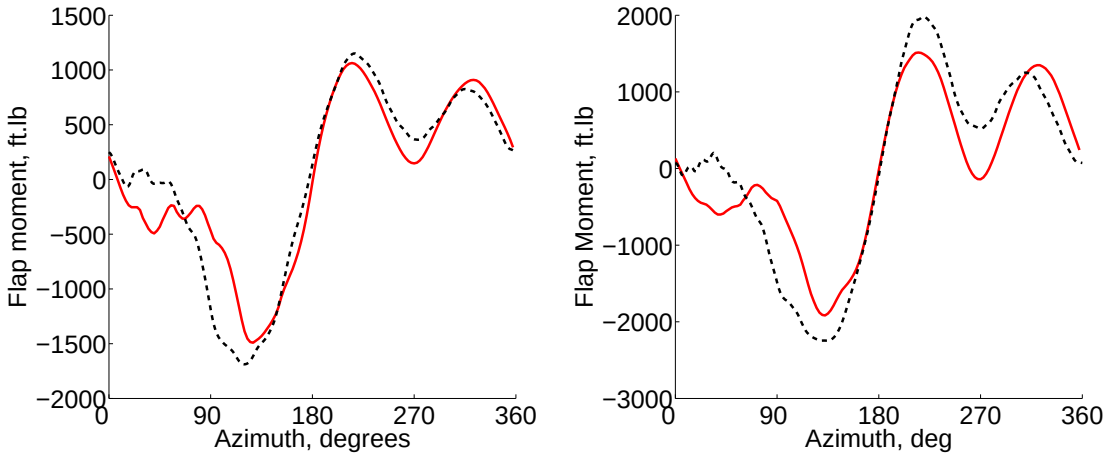

(c) $\mu = 0.7$ (d) $\mu = 0.9$

Figure 4.39: Oscillatory flap bending moment, r/R = 50%. $C_T/\sigma = 0.062$, $\alpha_s = 4°$ aft.

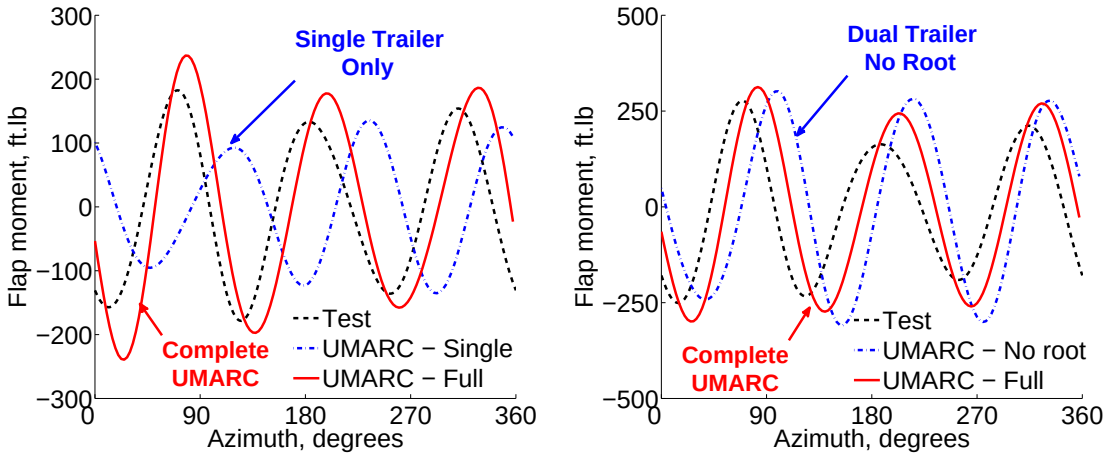

(a) $\mu = 0.4$

(b) $\mu = 0.5$

(c) $\mu = 0.7$

(d) $\mu = 0.9$

Figure 4.40: Vibratory (3-5/rev) flap bending moment, r/R = 50%. $C_T/\sigma = 0.062$, $\alpha_s = 4°$ aft.

4.5.1 Flap Bending Moment

Figure 4.39 shows the oscillatory (1/rev and up) flap bending moments at 50% span for the 4° aft shaft tilt cases. The predicted oscillatory loads show very good agreement with test data in the second, third and fourth quadrants although the peak bending moment in the second quadrant is somewhat under-predicted. The first quadrant prediction error is likely due to the short comings in the lift predictions in the first quadrant. Figures 4.39a and 4.39b highlight the improvement in the prediction compared to the single wake trailer model, and then the dual wake model without the root trailer. The improvement after the addition of the root trailer indicates that the blade–wake interactions on the aft rotor are important for peak-peak bending load prediction.

The rotating to non-rotating transform means that only blade loads at $pN_B - 1$, pN_B and $pN_B + 1$ (p is an integer) contribute to the vibratory loads, predominantly at $p = 1$. The vibratory harmonics (3, 4 and 5/rev) of flap bending, shown in fig. 4.40, show a strong 3/rev content from the second flap mode, which is well predicted. Excluding the dual wake trailers (fig. 4.40a) results in incorrect phase and amplitude of the dominant 3/rev loads. The root trailer predominantly improves the 3/rev phase.

4.5.2 Torsion Moment and Pitch Link Loads

The oscillatory torsional moments are shown in fig. 4.41. The mean trend and the peak-to-peak of the oscillatory torsional (1/rev) moments at 50% span

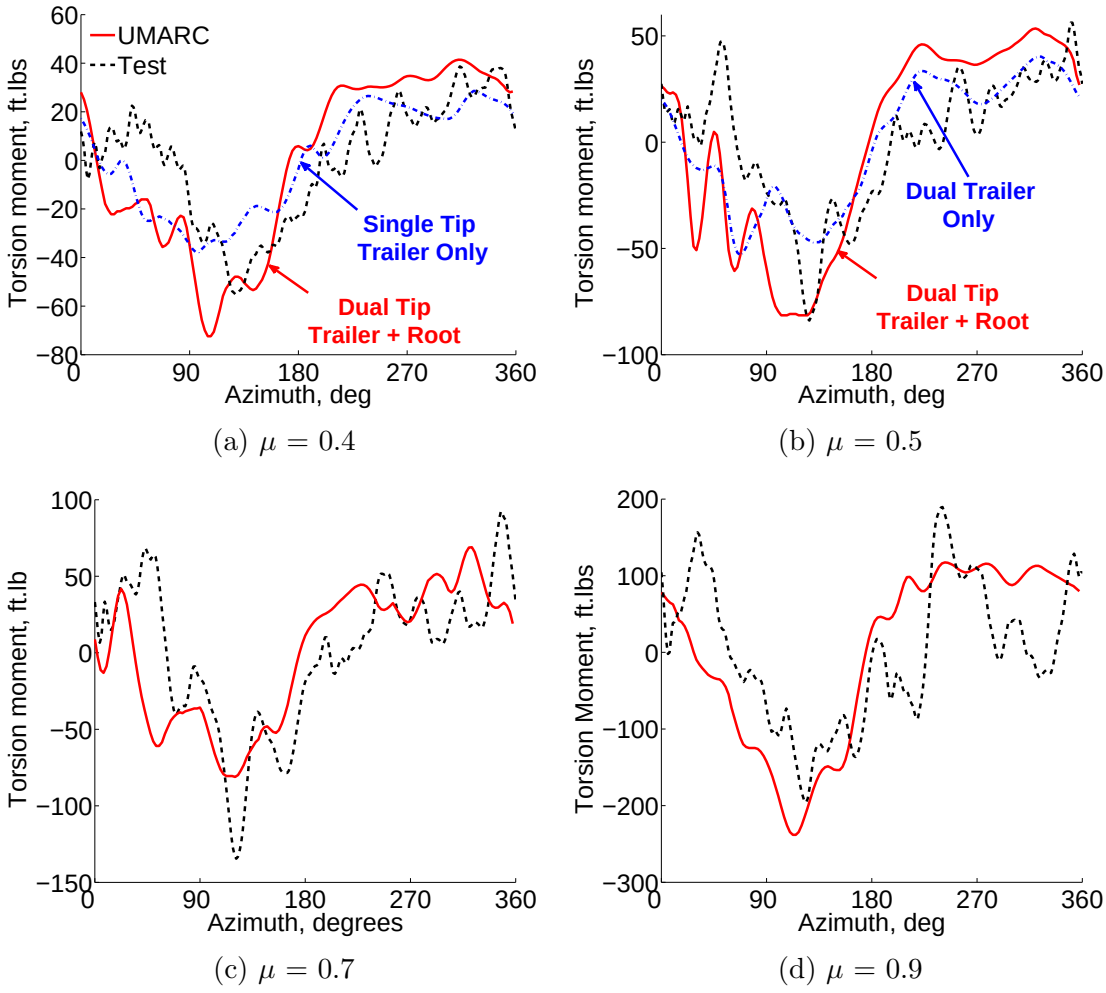

(a) $\mu = 0.4$

(b) $\mu = 0.5$

(c) $\mu = 0.7$

(d) $\mu = 0.9$

Figure 4.41: Oscillatory torsional moment, r/R = 50%. $C_T/\sigma = 0.062$, $\alpha_s = 4°$ aft.

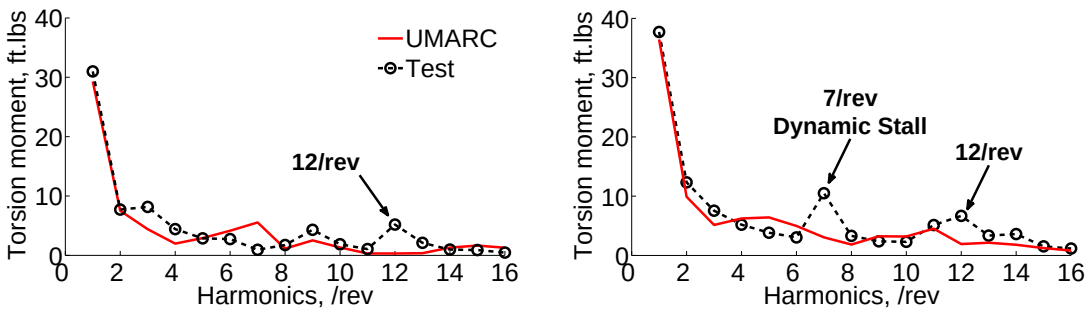

(a) $\mu = 0.4$

(b) $\mu = 0.5$

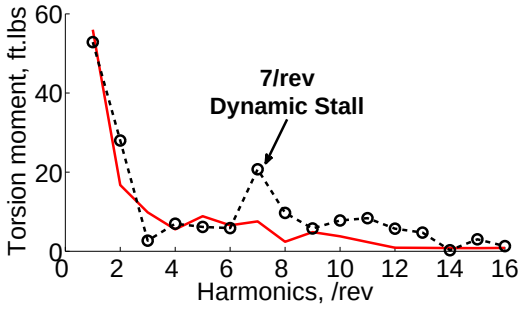

(c) $\mu = 0.7$

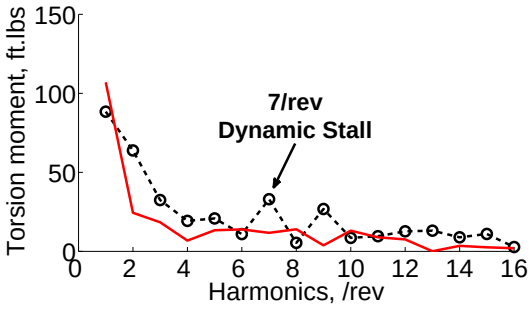

(d) $\mu = 0.9$

Figure 4.42: First 16 harmonics of torsional moment, r/R = 50%. $C_T/\sigma = 0.062$, $\alpha_s = 4°$ aft.

location are quite well predicted by the analysis but the measured data contains higher harmonics that are not captured by the analysis. The good peak-to-peak agreement is despite the poor prediction of pitching moments at 92% radius. This could be due to a relative dominance of pitching moments in the tip swept region (starting from 20% radius). Assuming that the lift in the tip region is well predicted, the pitching moment due to the aerodynamic offset is large and may determine the torsion response at 50% radius more than the the pitching moment of the unswept blade between 50% and 94% radius. A harmonic analysis of the torsion moments at 50% station is shown in fig. 4.42. Generally the 1/rev and 2/rev torsion are well predicted while 3/rev and 4/rev are not as well predicted. The test also shows some amplification at 12/rev which is likely the torsion mode. The analysis does

not predict this. It is possible to artificially move the torsion closer mode to 12/rev by adjusting torsion stiffness (33% increase in GJ is required), but this still did not result in 12/rev excitation for any of these cases. The analysis used 10 modes for the analysis and the 8^{th} mode is already at 22/rev. Increasing the number of modes is not expected to change the prediction.

At 7/rev, a peak magnitude grows from above $\mu = 0.5$ corresponding to when the reverse flow extends past the 50% station. This is likely a result of dynamic stall in the reverse flow. The peak is substantial by $\mu = 0.5$ despite this being at the border of the reverse flow with benign flow conditions expected.

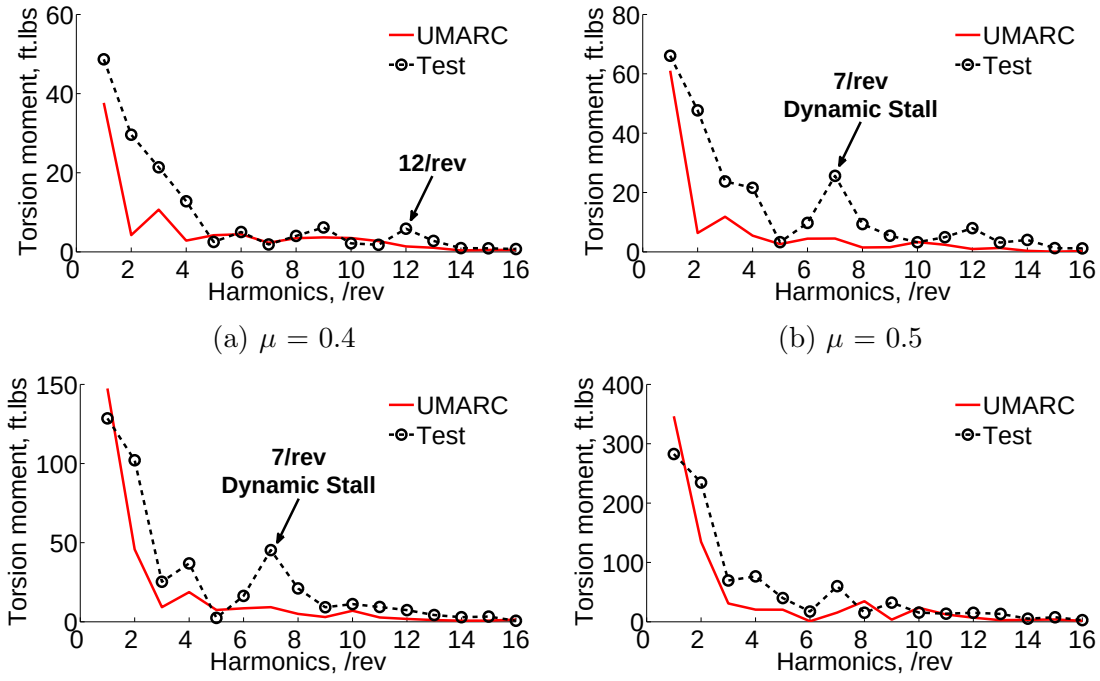

(a) $\mu = 0.4$ (b) $\mu = 0.5$

(c) $\mu = 0.7$ (d) $\mu = 0.9$

Figure 4.43: First 16 harmonics of torsional moment at pitch link, r/R = 5%. C_T/σ = 0.062, $\alpha_s = 4°$ aft.

A harmonic analysis on the root torsion moment (5% station corresponding to the pitch link location) in fig. 4.43 shows that the 1/rev root torsion moment is

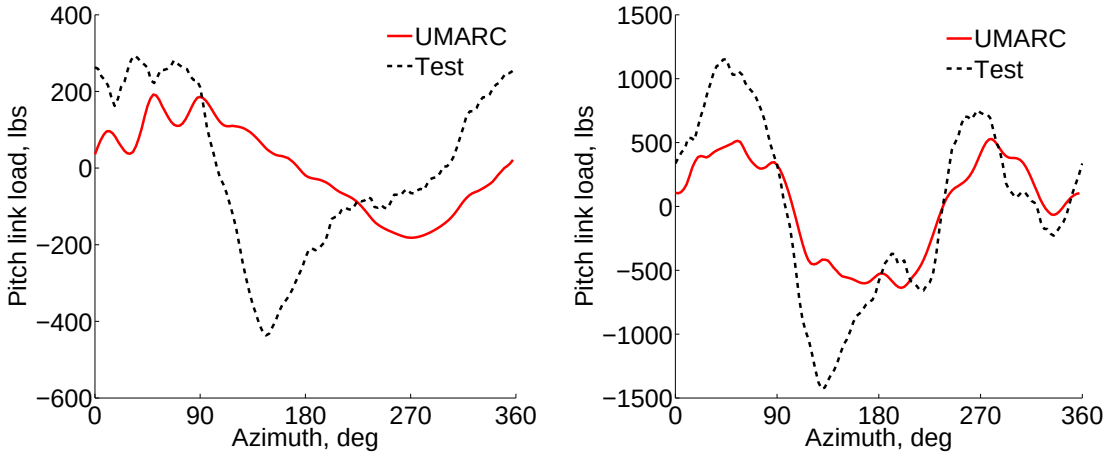

(a) $\mu = 0.4$ (b) $\mu = 0.9$

Figure 4.44: Pitch link loads, $C_T/\sigma = 0.062$, $\alpha_s = 4°$ aft.

reasonably well predicted, but 2, 3, 4 and 7/rev harmonics are not predicted. The resulting prediction of pitch link loads, shown in fig. 4.44, does not capture the peak-to-peak magnitudes. At 0.9 advance ratio, the pitch link loads are dominated by 1–4/rev harmonics, in particular it is the under-prediction of 2/rev that results in the significant peak-to-peak error. Outside of the reverse flow (fig. 4.42), the 2/rev harmonic is well predicted, so the discrepancy comes from reverse flow aerodynamics.

4.6 Chapter Summary

The chapter has investigated the prediction of helicopter performance at high advance ratios using a lifting line analysis, UMARC. The test data is of the UH-60A rotor, which was tested up to an advance ratio of 1.0 for 0° and 4° aft shaft angle. The baseline analysis is the same as has been used for the variable tip speed studies in chapters 2 and 3. Modifications and added modeling fidelity have been introduced to the baseline analysis and investigated for their impact on performance prediction

and predicted airloads and blade loads at high advance ratios. The modeling refinements investigated include: modeling a fuselage under the rotor to investigate disturbance of the free stream; showing the influence of the nearwake in the reverse flow, including an approximation for deformation of the nearwake by the freestream velocity; multiple wake trailer modeling including dual tip trailers, a trailer from the reverse flow boundary and root wake trailers; yawed flow corrections; and modeling the root cut-out. Based on this study, the following key conclusions can be drawn:

1. The baseline analysis under-predicts thrust by about ${}^{C_T}/_{\sigma}$ of 0.013 and this is not completely corrected by any of the investigated modifications to the analysis. The wake system, including dual tip trailers and root trailers, and correcting the root cut-out to the physical blade edge improves the prediction.

2. The slope of thrust versus collective is decreasing with increasing advance ratios. The baseline analysis is able to predict the slope below $\mu = 0.6$, but over-predicts the slope thereafter. The yawed flow corrections acted to delay stall in the reverse flow and gave a very good agreement of predicted thrust slope up to $\mu = 1.0$. Nearwake in the reverse flow independently improved the slope prediction at high advance ratios by reducing the angle of attack in the reverse flow and reducing stall.

3. The baseline axial force is under-predicted by as much as 30% at high advance ratios. Accounting for drag in the blade shank region, $c_{d_{shank,1}} = 0.4$ in 8%–13%, improves axial force prediction at all advance ratios.

4. Shaft power is well predicted for $\mu = 0.3$ and the correct trend with increasing

collective is captured for all advance ratios. The magnitude at 0° collective is over-predicted by the baseline. The dual trailer wake model had the largest influence on decreasing the power prediction, helped by the fuselage and wake from the blade root. Yawed flow corrections increased the predicted power.

5. The final correlation of lift-to-drag ratio after applying the important modifications showed a very good prediction of rotor efficiency for all advance ratios.

6. The sectional airloads show good lift prediction at the blade tip after accounting for dual wake trailers. Lift at the blade root end (22.5%) remains underpredicted on the advancing side and over the front of the rotor. The source of missed lift on the front of the rotor is uncertain considering the relatively low dynamic pressures.

7. Sectional pitching moments near the blade tip are not predictable with the baseline nor with any modifications to the analysis. The discrepancy has been shown with CFD and is not currently understood. The torsion moment at 50% station is reasonably well resolved and does not show any gross errors. Comparing the torsion moment at the blade root and at 50% radius suggest that reverse aerodynamics are exciting 2/rev torsion response that is underpredicted by the analysis.

8. Measured torsion moments shows 7/rev peaks that correlate with dynamic stall in the reverse flow. This is not modeled in the analysis and may be important to predict the torsion response of the rotor.

9. Pitch link loads are not well predicted. At high advance ratios, under-prediction of the 2/rev torsion moment is the main difference. At low advance ratios, 2, 3 and 4/rev harmonics are poorly predicted.

10. Flap bending moments are generally predicted well at 50% radius. Both dual tip trailers and root trailers are important for predicting the peak-to-peak loads, dominated by a negative impulse on the advancing rotor.

11. The aft rotor interacts with wake from the blade tip and the blade root to result in highly impulsive loading. The well-defined wake models in the analysis are sufficient to predict the general behavior, but may be too simplified for the complex wake interactions that exist (based on CFD visualization). The interaction of the root vortex is important for the magnitude and phase of the vibratory flap bending loads (3, 4 and 5/rev), which contribute to 4/rev fixed frame loads.

12. The sensitivity of rotor performance to the nearwake geometry in the reverse flow is small. The nearwake inflow improves thrust prediction at high advance ratios by delaying stall. Allowing the nearwake to deform with the freestream slightly improved the prediction of the thrust slope at high advance ratios by reducing stall in the reverse flow.

13. Yawed flow corrections were effective at delaying reverse flow stall and improving thrust correlation at high advance ratios. There is a question about the validity of the model beyond stall that requires CFD or experimental valida-

tion.

14. Modeling upwash from the fuselage only slightly increases thrust because the lateral cyclic acts to counteract changes on the front rotor. Including the downwash on the aft rotor results in a decrease in thrust at high advance ratios.

°

Chapter 5: University of Maryland High Advance Ratio Tests

The previous chapter investigated the high advance ratio performance and loads predictions of the UH-60A slowed rotor wind tunnel tests. The comprehensive analysis code, UMARC, was refined with corrections and improved capability to study high advance ratio aeromechanics. The UH-60A tests provided a comprehensive data set at high advance ratios, but the test envelope did not exceed an advance ratio of 1.0 for safety and affordability concerns. This chapter presents prediction and validation against even higher advance ratio wind tunnel tests carried out at the University of Maryland.

The Maryland test on a model-scale rotor reached an advance ratio of 1.6 and allows for extended validation of the UMARC analysis to advance ratios higher than 1.0 and into a unique flow environment called "thrust reversal". Once the analysis has been validated for the Maryland rotor at high advance ratios, the sensitivity of high advance ratio performance to flight condition is investigated.

Berry and Chopra [60–64] have carried out a range of tests on a Mach-scaled rotor up to an advance ratio of 1.6 over several wind tunnel entries between 2011–2014. The goal of the wind tunnel tests is to examine aeromechanics at high advance ratios up to 2.0. The early wind tunnel tests by Berry were on a 4-bladed, articulated,

twisted rotor (-12°) with the SC1095 airfoil (one of the two UH-60A airfoils) and achieved an advance ratio of 0.65 [60]. The test envelope of the twisted rotor was later expanded to an advance ratio of 1.2 [61]. These early tests faced challenges when trimming at high advance ratios, had a limited number of sensors (limited slip ring space) as well as uncertainty about the airfoil used. Following from this, Berry tested a relatively simplified, untwisted, NACA0012 rotor, which is the baseline for all subsequent tests. Upgrades to the slip ring and the simplified rotor geometry allowed the 2013 test to include blade pressure measurements at a single station for the first time. This test was also the first to use a shaker to determine the dynamic calibration of the rotor stand in the wind tunnel, necessary for accurate vibratory loads measurement [63]. The test reached an advance ratio of 1.4; however, blade differences made trimming at advance ratios above 1.0 difficult and there were several sensor failures during testing resulting in an incomplete set of data. Berry and Chopra [64] completed a final test on the untwisted rotor that achieved an advance ratio of 1.6 with satisfactory rotor trim and all important sensors working. Investigating this latest test data is the objective for this chapter.

The final wind tunnel test provides a relatively simple rotor with which to validate the analysis as a compliment to the validation of the UH-60A slowed rotor tests shown in the previous chapter. The Maryland test instrumentation included comprehensive performance measurements as well blade loads and vibratory loads. These are all used in the validation of the analysis. Blade pressure data is used to help identify important phenomena, but complete sectional airloads are not available at this time.

The goal of this chapter is to continue to expand the understanding of the aeromechanics of high advance ratio rotors with a particular focus on the important phenomena of thrust reversal.

5.1 UMARC Modeling

The modified University of Maryland Advanced Rotorcraft Code, as described in Chapter 4, was used in this study. A number of the modifications made for the investigation of the UH-60A rotor were unnecessary for the Maryland tests. The Maryland test did not have a faired fuselage so there was no need to include it in the analysis. The blade root of the Maryland rotor is simpler than the UH-60A and allowed the tare measurements to include all contributions to shank drag so that corrections to root drag were unnecessary. The Maryland rotor is untwisted so that lift on the advancing rotor does not generally change sign along the span so that the use of more than a single tip trailer was unnecessary. The inclusion of a wake trailer from the blade root is investigated only when considering the flap bending loads, but otherwise had a minimal effect on performance.

The rotor trim for the Maryland test data was the same as that for the UH-60A slowed rotor tests and targeted zero first harmonic flapping at the blade root for fixed collectives. The measured root angles for some flight conditions at high advance ratios indicated that the ideal trim was not achieved, in which cases the analysis was trimmed to match the actual first harmonic flapping of the wind tunnel test.

5.2 Test Description

Table 5.1: Maryland rotor properties (at 100% rotor speed).

Rotor	Maryland 2014
Rotor Speed (rad/s)	240
Radius (ft)	2.78
Solidity	0.117
Lock No. (γ)	5.6
Tip Speed (ft/s)	675
Tip Mach No. (M)	0.6
Tip Reynolds No.	1.1×10^6
Airfoil	NACA0012
Hinge offset	6.3%
Root cut-out	22.5%
Twist	untwisted
Sweep	unswept

The primary data set used in this work are the tests carried out in 2014 by Berry and Chopra [64]. The important properties of the rotor are given in table 5.1. The rotor radius is 2.78 ft and roughly a $1/9^{th}$ scale of the full-scale UH-60A rotor. The baseline rotor speed is 240 rad/s (100% RPM), giving a hover tip Mach number of 0.6 in-line with the UH-60A rotor. The slowed rotor speeds refer to this baseline.

Table 5.2: Blade sectional properties.

Rotor	UM-2014
Flapwise stiffness, EI_y (lb-ft^2)	70
Lagwise stiffness, EI_z (lb-ft^2)	1000
Torsional stiffness, GJ (lb-ft^2)	70
Blade mass†, m_0 (slugs/ft)	0.00725
Flap inertia*, I_β (slugs-ft^2)	0.0428

† Excluding blade cuff.
* From flap hinge.

The sectional properties of the rotor are listed in table 5.2. The sectional properties were determined from bending tests using a Vicon-like system to measure the

deflections. Due to high relative stiffness of the beam, there is some uncertainty in the measurements that is discussed further in the section on bending load predictions. Uniform sectional properties are assumed.

Figure 5.1: University of Maryland rotor in Glenn L. Martin wind tunnel.

Advance ratios up to 1.61 were achieved in the test by varying the rotor speed between 20% (450 RPM) and 40% (1000 RPM) with the majority of test points collected at 30% (700 RPM). The maximum tunnel speed was 125 knots. Most of

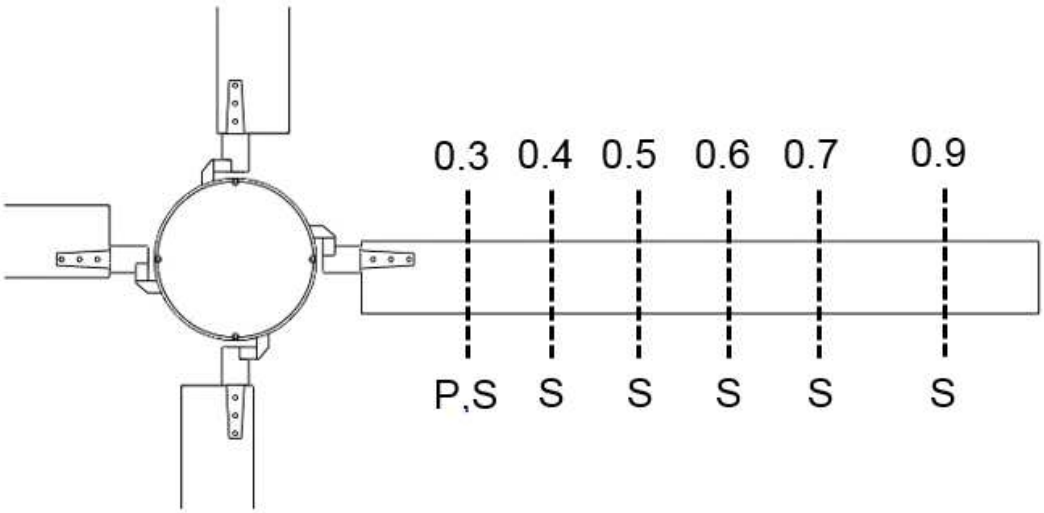

Figure 5.2: Layout of the strain gauges and pressure sensors on the blade. 'S' – Strain gauge, 'P' – Pressure sensors.

the data was collected for 0° shaft angle with limited data at 4° aft shaft angles. Trim was measured in terms of first harmonic (1/rev) root flapping angle and was minimized close to zero using cyclic inputs for a fixed collective. The test stand, shown in fig. 5.1, was not shrouded by any fuselage due to concerns that it could contribute to uncertainty by disturbing the airflow at the rotor plane. This concern arose after a consistent thrust offset was observed in the 2012 wind tunnel tests that could not be duplicated with analysis. The four bladed, articulated rotor had two instrumented rotor blades and two aerodynamically clean rotor blades, arranged in opposing pairs. Blade 1 was instrumented at 30% radial station with 19 chordwise pressure sensors. Blade 3 was instrumented with full bridge strain gauges to measure flapwise and torsion moments places at 30%, 40%, 50%, 60% and 70% radial stations. Figure 5.2 summarizes the placements of the strain gauges and pressure sensors. All four blades were instrumented for root flap, lag and pitch angles. Two pitch

links were strain gauged and the hub accelerations were measured. The rotor was mounted on a 6 component balance in the fixed frame but the shaft torque was measured independently using a torque sensor. A dynamic calibration of the rotor stand was performed to allow extraction of the vibratory hub loads.

The test conditions evaluated in this chapter are listed in table 5.3. Above advance ratios of 1.2, trimming the analysis became more challenging and as a result, a complete sweep is not shown. Results available from the test include the performance, blade loads and vibrations data (corrected after dynamic calibration of the test stand). Finally, the data from the pressure sensors was not sufficient to integrate sectional airloads, although measurements from individual sensors provide some insight into the analysis.

Table 5.3: Test conditions for the Maryland rotor tests.

Rotor	Maryland 2014
RPM Reduction	26% & 30%
Shaft Angle (Degrees)	0°,2°,4°
Wind Speed (knots)	0-125
Advance Ratio	1.20
Dynamic Calibration	For 700 RPM cases only
Fuselage	no

5.3 High Advance Ratio Performance Validation

The following section presents the baseline validation of the high advance ratio performance predictions, including descriptions of key high advance ratio phenomena. The prediction of rotor thrust at high advance ratios will introduce the concept of thrust reversal and discuss the limitations of the analysis. This is followed by the

predictions of shaft power and rotor drag, which determine lift-to-drag ratio and finally the trim cyclic controls are correlated.

5.3.1 Thrust Prediction

Figure 5.3 shows the validation of thrust versus collective for a range of advance ratios (μ) increasing from 0.25 to 1.2. The predicted thrust agrees with the experiment very well at $\mu = 0.25$, which is the expectation for this relatively low advance ratio. Advance ratios of 0.41 and 0.62 continue to be predicted well with some evidence of premature stall being predicted at 10° collective for $\mu = 0.41$ and a small thrust offset at $\mu = 0.62$. The slopes are well predicted and show that the sensitivity of thrust to collective is decreasing with increasing advance ratio. The trend comes from increasing flow asymmetry, resulting in increasing roll moment imbalance, which limits thrust. At an advance ratio of 0.825, the measured thrust is almost insensitive to collective. For advance ratios above 0.825, there is an increased scatter in the experimental data, attributed to challenges associated with trimming the rotor at high advance ratios. The blade flapping motions show larger dissimilarity between blades at high advance ratios, which could be due to perceived small aerodynamic and inertial differences between blades. At advance ratios of 1.03 and 1.2, the measured thrust decreases with increasing collective. This behavior is termed thrust reversal, a high advance ratio phenomena seen in the Jenkins tests [51] and the UH-60A tests [59]. The analysis shows a mixed correlation. Over a range of low collectives (-3° to 3°), a negative thrust slope is predicted, which is in gen-

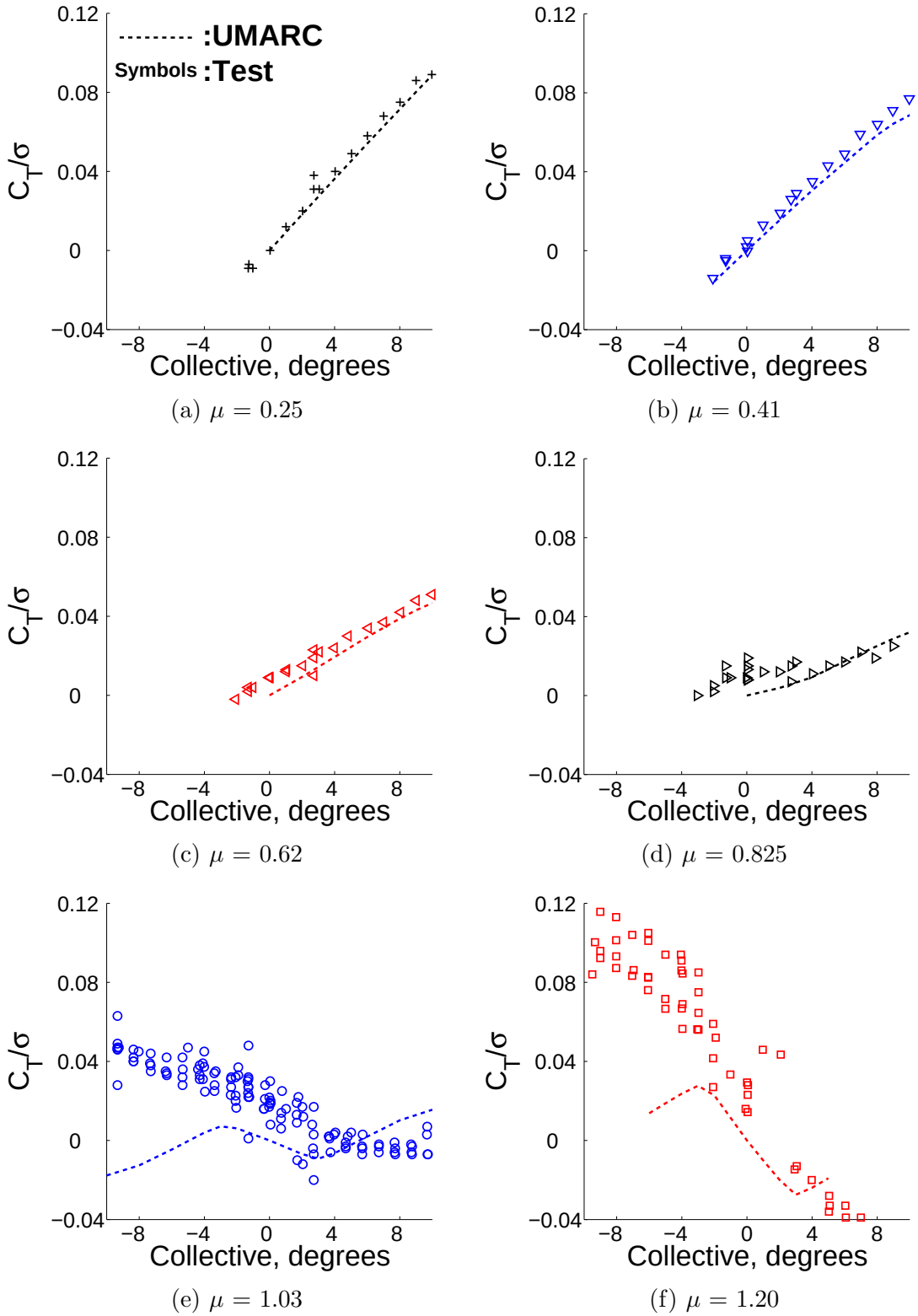

(a) $\mu = 0.25$

(b) $\mu = 0.41$

(c) $\mu = 0.62$

(d) $\mu = 0.825$

(e) $\mu = 1.03$

(f) $\mu = 1.20$

Figure 5.3: Rotor thrust versus collective, $\alpha_s = 0°$.

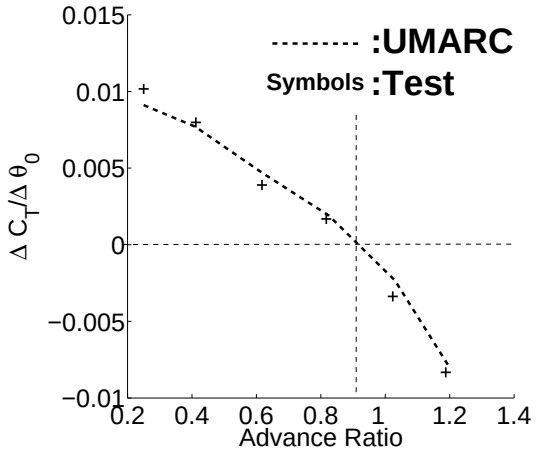

Figure 5.4: Change of thrust slope with advance ratio, $\alpha_s = 0°$.

eral agreement with the experiment. Increasing the absolute collective results in an abrupt change in the predicted thrust, and the thrust slope changes from negative to positive, which is maintained for larger collectives.

The change in slope of the thrust with increasing advance ratios is summarized in fig. 5.4 for 0° shaft angle. Only small collectives around 0° are considered in evaluating the slope. The agreement is very good for all advance ratios and shows that thrust reversal occurs near an advance ratio of $\mu = 0.9$, for this rotor.

Table 5.4: Trim controls spanning thrust reversal at $\mu = 1.03$.

Collective	Lateral cyclic	Longitudinal cyclic
0.0°	0.00°	0.00°
2.0°	0.30°	-2.46°
3.0°	0.45°	-3.70°
4.0°	0.60°	-4.91°
6.0°	1.00°	-7.20°

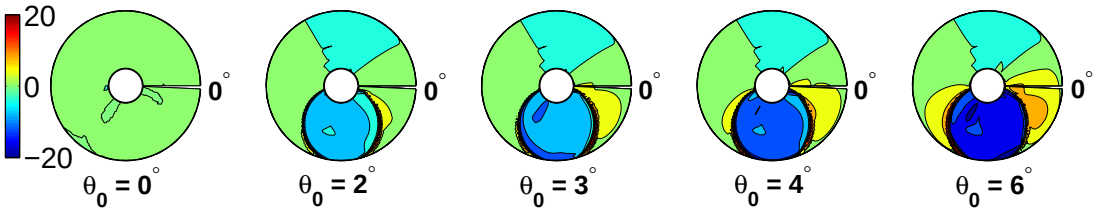

(a) Angle of attack distribution, degrees.

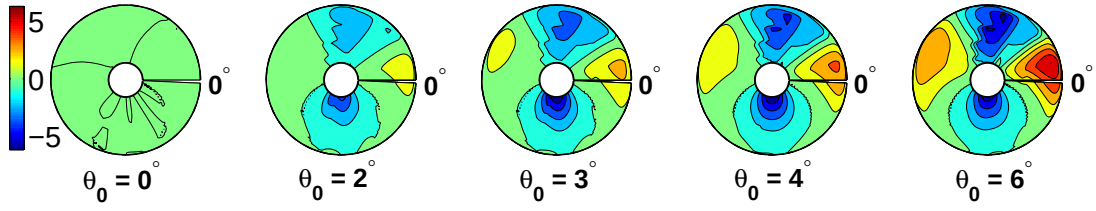

(b) Normal force distribution, lb/ft.

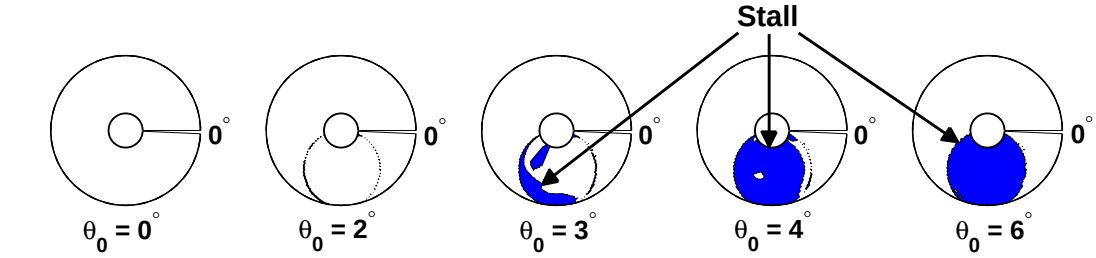

(c) Stall locus (shaded regions are stalled).

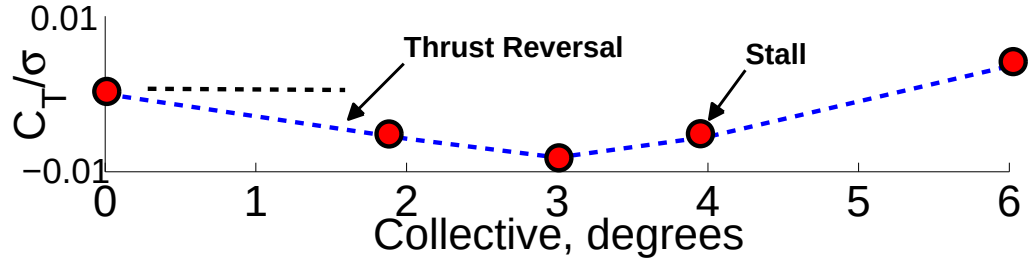

(d) Rotor thrust versus collective.

Figure 5.5: Airloads showing thrust reversal trend with increasing collective, $\mu = 1.03$, $\alpha_s = 0°$.

5.3.2 Physics of Thrust Reversal Prediction

Figure 5.5 shows the predicted airload distribution at an advance ratio of 1.03 and for collectives from 0° to 6.0°, which corresponds to both thrust reversal and the change in thrust slope thereafter. The contours include the angle of attack and normal force distributions; the stall distribution, which is determined by comparing the local angle of attack to the static lift stall angles; and finally the thrust behavior from fig. 5.3e is repeated. The corresponding trim cyclics are listed in table 5.4. The angle of attack and normal force distributions (figs. 5.5a and 5.5b respectively) show that both the advancing and retreating sides are negatively loaded for positive collectives at this advance ratio. The retreating blade is entirely in reverse flow so that positive collectives results in negative pitch and thereby negative lift, relative to the flow. Longitudinal cyclic maintains the advancing rotor at a negative pitch to balance lateral trim. The fore and aft rotor lift increases with collective and is biased somewhat to the advancing side because of higher dynamic pressure. Thrust reversal occurs when the negative lift created in the reverse flow is larger than the balance of lift on the advancing rotor. The magnitude of reverse flow lift will be influenced by the size of the reverse flow region (advance ratio), the dynamic pressure at the inboard blade end (root cut-out) and the aerodynamic description of the inboard blade (chord, camber, and lift coefficient). In the analysis, thrust reversal ends abruptly between 3° and 4° collective. The stall contour plot (fig. 5.5c) indicates that between 3° and 4° collective, the reverse flow angles of attack are exceeding the reverse flow lift stall angle (7.5° relative to the flow) and thereby stalling. The

lift in the reverse flow stagnates and no longer increases linearly with collective (fig. 5.5b 4° and 6° collective), lift on the fore and aft continue to increase linearly and dominate the rotor thrust resulting in the return to positive thrust slopes and the end of thrust reversal.

The predicted lift shows an abrupt change in thrust slope at ±4°, which is somewhat supported by the measured thrust, but with a lesser change in slope. Figure 5.6a shows the measured and predicted thrust at $\mu = 1.03$ with a trend line for the measured data, which clearly shows the change in slope of the measured thrust at large positive and negative collectives. From the preceding analysis, thrust reversal should appear in the trim cyclics corresponding to the change in thrust slope. The measured and predicted lateral cyclic at $\mu = 1.03$ is shown in fig. 5.6b where both indicate a change in slope corresponding to the predicted thrust reversal phenomena (±4° collective). The strong correlation suggests that the reverse flow is indeed stalling as predicted, but that lift in the reverse flow does not drop off as fast as in the prediction.

The discrepancy in thrust reversal at high collectives ($\theta_0 > \pm\ 4°$) can be attributed to reverse flow dynamic stall. Preliminary pressure data from the test in fig. 5.7a (the magnitudes are shifted to clarify the result) shows a dynamic stall like vortex moving from the geometric trailing edge towards the leading edge in the reverse flow at $\mu = 1.20$. A similar result was shown in the UH-60A tests [59]. Figure 5.7b shows the change in pressure at a single chordwise station (0.79 x/c, near the leading edge relative to the reverse flow), which shows a peak in pressure in the reverse flow beginning between 2.6° and 3.7° collective. The analysis does

not yet include a reliable dynamic stall model for the reverse flow, needed to model the effect of dynamic stall on rotor thrust.

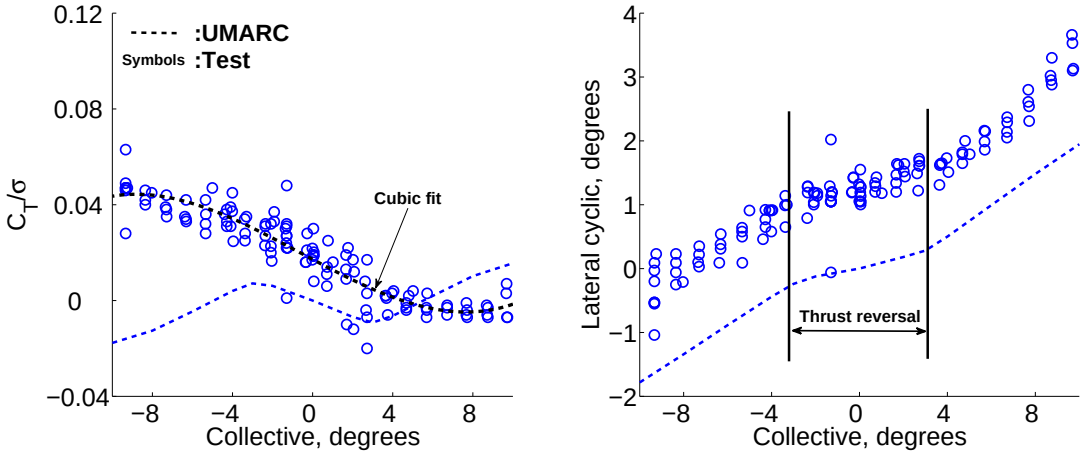

(a) Thrust reversal with trends. (b) Lateral cyclic at thrust reversal.

Figure 5.6: Rotor trim cyclic at thrust reversal, $\mu = 1.03$, $\alpha_s = 0°$.

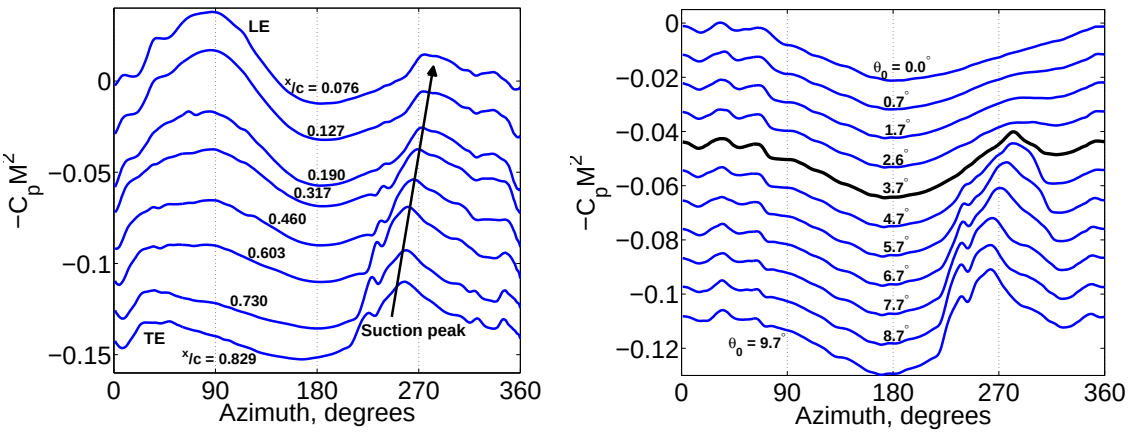

(a) Upper surface pressure, $\mu = 1.2$, θ_0 = -6°. (b) Lower surface pressure at $x/c = 0.79$.

Figure 5.7: Pressure distribution at 30% radius showing a) progression of dynamic stall vortex along chord in reverse flow, and b) dynamic stall pressure peak with increasing collective.

5.3.3 Shaft Power and Rotor Drag

The correlation of predicted shaft power with the wind tunnel tests for advance ratios from 0.25 to 1.2 is shown in fig. 5.8 and this overall shows a good agreement, especially at lower collectives. At $\mu = 0.825$, just before thrust reversal, the correlation is excellent and shows that the shaft power is nearly insensitive to collective. At $\mu = 1.03$ and 1.2, the shaft power trend is decreasing as the magnitude of collective increases. The analysis predicts the concave trend, but begins to under-predict the decrease in power at larger collectives. The decrease in shaft power at high advance ratios is from reverse flow drag that acts to accelerate the rotor. At high advance ratios, the analysis under-predicts reverse flow drag, possibly also due to missing dynamic stall model.

The correlation of UMARC with the measured rotor drag is shown in fig. 5.9. The general trends of the rotor drag are reasonably well predicted, but with a zero offset. The measured rotor drag at lower advance ratios is often negative at all collectives, which is not expected and suggests that the zero error lies in the experiment rather than in the analysis. The rotor drag measurement is determined after subtracting the tare of the stand and hub from the measured drag. The rotor drag is relatively small compared to the stand and this can introduce the error. At higher advance ratios, the rotor drag increases and the agreement between the analysis and measurement improves.

The rotor drag and the shaft power describe the total power and the equivalent drag (D_e) that help to determine the lift-by-drag ratio ($^L/_D$) of the rotor:

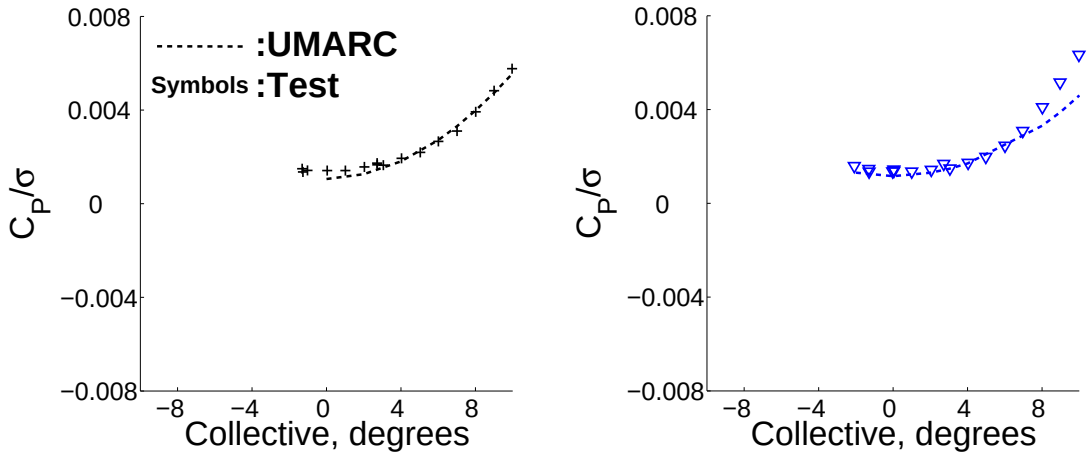

(a) $\mu = 0.25$

(b) $\mu = 0.41$

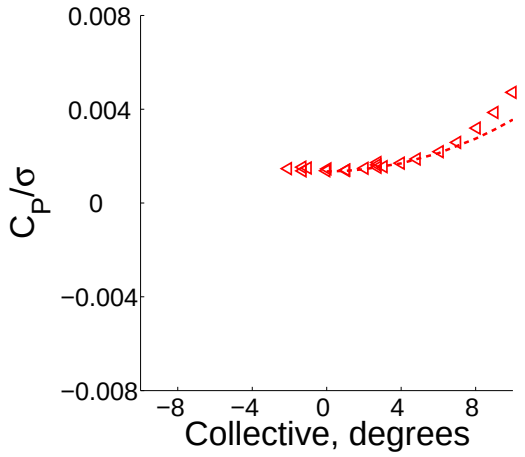

(c) $\mu = 0.62$

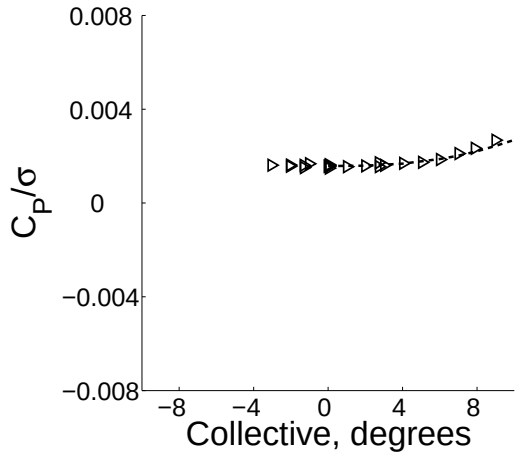

(d) $\mu = 0.825$

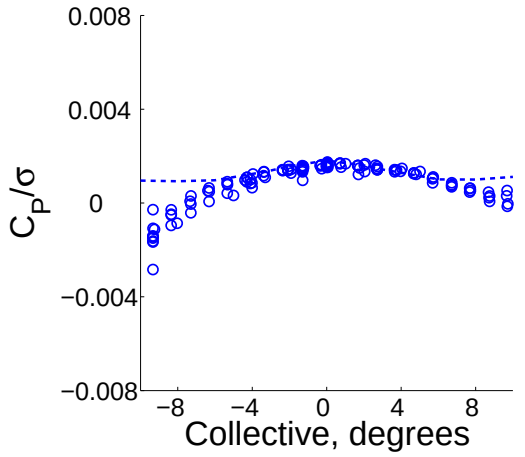

(e) $\mu = 1.03$

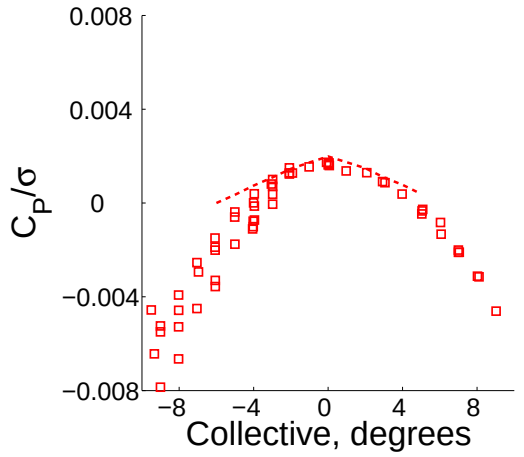

(f) $\mu = 1.20$

Figure 5.8: Shaft power versus collective, $\alpha_s = 0°$.

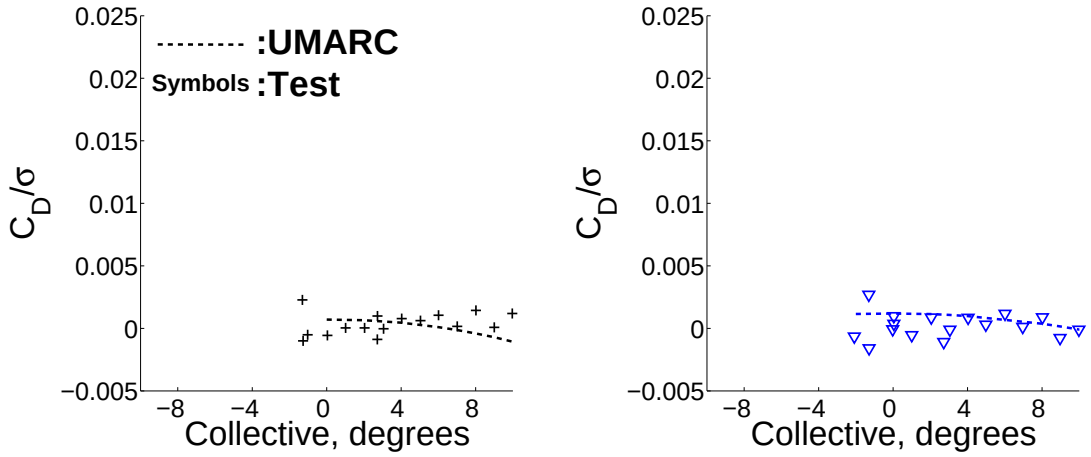

(a) $\mu = 0.25$

(b) $\mu = 0.41$

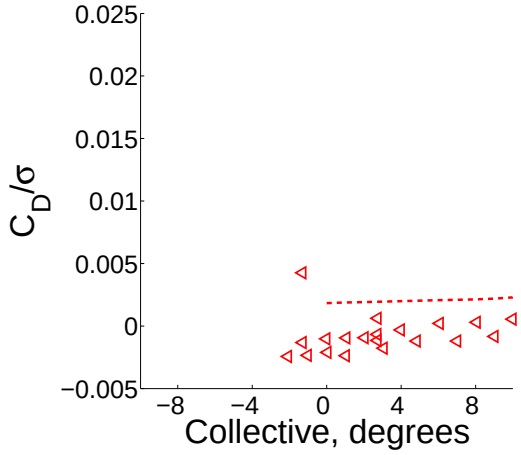

(c) $\mu = 0.62$

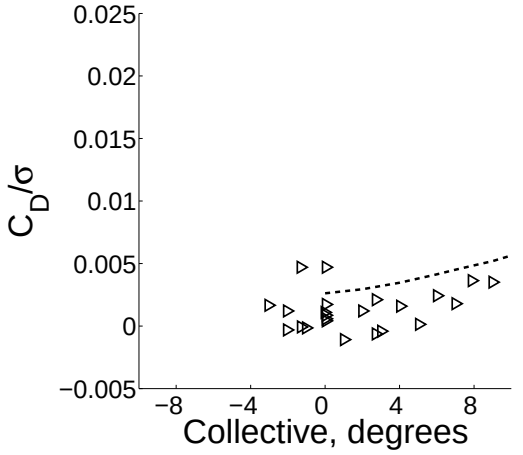

(d) $\mu = 0.825$

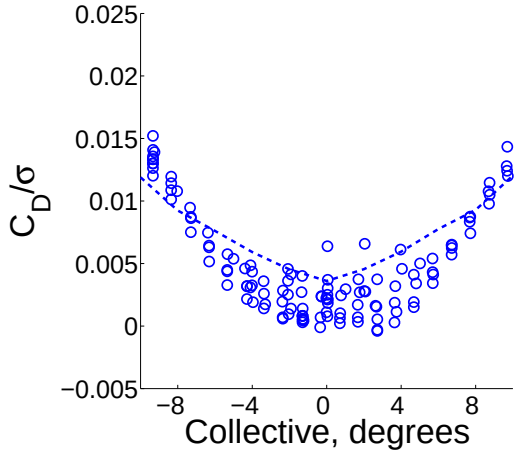

(e) $\mu = 1.03$

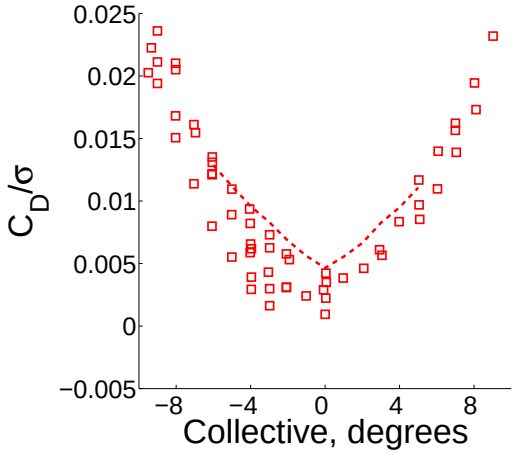

(f) $\mu = 1.20$

Figure 5.9: Shaft drag versus collective, $\alpha_s = 0°$.

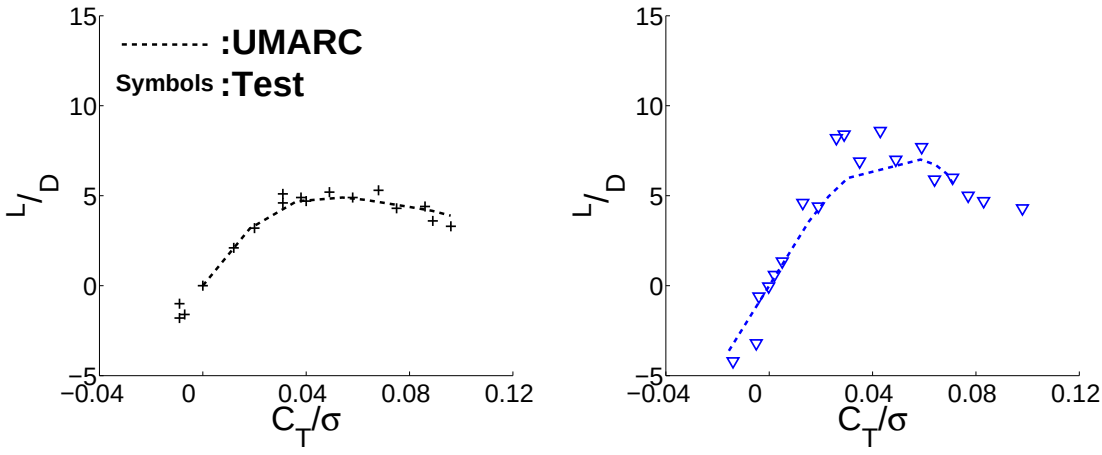

(a) $\mu = 0.25$ (b) $\mu = 0.41$

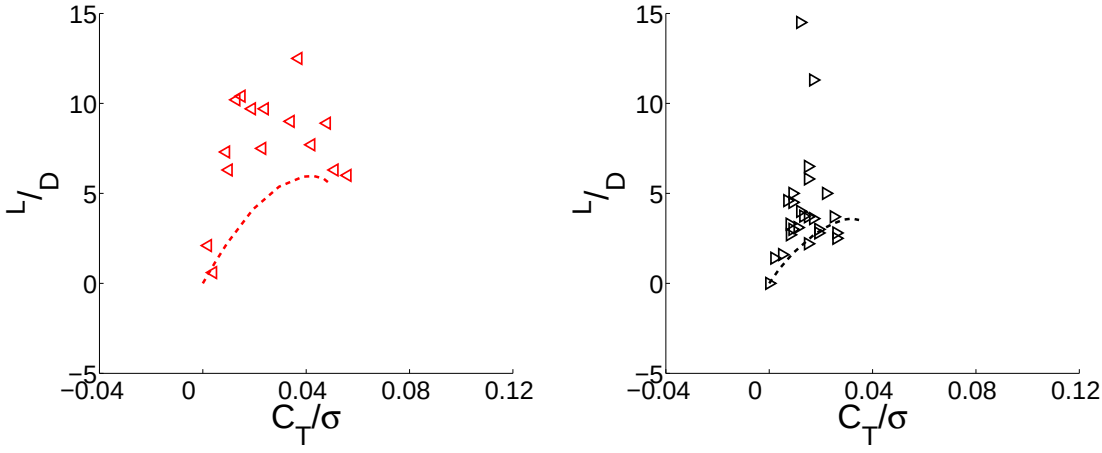

(c) $\mu = 0.62$ (d) $\mu = 0.825$

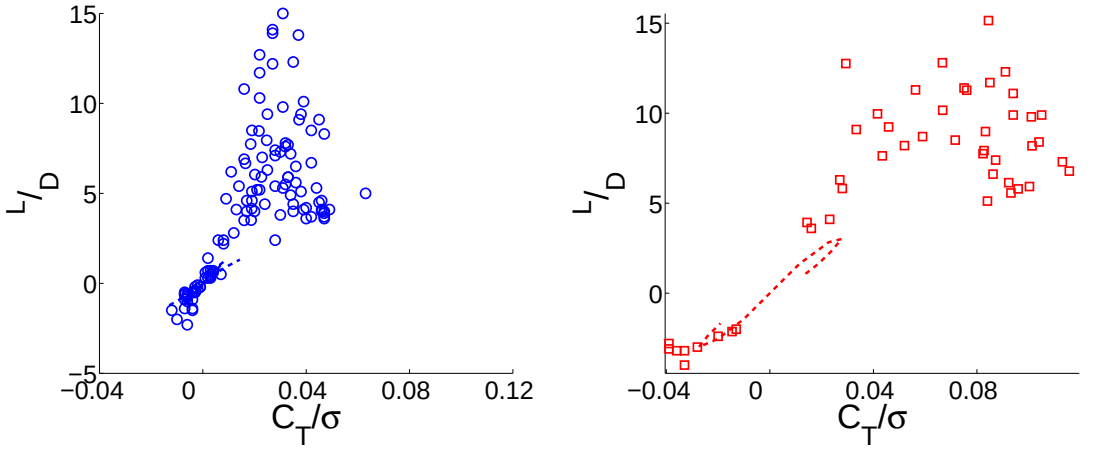

(e) $\mu = 1.03$ (f) $\mu = 1.20$

Figure 5.10: Rotor lift-to-drag ratio versus thrust, $\alpha_s = 0°$.

$$C_{DE} = \frac{C_P}{\mu} + C_D \tag{5.1}$$

$$\frac{L}{D} = \frac{C_L}{C_{DE}} \tag{5.2}$$

The lift-to-drag predictions and measurements are shown in fig. 5.10. At the lower advance ratios, $\mu = 0.25$ and 0.41, the prediction agrees well with experiment. For these cases, the very good thrust and power predictions outweigh the differences in the prediction of drag (drag values are small). At advance ratios of 0.62 and 0.825, the lift-to-drag ratio is under-predicted by the analysis despite the thrust and power prediction remaining good. The difference comes from the difference in the drag force prediction. The measured drag is sometimes negative and with large scatter resulting in higher lift-to-drag values. At $\mu = 1.03$ and 1.20, the correlation is poor. This is perhaps due to the poor prediction of thrust at larger collectives as a result of the premature and abrupt end to thrust reversal predicted by the analysis. The scatter in the experiment comes from uncertainty in the rotor drag measurement, but plays a lesser role in the overall correlation.

5.3.4 Trim Cyclics

The validation of lateral (θ_{1C}) and longitudinal (θ_{1S}) cyclics are shown in fig. 5.11. The lateral cyclic trend is reasonably well predicted, but with an offset of about 1° to 2°. It has already been pointed out that the trend at high advance ratios around thrust reversal are very well represented by the analysis. The lateral

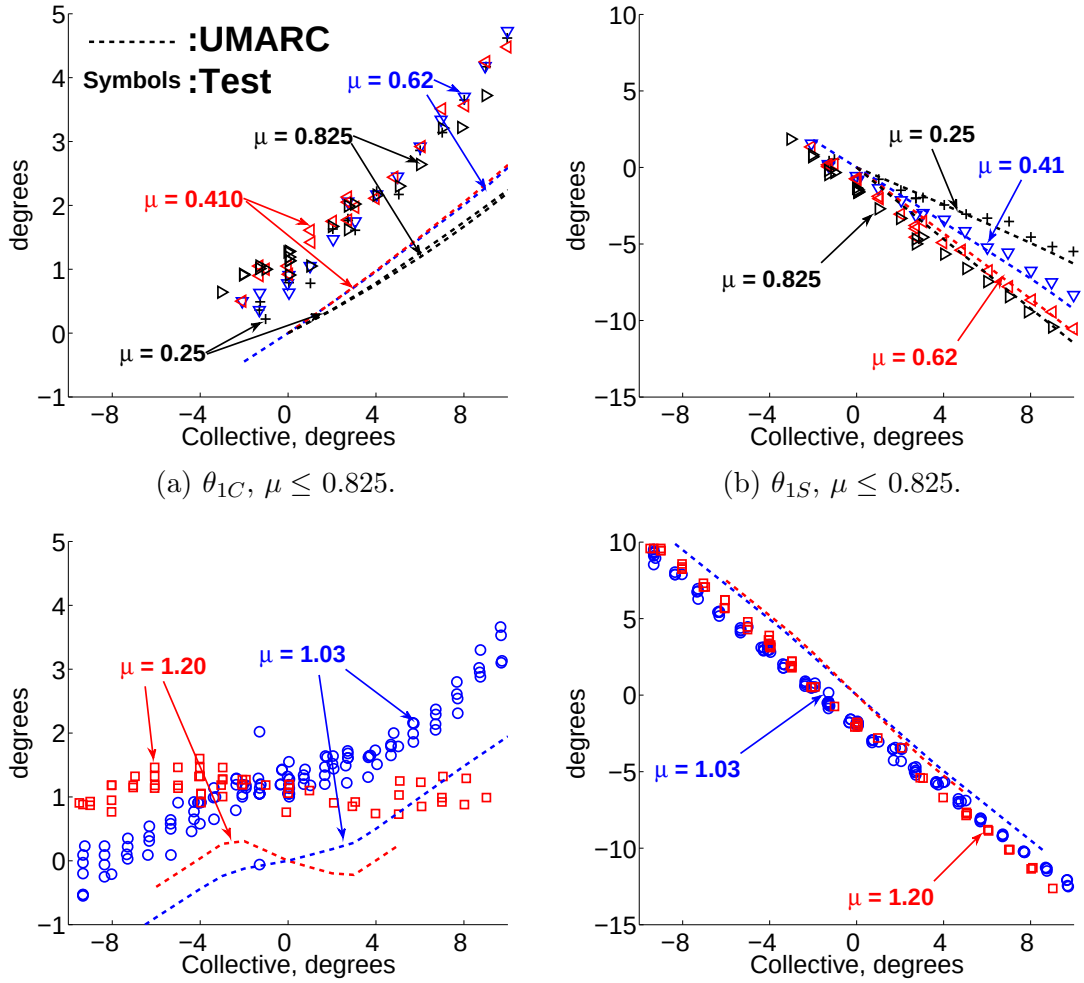

(a) θ_{1C}, $\mu \leq 0.825$.

(b) θ_{1S}, $\mu \leq 0.825$.

(c) θ_{1C}, $\mu > 0.825$.

(d) θ_{1S}, $\mu > 0.825$.

Figure 5.11: Trim cyclics versus collective, $\alpha_s = 0°$.

cyclic offset could be due to disturbances in the flow from the hub, which affects the lift on the aft rotor. Longitudinal cyclic is well predicted at all advance ratios with an offset for the higher advance ratio cases only.

5.4 High Advance Ratio Studies

The discussion of several factors that can impact the prediction of thrust reversal and thrust at high advance ratios are discussed.

i **Shaft angle:** An aft shaft tilt changes the increases the vertical flow component (u_p), alters the reverse flow angles of attack and therefore affects reverse flow stall behavior.

ii **Blade root pitch:** Blade twist results in a positive pitch bias of the root relative to the 75% station, which will effect when the reverse flow begins to stall.

iii **Reverse flow stall:** The baseline C-81 airfoil tables used in the analysis are not reliable in reverse flow. Stalling at higher (reverse flow) angles would extend the thrust reversal over larger collective ranges.

iv **Root cut-out:** Thrust produced at the inboard region of the reverse flow determines when thrust reversal occurs and at what magnitude. The root cut-out and advance ratio define the dynamic pressures at the blade root.

v **Yawed flow corrections:** The radial flow component is generally ignored under the independence principle. It has been shown experimentally that radial flow can delay stall, an important component to thrust reversal prediction.

vi **Unsteady loads:** The airfoil entering and leaving the reverse flow is subject to large equivalent pitch rates ($\dot{\alpha}$) that will induce unsteady loads and possible reverse flow dynamic stall.

vii **Manufacturing inconsistencies:** Despite the general high quality of the test data, the rotor blades were each individually handmade which could introduce unknowns including inaccurate airfoil shapes and inter-blade dissimilarity.

Some of these are discussed in this section.

5.4.1 Shaft Angle

The test data included some limited results at 4° aft shaft angle. Figure 5.12 presents the performance measurements and predictions for the 4° aft shaft angle at an advance ratio of 1.03. There are two predictions from UMARC, at 4° and 6° shaft angles. The initial results from the analysis at 4° show a large under-prediction of thrust in fig. 5.12a. Part of the discrepancy can be explained by the trim condition of the rotor. Figure 5.12b shows the β_{1C} flapping angles for all four blades. The rotor was trimmed for blade 1 but blades 2–4 have a consistent 1°–2° β_{1C} flapping (nose up), effectively increasing the aft shaft angle. The analysis was repeated at 6° aft shaft angle to account for this and improves the thrust prediction but it remains under-predicted. The generally less satisfactory predictions for the aft shaft tilt cases is as of yet unresolved and the subject of future investigation, both by experiment and analysis.

Both test data and the analysis show that the region of thrust reversal is shifted

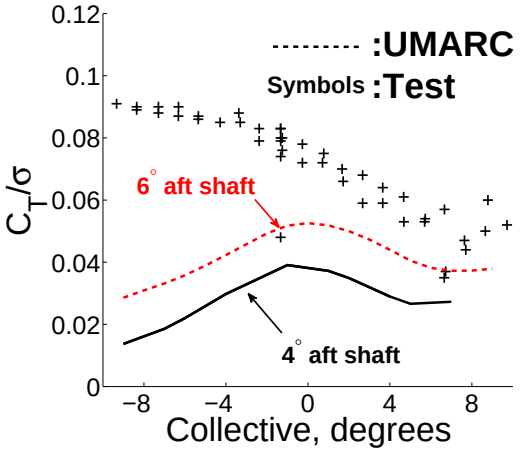

(a) Thrust.

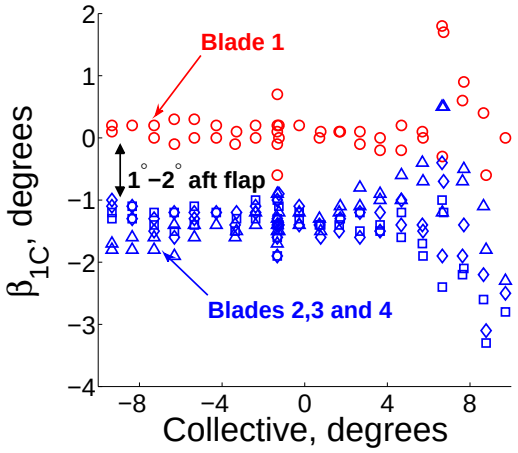

(b) β_{1C} flapping.

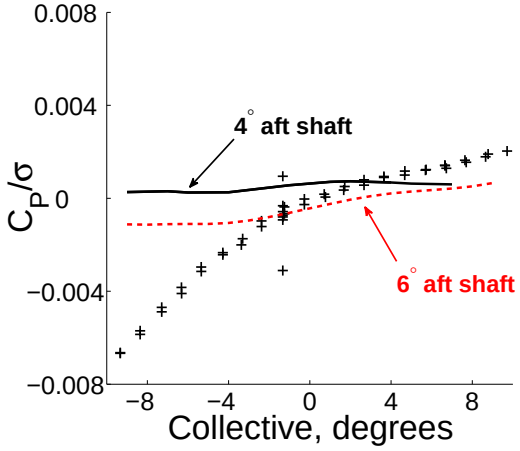

(c) Shaft power.

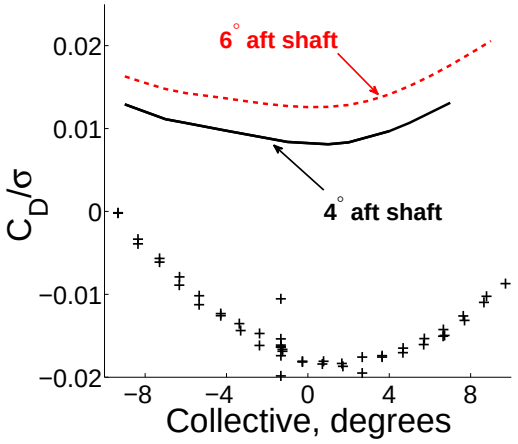

(d) Drag.

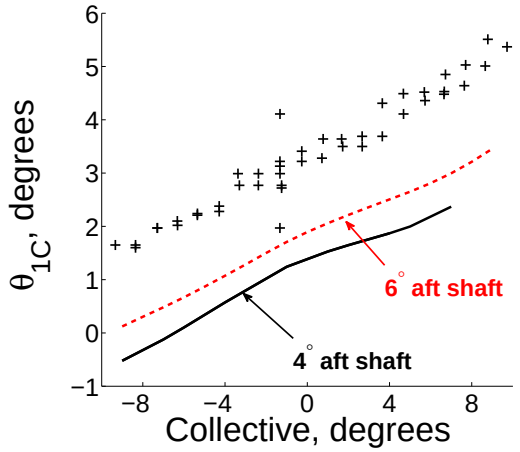

(e) Lateral cyclic.

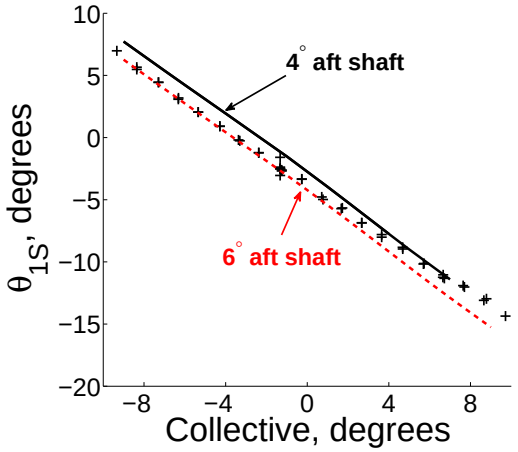

(f) Longitudinal cyclic.

Figure 5.12: Thrust reversal with 4° aft shaft angle, including a correction for flapping, $\mu = 1.03$.

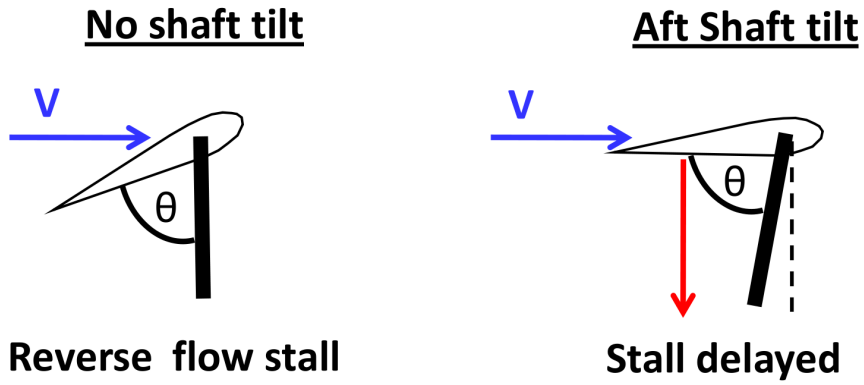

Figure 5.13: Aft shaft angle delays stall in reverse flow to higher collectives.

to higher positive collectives by aft shaft angle. Figure 5.13 shows an airfoil section at a constant pitch with and without aft shaft angle. Aft shaft angle introduces a bias to the reverse flow pitch, equal to the shaft angle. Stall is effectively delayed by 4°, supported by the measured data.

The shaft power prediction is poor (fig. 5.12c), particularly at large negative collectives where the analysis does not prediction the large negative power. The measured drag is negative, implying that the rotor produces a strong forward force with an aft shaft angle. The analysis predicts the drag force trend but with positive drag force, increasing in magnitude the correction for blade flapping (fig. 5.12d). The cyclics prediction is good and retains the constant offset in lateral cyclic.

5.4.2 Blade Twist

Blade twist applies a bias to the root pitch relative to the collective setting. At 0° collective, the root pitch for the blade with -16° twist is near -8° relative to the reverse flow, and already at the reverse flow stall boundary (see the stall boundary

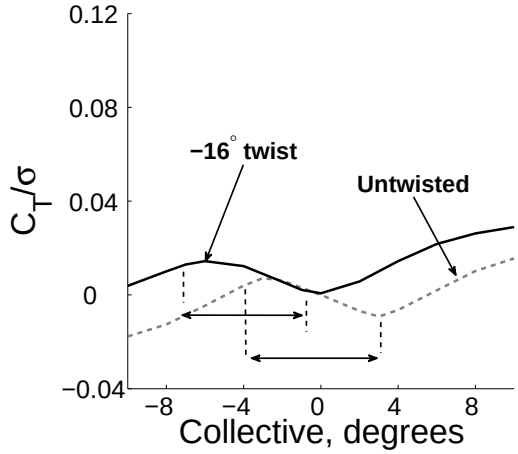

(a) Rotor thrust versus collective.

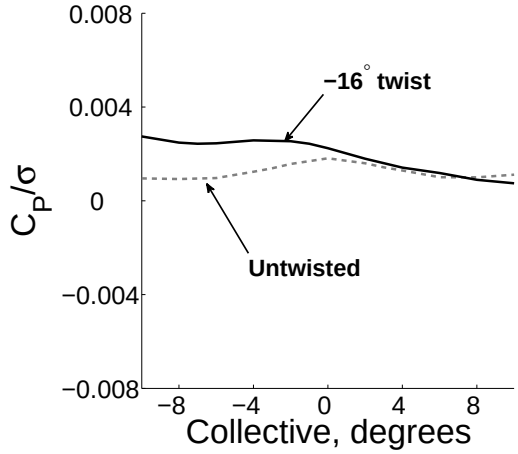

(b) Shaft power versus collective.

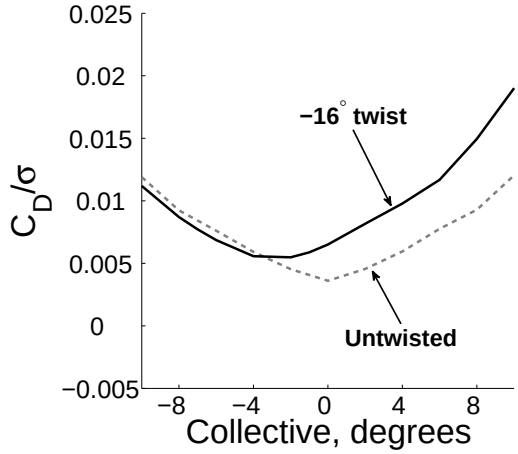

(c) Rotor drag versus collective.

Figure 5.14: Effect of negative blade twist on performance and thrust reversal, $\mu = 1.03$, $\alpha_s = 0°$.

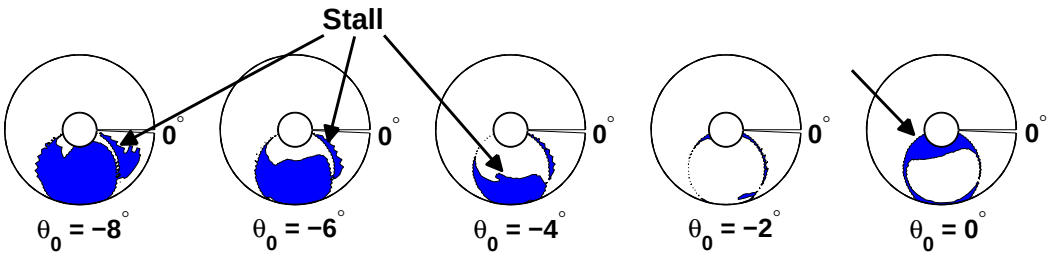

Figure 5.15: Stall locus for a rotor with blade twist (shaded regions are stalled), μ = 1.03, $\alpha_s = 0°$.

in fig. 5.15). Twist therefore shifts the region of thrust reversal to more negative collectives as shown in fig. 5.14a. The thrust reversal is somewhat less linear than for the untwisted rotor because the rotor stalls more progressively (from tip towards the root) rather than abruptly for the untwisted case. The predicted power is no longer symmetric, requiring more power for negative collectives, and is not centered about 0° collective. Power increases relative to the untwisted rotor for negative collectives because of higher drag on the fore and aft rotor, which are near stall (see fig. 5.15 at -8°). The rotor drag remains nominally symmetric because the increased drag on the fore and aft rotor are not resolved into the axial direction.

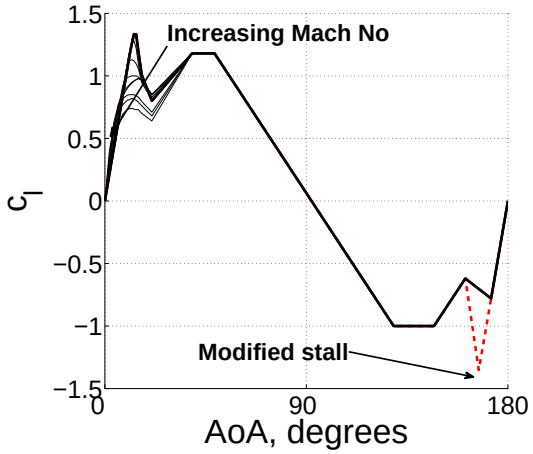

(a) Modified NACA0012 airfoil tables.

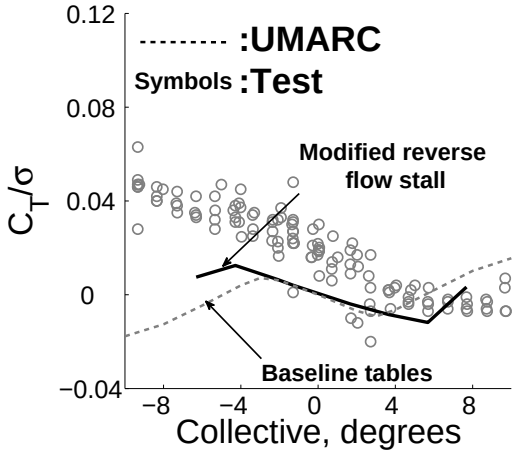

(b) Thrust reversal at $\mu = 1.03$.

Figure 5.16: Thrust reversal with modified tables.

5.4.3 Reverse Flow Stall

The limits of the predicted thrust reversal are determined by stall in the reverse flow. Figure 5.16a shows the baseline NACA0012 lift coefficient used in this study showing a reverse flow stall angle at 172.5° (7.5° relative to the flow direction). Also shown is a modified reverse flow stall angle chosen to match the stall angle of forward flow (13° relative to the flow). The modified thrust prediction is shown in fig. 5.16b and shows that the region of thrust reversal is elongated, but the abrupt change in thrust remains, now at 6° rather than at 3° collective.

5.4.4 Root Cut-out

The effect of the root cut-out on thrust, power and drag is shown in fig. 5.17. Extending the root cut-out to 30% (from 22.5%) removes the highest dynamic pressure region of the reverse flow and this delays thrust reversal to higher advance ratios. Delayed thrust reversal is shown by the decreased slope for the 1.03 advance ratio case in fig. 5.17a. The thrust for the low advance ratio case ($\mu = 0.825$) is not affected. Figure 5.18 shows the change in thrust slope with advance ratio for the two root cut-out sizes. The advance ratio when the thrust is insensitive to collective moves from near $\mu = 0.9$ towards 1.0 with the larger root cut-out. Both the power and drag decrease for the larger root cut-out, but this is misleading because there is no drag assigned to the region from 22.5% to 30% radius for the larger root cut-out case.

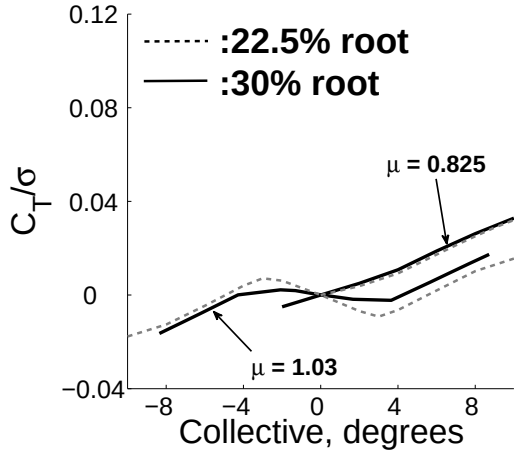

(a) Rotor thrust versus collective.

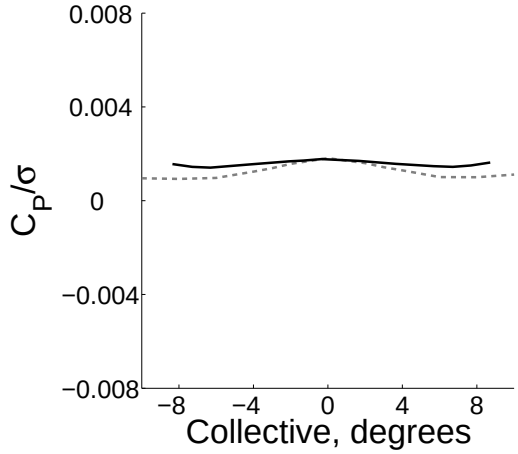

(b) Shaft power versus collective.

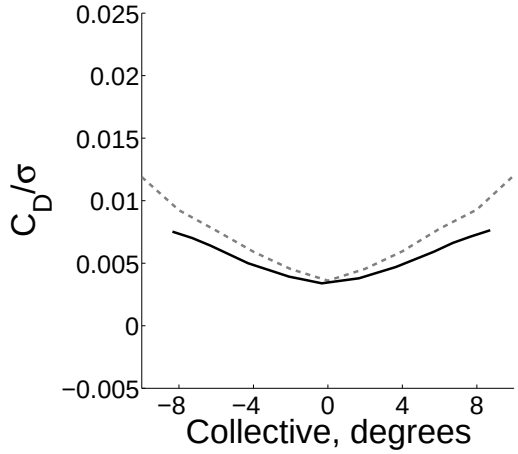

(c) Rotor drag versus collective.

Figure 5.17: Effect of root cut-out on performance, $\mu = 1.03$, $\alpha_s = 0°$.

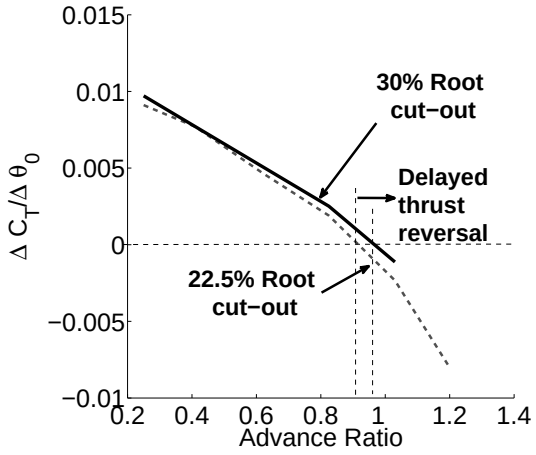

Figure 5.18: Effect of root cut-out on thrust slope with advance ratio, $\alpha_s = 0°$.

5.4.5 Yawed Flow Corrections

$$c_l(\alpha) = \frac{c_{l_{2D}}(\alpha cos^2\Lambda)}{cos^2(\Lambda)} \tag{5.3}$$

$$c_d(\alpha) = \frac{c_{d_{2D}}(\alpha cos\Lambda)}{cos(\Lambda)} \tag{5.4}$$

The radial component of flow, u_r, is often ignored and the airfoil coefficients are assumed to depend on the perpendicular velocity components only. However, both CFD and experiment [112, 113] have shown that radial flow impacts drag and stall for incompressible flows. The yawed flow corrections in (5.3) and (5.4) are from Johnson [111] and correct the lift and drag coefficients for yawed flow angle, Λ. The yawed flow correction does not affect lift coefficient below stall, but acts to delay stall to higher angles of attack. Drag coefficient is generally increased even below stall. The effect of the yawed flow corrections on thrust, power and drag are

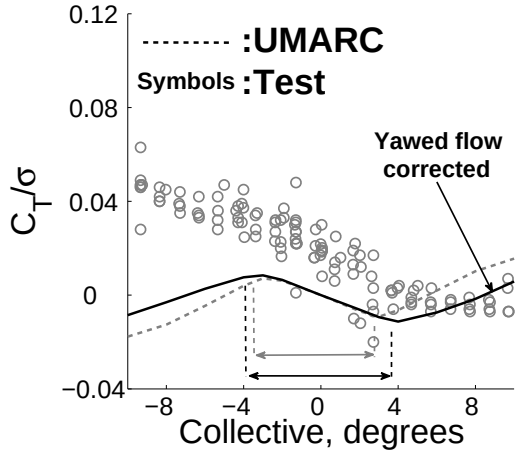

(a) Rotor thrust versus collective.

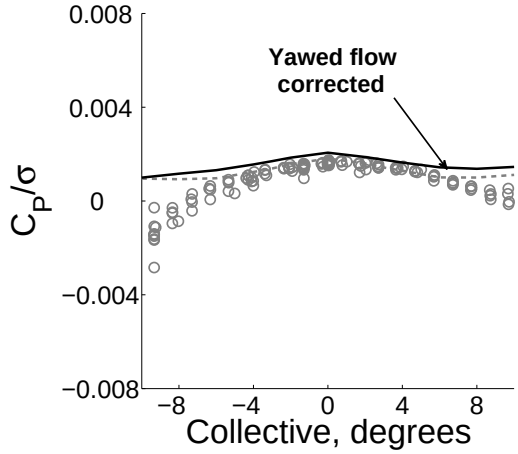

(b) Shaft power versus collective.

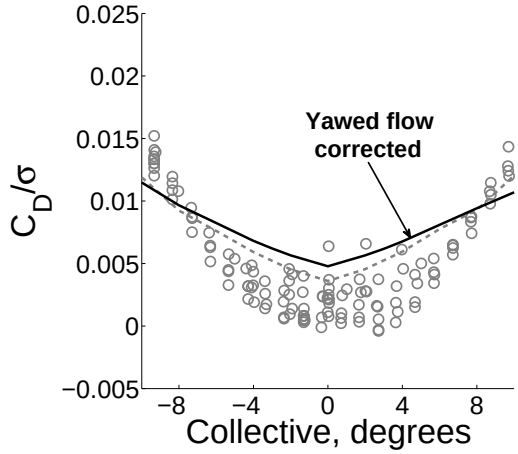

(c) Rotor drag versus collective.

Figure 5.19: Effect of yawed flow corrections on performance, $\mu = 1.03$, $\alpha_s = 0°$.

shown in fig. 5.19. The region of reverse flow is increased due to delaying stall in the reverse flow, drag and shaft power increase due to increased drag on the yawed sections. The post stall behavior is not significantly modified and there remains an abrupt change of slope.

5.5 High Advance Ratio Structural Loads

Figure 5.20 shows the fanplot generated for the UM-2014 rotor test and highlights the two rotor speeds used for the current results (700 RPM for μ 0.25 to 1.03 and 600 RPM for $\mu = 1.2$). To generate the fanplot, the blade sectional properties (table 5.2) were determined experimentally. Uncertainty in the stiffness measurements is due to the difficulty in measuring the deflections for relatively stiff blades. $\pm 10\%$ uncertainty in the flapwise and torsional stiffness values are illustrated by the widening of the flap mode frequencies. Near 600 and 700 RPM, the second flap mode approaches 4/rev, within the stiffness measurement error, third flap can be between 8 and 10/rev and the torsion mode is between 13 to 14/rev for 700 RPM and higher for 600 RPM.

5.5.1 Flap Bending Loads

Figure 5.21 shows the predicted and measured flap bending moment at 50% radius. At the 0.25 advance ratio case with little reverse flow, the analysis predicts the flap bending trend but under-predicts the magnitude. For advance ratios between 0.41 to 0.825, the analysis does not show a good correlation with the test

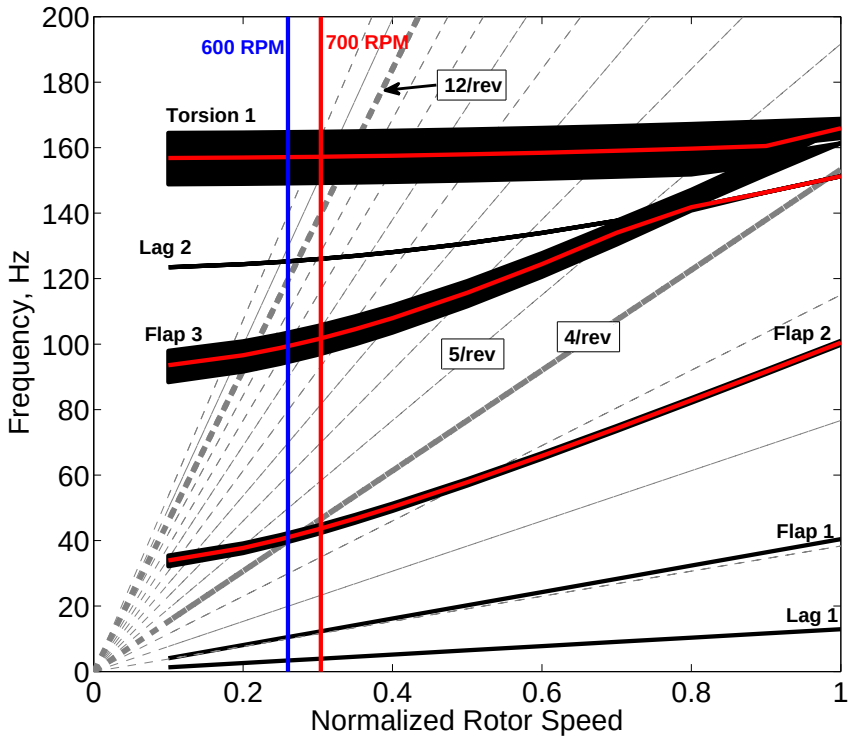

Figure 5.20: Fanplot for 2014 Maryland rotor, highlighting the RPM important for these results.

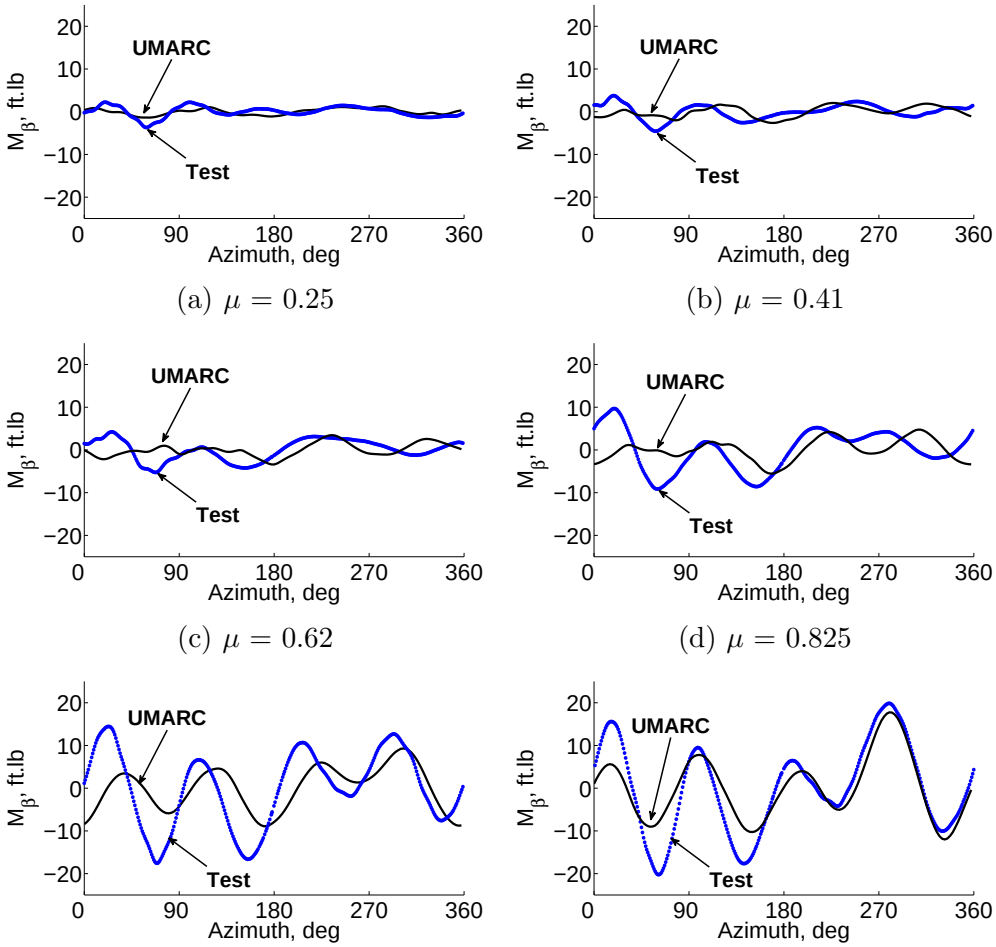

(a) $\mu = 0.25$ (b) $\mu = 0.41$

(c) $\mu = 0.62$ (d) $\mu = 0.825$

(e) $\mu = 1.03$ (f) $\mu = 1.20$

Figure 5.21: Oscillatory flap bending moment (M_{Flap}) at r/R = 50%, $\theta_0 = 4°$, $\alpha_s = 0°$.

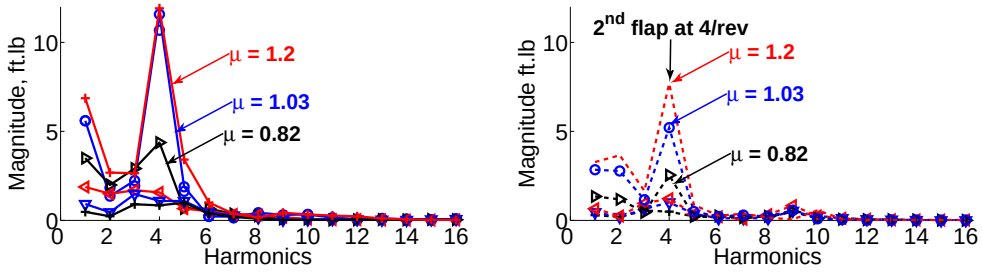

(a) Test. (b) UMARC.

Figure 5.22: Harmonics of flap bending moment at r/R = 50%, $\theta_0 = 4°$, $\alpha_s = 0°$.

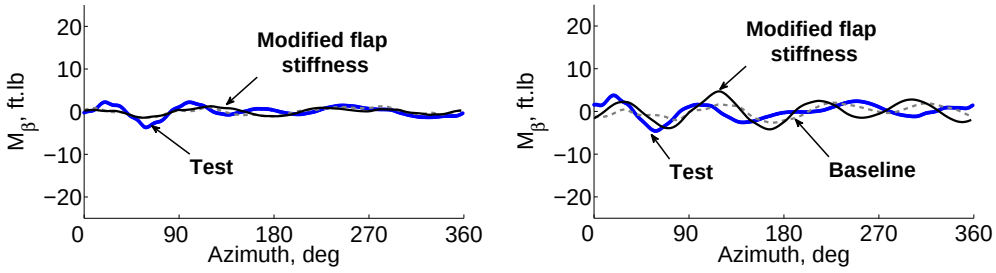

(a) $\mu = 0.25$

(b) $\mu = 0.41$

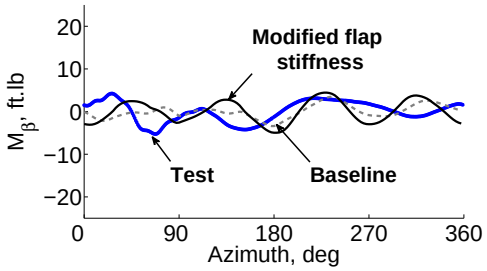

(c) $\mu = 0.62$

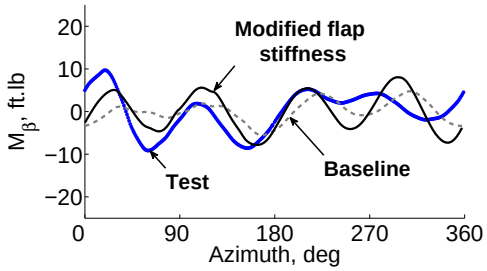

(d) $\mu = 0.825$

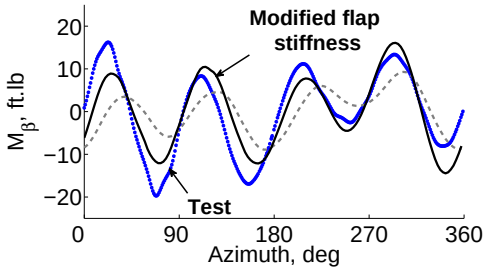

(e) $\mu = 1.03$

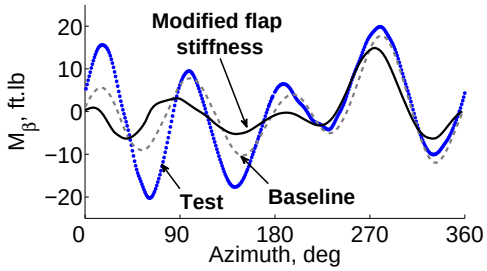

(f) $\mu = 1.20$

Figure 5.23: Sensitivity of flap bending to 2^{nd} flap at 3.7/rev (dashed) and 4/rev (solid) at r/R = 50%, $\theta_0 = 4°$, $\alpha_s = 0°$.

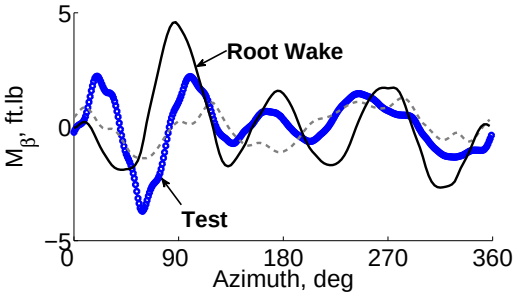

(a) Flap bending moment with root trailer.

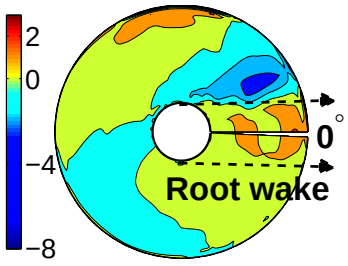

(b) Change in normal force ($\Delta C_N M^2$).

Figure 5.24: Effect of root wake trailer on flap bending loads at r/R = 50%, $\theta_0 = 4°$, $\alpha_s = 0°$.

data. However, the peak-to-peak magnitude is comparatively small. The prediction improves somewhat at advance ratios of 1.03 and at 1.2, where the trend and the phase of the dominant 4/rev loading is predicted well by the analysis. The harmonic content of flap bending is shown in fig. 5.22 and compares the predicted and measured harmonics. The dominant 4/rev harmonic component increases with advance ratio and is caused by excitation of the second flap mode. The analysis predicts the 4/rev harmonic trend with advance ratio, but it is under-predicted compared to the test.

The flap bending moment prediction is somewhat contrary to the good general prediction of the UH-60A slowed rotor at high advance ratio shown in the previous chapter. Part of the discrepancy can be from the uncertainty in blade properties as well as issues arising directly from the blade flapping in resonance at 4/rev. To show the sensitivity of the results to blade properties, the blade frequencies were adjusted to move second flap mode from 3.77/rev (700 RPM) to exactly 4/rev. The resulting bending moments are shown in fig. 5.23 and compared to the baseline results. The correlation improves with the modified blade stiffness, particularly at higher advance ratios up to 1.03. The 1.2 advance ratio case prediction degrades because, at a lower rotor speed (700 RPM), the stiffness modification moves second flap away from 4/rev.

The prediction with CFD of the UH-60A tests showed that blade root vorticity can produce a root wake trailer and analysis of the previous chapter showed that a root trailer improves flap bending predictions. Figure 5.24a shows the flap bending moment for the 0.25 advance ratio case with wake trailed from the root with a sign

opposite the conventional tip wake trailer. The addition of the root trailer has a significant impact on the prediction and improves the magnitude on the advancing side. Figure 5.24b shows the change in normal force distribution (from the baseline) after including the root wake trailers. The inflow induced by the root trailers induced a normal force impulse on the aft rotor that appears to excite a flapping response. The effect of the root wake decreases with increasing advance ratio as it is swept aft.

5.5.2 Torsion Bending Loads

Torsional moments at 30% radius (nearest the root) are shown in fig. 5.25 with the harmonic content shown in fig. 5.26. The test shows high frequency content in the torsional bending at all advance ratios that is not captured by the analysis and the correlation is less satisfactory at all advance ratios. The negative pitching moment in the reverse flow is consistently over-predicted. The peak-to-peak torsion moment is dominated by torsion in the first quadrant which the analysis predicts to be benign.

The sectional airloads at 30% radius showed evidence of reverse flow dynamic stall, which can be a cause of torsional excitation. The Leishman-Beddoes dynamic stall model in UMARC does not have a provision for reverse flow dynamic stall. However, the impact of a dynamic stall vortex has been simulated by applying a normal force increment at the $^3/_4$ chord, starting from the reverse flow boundary as shown in fig. 5.27a. The impulse is assumed to scale linearly with in-plane velocity

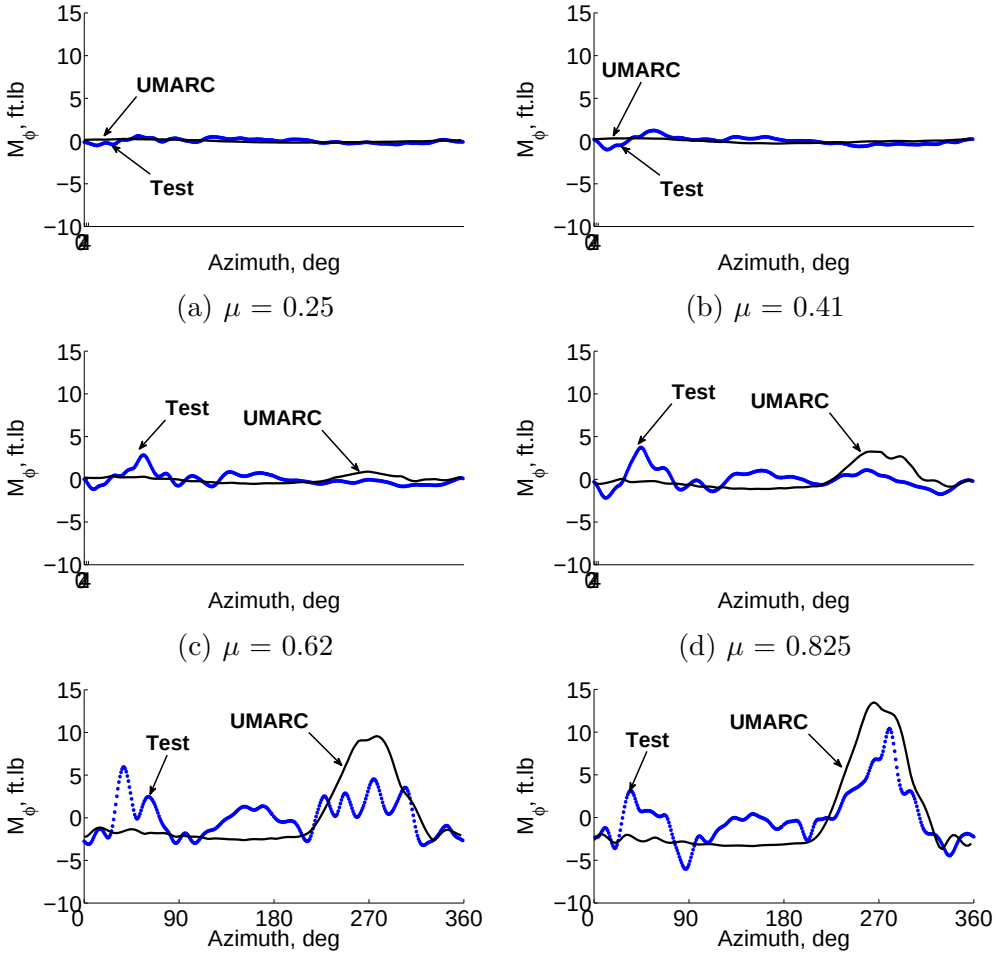

(a) $\mu = 0.25$ (b) $\mu = 0.41$

(c) $\mu = 0.62$ (d) $\mu = 0.825$

(e) $\mu = 1.03$ (f) $\mu = 1.20$

Figure 5.25: Oscillatory torsional moment ($M_{Torsion}$) at r/R = 30%, $\theta_0 = 4°$, $\alpha_s = 0°$.

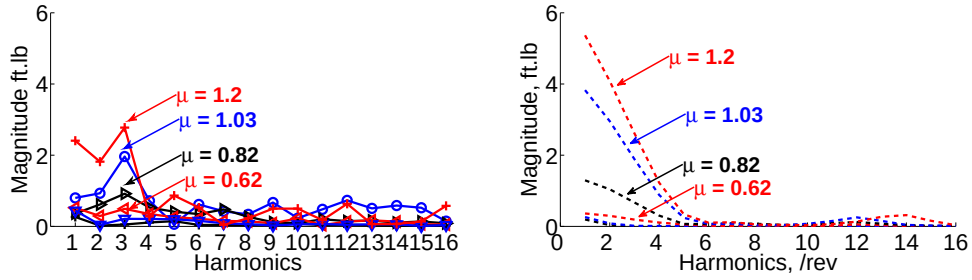

(a) Test. (b) UMARC.

Figure 5.26: Harmonics of torsional moment at r/R = 30%, $\theta_0 = 4°$, $\alpha_s = 0°$.

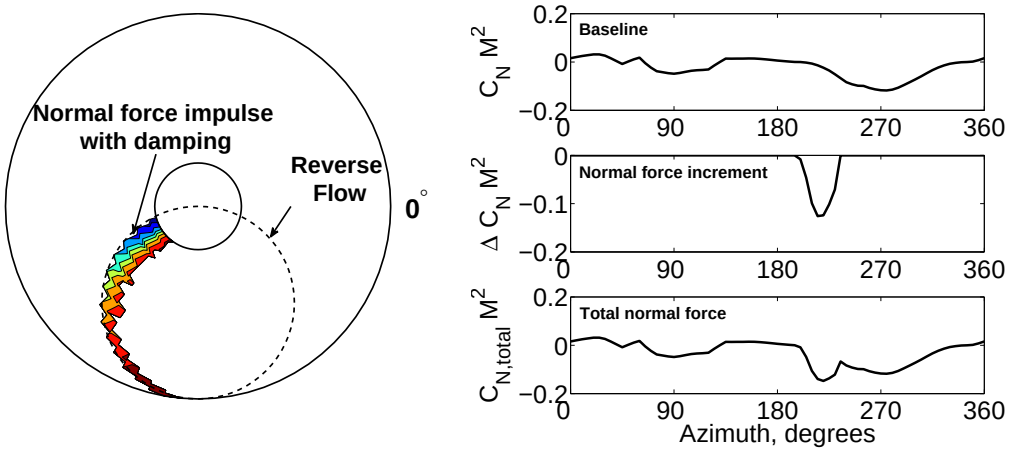

(a) ΔC_N. (b) Normal force at 30% radius.

Figure 5.27: Dynamic stall simulated with normal force impulse at $^3/_4$ chord in reverse flow, $\mu = 1.03$.

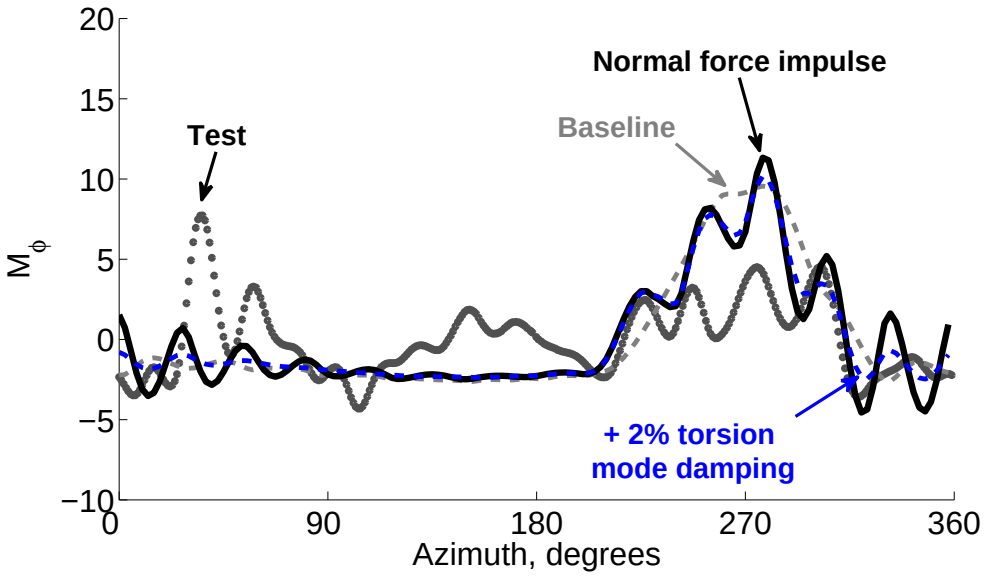

Figure 5.28: Torsion moment with dynamic stall-like lift increment for $\mu = 1.03$ at r/R = 30% and including 2% damping in the torsion mode (blue, dashed), $\theta_0 = 4°$, $\alpha_s = 0°$.

(u_t) so that it is largest at the blade root and disappears at the end of the reverse flow. The lift impulse is damped to represent the vortex movement along the chord. The magnitude of the lift increment and the damping rate are arbitrary and chosen to represent what is seen in the airloads from the Maryland and UH-60A rotors. Figure 5.27b illustrates the relative magnitude of the lift increment for a single case at $\mu = 1.03$ and 4° collective at 3% radius. The lift increment generates a pitching moment increment through the chordwise offset from the pitch axis. Figure 5.28 shows the effect of the dynamic stall-like lift impulse on the torsion moment at 30% radius. The predicted torsion moment now includes additional higher harmonic content (13 to 14/rev) and better represents the test in the reverse flow. The torsional response, initiated at the onset of reverse flow, continues well into the first quadrant due to little damping. Figure 5.28 includes a result including 2% damping on the torsion mode, which appears to improve the predicted response.

The peak-to-peak torsion moment is determined by the first quadrant response between 30° and 60° azimuth. A second pitching moment impulse appears to excite the torsional response. The impulse peak moves to earlier azimuth with increasing advance ratio ($\approx 60°$ azimuth at $\mu = 0.41$ and $\approx 34°$ azimuth at $\mu = 1.20$), which suggests the forcing can be from wake interaction. The analysis has been repeated to include multiple wake trailers (from the tip, from the edge of reverse flow and the root) but this has not resulted in a similar torsional response. The angle of attack on the aft rotor remains below stall regardless of the wake, which cannot excite a pitching moment response (the NACA0012 tables have no pitching moment below stall). It is possible that the wake interaction is causing an unsteady pitching

moment response that is not being captured in the quasi-steady analysis.

5.5.3 Vibratory loads

Finally, fig. 5.29 shows the 4/rev vertical shear (F_z) forces versus collective for increasing advance ratio and the in-plane forces and moments are shown in fig. 5.30. Notice that the vibratory hubloads appear to have a minimum between -3° and -4° collective and not at 0°, which is the expected and predicted result. Recalling fig. 5.11, the lateral cyclic prediction was offset by 1° to 2° cyclic, resulting in a zero offset of about -4° collective. It appears likely that the hubload offset is related to the lateral cyclic, which may be due to hub wake disturbances. The calculated loads have been shifted -3.3° collective to better match this. The test shows that the 4/rev loads increase significantly at and above $\mu = 0.825$. The 4/rev vertical shear vibrations originate from the resonant 4/rev rotating blade loads, which explains the large increase at high advance ratios. The prediction of the vertical shear force is reasonable and captures the trend of increasing magnitudes at advance ratios of 0.825 and above. The baseline sectional properties (second flap at 3.77/rev for 700 RPM cases) have been assumed, but note that that the magnitudes of the 1.03 and 1.2 advance ratio cases will be affected in the same way as the blade loads by sectional stiffness variations. The predictions at $\mu = 1.03$ and 1.2 have a distinct slope change that corresponds to the reverse flow stall after which the predictions start to under-predict the test data. The in-plane force magnitudes (F_{xy}) are not predicted satisfactorily and the predicted in-plane moments (M_{xy}) follow the same

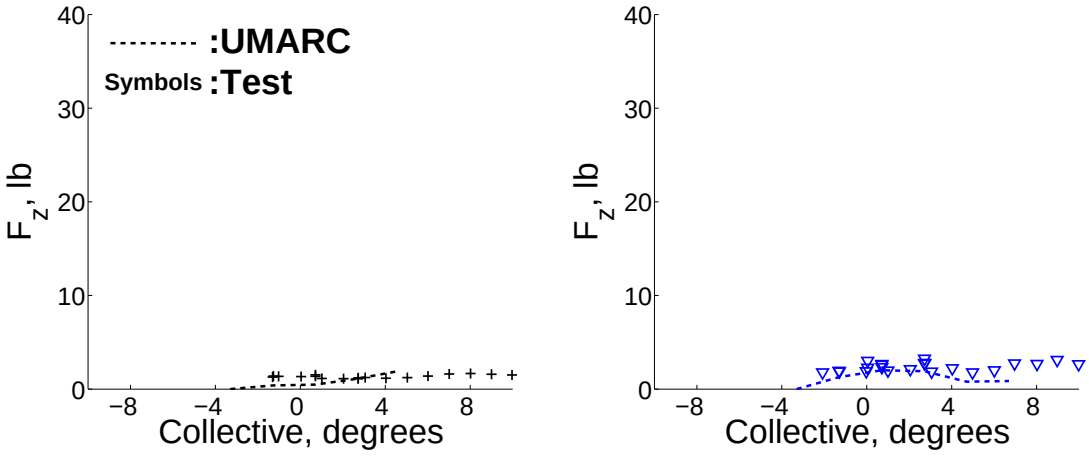

(a) $\mu = 0.25$

(b) $\mu = 0.41$

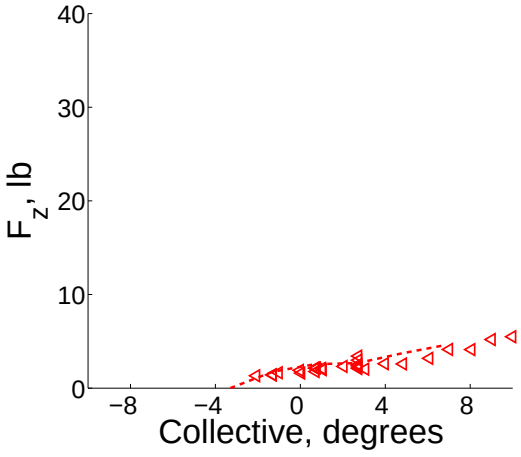

(c) $\mu = 0.62$

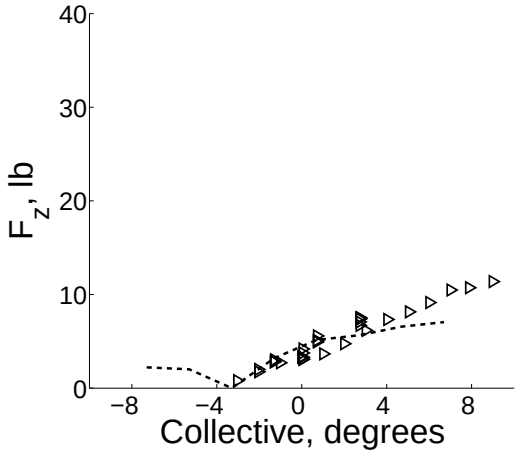

(d) $\mu = 0.825$

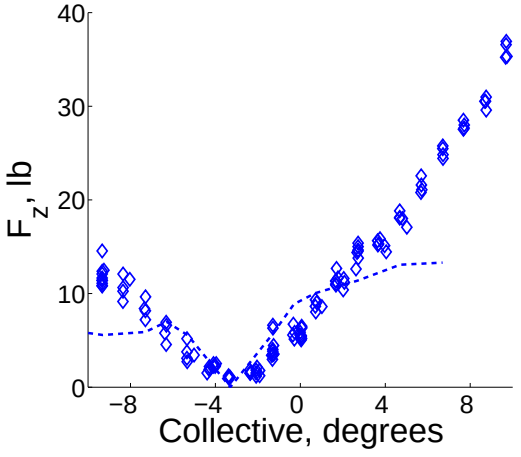

(e) $\mu = 1.03$

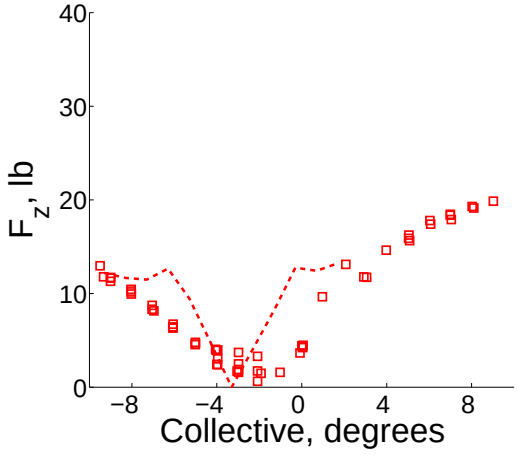

(f) $\mu = 1.20$

Figure 5.29: 4/rev Vertical shear force versus collective, $\alpha_s = 0°$ (zero offset corrected).

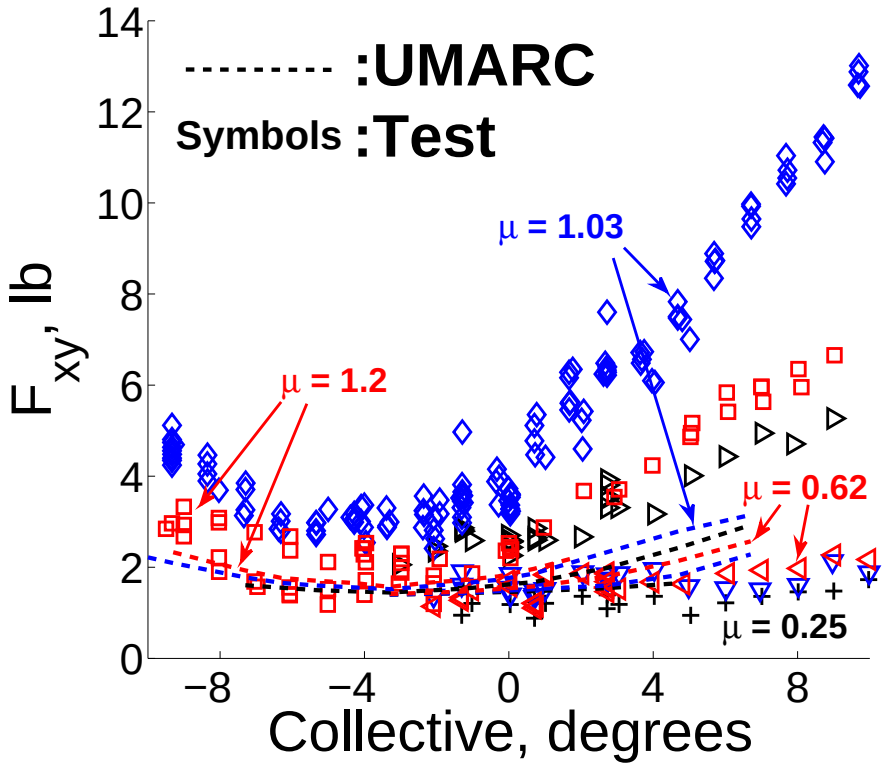

(a) 4/rev In-plane shear force.

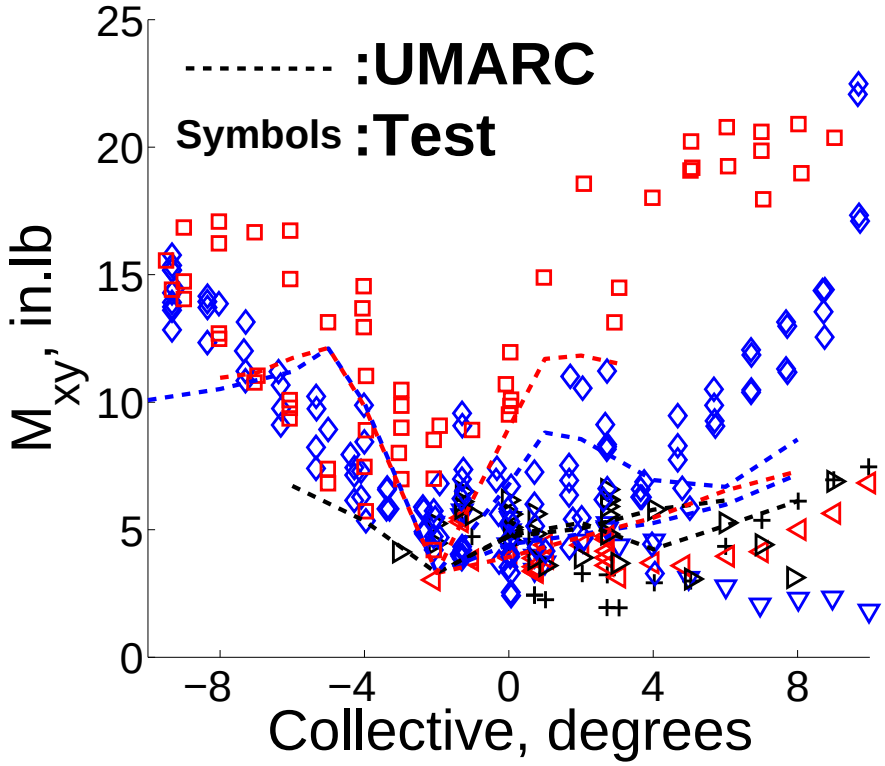

(b) 4/rev In-plane moments.

Figure 5.30: 4/rev hubloads versus collective, 0° shaft angle (zero offset corrected).

trend as the vertical shear and is reasonably predicted by the analysis.

5.6 Airloads Correlation

The results of the analysis have focused on the prediction of performance with some discussion of the blade bending loads. The measured airloads at 30% station are still being evaluated and have not been available until recently. This section presents comparisons of the measured and predicted airloads. In addition, a separate effort is dedicated to predicting the Maryland airloads with a CFD-CSD analysis. This will be useful to evaluate the quality of the measured airloads data and to compare to the lifting line prediction to identify any limitations. Only two cases are available from CFD-CSD and these are for 4° collective at $\mu = 0.25$ and 0.41. These preliminary results are included before considering the airloads at higher advance ratios.

5.6.1 Description of CFD

A detailed description of the CFD-CSD model can be found in [115,116]. The approach is a hybrid method with a CFD grid of the blade nearfield coupled to a prescribed farwake. The blade grid for this work was 101x101x70 that contribute to about 710,000 grid points. The prescribed wake includes four trailers spread between the tip and blade root with a 4° azimuth resolution. The blade dynamic solution is described in [115]. The blade model is based on the Maryland rotor.

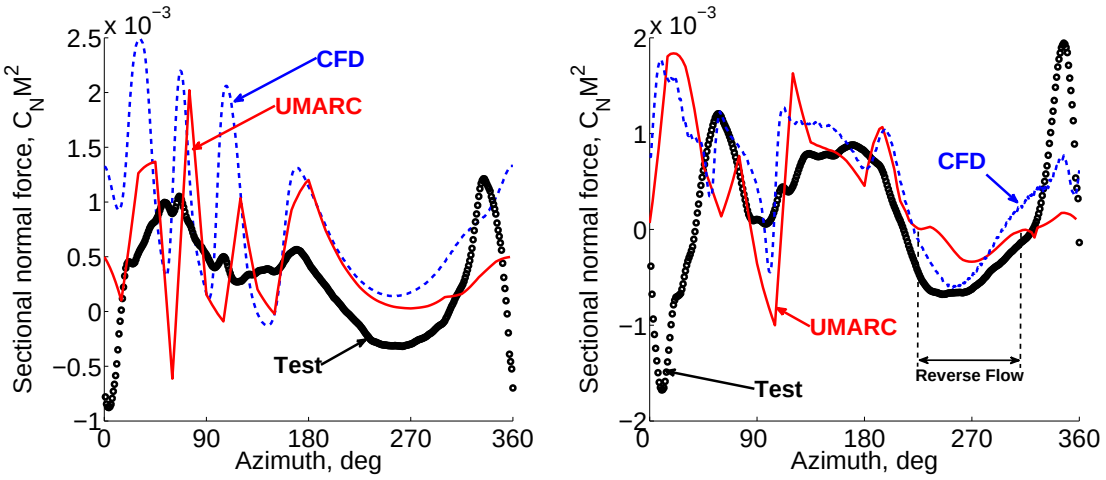

(a) $\mu = 0.25$ (b) $\mu = 0.41$

Figure 5.31: Sectional normal force comparison with CFD, r/R = 30%. $\theta_0 = 4°$.

5.6.2 Low Advance Ratio Validation with CFD

The two normal force results including CFD-CSD are shown in fig. 5.31 for advance ratios of 0.25 and 0.41 and 4° collective. Figure 5.31a shows the 0.25 advance ratio case where the CFD-CSD and UMARC show very similar airloads. On the advancing side, both predictions show strong blade vortex interaction, however, these are less obvious in the measured airloads. The similarity between CFD-CSD and UMARC is somewhat expected because of the similarity of the prescribed and free wake models at high speeds. The UMARC wake has a resolution of 15°, significantly more coarse than in the CFD-CSD, but there does not appear to be much improvement with the added resolution (UMARC was run with 10° with no significant change to the results). The measured airloads show some evidence of wake interactions, but these are much less severe. The sampling frequency of the measured result is 1000 Hz, sufficient for the frequency content of the BVI, and examining in-

dividual revolutions of the data showed that there was no smearing in the averaging process (100 revs are averaged). Other possibilities for these differences may be that the pressure sensors are not responding fast enough (possibly due to the blade construction), the wake vortex is more diffuse than predicted or there is an error in the predicted wake trajectory (possibly from a wrong trim solution/blade flapping).

On the aft rotor, the measured normal force shows a large impulse, which remains for the 0.41 and higher advance ratio results shown in the following section. The impulse is not predicted by the CFD and its consistency for all advance ratios suggests that this could be due to wake from the rotor stand/hub, which is not modeled in either analysis. On the retreating side, the analyses show some agreement with each other, although UMARC under-predicts the lift in the fourth quadrant. There is a more significant difference between the analyses and the test data. The measured lift is negative despite the 30% station being outside of the reverse flow, which suggests a mean error in the pressure data. The error could be due to calibration, which should show a consistent bias for each advance ratio, or due to the limited number of pressure sensors causing an integration error. The small chord of the Mach-scale rotor limited the number pressure sensors as well as limited their position near the trailing edge. At higher advance ratios that are in reverse flow, too few pressure sensors at the geometric trailing edge (aerodynamic leading edge) could contribute to measurement error.

Figure 5.31b shows that at $\mu = 0.41$ the CFD and UMARC provide a satisfactory agreement with each other. In the reverse flow, CFD agrees quite well with the test and UMARC under-predicts the negative lift. It is interesting to note that

neither the CFD nor the measured normal force have zero lift at the reverse flow boundary ($u_t = 0$ at 230° and 312° azimuth), which is the expected result for a lifting line analysis. The discrepancy could be from the highly 3D flow at these azimuth where radial flow contributions are significant. Radial flow is non-zero at the reverse flow boundary and lift should be expected. The yawed flow corrections introduced in chapter 4 are not valid for the extreme angle of attack and yaw angles in this region.

5.6.3 Normal Force Collective Sweeps

Figures 5.32a and 5.32b show a collective sweep from 0° to 6° at 0.62 advance ratio for the measured and UMARC predictions respectively. Note that the vertical scale magnifies differences, otherwise the lift magnitudes are quite low. The features of the advancing side are reasonably well predicted, particularly in the second quadrant. The BVI in the first quadrant remains over-predicted by the analysis, but the phase agrees well with the test. The measured lift impulse on the aft rotor is independent of collective, which supports the argument for rotor hub interference. Evidence of the impulse helps confirm that the lateral cyclic offset shown earlier in fig. 5.11 is due to rotor hub interference. At 0° collective, there should not be any lift generated for the untwisted rotor, but the measured lift is non-zero (albeit small). This is possibly also in response to the hub wake interference. In the reverse flow, the predicted lift is nearly constant with increasing collective because the longitudinal cyclic cancels collective changes to maintain trim, however, the measured

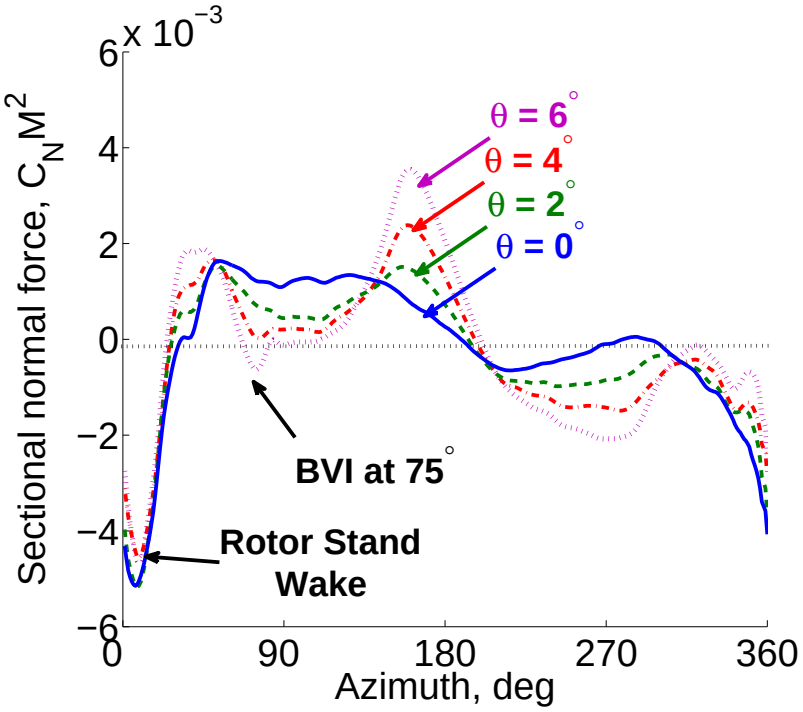

(a) Measured

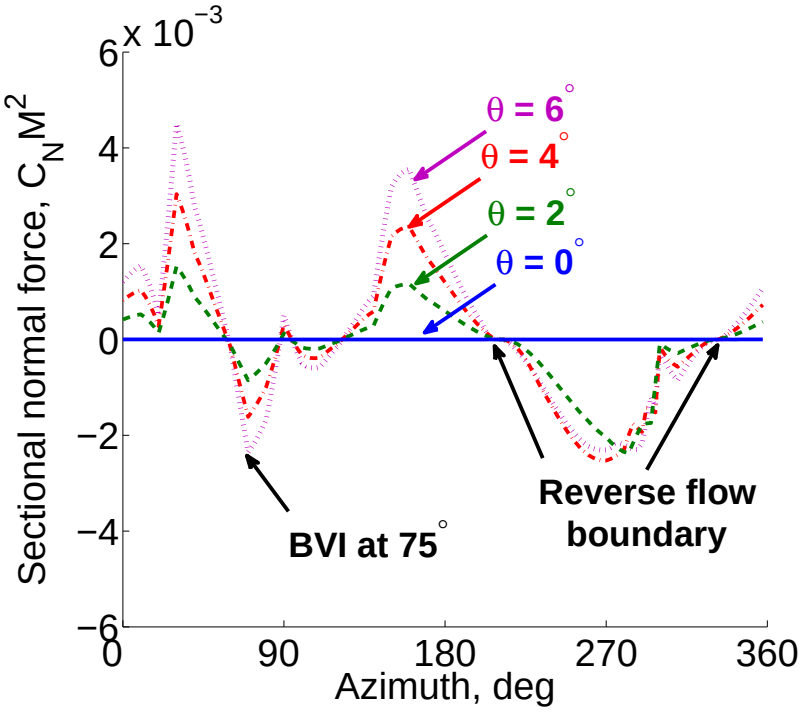

(b) UMARC

Figure 5.32: Sectional normal force, r/R = 30%, $\mu = 0.62$.

lift magnitude appears to increase with collective. Part of the discrepancy could arise from integration errors, however, the very small forces at this station make the differences somewhat insignificant to the overall rotor thrust.

A second collective sweep, at an advance ratio of 1.03, is shown in fig. 5.33. At this advance ratio, the rotor is beyond thrust reversal and the reverse flow root is producing the majority of the rotor lift (negative). Qualitatively, the predicted and measured normal force show reasonable agreement. Compared to the predicted normal force, the measured normal force has a positive offset, particularly on the advancing side. At the reverse flow boundary (near 195° azimuth) the measured normal force collapses to a constant, non-zero lift even though zero lift is expected. The complex 3D flow is far removed from the 2D lifting line analysis assumptions and this could be responsible for the differences. CFD results may be useful to identify the exact role of 3D flow effects and isolate any shortcomings in the test. Finally, the trends in the reverse flow are similar, although, UMARC predicts larger magnitudes. Once again, the discrepancy could be due to integration errors, which CFD may confirm this. There is evidence of stall in the predicted lift in the reverse flow (3.7° to 5.7°) as discussed previously. Stall is not obvious in the measured data, which shows no drop-off in the reverse flow lift for the collectives shown. Furthermore, there is no evidence of dynamic stall in the measured lift in the reverse flow, although the pitching moments would provide a more clear picture.

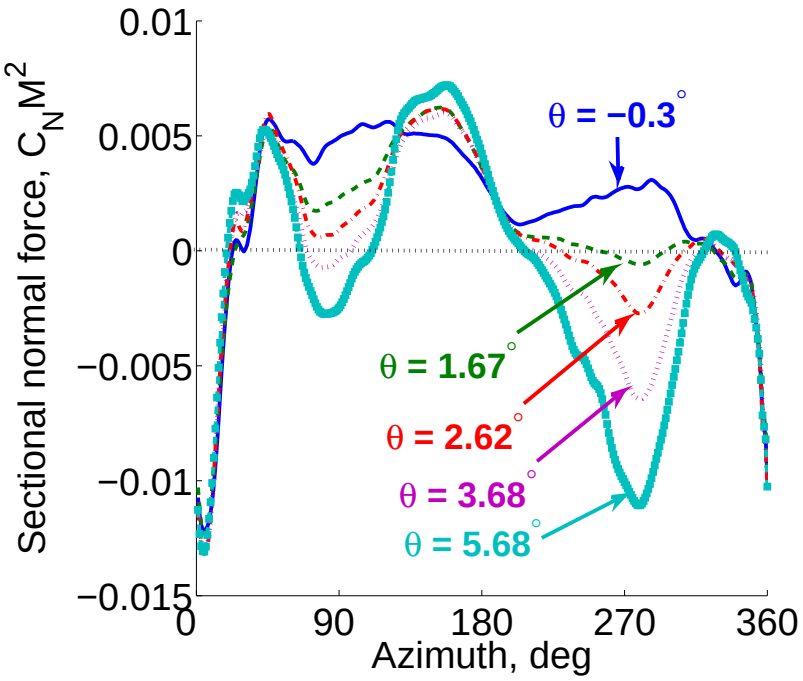

(a) Measured

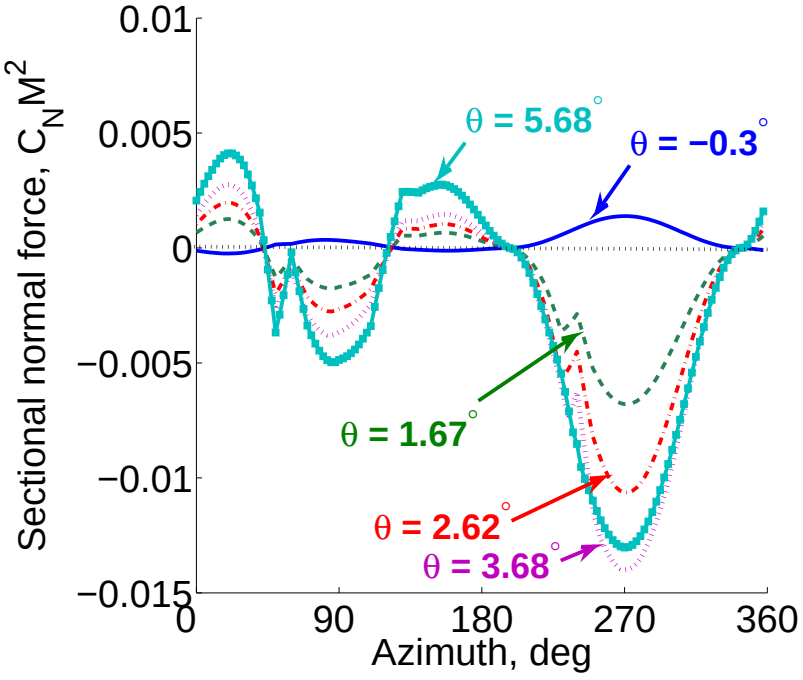

(b) UMARC

Figure 5.33: Sectional normal force, r/R = 30%. $\mu = 1.03$.

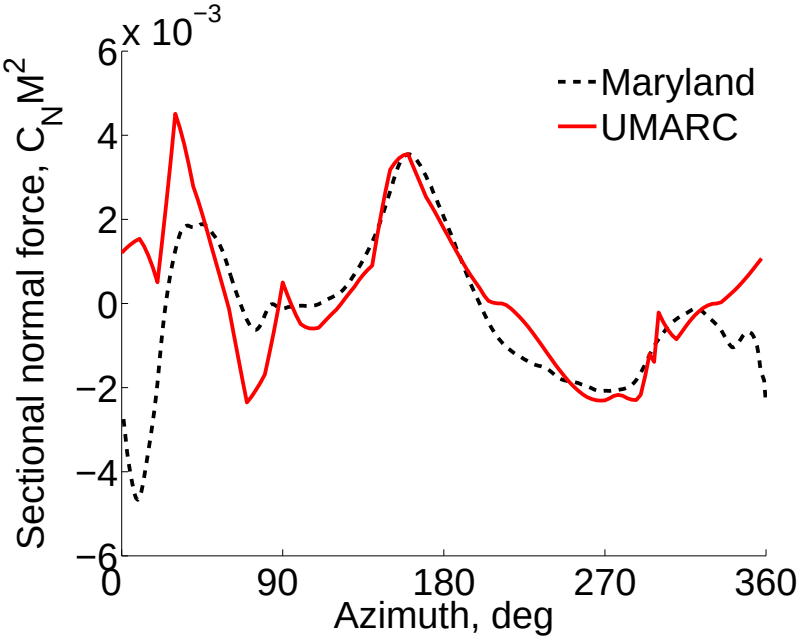

(a) Maryland, r/R = 30%, $\mu = 0.62$, $\theta_0 = 6.0°$

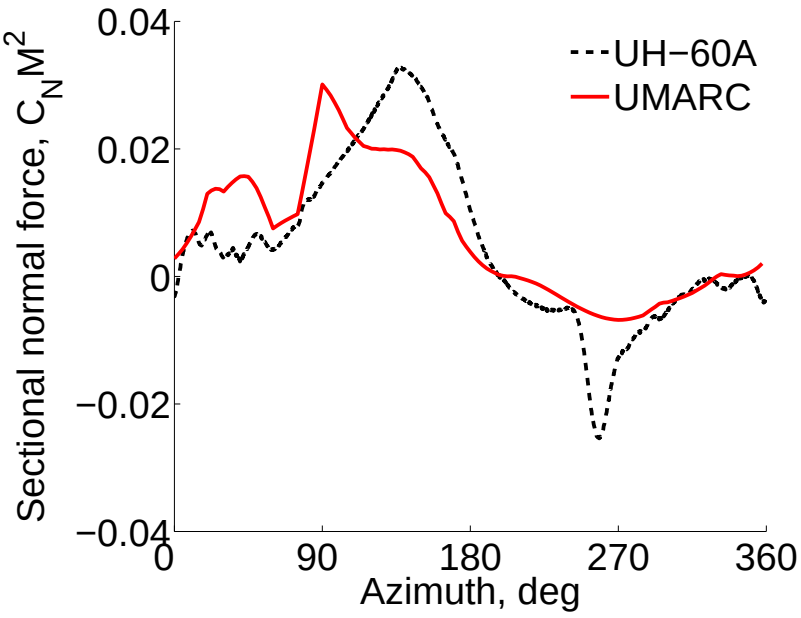

(b) UH-60A, r/R = 22.5%, $\mu = 0.60$, $\theta_0 = 7.8°$

Figure 5.34: Sectional normal force comparison of Maryland and UH-60A, $\mu \approx 0.6$.

5.6.4 Comparison to UH-60A Airloads

A comparison of the normal force measurements and predictions at similar flight conditions (limited by scarcity of available data) are shown for the Maryland test in fig. 5.34a and the UH-60A in fig. 5.34b. The magnitude of the lift on the Maryland rotor is significantly lower than on the UH-60A at this station, which is because of the inbuilt blade twist in the later giving a higher root pitch. The correlation of the prediction is reasonable for both rotors, but somewhat better for the Maryland rotor. In particular, the under-prediction of lift in the second quadrant of the UH-60A rotor is not shown in the Maryland rotor. This was discussed in chapter 4 where it appeared that the root vortex played an important role in the lift prediction near the root. The much higher lift for the UH-60A rotor creates a stronger vortex and has a larger influence. The lift impulse on the aft rotor that is relatively large for the Maryland data is not apparent for the UH-60A test. The impulse from rotor stand flow disturbance may be present in the UH-60A lift, but is less significant compared to the higher variation in lift around the azimuth. Finally, the UH-60A rotor appears to have a dynamic stall like lift increment in the reverse flow, which is not present in this Maryland data nor any of the cases shown previously. Despite the similar flight conditions, the dynamic pressure in the reverse flow of the UH-60A rotor is roughly three times that of the Maryland rotor and the pitch is significantly larger due to the twist (-25° vs -12°), which combine to promote dynamic stall.

5.7 Chapter Summary

This chapter has investigated high advance ratio wind tunnel test data on a 4-bladed, Mach-scaled, articulated rotor carried out in the Glenn L. Martin wind tunnel. The analysis is a modified comprehensive lifting line code, UMARC. The rotor performance predictions are evaluated before investigating the sensitivity of thrust reversal to rotor design and modeling refinements. The sectional bending loads and 4/rev vibratory loads are investigated and some limited sectional airload measurements in the reverse flow are explored. The following are the key conclusions:

1. Rotor thrust is satisfactorily predicted for collectives from 0° to 10° up to an advance ratio of 0.825. Near an advance ratio of $\mu = 0.9$, thrust response to increasing collective becomes negative, called thrust reversal. This is predicted by the analysis for small collectives only ($\pm 3^\circ$). At higher collective magnitude, the predicted thrust slope reverts to positive abruptly compared to a gradual change in slope seen in the test.

2. Thrust reversal results because of lateral trim balance that limits thrust on the advancing rotor, and high reverse flow dynamic pressure that generates enough lift in the reverse flow to dominate rotor total thrust.

3. Thrust reversal is halted abruptly (in the analysis) when the angle of attack in the reverse flow exceeds static stall. When stalled, the reverse flow lift no longer increases linearly with pitch, while it continues to do so on the fore and aft rotor, and the thrust response becomes dominated by the lift on the

fore and aft rotor. The test also shows a change in trend at high collectives suggesting that stall is also playing a part. Measured sectional airloads suggest that dynamic stall in the reverse flow produces additional post-stall lift that accounts for the difference with analysis.

4. With aft shaft tilt, the analysis under-predicts the measured thrust, although some of the differences can be explained by blade dissimilarity resulting in blade flapping (β_{1C}) effectively increasing the aft shaft angle. Aft shaft angle moves the region of thrust reversal to higher positive collectives which is well predicted by the analysis. 4° shaft angles moved the center of thrust reversal about 4° collective.

5. Thrust reversal is sensitive to reverse flow aerodynamics.

   (a) Aft shaft tilt gives a negative bias to the reverse flow angle of attack equal to the shaft tilt and promotes thrust reversal at more positive collectives.

   (b) Nose down twist biases the root pitch to positive collectives and promotes thrust reversal at more negative collectives.

   (c) Increasing reverse flow stall angles, extends the region of thrust reversal.

   (d) Enlarging the root cut-out delays thrust reversal to higher advance ratios.

6. Classical yawed flow corrections extend thrust reversal by reducing stall in the reverse flow region at high yaw angles.

7. Shaft power is well predicted for each advance ratio when the reverse flow remains unstalled. Shaft power prediction degrades at high advance ratios after

the reverse flow stalls because reverse flow drag after stall is under-predicted.

8. The measured rotor drag forces at low advance ratios are small and the measurement error is large, sometimes negative. The prediction of drag is reasonable at higher advance ratios ($\mu = 1.03, 1.2$) where the measured drag values are larger. This provides confidence in the analysis and suggests a zero offset error in the measurements.

9. Both the lateral and longitudinal cyclics are well predicted by the analysis, but with a small offset of about 1° to 2°. Stall during thrust reversal is evident in both the measured and predicted cyclics.

10. Flap bending moment predictions are evaluated at 50% radius and show poor correlation at low advance ratios, improving at high advance ratios. The second flap mode is near 4/rev and this dominates the phase and magnitude at high advance ratios. At low advance ratios, including a wake trailer from the blade root has a significant impact on the flap bending at 50% and improves the advancing side correlation somewhat.

11. Torsional moment at 30% radius is not well predicted with the baseline analysis. The analysis over-predicts the pitching moment in the reverse flow compared to the test. The test contains higher harmonic content between 4 and 16/rev that is not seen in the analysis. Adding a dynamic stall-like lift increment to the analysis improves correlation by exciting the torsion mode. Torsion bending is also excited in the first quadrant, consistent with rotor wake interaction,

but this is not seen in the analysis because the airfoil tables do not provide pitching moment increment below stall.

12. 4/rev vertical hub shear vibrations grow significantly with increasing advance ratio and this is because of the proximity of second flap to 4/rev. The in-plane vibratory loads are not well predicted, suggesting that the resonant blade response is masking smaller blade load trends.

13. Preliminary airloads correlation show that most of the important features of the normal force are predicted satisfactorily. Blade–wake interactions are predicted to be more severe than are shown in the measured data.

Chapter 6: Summary and Conclusions

This chapter summarizes the key conclusions of this thesis. The focus of this research has been on refining the comprehensive analysis, prediction and validation of the performance and loads of a helicopter rotor with reduced rotor speed at high advance ratios with wind tunnel data. The objective was to identify the analysis methodology required to accurately predict the key performance and loads of a rotor at high advance ratios. The initial approach to this research was to investigate both variable rotor speed and variable radius as the two approaches to achieving high advance ratios and to refine the in-house prediction capability. The UH-60A Black Hawk was chosen as the baseline helicopter for this study. The UH-60A Black Hawk is representative of a modern 4-bladed, articulated helicopter that has been extensively studied in literature and for which the important rotor properties are known. The analysis was modified to model variable rotor speed and variable radius concepts in normal and high advance ratios. Variable rotor speed was chosen as the more promising approach to high advance ratios because of the potential for significant improvement in performance at moderate airspeeds and the feasibility of high speed flight with lower technology barriers.

The focus of the research at high advance ratios continued by evaluating the

correlation of the analysis code with high advance ratio test data. Two rotor tests were investigated. The UH-60A slowed rotor tests provided a large contribution to the experimental database at high advance ratios. In addition to performance and vibratory loads, the test data includes complete airload measurements and blade bending load measurements at high advance ratios that are not available elsewhere in literature. The UH-60A rotor was tested at advance ratios from 0.3 to 1.0 for the rotor slowed to 40% of its nominal speed (258 RPM, 27 rad/s). The analysis is refined systematically by evaluating the performance prediction and sectional airloads at high advance ratios. Enhancements and refinements to the analysis include: (i) first order model of the fuselage's effect on the flow at the rotor plane; (ii) nearwake calculations in the reverse flow and allowing the nearwake to deform with the freestream; (iii) radial flow effects by correcting the sectional lift, drag and pitching moment through the table look-up; (iv)refined aerodynamic modeling of the root cut-out; and (v) reverse flow airloads. The important role of the far wake modeling, including the number and point of release of the trailers on a twisted rotor at high advance ratios was also investigated. Corrections to the analysis included sign and large angle corrections for the reverse flow. New trim routines were added to model the wind tunnel trim procedure as well as improvements to the solution procedure to improve convergence at high advance ratios.

The second rotor test investigated in this research was an in-house high advance ratio test to an advance ratio of 1.2. The rotor tested in the Glenn L. Martin Wind Tunnel was a 4-bladed, articulated rotor and an approximate Mach-scale of the UH-60A rotor. The untwisted, untapered, NACA0012 planform provided a sim-

pler rotor (than the UH-60A) to correlate the analysis and infer new results. The new test data at higher advance ratios revealed more information about thrust reversal. The physics of thrust reversal was examined through correlation with the analysis and the important modeling refinements were investigated. The validated analysis was then used to investigate the effects of rotor twist, shaft angle, reverse flow stall, root cut-out and yawed flow corrections on performance predictions near thrust reversal.

Finally, it should be noted that this work is constrained to existing aircraft that have been designed for existing missions. Retrofitting advanced concepts onto existing aircraft can only provide little to modest gains. Integrated designs that incorporate advanced concepts, including variable radius and RPM and much more, open up a large space for more significant gains. Nonetheless, this work describes a start to establishing concrete benefits in a quantitative manner. Secondly, seeking improved performance in the scope of existing missions is only one part of the utility of advanced concepts. The real goal is to enable new missions altogether. The work here is meant to provide future designers a fundamental understanding of the physics of high advance ratios and a tool for its comprehensive analysis in order to go on to design new aircraft for new missions.

6.1 Key Conclusions

Detailed conclusions on each aspect of this research have been discussed respectively at the end of each chapter. The following are the key conclusions that

summarize the contributions of the current research effort.

1. The variable radius rotor concept was investigated for improving performance of a UH-60A like rotor within its normal flight envelope ($\mu < 0.4$, 14,000 to 20,000 lb gross weight). Reducing the rotor radius decreases the rotor power by up to 8% at 14,000 lb thrust, decreasing to 2% for 18,000 lb and has marginal effect on power at 20,000 lb. The power reduction increased with airspeed as profile power losses became more important, but was limited by stall above 150 knots. At low airspeeds, reducing the radius has an induced power penalty due to increased disk loading and this limits performance improvements. A peak reduction of power of about 210 hp is possible with radius reduction at 150 knots for 14,000 lb gross weight, 125 hp for 16,000 lb, 70 hp for 18,000 hp and less than 20 hp for 20,000 lb. At high speeds, reducing the rotor radius is accompanied by increased vibratory loads that can be significant for the in-plane shear forces and moments.

2. Variable rotor speed gave larger improvements in performance than the variable radius concepts, particularly at low airspeeds. The largest reduction in power was at high speeds by reducing the rotor speed because of reduced profile power losses. At low airspeeds, reducing rotor speed does not have the induced power penalty associated with the variable radius concept and the improvement in performance is significantly larger than the variable radius rotor. Stall continues to limit performance improvements beyond 160 knots. At the minimum power condition, the UH-60A rotor is defined by an optimum C_T/σ

as a function of advance ratio. The vibratory loads are either reduced or not significantly affected by rotor speed variation at low airspeeds, but vibratory loads increase at high airspeeds for the slowed rotor. The increase in vibratory loads at high airspeeds is a strong function of advance ratio.

3. Variable rotor speed is the more promising concept for improving performance for a conventional rotorcraft at normal airspeeds ($\mu < 0.4$). Variable rotor speed offers a larger reduction in power across the flight envelope considered (40 – 170 knots) than variable radius concepts and faces less technological challenges to practical implementation. The effect of decreased power turbine efficiency at reduced rotor speed was investigated and shown to be insignificant for the range of rotor speed reduction considered in this study (16%). At high airspeeds (greater than 170 knots) both variable radius and variable rotor speed concepts are limited by stall and require lift and thrust compounding to achieve trim and limit performance penalties.

4. High advance ratio performance is investigated for two rotors: UH-60A full-scale rotor and Maryland Mach-scale rotor. The thrust capability of the rotor decreases with advance ratio, and the sensitivity of rotor thrust to collective decreases. Decreasing thrust sensitivity to collective occurs because the rotor is required to remain in roll trim. At high advance ratios, the retreating rotor dynamic pressures is much lower than the advancing side and the rotor requires large cyclic inputs to reduce advancing side lift for trim. In the limit, the rotor becomes insensitive to collective, which occurs near an advance ratio of 1.0 for

the UH-60A and Maryland rotors. Further increasing the advance ratio results in thrust reversal when increasing collective results in decreasing thrust.

5. Thrust reversal was investigated with the analysis of the Maryland test data. Thrust reversal occurs when the dynamic pressure in the reverse flow at the blade root is large enough that the reverse flow lift determines the total rotor response. The UH-60A thrust response is not yet reversed at the highest advance ratio (1.0) tested, but the Maryland rotor is fully reversed by an advance ratio of 1.03. At large collectives (positive and negative), the reverse flow can stall, which results in a non-linear thrust slope. The analysis calculation predicts abrupt stall and loss of lift that results in an abrupt change in thrust slope, whereas the Maryland test data shows a more gradual change. A possible discrepancy is unsteady airloads and reverse flow dynamic stall that are not yet modeled in the analysis. Unsteady airload models that are applicable to the reverse flow are an important continuing research area.

6. The advance ratio where thrust reversal begins is shown to be a function of root cut-out, blade twist and shaft angle. Increasing the root cut-out, limits the highest dynamic pressures in the reverse flow and delays thrust reversal to higher advance ratios. Nose down twist results in a positive pitch at the root, which promotes thrust reversal at lower collectives. Aft shaft tilt causes the retreating side an effective negative angle of attack bias and promotes thrust reversal at higher positive collectives. Neither twist nor shaft tilt affect the slope of thrust reversal significantly.

7. The effect of modeling refinements was evaluated. A new model for the upwash due to the presence of the fuselage below the rotor is implemented, but only has a small impact on the rotor thrust predictions (decreases thrust). Yawed flow corrections that account for the effect of radial flow on the sectional lift can have a significant impact on the prediction of thrust reversal. The yawed flow corrections act to delay stall in the reverse flow to higher collectives and can be important for predicting the onset of thrust reversal as well as the thrust behavior after reverse flow stall. Modeling the nearwake in the reverse flow as deformable with the freestream gives a more physical description of the trailed wake and has been shown to impact the prediction of thrust at high advance ratios. However, treatment of the deformed nearwake in close vicinity of the blade requires careful modeling. A more detailed comparison with sectional airloads is required.

8. Both the trend and magnitude of rotor power are satisfactorily predicted for the untwisted Maryland rotor, but are over-predicted for the UH-60A full-scale rotor. The addition of the fuselage model in the analysis reduced the power predictions somewhat in better agreement with the UH-60A test (Maryland rotor does not have a fuselage). The trend of the rotor drag measurements are well predicted for both tests. The calculated drag for the UH-60A rotor test is significantly under-predicted unless the drag associated with the root cut-out is included. The Maryland test tared out the shank drag and the overall correlation is quite good. Significant scatter in the measured Maryland test

data calls its quality into question considering the very good prediction of thrust and power by the analysis.

9. Correctly accounting for the wake is important for accurately predicting the sectional lift of the highly twisted UH-60A full-scale rotor. Near the blade tip (92% radius) the magnitude and phase of the advancing side lift can only be predicted if at least two wake trailers are modeled to represent the change in sign of lift along the span. On the retreating side, the wake is not important and the airloads are benign. On the aft rotor, the measured airloads are highly oscillatory which is partly due to interaction with wake from the blade root (modeled in the analysis) and partly due to wake from the hub (not modeled). 15° azimuthal wake resolution was found sufficient to predict the important details of the wake except at the lowest advance ratio case ($\mu = 0.3$) when 10° resolution improves the prediction of wake interactions on the aft rotor somewhat.

10. Pitching moment prediction is poor for the UH-60A rotor, however similar type discrepancies are shown in literature. It has been speculated that blade torsion response is excited by unsteady airloads in the reverse flow - not yet modeled by any analyses in the literature. This behavior is not captured by the modified analysis and the unsteady models are not valid in the reverse flow.

11. The prediction of the UH-60A flap bending loads follows from the airloads prediction and is quite satisfactory when the wake is correctly modeled. In-

cluding a root vortex is important for the prediction of flap bending phase and magnitude because it interacts with the aft rotor and contributes to the impulsive blade loading that affects the flap bending. The Maryland rotor has its second flap mode near 4/rev and this dominates the blade loads at high advance ratios. The sectional properties of the Maryland rotor are not as well understood as for the UH-60A, which results in significant uncertainty in the blade frequencies. The promising UH-60A blade loads predictions suggest that error in the sectional properties are responsible for discrepancy in bending predictions for the Maryland rotor.

12. The lifting line analysis can predict the performance for a high advance ratio rotor beyond thrust reversal as well as predicting the trends of the important blade flapwise loads with satisfactory resolution. Unsteady airloads in the reverse flow are a current shortcoming; however, CFD predictions have not yet shown better resolution in this region.

6.2 Future Work

This section suggests directions for future research in the area of high advance ratio aeromechanics. The preceding sections have shown that a comprehensive analysis is able to adequately predict the thrust and power of an isolated rotor at high advance ratios as long as reverse flow stall is not reached and exceeded. The remaining key performance metric is rotor drag, for which the experimental measurements have significant unknowns and possibly large measurement errors, which result in

a poor correlation with predictions. These uncertainties in the test data need to be corrected if reliable predictive capability is to be confirmed. Blade loads for an articulated rotor are largest near 50% radius and these are predicted with satisfactory resolution after accounting for the presence of the dominant wake trailers in the analysis. However, for hingeless rotors, the important bending loads are near the blade root where prediction of airloads and blade loads is less satisfactory due to unknown unsteady reverse flow airloads. Unsteady airloads models that are validated for the reverse flow are needed to make further improvements in the loads predictions by lifting line analyses. The unsteady behavior of the stalled reverse flow region is also important for predicting the rotor performance after reverse flow stall.

CFD simulations of the UH-60 slowed rotor test data has shown very good agreement for the sectional lift and bending loads predictions (pitching moments and torsion moments show large errors on the advancing side), which exceeds the predictive capability of comprehensive analyses. Comparing lifting line results with CFD will enable refinement of the lifting line models and corrections for high advance ratio effects at a much reduced cost compared to further wind tunnel experiments.

The following are some of the broader research areas that will contribute to the objective of reliable high advance ratio predictive capability with lifting line analyses.

1. **Unsteady reverse flow airloads:** Errors in the predicted lift in the reverse flow region as well as large discrepancies in the pitching moments and tor-

sional blade moments suggest that the lifting line analysis with quasi-steady corrections is unable to predict the lift and pitching moments near the reverse flow. In addition, there is experimental evidence of a dynamic stall like vortex shed in the reverse flow that is not currently modeled in the analysis. In order to reliably model these phenomena, systematic experiments are needed to evaluate the unsteady airloads in reverse flow – characterized by large pitch rates at high angles of attack with a change in sign of free stream. Current unsteady models can then be evaluated against the test data and refinement and corrections derived that are suitable for lifting line.

2. **CFD and lifting line:** The validity of lifting line analyses is often called into question at the extremes of the flight envelope and more so for high advance ratio studies. However, lifting line analyses remain the most economical means to predict helicopter performance as CFD simulations methods remain too expensive. The present analysis show that lifting line analyses provide a satisfactory prediction of rotor performance and the trends of the blade loading (possibly with the exception of torsional loads) below stall. It may be important to characterize the limits of each approach as functions of rotor thrust and advance ratio so that the trade-off in prediction resolution is better understood.

3. **Rotor drag prediction:** The validation of the prediction of rotor drag has several unknowns across the two wind tunnel tests investigated. The UH-60A drag measurements included the blade shank which has not yet been aero-

dynamically characterized, which makes analysis challenging. The Maryland measurements of rotor drag suggest tare error. Accurately determining the rotor drag is a critical component of the rotor lift to drag ratio prediction, which is needed to compare rotor designs. Subsequent wind tunnel tests of high advance ratio concepts need to ensure accurate rotor drag measurements that are well characterized.

4. **Yawed flow corrections:** The present results illustrate that yawed flow can play an important role in predicting rotor thrust and drag at high advance ratios. The yawed flow corrections that have been investigated are simple modifications to the lifting line analysis but their validity for large yaw angles in reverse flow and the effect on dynamic stall may be questionable. CFD could provide valuable insight into yawed flow and provide new insight into models applicable to lifting line analyses.

Bibliography

[1] A. W. Linden, "Variable Diameter Rotor Study," tech. rep., DTIC Document, 1972.

[2] J. Sicard and J. Sirohi, "Aeroelastic Stability of an Extremely Flexible, Variable-Diameter Rotor in Hover," in *Fifth Decennial AHS Aeromechanics Specialists Conference*, (San Francisco, CA), January 2014.

[3] C. A. Fenny, "Mechanism for Varying the Diameter of Rotors Using Compound Differential Rotary Transmissions," in *Proceedings of the 61st Annual Forum of the American Helicopter Society*, (Grapevine, TX), June 2005.

[4] E. A. Fradenburgh, R. J. Murrill, and E. F. Kiely, "Dynamic Model Wind Tunnel Tests of a Variable-Daimeter, Telescoping-Blade Rotor System (TRAC Rotor)," Tech. Rep. USAAMRDL Technical Report 73-32, 1973.

[5] E. A. Fradenburgh, L. N. Hager, and N. F. K. Keffort, "Evaluation of the TRAC Variable Diameter Rotor: Preliminary Design of a Full-Scale Rotor and Parametric Mission Analysis Comparisons," Tech. Rep. USAAMRDL Technical Report 75-54, 1976.

[6] D. Matuska, A. Dale, and P. Lorber, "Wind Tunnel Test of a Variable-Diameter Tiltrotor (VDTR) Model," Tech. Rep. NASA CR 177629, National Aeronautics and Space Administration, 1994.

[7] T. Prabhakar and F. Gandhi, "A Centrifugal Force Actuated Variable Span Morphing Helicopter Rotor," in *Proceedings of the 63rd Annual Forum of the American Helicopter Society*, (Virginia Beach, VA), May 2007.

[8] M. Mistry and F. Gandhi, "Performance Improvement with Variable Rotor Span and RPM," in *Proceedings of the 66th Annual Forum of the American Helicopter Society*, (Pheonix, AZ), May 2010.

[9] J. G. Leishman, *Principles of Helicopter Aerodynamics*. Cambridge University Press, 2002.

[10] F. B. Gustafson and A. Gessow, "Effect of Rotor-Tip Speed on Helicopter Hovering Performance and Maximum Forward Speed," Tech. Rep. NACA ARR-L6A16, 1946.

[11] J. DiOttavio and D. Friedmann, "Operational Benefits of an Optimally, Widely Variable Speed Rotor," in *Proceedings of the 66th Annual Forum of the American Helicopter Society*, (Phoenix, AZ), May 2010.

[12] A. E. Karem, "Optimum Speed Rotor." https://www.google.com/patents/US6007298, 1999. US Patent 6,007,298.

[13] J. H. Steiner, "An Investigation of Performance Benefits and Trim Requirements of a Variable Speed Helicopter Rotor," Master's thesis, The Pennsylvania State University, Department of Aerospace Engineering, Pennsylvania, USA, 2008.

[14] J. H. Steiner and F. Gandhi, "An Investigation of Variable Rotor RPM on Performance and Trim," in *Proceedings of the 64th Annual Forum of the American Helicopter Society*, (Montreal, Canada), April 29 – May 1 2008.

[15] W. Guo and J. F. Horn, "Helicopter Flight Control woth Variable Rotor Speed and Torque Limiting," in *Proceedings of the 64th Annual Forum of the American Helicopter Society*, (Grapevine, TX), May 2009.

[16] J. J. Howlett, "UH-60A Black Hawk Engineering Simulation Program: Volume 1 - Mathematical Model," Tech. Rep. NASA CR 166309, 1981.

[17] M. Mistry, *Quasi-Static Rotor Performance Morphing Concepts for Rotorcraft Performance Improvements*. PhD thesis, The Pennsylvania State University, Department of Aerospace Engineering, Pennsylvania, USA, 2012.

[18] R. Blackwell and T. Millott, "Dynamics Design Characteristics of the Sikorsky X2 Technology Demonstrator Aircraft," in *Proceedings of the 68th Annual Forum of the American Helicopter Society*, (Montreal, Canada), April 29–May 2 2008.

[19] D. Nelms, "Speed streak: Eurocopter's X^3 High-Speed Hybrid Helicopter Combines Fixed and Rotary-Wing Flying Characteristics," *Aviation Week & Space Technology*, vol. 174, no. 24, 2012.

[20] "V-22 Osprey 2010 Guidebook," Tech. Rep. NAVAIR PMA-275 Control Number 10-28, NAVAIR, 2010.

[21] P. P. Walsh and P. Fletcher, *Gas Turbine Performance*. Blackwell Science Ltd and The American Society of Mechanical Engineers, 1998.

[22] M. D'Angelo, "Wide Speed Range Turboshaft Study," Tech. Rep. NASA CR 198380, National Aeronautics and Space Administration, 1995.

[23] G. E. Welch, "Assessment of Aerodynamic Challenges of a Variable-Speed Power Turbine for Large Civil Tilt-Rotor Application," in *Proceedings of the 66th Annual Forum of the American Helicopter Society*, (Pheonix, AZ), May 2010.

[24] G. E. Welch, "Computational Assessment of the Aerodynamic Performance of a Variable-Speed Power Turbine for Large Civiil Tilt-Rotor Applications," in *Proceedings of the 67th Annual Forum of the American Helicopter Society*, (Virginai Beach, VA), May 2011.

[25] A. Garavello and E. Benini, "Preliminary Study on a Wide-Speed-Range Helicopter Rotor/Turboshaft System," *Journal of Aircraft*, vol. 49, no. 4, pp. 1032–1038, 2012.

[26] G. A. Misté and E. Benini, "Performance of a Turboshaft Engine for Helicopter Applications Operating at Variable Shaft Speed," in *ASME 2012 Gas Turbine India Conference*, pp. 701–715, 2012.

[27] M. A. Stevens, R. F. Handschuh, and D. G. Lewicki, "Concepts for Variable/Multi-Speed Rotorcraft Drive System," Tech. Rep. NASA/TM-2008-215276, 2008.

[28] D. G. Lewicki, H. DeSmidt, E. C. Smith, and S. W. Bauman, "Two-Speed Gearbox Dynamics Simulation Predictions and Test Validation," Tech. Rep. NASA/TM-2010-216363, National Aeronautics and Space Administration, 2010.

[29] H. DeSmidt, K. Wang, E. C. Smith, and D. G. Lewicki, "Variable-Speed Simulation of a Dual-Clutch Gearbox Tiltrotor Driveline," Tech. Rep. NASA/TM-2012-217212, 2012.

[30] Z. B. Sarıbay, E. C. Smith, A. J. Lemanski, R. C. Bill, K. Wang, and S. Rao, "Compact Pericyclic Continuously Variable Speed Transmission Systems: Design Features and High-Reduction Variable Speed Case Studies," in *Proceedings of the 63rd Annual Forum of the American Helicopter Society*, (Virginia Beach, VA), May 2007.

[31] Z. B. Sarıbay, *Analytical Investigation of the Pericyclic Variable-Speed Transmission System for Helicopter Main-Gearbox*. PhD thesis, The Pennsylvania State University, 2009.

[32] P. X. Palcic, T. Garcia, and Y. Gmirya, "Variable Speed Transmission for a Rotary Wing Aircraft," Nov. 20 2007. US Patent 7,296,767.

[33] "XV-1 Convertiplane (McDonnell 1954)." http://www.boeing.com/history/mdc/graphics/his 2014. [Online; accessed 26-November-2014].

[34] T. Dirk, "Fairey Rotodyne, 1957." http://www.aviastar.org/helicopters_eng/fairey_rotodyne.php, 2014. [Online; accessed 26-November-2014].

[35] "CarterCopter Technology Demonstrator." http://www.cartercopters.com/cctd_images#photoGallery[gal]/0/, 2014. [Online; accessed 26-November-2014].

[36] "SP-3300 Flight Research at Ames, 1940-1997." http://history.nasa.gov/SP-3300/ch8.htm, 2014. [Online; accessed 26-November-2014].

[37] "AgustaWestland and BA609 - Bell Finally Ready to Sell?." http://fothesky.blogspot.com/2011/03/agustawestland-and-ba609-bell-finally.html, 2014. [Online; accessed 26-November-2014].

[38] "Lockheed XH-51A Compound." http://www.aviastar.org/helicopters_eng/lok_compaud.php, 2014. [Online; accessed 26-November-2014].

[39] "S-69 (XH-59A) Advancing Blade Concept Demonstrator." http://www.sikorskyarchives.com/S-69%20(XH-59A).php, 2014. [Online; accessed 26-November-2014].

[40] "X2 Technology Demonstrator." http://www.sikorsky.com/Innovation/Technologies/X2+Technology, 2014. [Online; accessed 26-November-2014].

[41] F. D. Harris, "An Overview of Autogyros and the McDonnell XV-1 Convertiplane," Tech. Rep. NASA/CR-2003-212799, 2003.

[42] J. W. Carter, "Extreme Mu Rotor," Jan. 17 2006. US Patent 6,986,642.

[43] M. D. Maisel, D. J. Giulianetti, and D. C. Dugan, "The History of the XV-15 Tilt Rotor Research Aircraft from Concept to Flight," 2000.

[44] W. E. Spreuer, "Experimental Flight Tests of the XH-51A Compound Helicopter," in *Proceedings of the 24th Annual Forum of the American Helicopter Society*, (Washington, DC), May 1968.

[45] F. P. Lentine, W. P. Groth, and T. H. Oglesby, "Research in Maneuverability of the XH-51A Compound Helicopter," tech. rep., DTIC Document, 1968.

[46] "Flying the Future." http://www.verticalmag.com/features/features_article/21326-flying-the-future.html, 2015. [Online; accessed 4-March-2015].

[47] A. J. Ruddell, "Advancing Blade Concept (ABC) Technology Demonstrator," Tech. Rep. USRADCOM-TR-81-D-5, Applied Technology Labratory U. S. Army Research and Technology Laboratories, 1981.

[48] A. Bagai, "Aerodynamic Design of the X2 Technology Demonstrator Main Rotor Blade," in *Proceedings of the 64th Annual Forum of the American Helicopter Society*, (Montreal, Canada), April 29–May 1 2008.

[49] D. Walsh, S. Weiner, K. Arifian, A. Bagai, T. Lawrence, and R. Blackwell, "Development Testing of the Sikorsky X2 Technology Demonstrator," in *Proceedings of the 65th Annual Forum of the American Helicopter Society*, (Grapevine, TX), American Helicopter Society, May 2009.

[50] "Full-Scale Wind-Tunnel Tests of a PCA-2 Autogiro Rotor," Tech. Rep. NACA 515, 1935.

[51] J. L. Jenkins, Jr, "Wind Tunnel Investigation of a Lifting Rotor Operating at Tip-Speed Ratios from 0.65 to 1.45," Tech. Rep. NASA TN-D-2628, 1965.

[52] A. Gessow and A. D. Crim, "A Method for Studying the Transient Blade-Flapping Behavior of Lifting Rotors at Extreme Operating Conditions," Tech. Rep. NASA TN-3366, 1955.

[53] J. L. McCloud, J. Biggers, and R. H. Stroub, "An Investigation of Full-Scale Helicopter Rotors at High Advance Ratios and Advancing Tip Mach Nnumbers," Tech. Rep. NASA TN-D-4632, National Aeronautics and Space Administration, 1968.

[54] B. D. Charles and W. H. Tanner, "Wind Tunnel Investigation of Semirigid Full-Scale Rotors Operating at High Advance Ratios," Tech. Rep. DAAJ02-67-C-0061, U.S. Army Aviation Materiel Laboratories, 1969.

[55] T. R. Quackenbush and D. A. Wachspress, "Aerodynamic Studies of High Advance Ratio Rotor Systems," in *Proceedings of the 67th Annual Forum of the American Helicopter Society*, (Virginia Beach, VA), May 2011.

[56] F. D. Harris, "Rotor Performance at High Advance Ratio: Theory versus Test," Tech. Rep. NASA/CR-2008-215370, 2008.

[57] R. M. Kufeld and W. G. Bousman, "UH-60A Helicopter Rotor Airloads Measured in Flight," *Aeronautical Journal*, vol. 101, no. 1005, pp. 217–227, 1997.

[58] T. R. Norman, P. Shinoda, R. L. Peterson, and A. Datta, "Full-Scale Wind Tunnel Test of the UH-60A Airloads Rotor," in *Proceedings of the 67th Annual Forum of the American Helicopter Society*, (Virginia Beach, VA), May 2011.

[59] A. Datta, H. Yeo, and T. R. Norman, "Experimental Investigation and Fundamental Understanding of a Full-Scale Slowed Rotor at High Advance Ratios," *Journal of the American Helicopter Society*, vol. 58, no. 2, pp. 1–17, 2013.

[60] B. Berry and I. Chopra, "Wind Tunnel Testing for Performance and Vibratory Loads of a Variable-Speed Mach-Scale Rotor," in *Proceedings of the 67th Annual Forum of the American Helicopter Society*, (Virginia Beach, VA), May 2011.

[61] B. Berry and I. Chopra, "Performance and Vibratory Load Measurements of a Slowed-Rotor at High Advance Ratios," in *Proceedings of the 68th Annual Forum of the American Helicopter Society*, (Fort Worth, TX), May 2012.

[62] B. Berry and I. Chopra, "High-Advance Ratio Wind Tunnel Testing of Two Mach-Scale Rotor Geometries," in *Proceedings of the 69th Annual Forum of the American Helicopter Society*, (Phoenix, AZ), May 2013.

[63] B. Berry and I. Chopra, "High-Advance Ratio Wind Tunnel Testing of a Model Rotor with Pressure Measurements," in *Fifth Decennial AHS Aeromechanics Specialists Conference*, (San Francisco, CA), January 2014.

[64] B. Berry and I. Chopra, "Slowed Rotor Wind Tunnel Testing of an Instrumented Rotor at High Advance Ratio," in *40th European Rotorcraft Forum*, (Southampton, UK), September 2014.

[65] R. L. Bennett, "Rotor System Design and Evaluation Using a General Purpose Helicopter Flight Simulation Program," Tech. Rep. AGARD CP 122, Advisory Group for Aerospace Research and Development, 1973.

[66] R. A. Ormiston, M. J. Rutkowski, and G. C. Ruzicka, "Comprehensive Aeromechanics Analysis of Complex Rotorcraft Using 2GCHAS," in *AHS Fourth Decennial AHS Aeromechanics Specialists Conference*, (San Francisco, CA), January 1994.

[67] H. Saberi, M. Khoshlahjeh, R. A. Ormiston, and M. J. Rutkowski, "Overview of RCAS and application to advanced rotorcraft problems," in *Fourth Decennial AHS Aeromechanics Specialists Conference*, (San Francisco, CA), January 1994.

[68] M. Potsdam, H. Yeo, and R. A. Ormiston, "Performance and Loads Predictions of a Slowed UH-60A Rotor at High Advance Ratios," in *39th European Rotorcraft Forum*, (Moscow, Russia), September 2013.

[69] W. Johnson, "Technology Drivers in the Development of Camrad II," in *Fourth Deccenial AHS Aeromechanics Specialists Conference*, (San Francisco, CA), January 1994.

[70] W. Johnson, "CAMRAD II Comprehensive Analytical Model of Rotorcraft Aerodynamics and DynamicsTheory Manual," Tech. Rep. Johnson Aeronautics, 1993.

[71] G. Bir, I. Chopra, and K. Nguyen, "Development of UMARC (University of Maryland Advanced Rotorcraft Code)," May 1990.

[72] D. H. Hodges and E. H. Dowell, "Nonlinear Equations of Motion for the Elastic Bending and Torsion of Twisted Nonuniform Rotor Blades," Tech. Rep. NASA TP-1566/AVRADCOM TR 80-A-1, 1980.

[73] A. Bagai and J. G. Leishman, "Free-Wake Analysis of Tandem, Tilt-Rotor and Coaxial Rotor Configurations," *Journal of the American Helicopter Society*, vol. 41, no. 3, pp. 196–207, 1996.

[74] M. J. Bhagwat, *Mathematical Modeling of the Transient Dynamics of Helicopter Rotor Wakes Using a Time-Accurate Free-Vortex Method*. PhD thesis, The University of Maryland, Department of Aerospace Engineering, Maryland, USA, 2001.

[75] A. Datta, M. Nixon, and I. Chopra, "Review of Rotor Loads Prediction with the Emergence of Rotorcraft CFD," *Journal of the American Helicopter Society*, vol. 52, no. 4, pp. 287–317, 2007.

[76] A. Datta, J. Sitaraman, J. D. Baeder, and I. Chopra, "Analysis Refinements for Prediction of Rotor Vibratory Loads in High-Speed Forward Flight," in *Proceedings of the 60th Annual Forum of the American Helicopter Society*, (Baltimore, MD), June 2004.

[77] J. Sitaraman, *CFD Based Unsteady Aerodynamic Modeling for Rotor Aeroelastic Analysis*. PhD thesis, The University of Maryland, Department of Aerospace Engineering, Maryland, USA, 2003.

[78] A. Abhishek, *Analysis, Validation, Prediction and Fundamental Understanding of Rotor Blade Loads in an Unsteady Maneuver*. PhD thesis, The University of Maryland, Department of Aerospace Engineering, Maryland, USA, 2010.

[79] A. Datta and I. Chopra, "Validation of Structural and Aerodynamic Modeling Using UH-60A Airloads Program Data," *Journal of the American Helicopter Society*, vol. 51, no. 1, pp. 43–58, 2006.

[80] M. Potsdam, H. Yeo, and W. Johnson, "Rotor Airloads Prediction Using Loose Aerodynamic/Structural Coupling," *Journal of Aircraft*, vol. 43, no. 3, pp. 732–742, 2006.

[81] T. A. Nygaard, H. Saberi, R. A. Ormiston, R. C. Strawn, and M. Potsdam, "CFD and CSD Coupling Algorithms and Fluid Structure Interface for Rotorcraft Aeromechanics in Steady and Transient Flight Conditions," in *Proceedings of the 62nd Annual Forum of the American Helicopter Society*, (Phoenix, AZ), May 2006.

[82] V. Sankaran, J. Sitaraman, A. Wissink, A. Datta, B. Jayaraman, M. Potsdam, D. Mavriplis, Z. Yang, D. OBrien, H. Saberi, R. Cheng, N. Hariharan, and R. Strawn, "Application of the Helios Computational Platform to Rotorcraft Flowfields," January 2010.

[83] D. A. Wachspress, T. R. Quackenbush, and A. H. Boschitsch, "Rotorcraft Interactional Aerodynamics with Fast Vortex/Fast Panel Methods," *Journal of the American Helicopter Society*, vol. 48, no. 4, pp. 223–235, 2003.

[84] P. G. Buning, "Consolidation of Time-Accurate, Moving Body Capabilities in OVERFLOW," in *6th Overset Composite Grid and Solution Technology Symposium*, 2002.

[85] C. W. Acree, Jr, "Impact of Technology on Heavy Lift Tiltrotors," in *Proceedings of the 62nd Annual Forum of the American Helicopter Society*, (Phoenix, AZ), May 2006.

[86] C. W. Acree, Jr, H. Yeo, and J. D. Sinsay, "Impact of Technology on Heavy Lift Tiltrotors," in *AIAA Internation Powered Lift Conference*, (London, UK), July 2008.

[87] C. W. Acree, Jr and W. Johnson, "Aeroelastic Stability of the LCTR2 Civil Tiltrotor," in *AHS Technical Specialists Meeting*, (Dallas, TX), October 2008.

[88] C. W. Acree, Jr, "Integration of Rotor Aerodynamic Optimization with the Conceptual Design of a Large Civil Tiltrotor," in *AHS Aeromechanics Conference*, (San Francisco, CA), January 2010.

[89] W. Johnson, G. K. Yamauchi, and M. E. Watts, "NASA Heavy Lift Rotorcraft Systems Investigation," in *2nd International Basic Research Conference on Rotorcraft Technology*, (Nanjing, China), November 2005.

[90] W. Johnson, G. K. Yamauchi, and M. E. Watts, "Design and Technology Requirements for Civil Heavy Lift Rotorcraft," in *AHS Vertical Lift Design Conference*, (San Francisco, CA), January 2006.

[91] W. Johnson, H. Yeo, and C. W. Acree, Jr, "Performance of Advanced Heavy-Lift, High-Speed Rotorcraft Configurations," in *AHS International Forum on Rotorcraft Multidisciplinary Technology*, (Seoul, Korea), October 2007.

[92] H. Yeo and W. Johnson, "Aeromechanicss Analysis of a Heavy Lift Slowed-Rotor Compound Helicopter," *Journal of Aircraft*, vol. 44, no. 2, pp. 501–508, 2007.

[93] H. Yeo and W. Johnson, "Optimum Design of a Compound Helicopter," *Journal of Aircraft*, vol. 46, no. 4, pp. 1210–1221, 2009.

[94] H. Yeo and W. Johnson, "Performance and Design Investigation of Heavy Lift Tilt-Rotor with Aerodynamic Interference Effects," *Journal of Aircraft*, vol. 46, no. 4, pp. 1231–1239, 2009.

[95] M. W. Floros and W. Johnson, "Performance Analysis of the Slowed-Rotor Compound Helicopter Configuration," *Journal of the American Helicopter Society*, vol. 54, no. 2, pp. 22002–22002, 2009.

[96] R. A. Ormiston, "Induced Power of the Helicopter Rotor," in *Proceedings of the 60th Annual Forum of the American Helicopter Society*, (Baltimore, MD), June 2004.

[97] D. A. Peters and C. J. He, "Finite State Induced Flow Models Part II: Three-Dimensional Rotor Disk," *Journal of Aircraft*, vol. 32, no. 2, pp. 323–333, 1995.

[98] W. Johnson, "A Comprehensive Analytical Model of Rotorcraft Aerodynamics and Dynamics. Part 1. Analysis Development," tech. rep., DTIC Document, 1980.

[99] S. Kottapalli, "Performance and Loads Correlation of a UH-60A Slowed Rotor at High Advance Ratios," in *Future Vertical Lift Aircraft Design Conference*, (San Francisco, CA), January 2012.

[100] H. Yeo, "Investigation of Performance and Loads of a UH-60A Rotor att High Advance Ratios," in *Proceedings of the 68th Annual Forum of the American Helicopter Society*, (Fort Worth, TX), May 2012.

[101] R. A. Ormiston, "Rotor Aerodynamic Characteristics at High Advance Ratio Relevant to Compound Rotorcraft," in *Future Vertical Lift Aircraft Design Conference*, (San Francisco, CA), January 2012.

[102] M. Potsdam, A. Datta, and B. Jayaraman, "Computational Investigation and Fundamental Understanding of a Slowed UH-60A Rotor at High Advance Ratios," in *Proceedings of the 68th Annual Forum of the American Helicopter Society*, (Fort Worth, TX), May 2012.

[103] J. G. Leishman, "Validation of Approximate Indicial Aerodynamic Functions for Two-Dimensional Subsonic Flow," *Journal of Aircraft*, vol. 25, no. 10, pp. 914–922, 1988.

[104] J. G. Leishman and T. S. Beddoes, "A Semi-Empirical Model for Dynamic Stall," *Journal of the American Helicopter Society*, vol. 34, no. 3, pp. 3–17, 1989.

[105] I. Chopra and G. Bir, "University of Maryland Advanced Rotorcraft Code: UMARC," in *Fourth Decennial American Helicopter Society Aeromechanics Specialists Conference*, January 1994.

[106] J. Davis tech. rep.

[107] F. McHugh, R. Clark, and M. Soloman, "Wind Tunnel Investigation of Rotor Lift and Propulsive Force at High Speed: Data analysis," 1977.

[108] M. G. Ballin, *A High Fidelity Real-Time Simulation of a Small Turboshaft Engine*. National Aeronautics and Space Administration, Ames Research Center, 1988.

[109] A. H. Lind, J. N. Lefebvre, and A. R. Jones, "Experimental Investigation of Reverse Flow over Sharp and Blunt Trailing Edge Airfoils," 2013.

[110] M. Amiraux, S. Medida, D. Ghosh, S. Thomas, S. Boyer, and J. D. Baeder, "Fuselage Modelization for Multi-Fidelity Coupled CFD/CSD Simulation of Rotorcrafts in BVI Condition," in *AIAA Applied Aerodynamics Conference*, (San Diego, CA), June 2013.

[111] W. Johnson, *Rotorcraft Aeromechanics*. Cambridge University Press, 2013.

[112] F. D. Harris, "Preliminary Study of Radial Flow Effects on Rotor Blades," *Journal of the American Helicopter Society*, vol. 11, no. 3, pp. 1–21, 1966.

[113] J. Hodara and M. J. Smith, "Improvement of Crossflow Aerodynamic Predictions for Forward Flight at All Advance Ratios," in *40th European Rotorcraft Forum*, (Southampton, UK), September 2014.

[114] T. R. Norman, R. L. Peterson, T. H. Maier, and H. Yeo, "Evaluation of Wind Tunnel and Scaling Effects with the UH-60A Airloads Rotor," tech. rep., DTIC Document, 2011.

[115] Y. Tanabe, S. Saito, and H. Sugawara, "Evaluation of RotorNoise Reduction by Active Devices Using a CFD/CSD Coupling Analysis Tool Chain," in *1st Asian Australian Rotorcraft Forum and Exhibition*, (Busan, Korea), February 2012.

[116] M. Sgiura, Y. Tanabe, and H. Sugawara, "Development of a Hybrid Method of CFD and Prescribed Wake Model for Helicopter BVI Prediction," *Transactions of the Japan Society for Aeronautical and Space Sciences*, vol. 56, no. 6, 2013.